The SLD Vertex Detector Upgrade (VXD3) and a Study of $b\bar{b}g$ Events

A thesis submitted for the degree of Doctor of Philosophy

by

Paul John Dervan

Department of Physics, Brunel University

October 1998

Abstract

This thesis presents a variety of work concerning the design, construction and use of the SLD's vertex detector.

SLD's pioneering 120 Mpixel vertex detector, VXD2, was replaced by VXD3, a 307Mpixel CCD vertex detector in January 1996. The motivation for the up-grade detector and its subsquent construction and testing are described in some detail. This work represents the collaborative work of a large number of people. My work was mainly carried out at EEV on the testing of the CCDs and subsequent ladders. VXD3 was commissioned during the 1996 SLD run and performed very close to design specifications.

Monitoring the position of VXD3 is crucial for reconstructing the data in the detector for physics analysis. This was carried out using a capacitive wire position monitoring system. The system indicated that VXD3 was very stable during the whole of the 1996 run, except for known controlled movements. VXD3 was aligned globally for each period in-between these known movements using the tracks from $e^+e^- \rightarrow Z^0 \rightarrow hadrons$.

The structure of three-jet $b\bar{b}g$ events has been studied using hadronic Z^0 decays from the 1993-1995 SLD data. Three-jet final states were selected and the CCD-based vertex detector was used to identify two of the jets as a b or $\bar{b}$. The distributions of the gluon energy and polar angle with respect to the electron beam direction were examined and were compared with perturbative QCD predictions. If was found that the QCD Parton Shower prediction was needed to describe the data well. These distributions are potentially sensitive to an anomalous b chromomagnetic moment κ. κ was measured to be $-0.031^{+0.038}_{-0.039}(Stat.)^{+0.003}_{-0.004}(Syst.)$, which is consistent with the Standard Model, with 95% confidence level limit, $-0.106 < \kappa < 0.044$.

Acknowledgements

Many people have contributed to the work covered in this thesis. I would like to thank them all. In particular I would like to thank the following:

My supervisor, Steve Watts, and Chris Damerell and Phil Burrows without whom you would not be reading this thesis.

Everybody at EEV, in particular Colin Hotston, John Bloomer, Wolfgang Suske and all the clean room staff.

All my colleagues at SLAC and Brunel. There are too many to mention by name, but they know who they are. Special thanks go to Dave Muller, Tom Rizzo, Erez Etzion, Dave Jackson, Su Dong, John Jaros, Adrian McKemey, Derek Imrie, the tracking group and the QCD group.

PPARC for funding my Ph.D. study and PPARC and the Department of Energy, USA, for funding the experiment which made this thesis possible.

Finally, I would especially like to thank my family and friends, especially my mum and dad, Andrew, Mark, Karl, Michelle, Sarah and Claire who have supported me throughout the Ph.D. Special thanks also go to Julia Schoots, whose endless supply of letters were a continuous source of humour.

Contents

List of Figures

List of Tables

Chapter 1

Standard Model

1.1 Introduction

The term 'Standard Model' refers to our understanding of the fundamental particles that make up our universe, and their interactions. The Standard Model is formed from the quantum field theories of the electroweak (unified theory of the electromagnetic and the weak interactions) and the strong interactions.

The fundamental particles, all of which are fermions (spin $\frac{1}{2}$), are divided into three generations of quarks and leptons. The leptons consist of the electron, muon and tau, which carry the electroweak charges, and their associated neutrinos, which only carry the weak charge. The quarks consist of the up, down, strange, charm, bottom and top quarks, which carry the electroweak and colour charges, and thus interact via both the electroweak and the strong interactions. They combine in groups of quark and anti-quark (mesons) or three quarks (baryons) to form hadrons.

The fundamental forces of nature are represented by vector (spin 1) bosons which mediate the interactions between the leptons and the quarks. The electroweak interactions are mediated by four such bosons: the massless photon (γ), which mediates the electromagnetic force, the neutral Z^0 ($M_Z = 91.187$ GeV/c^2 [1]), and the charged W^+ and W^- ($M_{W\pm} = 80.33$ GeV/c^2 [1]), all of which are responsible for the weak force. The stong interactions are mediated by massless particles called gluons.

The masses of the fundamental fermions and bosons are believed to be generated via the scalar (spin 0) Higgs boson [2], which has yet to be verified by experiment.

$$\begin{pmatrix} \nu_e \\ e \end{pmatrix} \quad \begin{pmatrix} \nu_\mu \\ \mu \end{pmatrix} \quad \begin{pmatrix} \nu_\tau \\ \tau \end{pmatrix}$$

$$\begin{pmatrix} u \\ d \end{pmatrix} \quad \begin{pmatrix} c \\ s \end{pmatrix} \quad \begin{pmatrix} t \\ b \end{pmatrix}$$

Table 1.1: Fermion constituents of the Standard Model.

The fermions of the Standard Model are summarized in Table 1.1.

This thesis presents an analysis of the strong interaction involved in $b\bar{b}g$ events. The next sections briefly describes the electroweak and strong interactions. The discussions on strong interactions are based on those given in [3]. For more details see references [4] and [5].

1.2 The Electro-Weak Interaction

The theory of electroweak (EW) interactions was developed by Glashow, Weinberg and Salam [4]. This theory successfully unified the electromagnetic theory (QED) and the theory of weak interactions in the framework of a gauge invariant quantum field theory with the symmetry group SU(2) $\times$ U(1).

This gauge theory has the advantage that the gauge bosons occur naturally by requiring invariance under local gauge transformations, and the theory is renormalisable. But the gauge bosons are massless, while the mediators of the weak interactions must be massive to account for the short range nature of the weak interactions. This problem is solved by the introduction of scalar fields that spontaneously break the SU(2) $\times$ U(1) symmetry and provide the weak vector bosons with mass while leaving the photon massless. The source of this mechanism is the Higgs boson.

In the process $e^+e^- \rightarrow f\overline{f}$ (where f is the final state fermion), there are two known neutral gauge bosons that may be exchanged: the photon and the Z^0. The lowest order Feynman diagrams for these processes are shown in Figure 1.1. The cross-section, σ, is proportional to the square of the sum of the two matrix ele-

ments represented by these diagrams, $|\mathcal{M}_\gamma + \mathcal{M}_{Z^0}|^2$. Hence there are three terms to consider: a purely electromagnetic term, a purely weak term and an interference term.

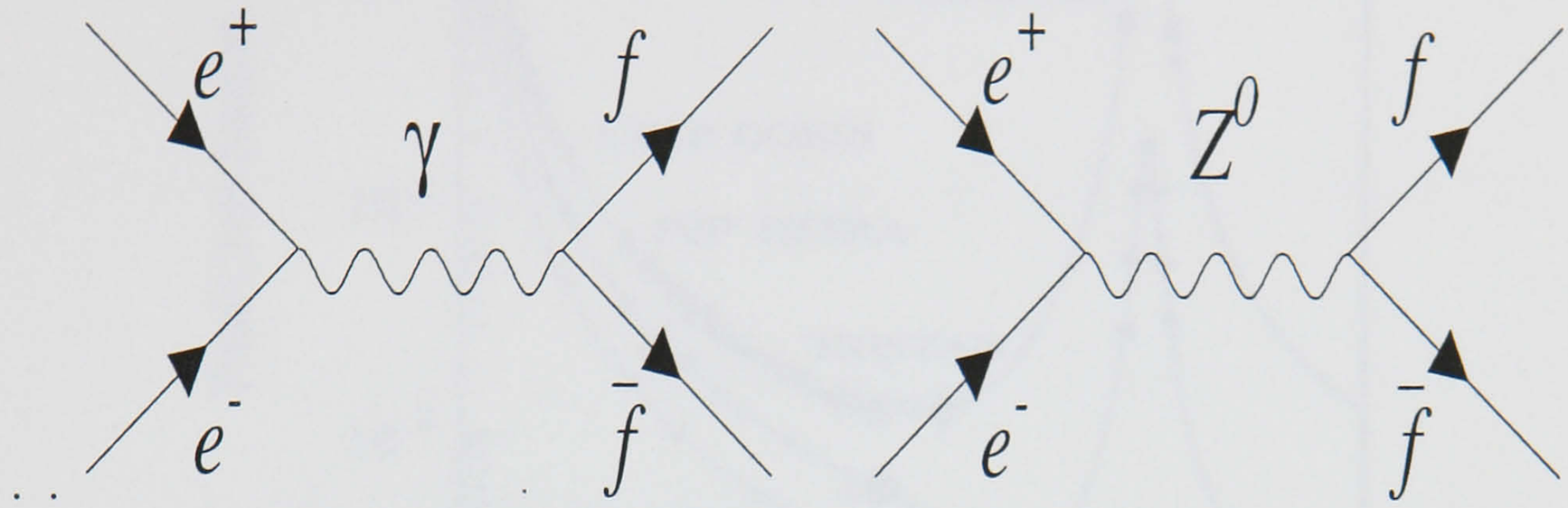

Figure 1.1: Tree level Feynman diagrams representing $e^+e^- \rightarrow f\overline{f}$.

The total cross section for $e^+e^- \rightarrow hadrons$ as a function of center-of-mass energy is shown in Figure 1.2. The Z^0 pole is clearly seen. Around the Z^0 mass the effects of the electromagnetic term can be safely neglected, as the weak term dominates. Additionally the $\gamma - Z^0$ term is very small. Thus the Z^0 exchange term is the dominant one.

The cross-section (for massless fermions) for $e^+e^- \rightarrow f\overline{f}$ at the Z^0 pole (with unpolarised positrons and longitudinally polarised electrons, as at Stanford Linear Collider) can be expressed by:

$$\frac{d\sigma}{d\Omega} = K(\nu_e^2 + a_e^2)(\nu_f^2 + a_f^2)[(1 - A_e P_e)(1 + \cos^2\theta) + 2A_f(A_e - P_e)\cos\theta]. \quad (1.1)$$

Where, P_e is the signed longitudinal polarisation of the electron ($P_e > 0$ for right handed electrons), ν_f and a_f donate the vector and axial-vector couplings of the Z^0 to the fermions f (a_e and v_e are the couplings specifically to electrons), and θ is the angle of the final state fermion f with respect to the initial state electron beam. The quantity A_f is defined as:

$$A_f = \frac{2\nu_f a_f}{\nu_f^2 + a_f^2} \quad (1.2)$$

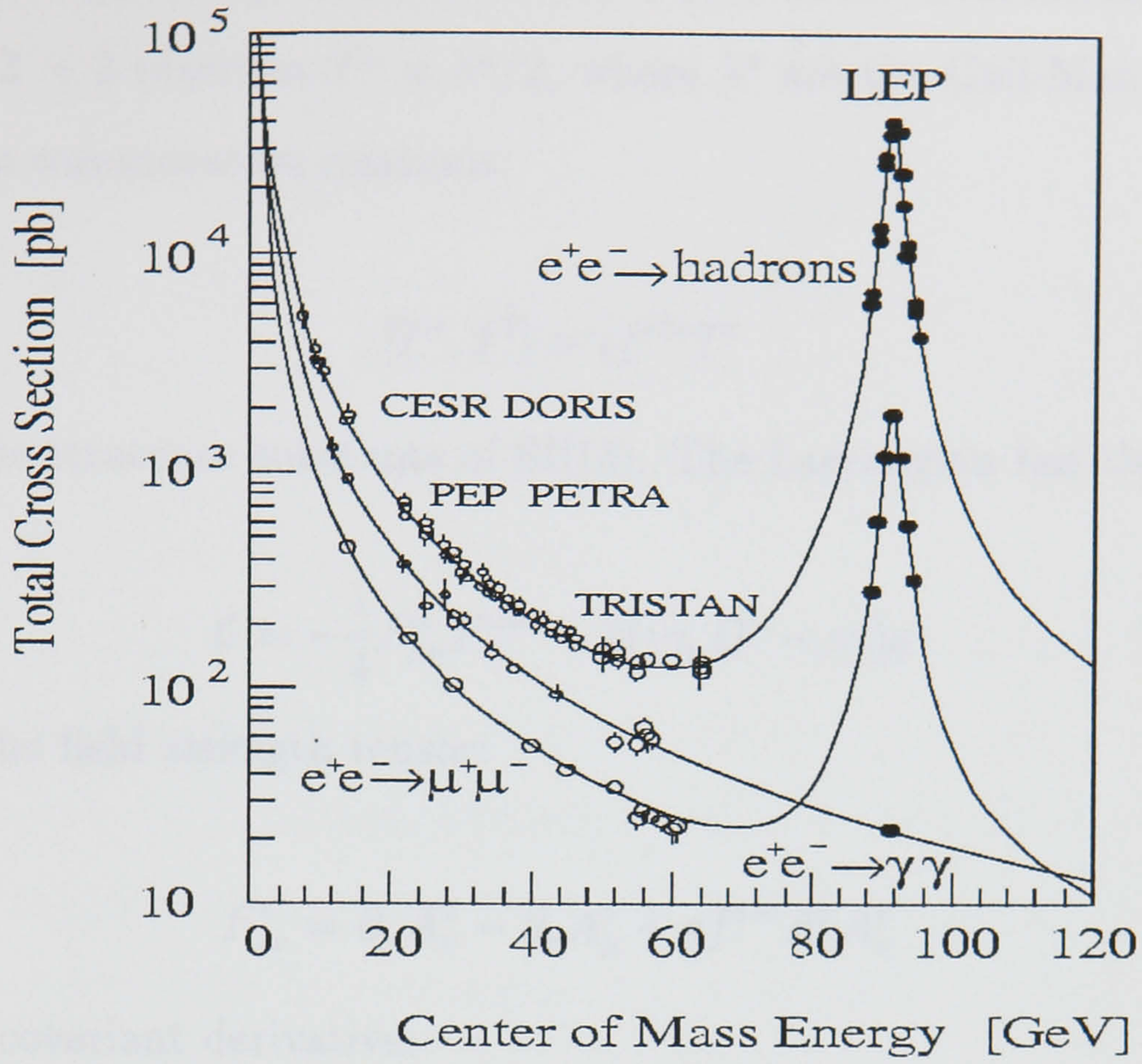

Figure 1.2: The $e^+e^- \rightarrow hadrons$ cross-section as a function of centre of mass energy [6].

and the coefficient:

$$K = \frac{\alpha^2}{4\sin^4 2\theta_w} \frac{s}{(s - M_z^2)^2 + \frac{\Gamma_z^2 s^2}{M_z^2}} \tag{1.3}$$

with α being the electromagnetic structure constant, and $s = E_{cm}^2$. M_z and Γ_z are the mass and total decay width of the Z^0 boson, respectively.

1.3 The Strong Interaction

The theory of the strong interactions between quarks and gluons (collectively referred to as partons) is known as Quantum Chromodynamics (QCD) [7]. It is a non-Abelian Yang-Mills gauge theory that describes the interactions of the triplet of spin-$\frac{1}{2}$ quarks possessing the colour quantum number (c = r,b,g) via an octet of vector gluons. The spinor quark fields $q_c(x)$ transform as the fundamental representation of the SU(3) group, whilst the gluon fields $A_\mu^a(x)(a = 1, 2, ..., 8)$ transform

according to the adjoint representation. The SU(3) colour transformations are generated by the 3×3 matrices $T^a = \lambda^a/2$, where λ^a are the Gell-Mann matrices [8] which obey the commutation relations:

$$[T^a, T^b] = if^{abc}T^c \tag{1.4}$$

and f^{abc} are the structure constants of SU(3). The Lagrangian has the form:

$$\mathcal{L} = -\frac{1}{4}F^a_{\mu\nu}F^{\mu\nu a} + \overline{q}(i\gamma_\mu D^\mu - m)q \tag{1.5}$$

where $F^{\mu\nu}$ is the field strength tensor:

$$F^a_{\mu\nu} = \partial_\mu A^a_\nu - \partial_\nu A^a_\mu + gf^{abc}A^b_\mu A^c_\nu \tag{1.6}$$

and D_μ is the covariant derivative:

$$D_\mu = \partial_\mu - igT^a A^a_\mu(x) \tag{1.7}$$

g is the bare coupling constant of the theory, m is the bare mass of the quark field and the gluons are massless.

Physical quantities such as cross-sections can be calculated from the Lagrangian, but are found to be divergent. The infinities are removed by a process of renormalisation in which they are 'absorbed' into the basic constants of the theory such as the couplings and masses, which thereby acquire finite values. The couplings and masses are hence physical constants and cannot be calculated by the theory. The requirement of invariance under a mathematical operation known as a local gauge transformation, described by the gauge group SU(3), leads to a unique Lagrangian which severely restricts the possible interaction terms between quarks and gluons. This local gauge invariance is also necessary to ensure the theory is renormalisable.

The last term in Equation 1.6, required by local gauge invariance, separates the behaviour of QCD from that of Quantum Electrodynamics (QED), as it implies that the gluons themselves carry the colour charge. This is due to the non-Abelian nature of the gauge group. The Lagrangian can be written in symbolic form as:

$$\mathcal{L} = q\bar{q} + A^2 + gq\bar{q}A + gA^3 + g^2A^4 \tag{1.8}$$

The first three terms have QED analogues. They describe the free propagation of quarks and gluons and the quark gluon interaction. The remaining two terms show the presence of three and four gluon vertices in QCD and reflect the fact that gluons themselves carry colour charge. It has become normal to refer to the quantity $\alpha_s = g^2/4\pi$ as the strong coupling constant.

Another characteristic feature of non-Abelian gauge theories is that the coupling strength decreases with the four-momentum-transfered, Q^2, in the interaction. This leads to the property of asymptotic freedom in which, at high Q^2 or small distances, the coupling strength decreases and the quark and gluons are quasi-free, and explains the observation that in high energy electron-nucleon scattering experiments the electrons scatter off pointlike, quasi-freely moving partons within the nucleon [9]. By contrast in large distance or low Q^2 interactions, the coupling strength increases so that quarks and gluons remain bound together or 'confined' in the colour singlet states. This is also in agreement with the observation that only colour neutral hadrons, not free quarks and gluons, are produced in particle interactions. Unfortunately, because the coupling strength is relatively large in 'soft' low Q^2 processes, the transition of partons into hadrons, known as hadronisation or fragmentation, cannot be calculated by perturbative QCD methods. Non-perturbative calculations are very difficult. At present therefore, hadronisation can only be described by phenomenological models, to be discussed later in this chapter.

The essential features of QCD can be summarised as:

- quarks with spin $\frac{1}{2}$ exist as colour triplets
- gluons with spin 1 exist as colour octets
- the coupling $q\bar{q}g$ exists
- the couplings ggg and $gggg$ exist
- the couplings are equal

Quark Flavour	Spin	Baryon Number	Lepton Number	Charge
u (up)	$\frac{1}{2}$	$\frac{1}{3}$	0	$+\frac{2}{3}$
d $(down)$	$\frac{1}{2}$	$\frac{1}{3}$	0	$-\frac{1}{3}$
s $(strange)$	$\frac{1}{2}$	$\frac{1}{3}$	0	$-\frac{1}{3}$
c $(charm)$	$\frac{1}{2}$	$\frac{1}{3}$	0	$+\frac{2}{3}$
b $(bottom)$	$\frac{1}{2}$	$\frac{1}{3}$	0	$-\frac{1}{3}$
t (top)	$\frac{1}{2}$	$\frac{1}{3}$	0	$+\frac{2}{3}$

Table 1.2: Summary of the quark quantum numbers.

- the effective universal coupling α_s decreases with increasing energy scale like lnQ^2

The experimental evidence for the first three of these points will be described in some detail in the next few sections. For discussions of the other points see, for example, reference [3].

1.4 Experimental Verification of QCD

1.4.1 Quarks

Quarks were first postulated in 1964 by Gell-Mann and Zweig [10] to explain the rich spectroscopy of recently discovered mesons and baryons (collectively known as hadrons) in terms of $q\overline{q}$ and qqq (or $\overline{qqq}$). Quarks have spin $\frac{1}{2}$, and were assigned the quantum number of flavour ($f = u, d, s, c, b, t$), and baryon number $\frac{1}{3}$. It was also necessary to assign the quantum number of colour ($c = r, g, b$) to explain the existence of states such as Δ^{++} $(= u \uparrow u \uparrow u \uparrow)$, which otherwise would have been forbidden as they contain three quarks in identical quantum states, which would violate the Pauli exclusion principle. To explain the measured charges of the hadrons the quarks were assigned fractional charges. The quantum numbers of the quarks are summarised in Table 1.2

1.4.2 Experimental Evidence for Quarks

The first direct evidence for quarks came from observations at SLAC in the late 1960s that in electron nucleon scattering experiments at high Q^2 the electron scatters from quasi-free pointlike particles. Another experiment that also demonstrated the existence of quarks was the observation of jets in the Mark I experiment at SPEAR in 1975 [11]. The experiment used a quantity called sphericity [12], to measure the isotropy in the event particle flow,

$$S = \frac{\mathrm{Min}(\sum_i p_{\perp i}^2)}{\sum_i \vec{p}_i^2} \tag{1.9}$$

where $\vec{p}_i$ represents the momentum and $p_{\perp i}$ is the transverse momentum of the particle i and the sums run over all particles in each event. In each event an axis, the sphericity axis was defined so as to minimise the quantity in brackets in the numerator. A completely isotropic distribution of particles, or a spherical event, would have S $\sim$ 1, whilst a perfectly collimated back-to-back two jet event would have S $\sim$ 0. Figure 1.3 shows the sphericity distributions from Mark I at several center of mass (c.m.) energies. A clear change in the sphericity distribution can be seen as the energy is increased from 3.0 to 7.4 GeV. It is clearly seen that the distribution shifted to a lower value of sphericity as the energy increases. This was interpreted in terms of an increasing degree of collimation of particle production with c.m. energy, namely the onset of production of two back to back jets of hadrons. At higher energies the two jets become very clear. Figure 1.4 shows a two jet event in SLD, at the Z^0 pole.

1.4.3 The Spin of the Quarks

The spin of the quarks can be determined by studying the polar angle of the jets with respect to the beam direction. If two spin $\frac{1}{2}$ particles are produced the distribution is expected to have a $1 + \cos^2\theta$ shape.

The Mark I analysis also measured the spin of the quark and anti-quark to be $\frac{1}{2}$. Similar studies were repeated at higher energies at the PETRA collider. Figure 1.5

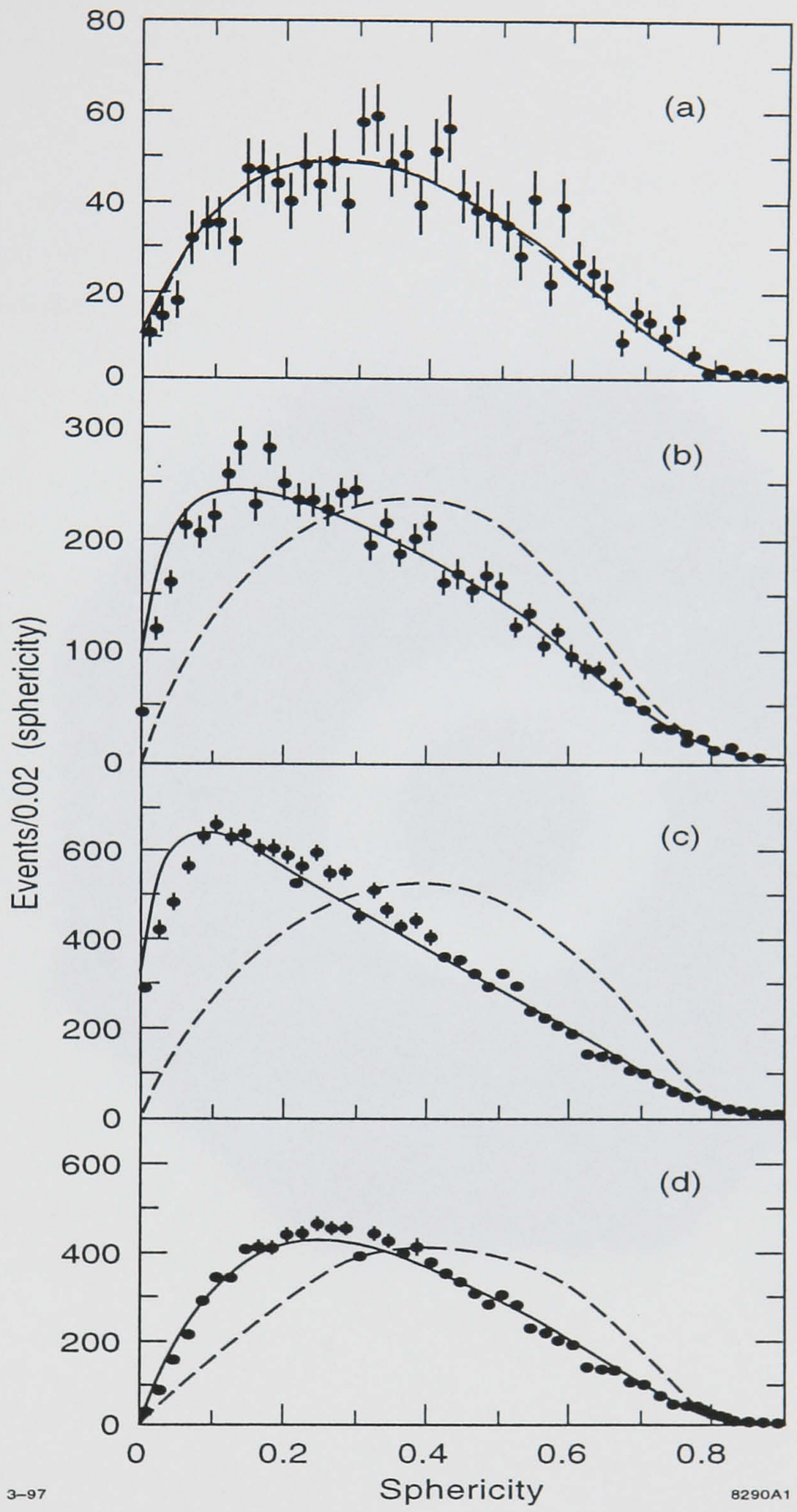

Figure 1.3: Sphericity distributions measured in Mark I [12] at (a) 3.0, (b) 6.2, (c) 7.4 GeV c.m. energy. The narrowing of the distribution, and the trend towards lower values as the c.m. energy increases, represents evidence for collimated production of hadrons in e^+e^- annihilation. The dashed line represents the expectation from a 'phase-space' model of hadron production. (d) as (c) but for a subset of events containing particles with scaled momentum, $2p/Q$, less than 0.4.

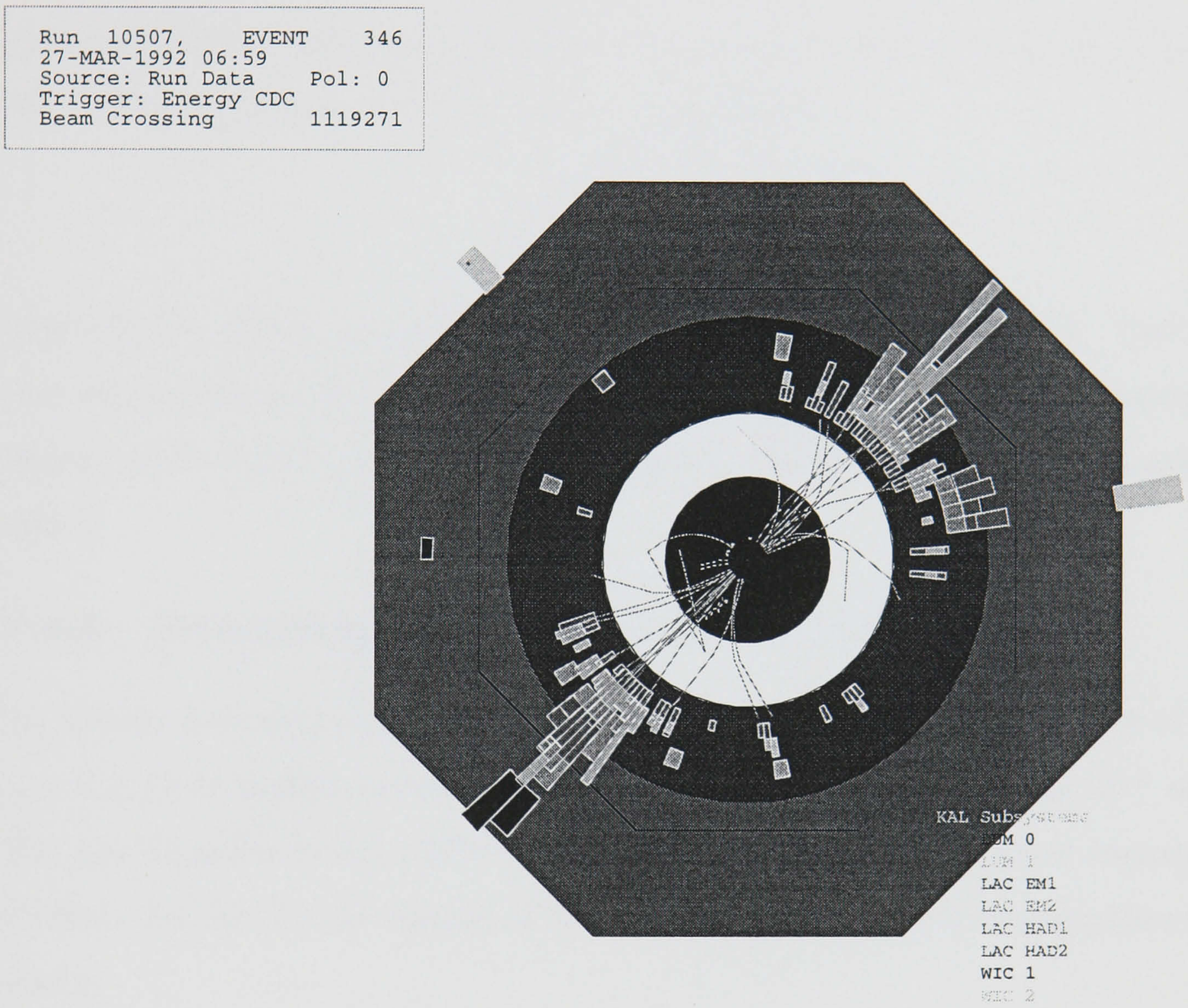

Figure 1.4: View of a 2-jet events in SLD. The curved lines originating from the centre of the detector are charged tracks; the irregular rectangular boxes that point back to the origin are energy deposits in the calorimeter system. See Chapter 2 for a description of the various detector elements.

shows the polar angle (θ_S) of the sphericity axis at 14, 22 and 34 GeV from TASSO [13]. A fit to the function:

$$\frac{dN}{d\cos\theta} \propto 1 + a_{S,T}\cos^2\theta_{S,T} \tag{1.10}$$

yielded, at 34 GeV, $a_S = 1.03 \pm 0.07$. This is close to unity, which is expected for the production of two spin $\frac{1}{2}$ particles. Also shown in Figure 1.5 is the polar angle (θ_T) of the thrust axis [14]. Thrust (T) is defined as:

$$T = \max\frac{\sum_i |\vec{n}\cdot\vec{p_i}|}{\sum_i |\vec{p_i}|} \tag{1.11}$$

where $\vec{n}$, the thrust axis, lies on the axis that maximises the sum T. The sum is over all particles in the event. The thrust axis polar angle distribution was fitted to obtain, at 34 GeV, $a_T = 1.01 \pm 0.06$. Again confirming the fact that quarks have spin $\frac{1}{2}$.

1.4.4 Determination of the Number of Colours

As already discussed, the quarks had to be assigned the quantum number of colour ($c = r, g, b$), to explain the existence of the spin $\frac{3}{2}$ baryon states such as Δ^{++} and Ω^-. The quark-parton model (QPM) hence requires that $N_c = 3$. Further experimental evidence for the N_c, the number of colours, was obtained by measuring the ratio R, where:

$$R = \frac{\sigma(e^+e^- \to hadrons)}{\sigma(e^+e^- \to \mu^+\mu^-)} = 3\sum_q e_q^2 \tag{1.12}$$

Figure 1.6 shows a summary of R measurements made up to 1988, as a function of c.m. energy [15]. There are a few points of interest in this plot. Firstly the increase in R just above $Q^2 = 10$ and 100 GeV^2 represent the $c\bar{c}$ and $b\bar{b}$ thesholds. Secondly the QPM+QCD+Z^0 prediction comes very close to data if the quarks are assigned fractional charges and the number of colours $N_c = 3$.

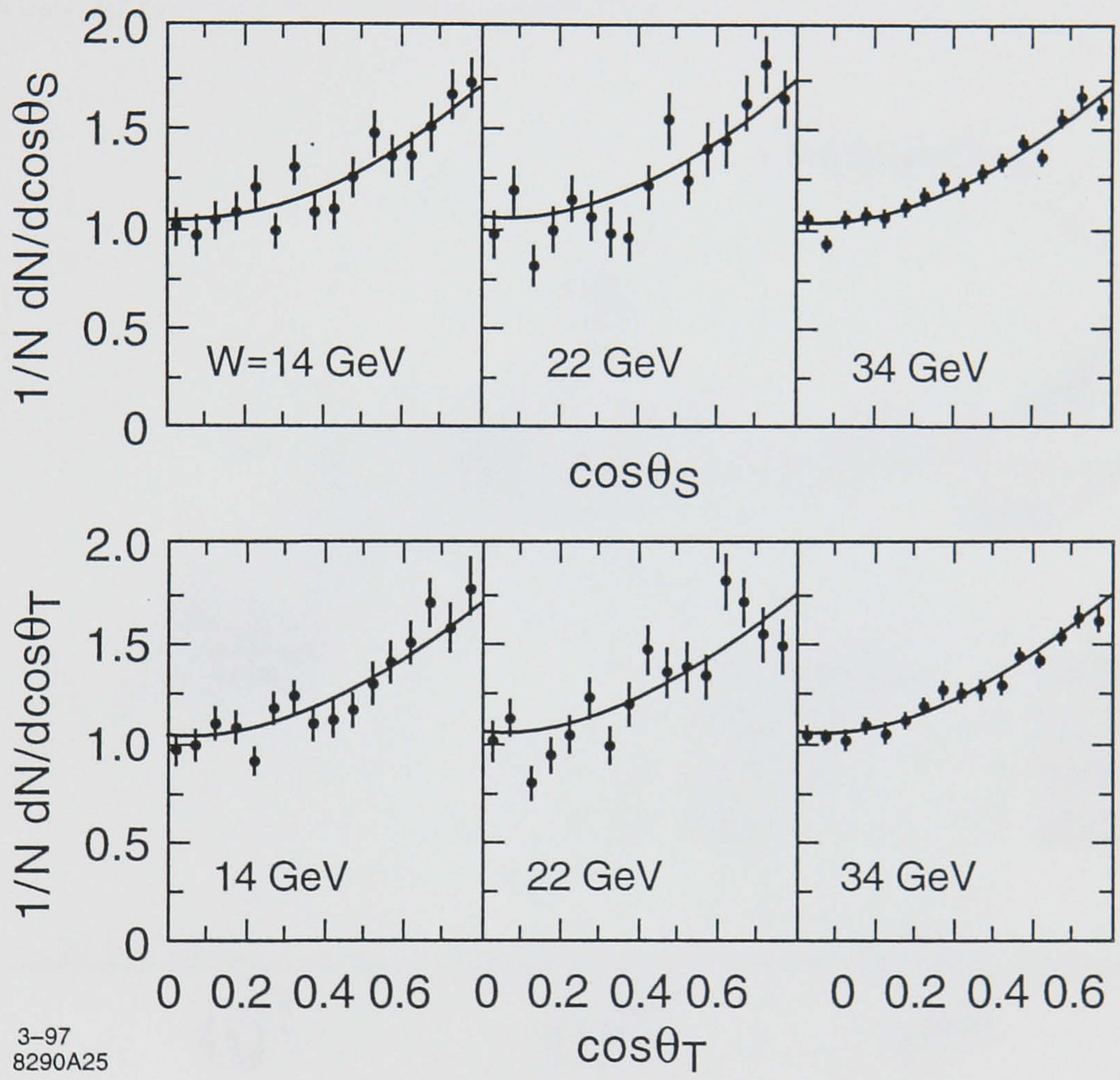

Figure 1.5: Polar-angle distributions of the sphericity and thrust axis from TASSO [13]. The $1+\cos^2\theta$ form is characteristic of the production of two spin-$\frac{1}{2}$ particles in e^+e^- annihilation.

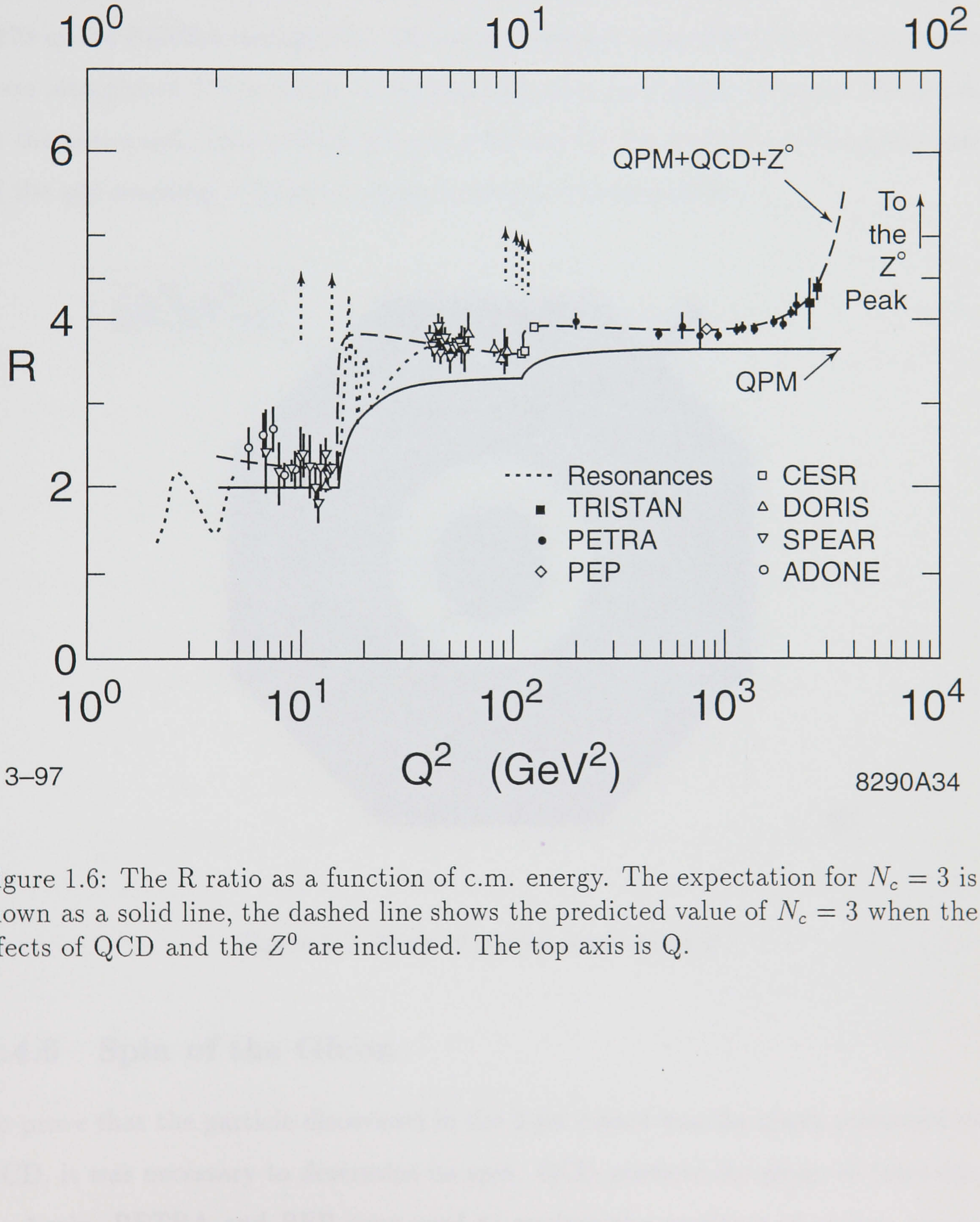

Figure 1.6: The R ratio as a function of c.m. energy. The expectation for $N_c = 3$ is shown as a solid line, the dashed line shows the predicted value of $N_c = 3$ when the effects of QCD and the Z^0 are included. The top axis is Q.

1.4.5 Experimental Evidence for the Gluon

Experimental evidence for the existence of massless neutral particles within the nucleus first came from electron-nucleon scattering experiments already mentioned. It was found that roughly only one half of the nucleon momentum was carried by the charged quarks, hence the remaining momentum must be carried by the gluons. The first direct evidence come from the observation of three distinct jets observed in 1979 at the PETRA storage ring [16] at c.m. energies around 20 GeV. These events were interpreted [17] in terms of the radiation of a hard gluon by either the quark or the anti-quark, thus providing direct evidence for the existence of the gluon and of the $q\bar{q}g$ coupling. Figure 1.7 shows a three-jet event in SLD.

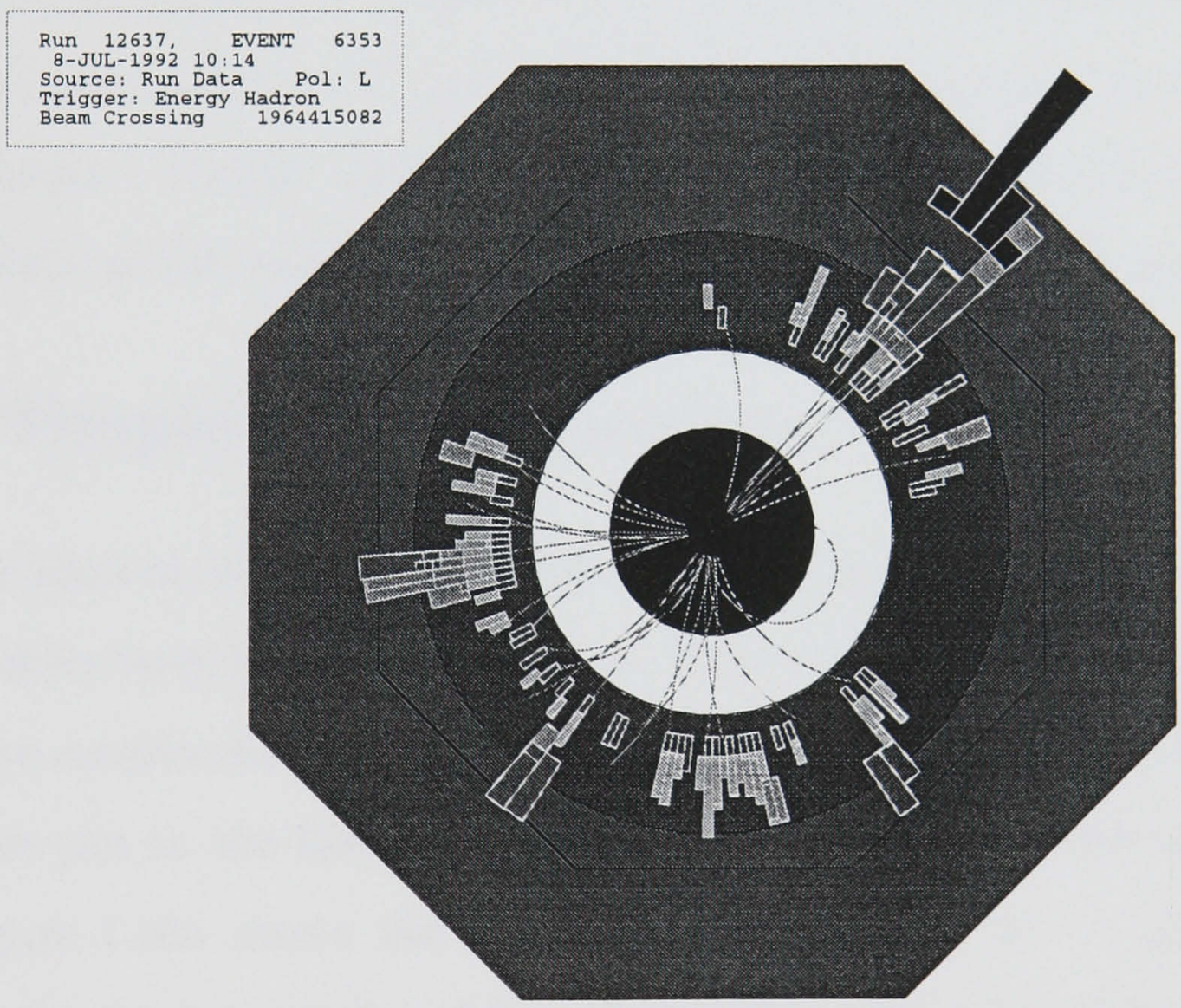

Figure 1.7: View of a 3-jet event in SLD.

1.4.6 Spin of the Gluon

To prove that the particle discovered in the 3-jet events was the gluon predicted by QCD, it was necessary to determine its spin. QCD predicts the gluon to have spin 1. Again, PETRA and PEP were used to analyse the partition of energy among

the three jets. The jets were ordered according to their energies $E_1 > E_2 > E_3$ and normalised by the c.m. energy Q, to obtain the scaled jet energies:

$$x_i = \frac{2E_i}{Q} \ (i = 1, 2, 3) \tag{1.13}$$

see Figure 1.8a. Making a Lorentz boost of the event into the rest frame of jets 2 and 3, the Ellis-Karliner angle θ_{EK} is defined [18] to be the angle between jets 1 and 2 in this frame, see Figure 1.8b. For massless partons at tree level:

$$\cos\theta_{EK} = \frac{x_2 - x_3}{x_1} \tag{1.14}$$

Figure 1.9 shows the Ellis-Karliner distribution from TASSO [13] at 30 GeV, compared with the prediction of QCD (spin-1 or vector). Also shown are the predictions of models assuming spin-0 (scalar gluon) [19]. The data of Figure 1.9 clearly favour spin-1 gluons. Similar studies have been carried out by the LEP and SLC [20] experiments, which reinforce the conclusion that gluons have spin-1.

1.5 Simple QCD Processes

QCD calculations of the total hadronic cross section involve amplitudes corresponding to parton-level Feynman diagrams. This cross section, derived by squaring the sum of the amplitudes, may be expanded in terms of α_s/π. The Feynman diagrams which give rise to the first three terms in the series are shown in Figures 1.10-1.12 [21]. Figure 1.10a shows the Feynman diagram for $e^+e^- \rightarrow q\bar{q}$ at 'zeroth' order. This process can be calculated from QED alone. However there are virtual corrections to this process from internal gluon loops shown in Figures 1.10b and 1.10c. Figure 1.11a shows the $O(\alpha_s)$ diagrams for $e^+e^- \rightarrow q\bar{q}g$ and Figure 1.11b shows the $O(\alpha_s^2)$ virtual corrections to the 3-parton state. Finally Figure 1.12 shows the diagrams for 4 partons. It is clear that with each step in the series the number of diagrams to be taken into consideration greatly increases.

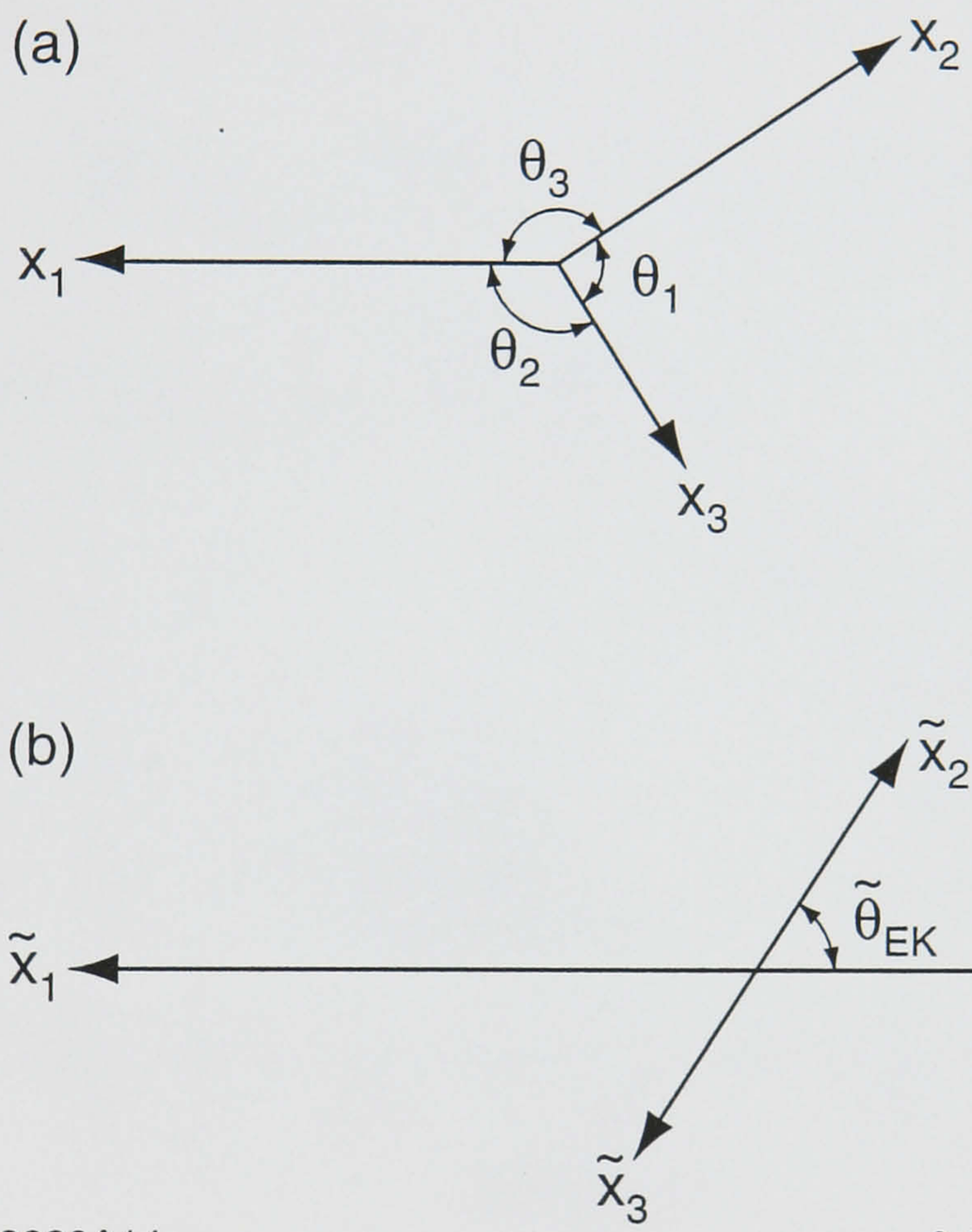

Figure 1.8: (a) Representation of the momentum vectors in a three-jet event, and (b) definition of the Ellis-Karliner angle.

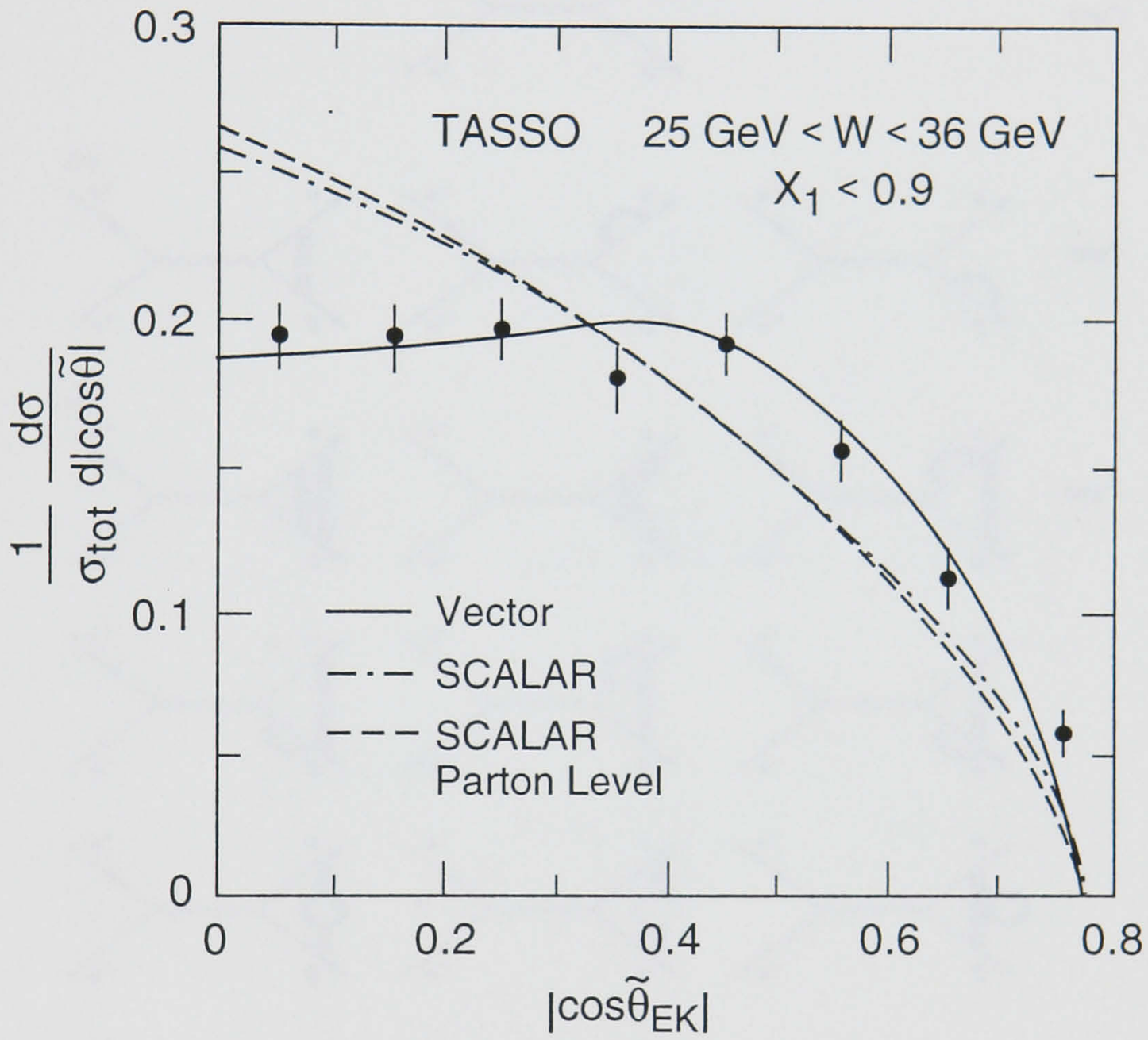

Figure 1.9: The Ellis-Karliner angle distribution of three-jet events obtained by TASSO [13] at Q~30 GeV; the data favour spin-1 (vector) gluons.

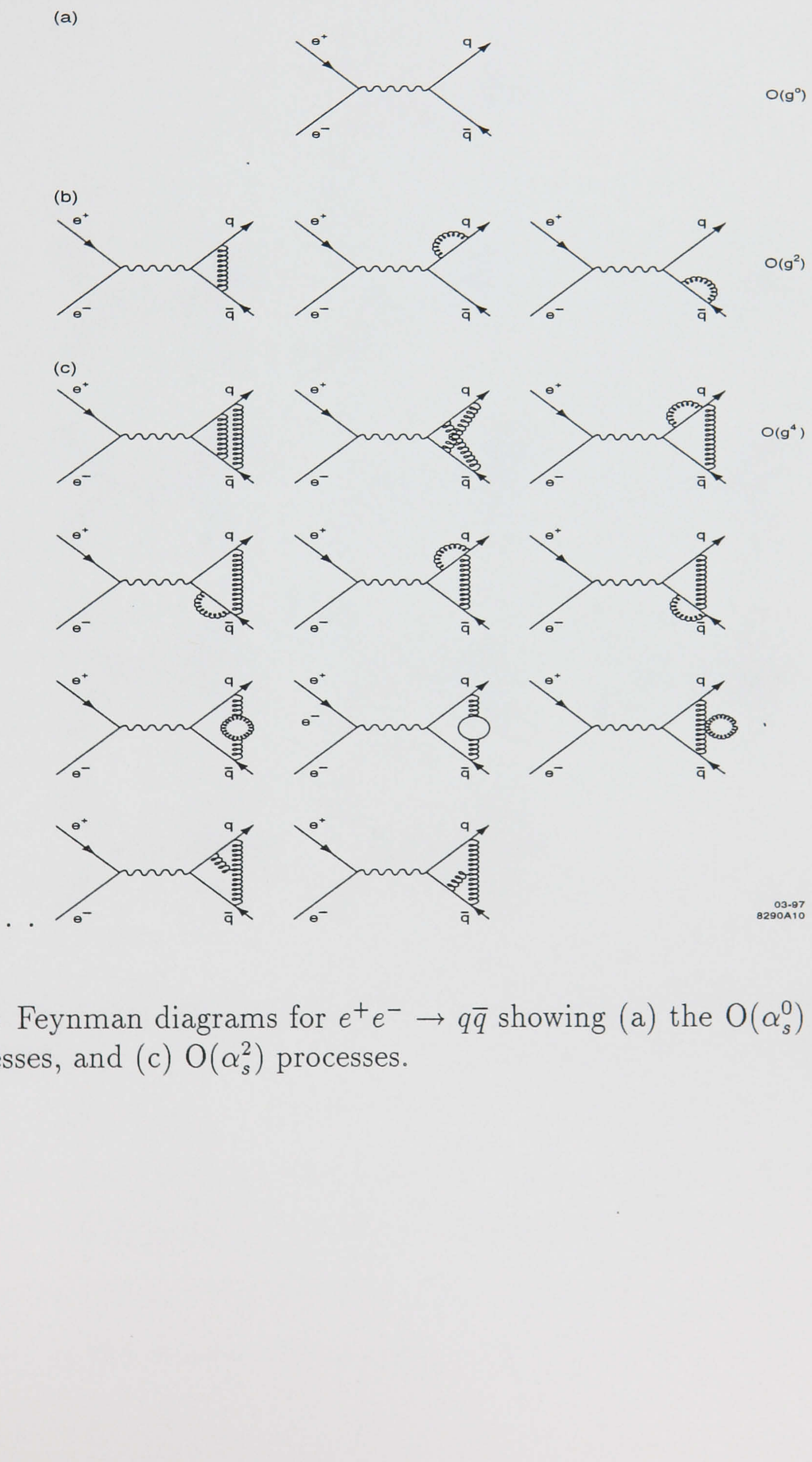

Figure 1.10: Feynman diagrams for $e^+e^- \to q\bar{q}$ showing (a) the $O(\alpha_s^0)$ process, (b) $O(\alpha_s)$ processes, and (c) $O(\alpha_s^2)$ processes.

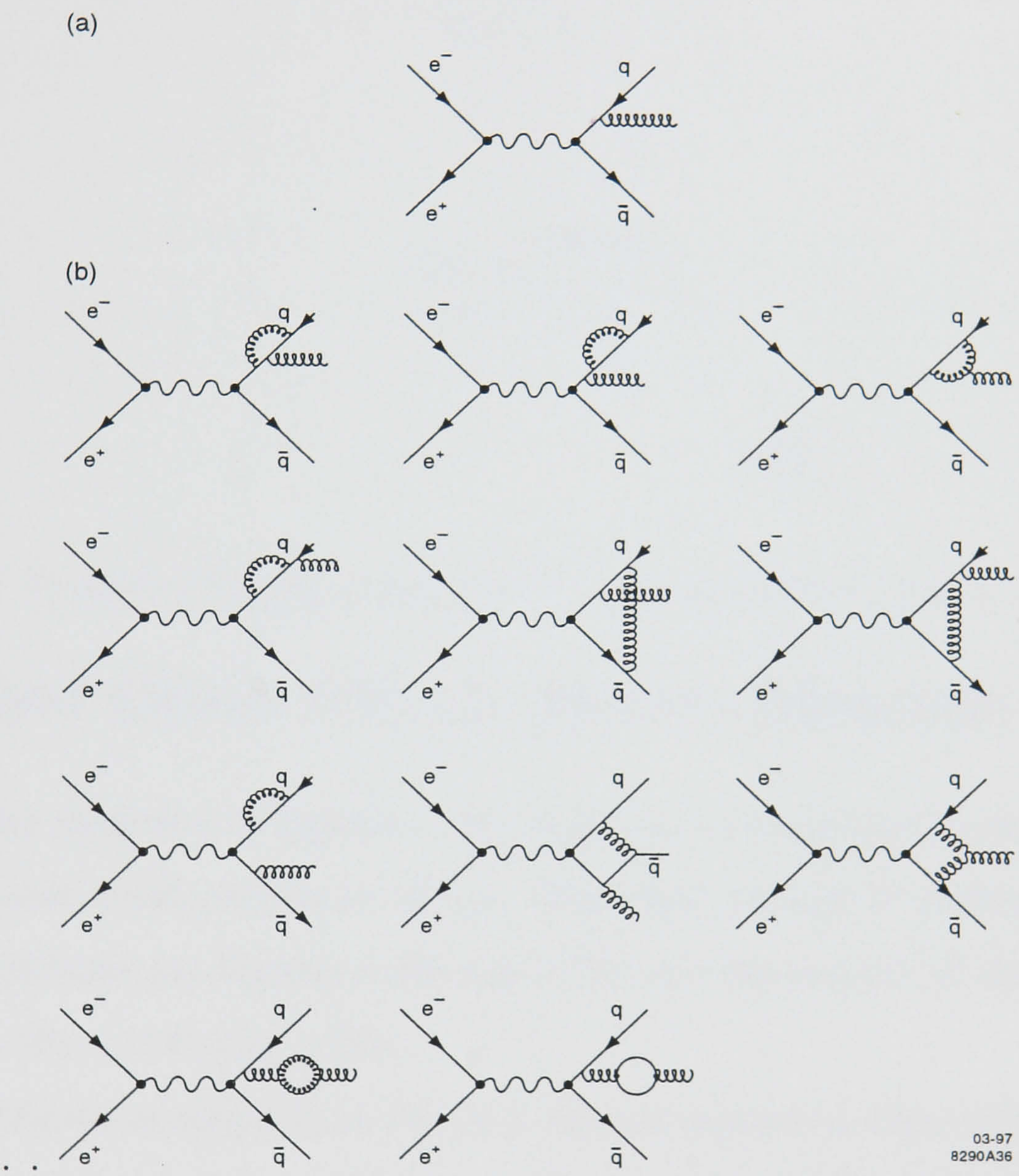

Figure 1.11: Feynman diagrams for $e^+e^- \rightarrow q\bar{q}g$ showing (a) the $O(\alpha_s)$ and (b) $O(\alpha_s^2)$ processes.

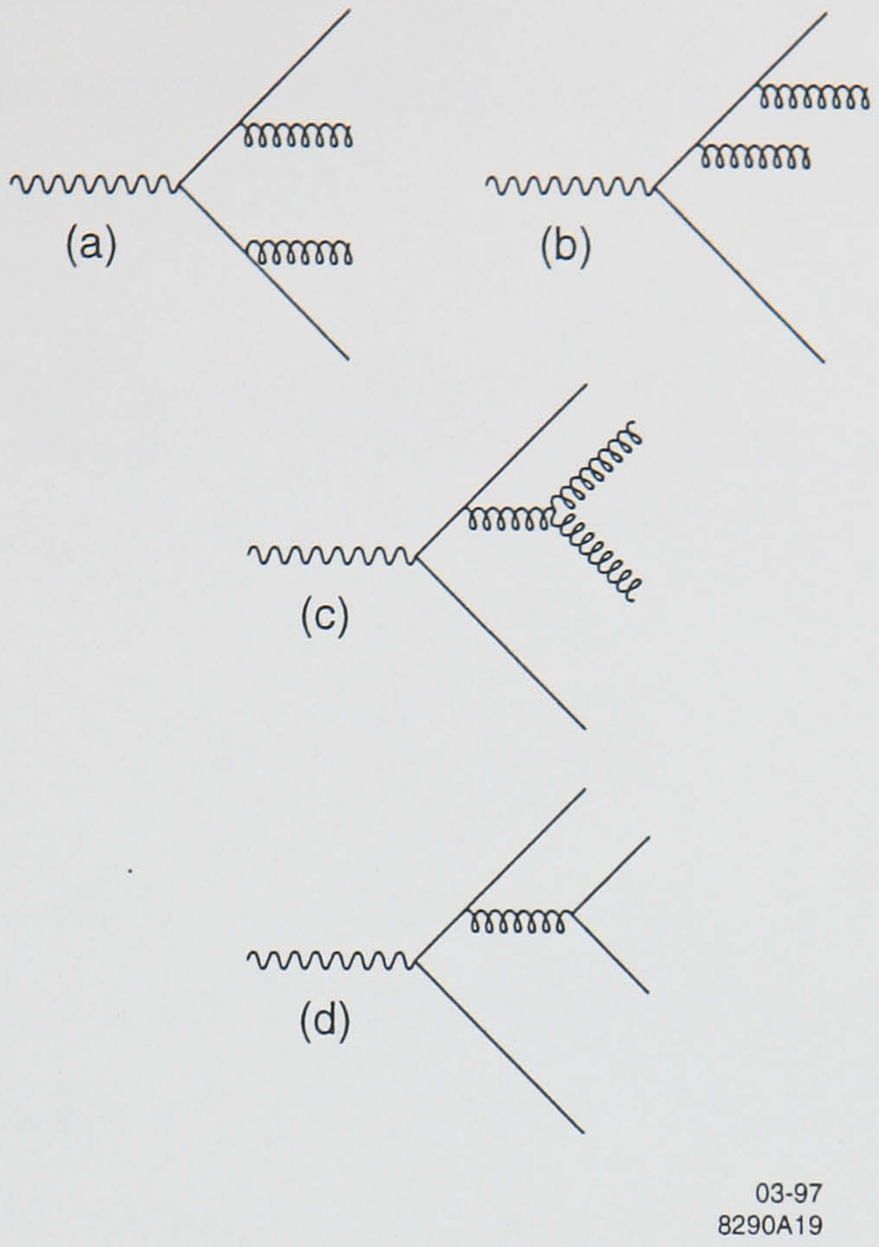

Figure 1.12: Tree-level Feynman diagrams for 4-jet production in e^+e^- annihilation.

1.6 First Order ($O(\alpha_s)$) Matrix Elements

The Feynman diagrams in Figures 1.10a, b and 1.11a contribute to the calculation of the hadronic cross section to $O(\alpha_s)$. The cross section is obtained from the squared amplitudes for Figures 1.10a and 1.11a and the product of the amplitudes for Figure 1.10a and Figure 1.10b.

Each of the three diagrams in Figure 1.10b are separately ultra-violet divergent, i.e. the integrals over the virtual gluon momenta k diverge for $k \to \infty$. However, The divergences cancel when the contributions of all three diagrams are taken into account. These diagrams are also infra-red divergent, i.e. they diverge as, $k \to 0$, but the divergences cancel if the contributions from the process $e^+e^- \to q\bar{q}g$ are included, Figure 1.11a, which is also infra-red divergent. If the quarks are assumed massless a further divergence arises for these diagrams, called the collinear divergence, where the virtual gluon is collinear to the outgoing quark. These divergences are controlled by the process of dimensional regularisation, in which the Feynman

diagrams amplitudes are calculated for arbitrary dimension $n > 4$ [22]. The differential cross section for the production of massless 3-parton final states to order α_s has been calculated [17] to be:

$$\frac{d^2\sigma}{dx_1 dx_2} = \sigma_0 \frac{2\alpha_s}{3\pi} \frac{x_1^2 + x_2^2}{(1-x_1)(1-x_2)} \tag{1.15}$$

where σ_0 is the lowest order cross section,

$$\sigma_0 = \frac{4\pi\alpha^2}{3s} N_c \sum_f e_q^2 \tag{1.16}$$

and $x_i = 2E_i/\sqrt{s}$ for $i = 1 = q$, $i = 2 = \overline{q}$ and $i = 3 = g$, $N_c = 3$, α is the electroweak coupling constant, and e_q is the charge of the quark flavour q.

The cross section diverges when $x_1 \to 1$ and/or $x_2 \to 1$. The case when x_1 and $x_2 \to 1$ corresponds to the emission of a gluon of vanishingly small momentum. This is the infra-red divergence. The other case $x_1 \to 1$ and $x_2 \neq 1$ corresponds to the radiation of a gluon which is collinear with the q or $\overline{q}$. This is the collinear divergence. In either case, the gluon is not resolvable from the q or $\overline{q}$. Hence it is possible to define a region of $q\overline{q}g$ space around the singularities where the gluon is irresolvable and we have a two parton configuration, whilst outside this region all three partons are resolved. The integral over the singular region actually cancels with the virtual one-loop corrections (e.g. Figure 1.10b) to $e^+e^- \to q\overline{q}$ and both $q\overline{q}$ and $q\overline{q}g$ cross sections remain finite.

'Resolvable' can be defined by a number of criteria. For example the energy of the outgoing gluon and its angles with respect to the two quarks must be greater than some defined threshold [23]. Another method [24] is to form the scaled invariant mass-squared:

$$y_{ij} = \frac{m_{ij}^2}{s} \tag{1.17}$$

for each pair of partons i, j, and to require that all $y_{ij} > y_{min}$ for the event to be classed as a 3-parton event. Note that the cross section for $e^+e^- \to q\overline{q}g$ and $e^+e^- \to q\overline{q}$ must now be functions of the resolution criteria [25]:

$$\sigma^{q\bar{q}}(y_{min}) = \sigma_0 \left[1 + \frac{4}{3}\frac{\alpha_s}{2\pi} \left(-2\log^2 y_{min} - 3\log y_{min} + 4y_{min}\log y_{min} - 1 + \frac{\pi^2}{3} \right) \right] \tag{1.18}$$

$$\sigma^{q\bar{q}g}(y_{min}) = \sigma_0 \frac{4}{3}\frac{\alpha_s}{2\pi} \left(2\log^2 y_{min} - 3\log y_{min} + 4y_{min}\log y_{min} + \frac{5}{2} + \frac{\pi^2}{3} \right) \tag{1.19}$$

Note that the cross section for the three-parton final state is proportional to α_s, which to first order is given by [26]:

$$\alpha_s^{(1)}(Q^2) = \frac{12\pi}{(33 - 2N_f)\ln(\frac{Q^2}{\Lambda^2})} \tag{1.20}$$

where N_f is the number of active flavours. The fundamental constant of QCD is hence not the coupling constant $\alpha_s(\sim g^2)$ but the scale parameter Λ. Here Q^2 is usually taken to be the hadronic c.m. energy squared, s.

Thus, whenever a measurement of α_s is made, the scale Q^2 must always be quoted, for example, $\alpha_s(M_Z^2)$ is α_s measured at the Z^0 pole [27].

1.7 Second Order ($O(\alpha_s^2)$) Matrix Elements

Second order perturbative QCD calculations are very complicated, the amplitudes from all the diagrams in Figures 1.10, 1.11 and 1.12 must be summed and squared. The collinear and infra-red divergences are dealt with as explained before, by dimensional regularisation and by isolating singular regions of phase space using the same parton resolution criteria. The diagrams in Figure 1.12 thus contribute to the 2,3 and 4 parton cross sections, the first (second) case is when two (one) pair of partons are collinear or two (one) partons are vanishingly soft. Those in Figure 1.11 contribute to the 2 and 3 parton cross sections and those in Figure 1.10 only to the 2 parton cross section. Again the singularities arising from the integrals over the degenerate regions of phase space cancel, yielding finite integrated 2, 3 and 4 parton cross sections which are functions of y_{min}.

1.8 Parton Shower QCD Calculations

For third or higher orders of QCD, the cross section calculations quickly become very complicated due to the large number of Feynman diagrams involved. An alternative is provided by the Leading Logarithm Approach (LLA). In this approach the quarks produced in $e^+e^- \rightarrow q\overline{q}$ radiate gluons ($q \rightarrow qg$), which in turn can branch into parton pairs ($g \rightarrow gg$ and $g \rightarrow q\overline{q}$). Hence a parton shower or cascade is then produced, Figure 1.13.

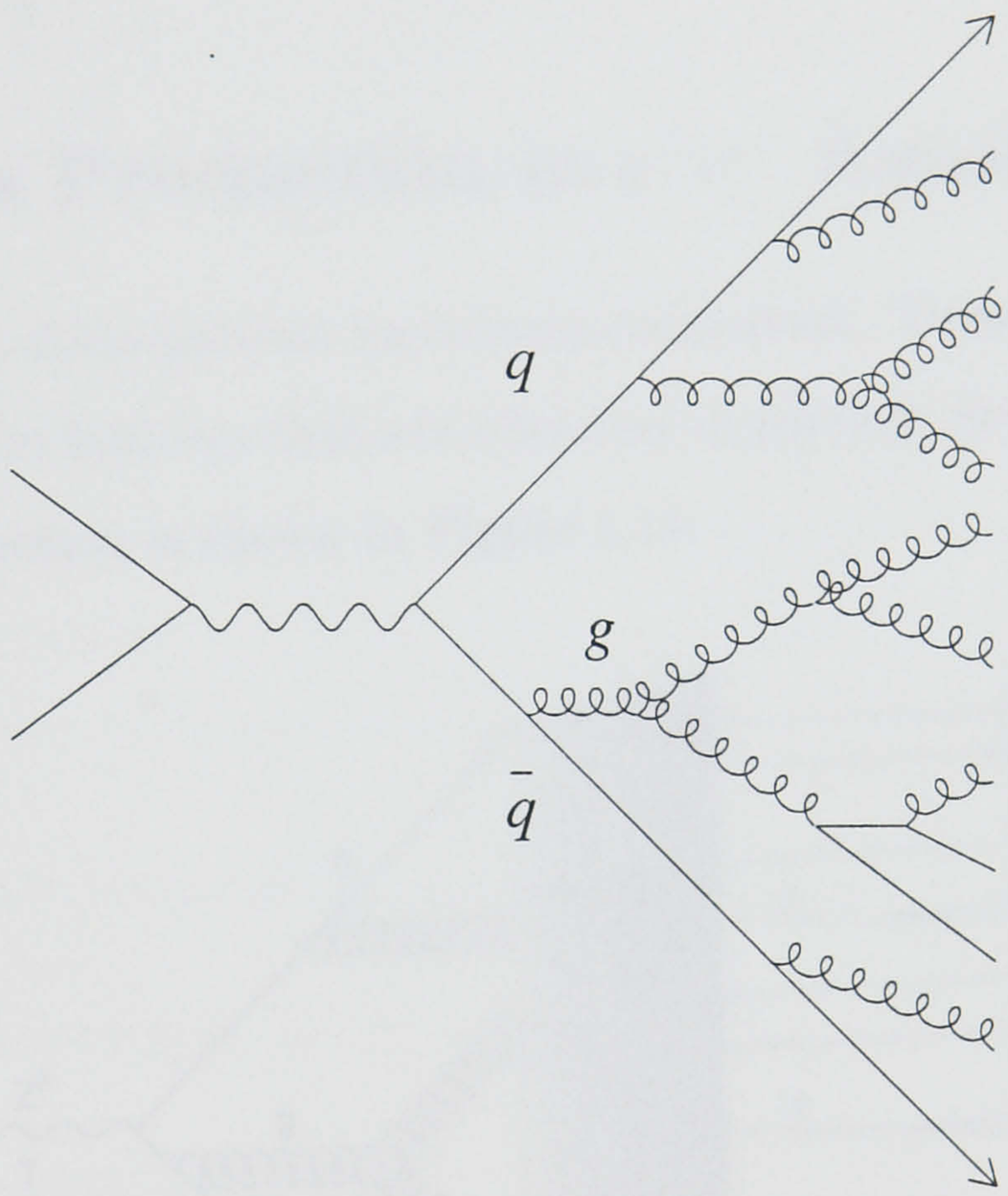

Figure 1.13: Schematic representation of a parton shower.

In the branching $a \rightarrow bc$, z is the fraction of the parent's 4-momentum carried away by daughter b (hence c has a momentum fraction $1 - z$). The probability that a branching $a \rightarrow bc$ will take place during a small interval dt of a "generalised evolution parameter" (e.g Q^2) is given by the Altarelli-Parisi equations [28]:

$$\frac{d\mathcal{P}_{a\rightarrow bc}(z)}{dt} = \int dz \frac{\alpha_s(Q^2)}{2\pi} \mathcal{P}_{a\rightarrow bc}(z) \tag{1.21}$$

$$\mathcal{P}_{q\to qg}(z) = \frac{4}{3}\left(\frac{1+z^2}{1-z}\right), \tag{1.22}$$

$$\mathcal{P}_{g\to gg}(z) = 6\left(\frac{1-z}{z} + \frac{z}{1-z} + z(1-z)\right), \tag{1.23}$$

$$\mathcal{P}_{g\to q\bar{q}}(z) = \frac{1}{2}(z^2 + (1-z)^2). \tag{1.24}$$

Partons are allowed to branch until the available Q^2 reaches some cut-off value Q_0^2, typically of $\mathcal{O}(1GeV)$.

1.9 Hadron Production in e^+e^- Annihilation

So far only the final state partons have been considered. These must be converted into the colour singlet hadrons that are observed in particle detectors. A schematic of the hadron production is shown in Figure 1.14.

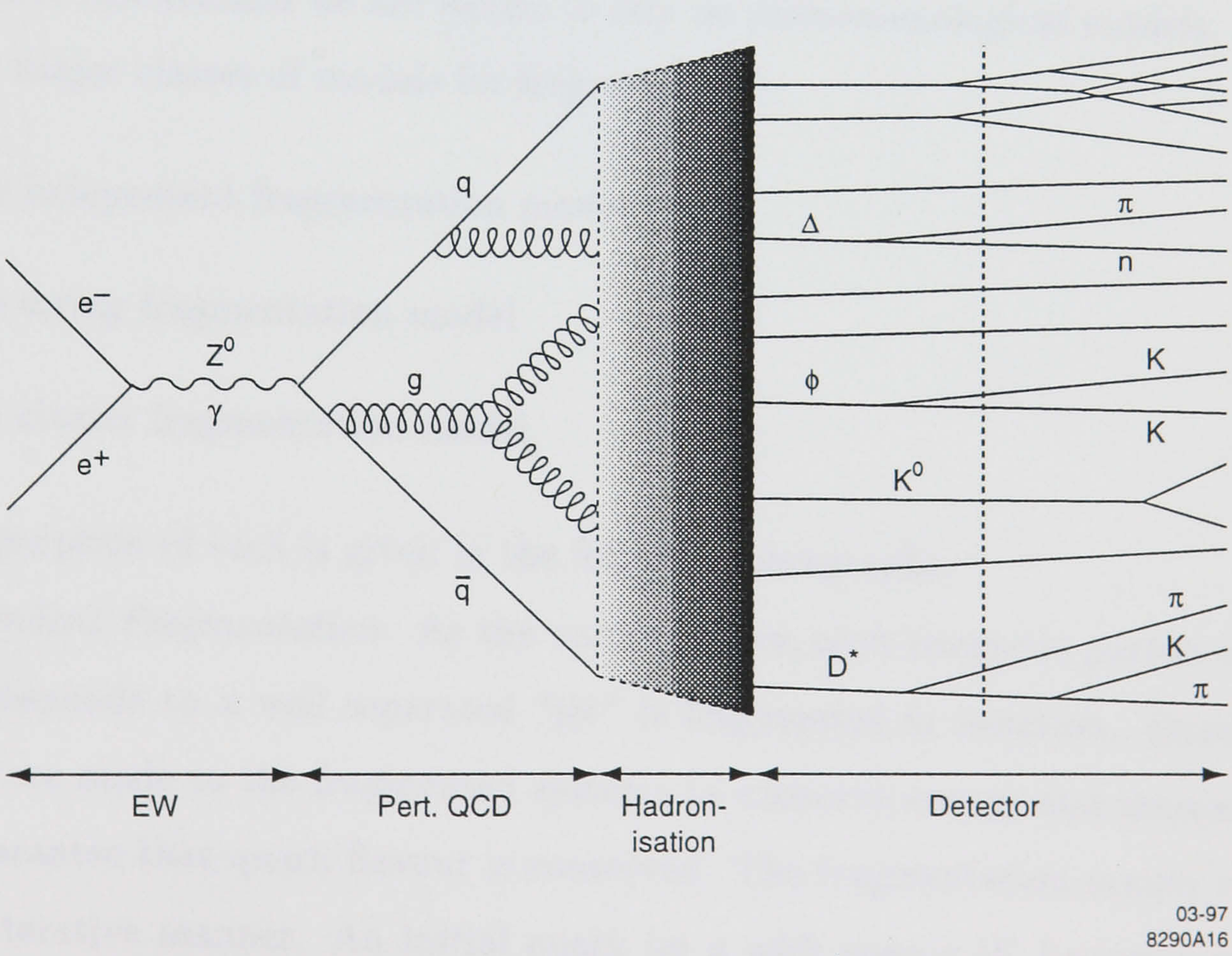

Figure 1.14: Schematic of hadron production in e^+e^- annihilation.

The production of hadrons in e^+e^- can be split into several stages:

1. A hard electroweak process in which the primary quark and anti-quark are produced:
   $e^+e^- \rightarrow q\overline{q}$

2. Perturbative QCD evolution of the primary $q\overline{q}$ via parton Bremsstrahlung:
   $q\overline{q} \rightarrow$ several $q, \overline{q}, g$

3. Hadronisation of partonic system:
   $(q, \overline{q}, g)$s $\rightarrow$ primary resonances

4. Decays of the primary resonances into 'stable' particles:
   $B, K_s^0, \phi, \Delta, \rho, ... \rightarrow \pi^{\pm}, K^{\pm}, p, \overline{p}, ...$(leptons)

Stages 1 and 2 are calculable using perturbation techniques, as already discussed above. Stages 3 and 4 are more problematic as they are non-perturbative processes that cannot in general be calculated from first principles. In the absence of non-perturbative calculations we are forced to rely on phenomenological models. There are three major classes of models for fragmentation:

- The indepentent fragmentation model
- The string fragmentation model
- The cluster fragmentation model

A brief desciption of each is given in the following paragraphs.

Independent Fragmentation. As the name implies, each energetic parton in the event corresponds to a well separated "jet" is fragmented in isolation. Small adjustments are made to the fragmented systems to conserve energy and momentum and to guarantee that quark flavour is conserved. The fragmentation occurs in the following iterative manner. An initial quark jet q with energy W becomes paired into a hadron $q\overline{q}_1$ carrying energy fraction $W \cdot z_1$, leaving behind a remanent jet q_1 with energy $(1 - z_1)W$. This jet in turn is split into another hadron $q_1\overline{q}_2$ carrying energy $z_2(1 - z_1)W$, leaving again a remnant jet q_2. This process continues until

the energy is too low to form the lightest hadron. The energy sharing between the daughter products is given by a fragmentation function, $f(x)$, which is assumed to be the same at each step of the fragmentation process. The Field and Feynman model [29] was one of the first versions of the scheme to be implemented by a Monte Carlo calculation. Various other independent fragmentation schemes have followed, the most commonly used is the ISAJET Monte Carlo [30].

String Fragmentation. This scheme was first introduced in 1974 by Artru and Mennessier [31]. The Lund group has been responsible for the development of the model of string fragmentation. Their Monte Carlo simulation JETSET 7.4 [32], is used for the analysis in this thesis.

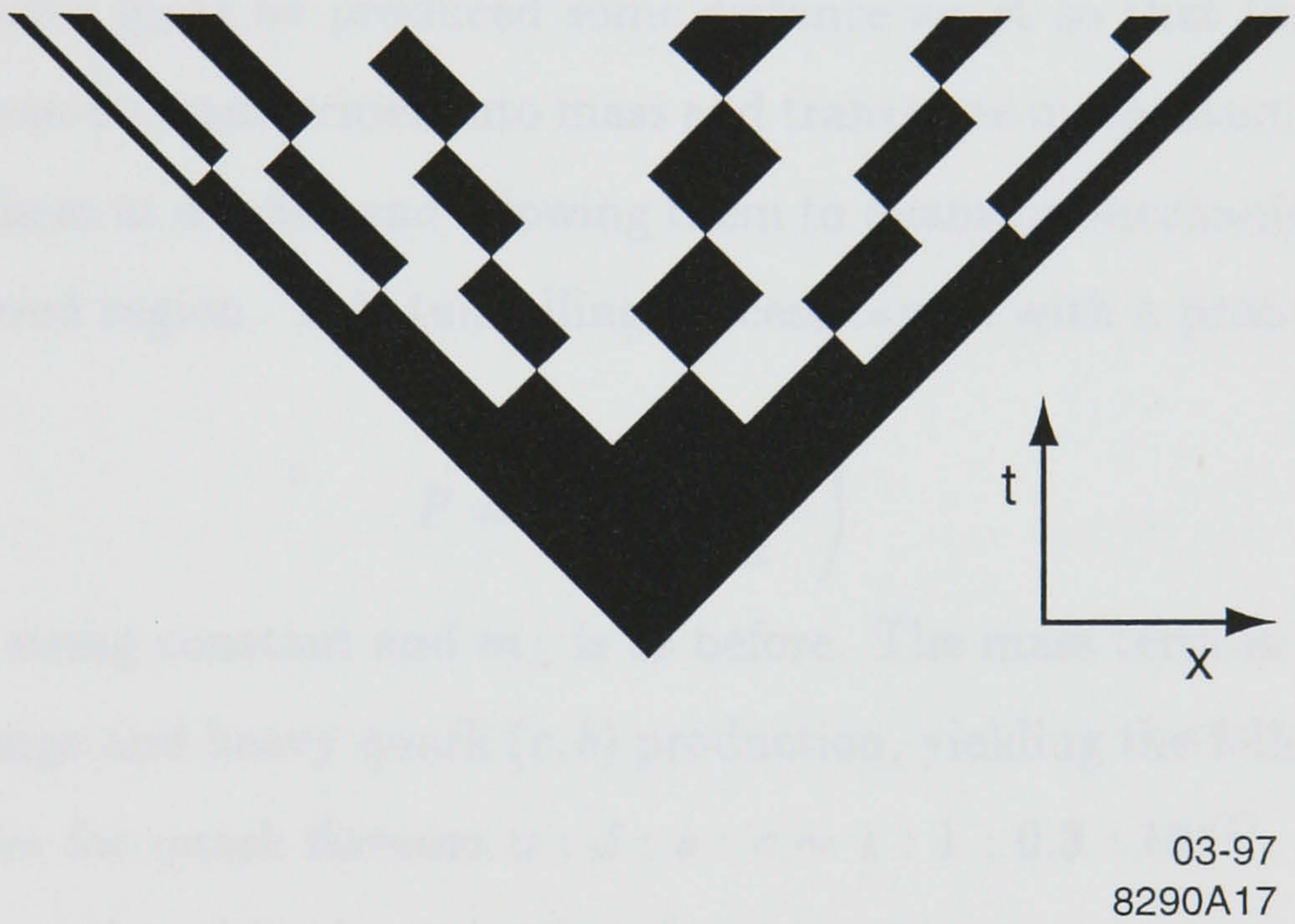

Figure 1.15: Schematic of hadronisation in JETSET.

The string model is based on the QCD idea that the partons are connected by a colour flux tube, or string. The transverse size of the string is small compared to its length, due to the couplings between gluons. The string has a constant energy density per unit length, or string constant, estimated to be 1 GeV/fm. As the partons move apart the energy of the string rises linearly. Once the potential energy has grown high enough to produce $q\overline{q}$ pairs, the string breaks to form two separate string objects. Figure 1.15 shows a schematic of the process. The probability for this to happen is given by:

$$f(z) = \frac{1}{z}(1-z)^a \exp\left(-\frac{bm_\perp^2}{z}\right) \tag{1.25}$$

Where z is the fraction of the energy and longitudinal momentum, $E + p_{||}$, of a parent string taken by the daughter, $m_\perp = \sqrt{p_\perp^2 + m^2}$, m is the quark mass and a and b are parameters of the model, and must be tuned to best fit the data [33]. $\perp$ and $||$ refer to the string axis. A large number of additional parameters are used to tune the relative production of particles [34].

The splitting is done is such a way that energy, momentum and all the quantum numbers are conserved. If the invariant mass of a string object is larger than a hadron mass, further breaks may occur until ordinary hadrons remain.

Massive quarks must be produced some distance apart so that the field energy between them can be transformed into mass and transverse momentum. This is done by producing them at a point and allowing them to quantum-mechanically "tunnel" out to the allowed region. This tunnelling process occurs with a probability [35]:

$$P = \exp\left(-\frac{\pi m_\perp^2}{\kappa}\right) \tag{1.26}$$

where κ is the string constant and $m_\perp$ is as before. The mass term in the exponent suppresses strange and heavy quark (c, b) production, yielding the following relative production rates for quark flavours $u : d : s : c \sim 1 : 1 : 0.3 : 10^{-11}$. Hence heavy quarks are not produced in the string break up.

In this model the gluons are treated as momentum carring "kinks" in the colour string, Figure 1.16

Cluster Fragmentation. In this model the parton shower is used to form colourless clusters. These clusters are assumed to be the basic units from which hadrons are produced. Heavy clusters fragment into lighter ones, and these ultimately fragment into the final state hadrons. Figure 1.17 shows a diagram of the cluster fragmentation.

The first widely successful model of this type was developed by Marchesini and Webber [36]. The present version of the program is known as HERWIG [37].

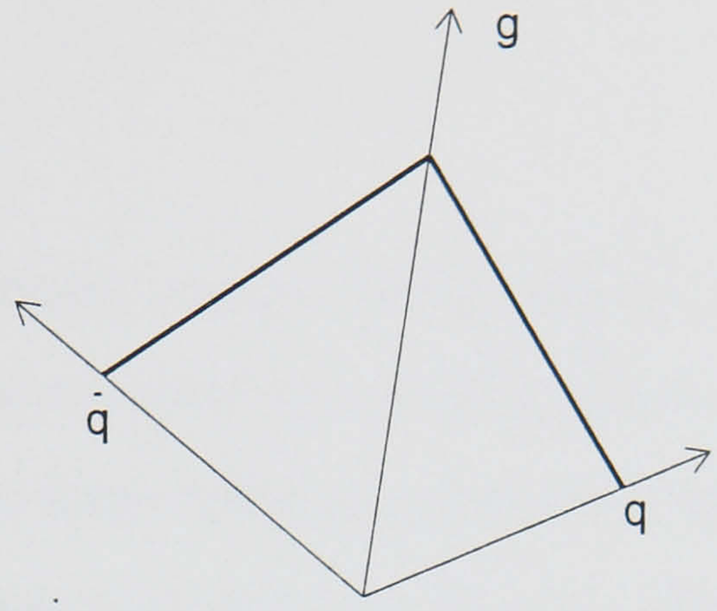

Figure 1.16: A $q\bar{q}g$ event in the string fragmentation scheme. The heavy line is the string stretched between the gluon and the two quarks.

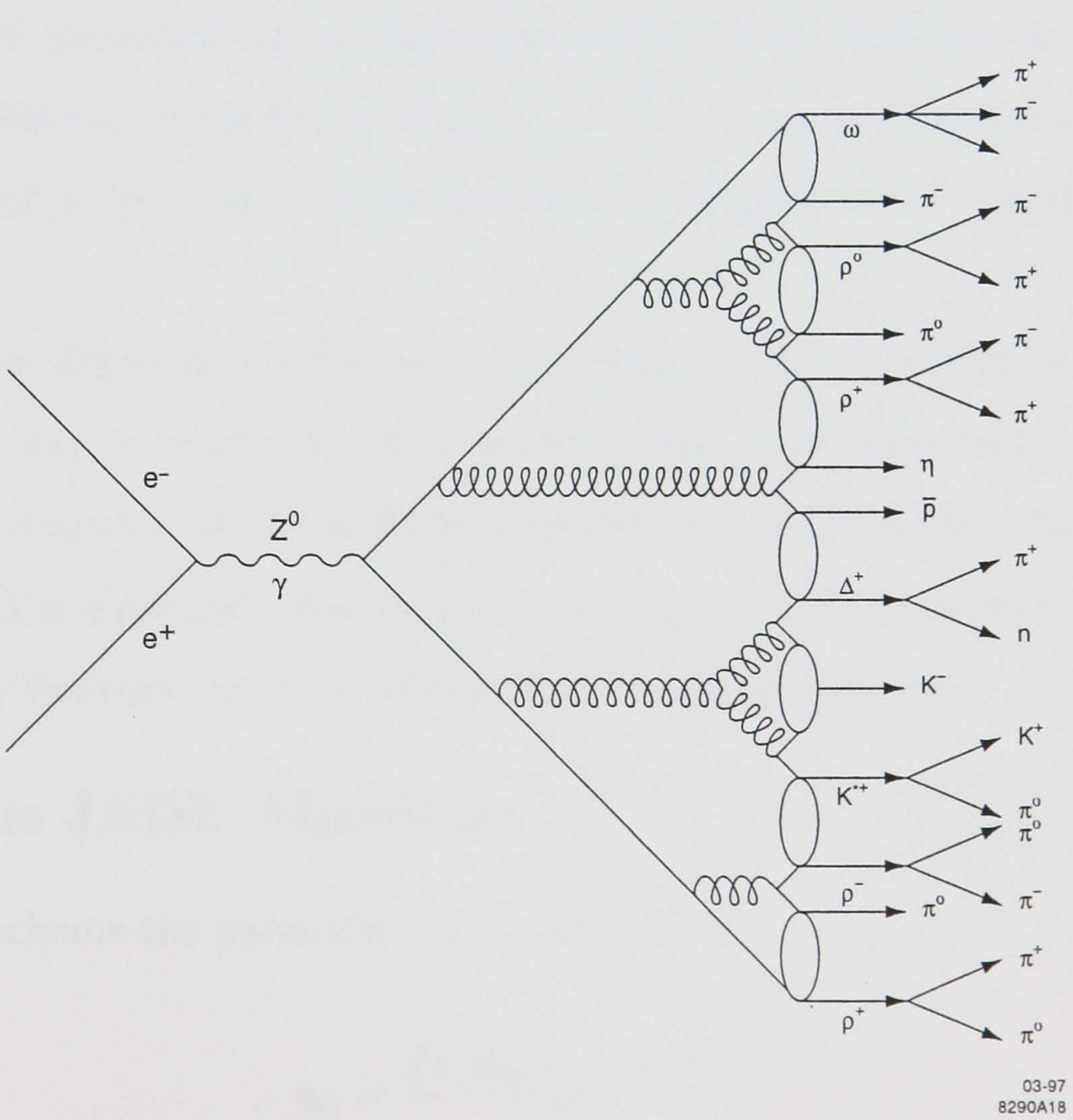

Figure 1.17: Schematic of hadronisation in HERWIG.

1.10 Jet Finding

In order to carry out an analysis involving jets it is first necessary to define what a jet is.

1.10.1 Jets

As already shown, when primary partons are produced via the decay of a Z^0, they shower. Most of the partons are emitted travelling close to the initial parton direction. If the primary partons have sufficient relativistic boost, the radiated partons, and hence their hadronic decay products, will form a collimated jet around the initial quark direction.

In particle physics experiments it is not easy to judge how many jets a particular event contains. Hence jet algorithms (see e.g. [38]) have been developed, which can be applied to the hadrons detected. The algorithms measure y_{ij}, for example, the invariant mass, of all pairs of particles i and j in an event, and the pair with the smallest y_{ij} are combined into a single (pseudo)-particle. This process is repeated until all pairs have y_{ij} exceeding a value y_{cut}. At this point each pseudo-particle that remains is called a "jet", and the jet multiplicity of the event is just the number of jets.

The different algorithms differ from each other by the definition of the measure of y_{ij}, and the way in which the two particles i and j are combined (known as the recombination scheme). In the analysis presented in this thesis the JADE algorithm [39] is used. This algorithm was chosen with a $y_{cut} = 0.02$ because it was used by the SLD heavy flavours group to develop the b-tagging routines.

1.10.2 The JADE Algorithm

In the JADE scheme the parameter y_{ij} is defined as:

$$y_{ij} = \frac{2E_iE_j(1-\cos\theta_{ij})}{E_{vis}^2} \tag{1.27}$$

where E_i is the energy of the i^{th} particle, θ_{ij} is the angle between the particles i and

j, and E_{vis} is the visible energy of the event. The recombination scheme is defined as the sum of the four momenta of particles i and j:

$$p^{\mu} = p_i^{\mu} + p_j^{\mu} \tag{1.28}$$

1.11 Hadronic Event and Detector Simulation

The development of the selection cuts used in the analysis presented in this thesis and the estimation of the backgrounds, purities and efficiencies required a detailed simulation of the detector and physics processes. The SLD Monte Carlo (MC) consisted of two separate units: an event generator, which modelled the underlying physics of Z^0 decays and the physics of the unstable products, and a detector simulation model.

The event generator used was JETSET 7.4 [32] which used the Lund fragmentation parameters determined using TASSO [40] and OPAL [41] data and particle production parameters tuned to reproduce data from other experiments at the Z^0 energies [42]. The Peterson fragmentation function was used for the b- and c- quarks [43]. A B hadron decay model was developed at SLD and tuned to CLEO and ARGUS data. Reference [44] gives a detailed description of this model.

The output of the event generator was passed through a simulation package, GEANT 3.21 [45], which was designed to simulate the detector response. The data from random triggers (Section 6.2.1) was "overlaid" to simulate the presence of machine backgrounds.

The simulated data was then reconstructed in the same manner as the data. For a detailed description of the SLD Monte Carlo see [46].

Chapter 2

Experimental Apparatus

2.1 Introduction

The data used in the work presented in this thesis were collected in the SLC Large Detector (SLD) using interactions produced by collisions of electron and positron bunches from the SLAC Linear Collider (SLC) [47]. The SLC is a unique e^+e^- linear accelerator that takes advantage of SLAC's existing 50 GeV electron accelerator, to produce electron-positron collisions with a center of mass energy of 91.2 GeV. The collisions take place in the geometrical center of SLD, which was designed to observe the Z^0 decay products. In the following sections the SLC and SLD will be described in more detail.

2.2 The SLAC Linear Collider

The layout of the SLC is shown in Figure 2.1. It consists of a 3 km long linear accelerator (Linac) and arcs which bring the bunches of electrons and positrons into collision. The Linac uses $\sim$ 244 65 MW klystrons [48] to accelerate the particles. The microwaves produced by the klystrons are guided by copper waveguides to the beam-pipe which is 25 feet below the surface. The microwaves create an alternating field in the cavities which is in phase with the passage of the electrons and the positrons such that they always experience an accelerating field. The electrons and the positrons are accelerated to 46.6 GeV by the time they reach the end of the Linac. The width of the beam is constrained throughout the Linac by quadrupole

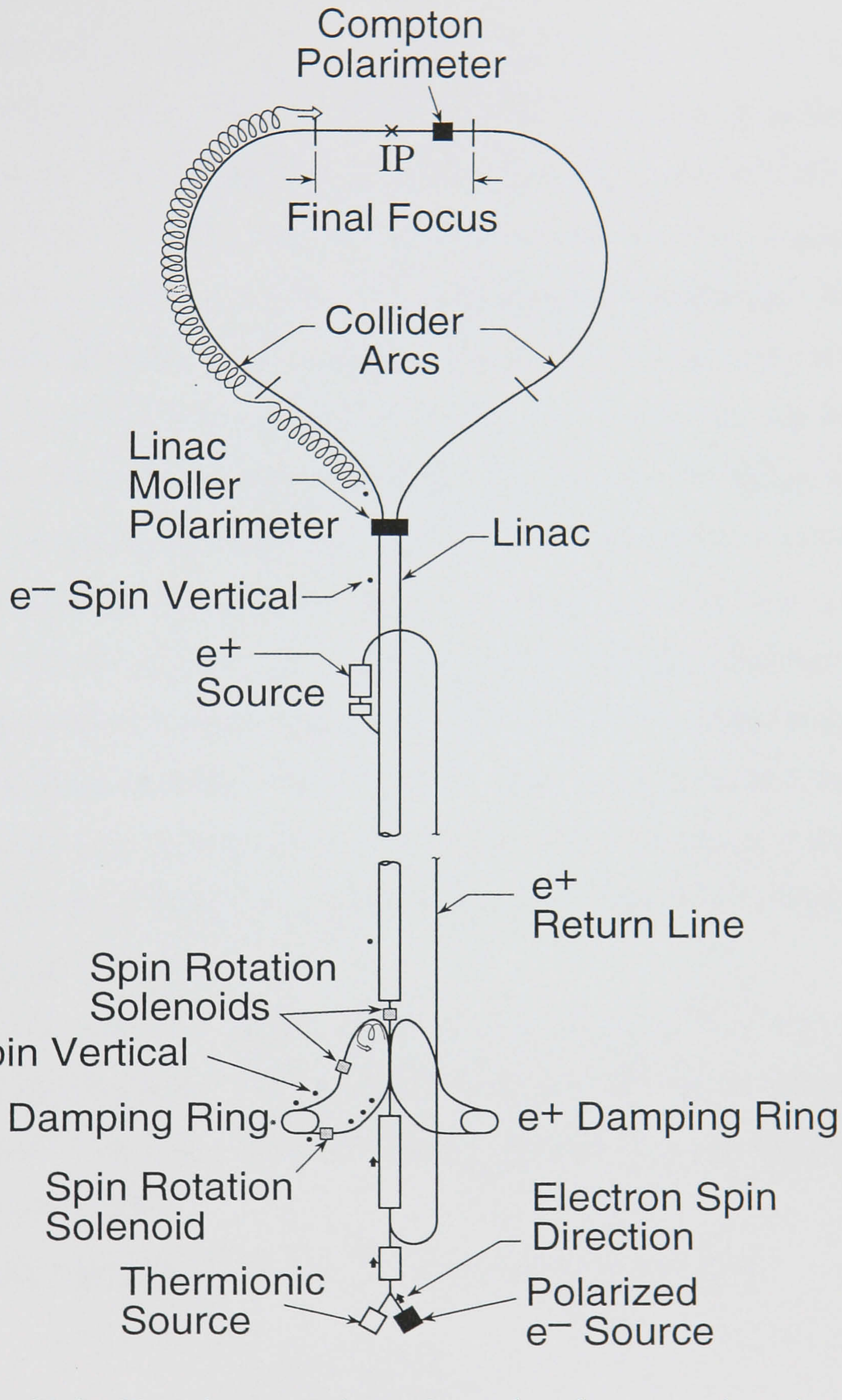

Figure 2.1: The SLC. This diagram shows how the electron spin orientation is controlled during acceleration and steering. The relative orientation of the electron spin vector is indicated at each stage of the transport [47].

and sextupole magnets. Collimators are used to remove the transverse tails of the bunches. These devices reduce the aperture for the beam and remove particles that are far from the ideal orbit.

In typical data-taking conditions the beams are bunches of $\sim 3 \times 10^{10}$ particles. They are produced at a rate of 120 Hz. Each bunch starts with the excitation of electrons from a strained GaAs cathode using two 2 ns pulses from an Nd:YAG-pumped Ti:sapphire laser [49]. The two electron bunches produced are then accelerated to 1.19 GeV and sent into the electron damping ring to reduce emittances. One bunch is accelerated down the Linac to an energy of 30 GeV and directed onto a tungsten positron target. Positrons emitted from the target are returned to the beginning of the Linac where they are accelerated and sent to a positron damping ring. The second electron bunch and the positron bunch from a previous cycle of the accelerator are accelerated to the end of the Linac at which point they have an energy of 46.6 GeV. At the end of the Linac, dipole magnets guide the electrons into the north arc and the positrons into the south arc. About 1 GeV of energy is lost in the arcs due to synchrotron radiation. After being focused by a set of super-conducting triplets the bunches pass through each other at the SLD interaction point, where occasionally an interaction between an electron and a positron occurs. This can lead to the production of a Z^0 boson.

To produce both reasonable luminosities and a stable interaction point the overlap of the beams must be small. The size of the beam-beam overlap at the interaction point is approximately 3μm horizontally by 2μm vertically. The length of the bunch is approximately 1mm [47].

The luminosity provided by SLC to SLD may be calculated from:

$$\mathcal{L} = \frac{f}{4\pi} \frac{N^+ N^-}{\sigma_x \sigma_y} H_d \tag{2.1}$$

Where $N^{-(+)}$ are the number of electrons (positrons) per bunch, $\sigma_{x,y}$ are the horizontal and vertical standard deviations of the bunches, f is the frequency of collisions (120 Hz), H_d is an enhancement factor due to beam-beam focusing [47]. Typical values of these numbers are summarised in Table 2.1.

Run	1992	1993	1994/95
σ_x μm	2.4	2.6	2.5
σ_y μm	2.2	0.8	0.6
$N^{\pm}$	2.8×10^{10}	2.9×10^{10}	3.5×10^{10}
H_d	1.0	1.05	1.20
Integrated Lum. pb^{-1}	0.3	1.8	3.6
Number of Z^0's	10k	50k	100k
Ave. Polarisation $< P_e >$ %	22.4±0.6	63.1±1.1	77.3±0.6

Table 2.1: A summary of the beam parameters delivered by SLC [50].

2.3 Polarised Electron Beam

The SLC provides SLD with highly polarised electrons. Longitudinally polarised electron bunches are produced by illuminating a strained lattice GaAs cathode with circularly polarised laser pulses [51]. The polarisation of the electrons is measured with a Compton Polarimeter [49]. The achieved electron beam polarisation history is shown in Figure 2.2. The average electron beam polarisation, measured for each run, is summarised in Table 2.1. Although the polarisation is a valuable tool for many analyses [52], it is not used for the analysis presented in this thesis.

2.4 The SLC Large Detector, SLD

The SLD, Figures 2.3 and 2.4, was designed [53] to test the Standard Model and to search for physics beyond the Standard Model. Hence the aims of the design were to provide a 4π coverage detector, suitable for center-of-mass energies of approximately 100 GeV. The detector consists of the following sub-detectors, starting at the beam pipe and moving outwards, Table 2.2.

- *The Vertex Detector*, which is used for high precision measurements of the trajectory of charged particles near the beam line (see Section 2.4.2)

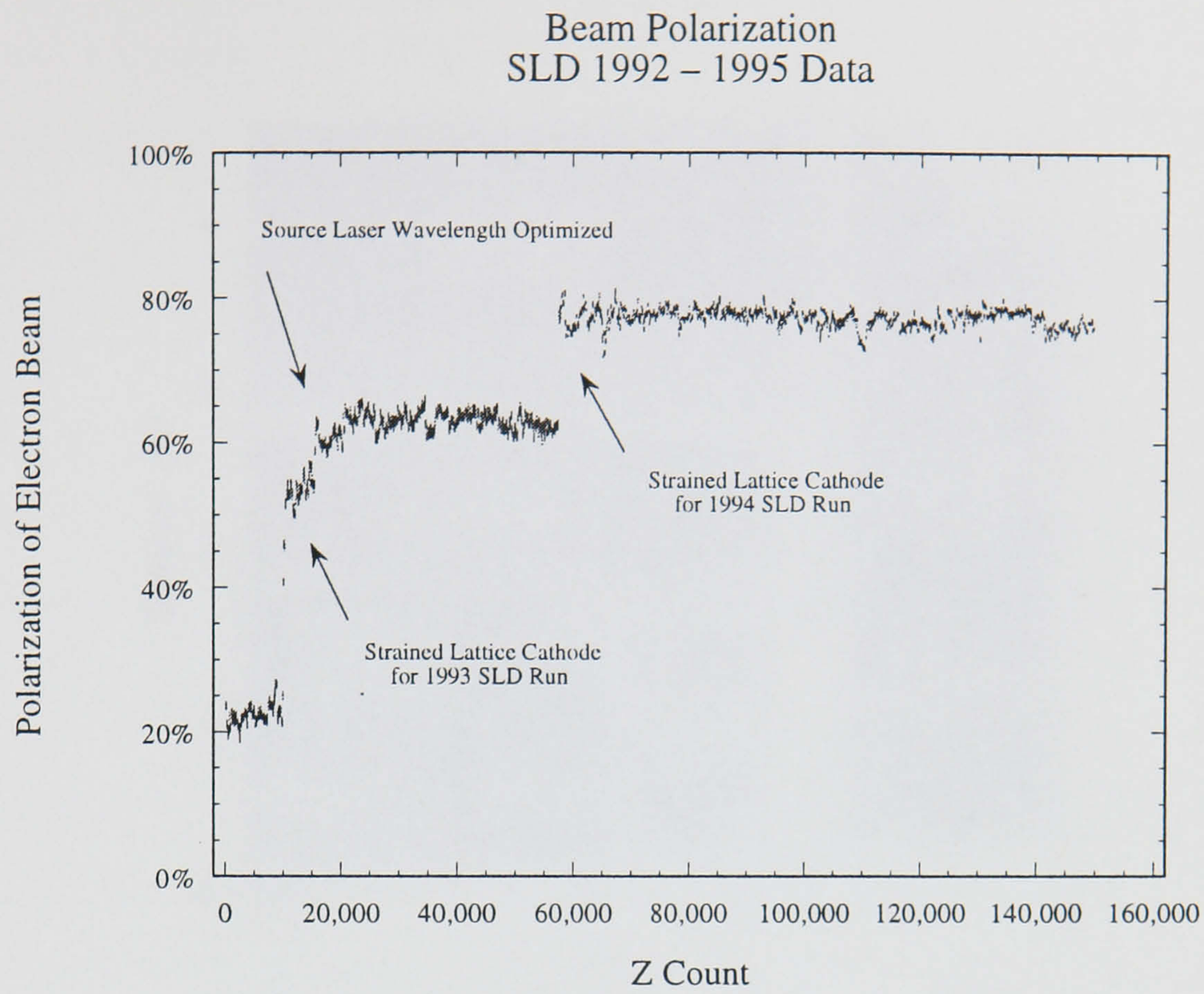

Figure 2.2: The SLC electron beam polarisation history from 1992-1995.

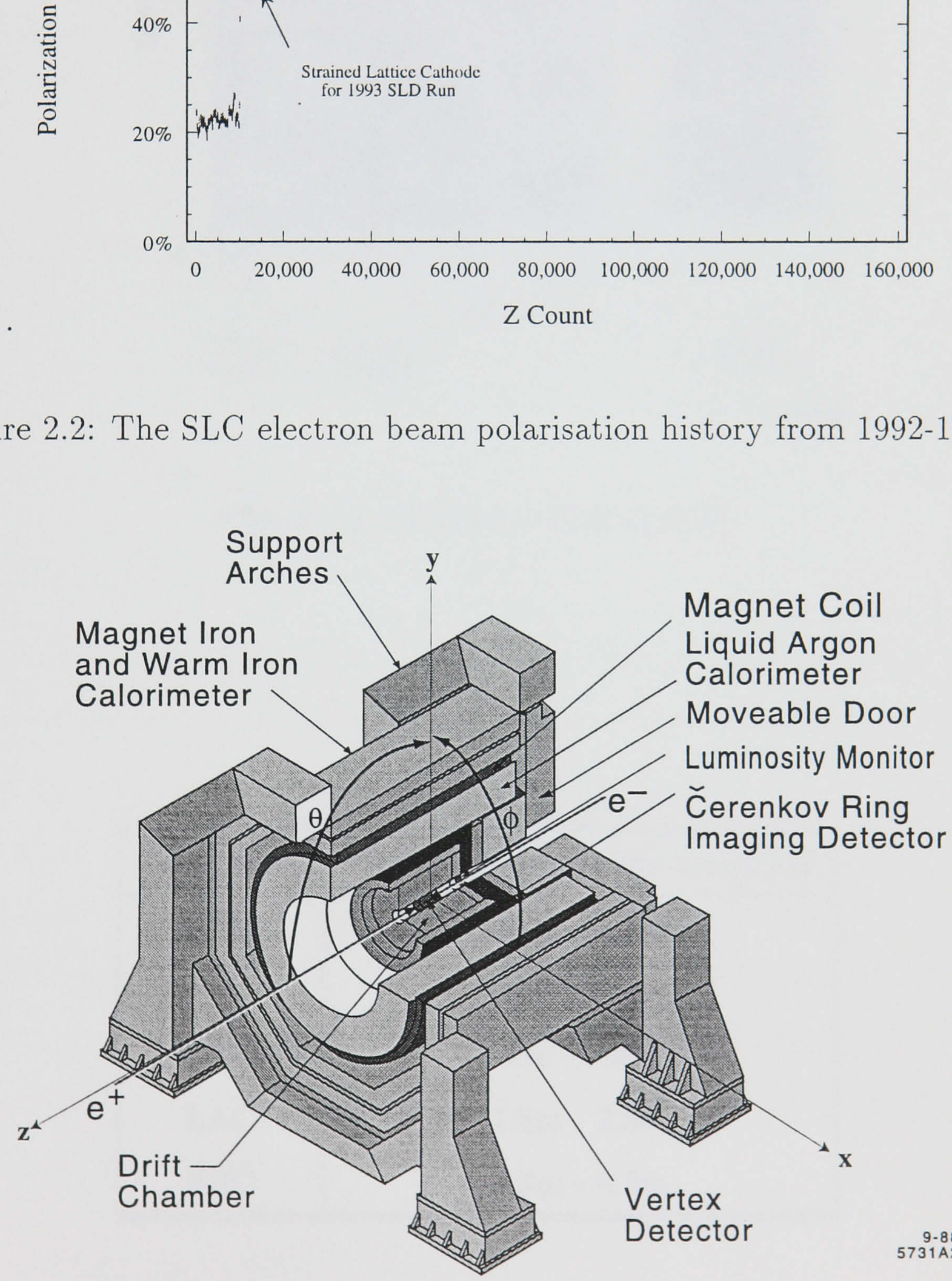

Figure 2.3: 3-D view of SLD with the electron and positron beam directions indicated and the SLD coordinate system defined.

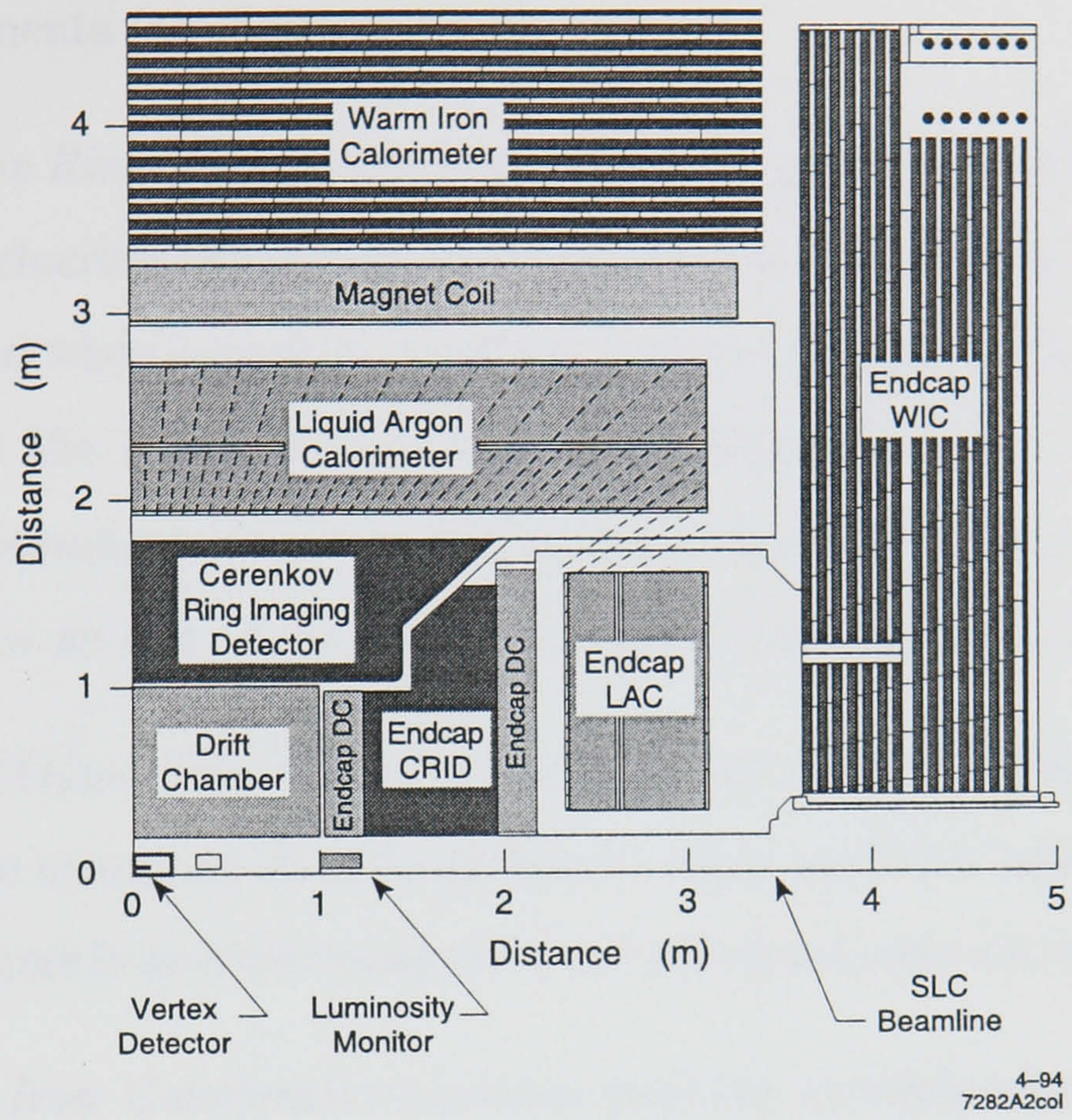

Figure 2.4: Quadrant view of SLD.

Sub-system	Radius (cm) from the beam line
VXD2	2.9cm - 4.2cm
CDC	20cm - 100cm
CRID	1m - 1.8m
LAC	1.8m - 2.9m
WIC	3.3m - 4.5m

Table 2.2: Radial distances of each barrel sub-system from the beam line

- *The Drift Chambers* provide measurements of charged particle trajectories and via their curvature in a 0.6T magnetic field provides a measurement of the particle momenta (see Section 2.4.4).

- *The Čerenkov Ring Imaging Detector* is used for particle identification by measuring the velocities of the particles from the radii of rings of Čerenkov radiation produced when a particle traverses its liquid and gas radiators at a velocity greater than the phase velocity of light in these materials. When combined with the momentum of the associated drift chamber, track probabilities that the particle is an e, π, K or p are determined (see Section 2.4.5).

- *The Liquid Argon Calorimeter* provides energy measurements of particles by sampling the energy of showers produced when particles interact in its dense material. There is an electromagnetic and a hadronic section (see Section 2.4.6).

- *The Warm Iron Calorimeter* provides position measurements of muons and energies of particles escaping the Liquid Argon Calorimeter (see Section 2.4.8).

2.4.1 The SLD Coordinate System

The standard SLD coordinate system is illustrated in Figure 2.3. The z coordinate is longitudinal along the beam axis and points in the direction of the positron beam, to the North. The x and y axes are transverse to the beam axis with positive y pointing vertically upwards and positive x pointing westwards. x, y and z form a right-handed coordinate system. The angle θ is measured with respect to the z axis ($\cos\theta = 0$ corresponds to the xy plane). Often, the xy plane is also referred to as the rϕ plane, where r is the radial distance from the beam pipe and ϕ is measured in the xy plane counter-clockwise from the x axis. The dip angle is the angle measured with respect to the xy plane.

2.4.2 Vertex Detector, VXD2

The VXD2 [54], Figure 2.5, is a novel silicon vertex detector. The VXD2 uses Charged Coupled Devices (CCD) as the medium for detecting the deposition of

ionisation from charged particles traversing the device.

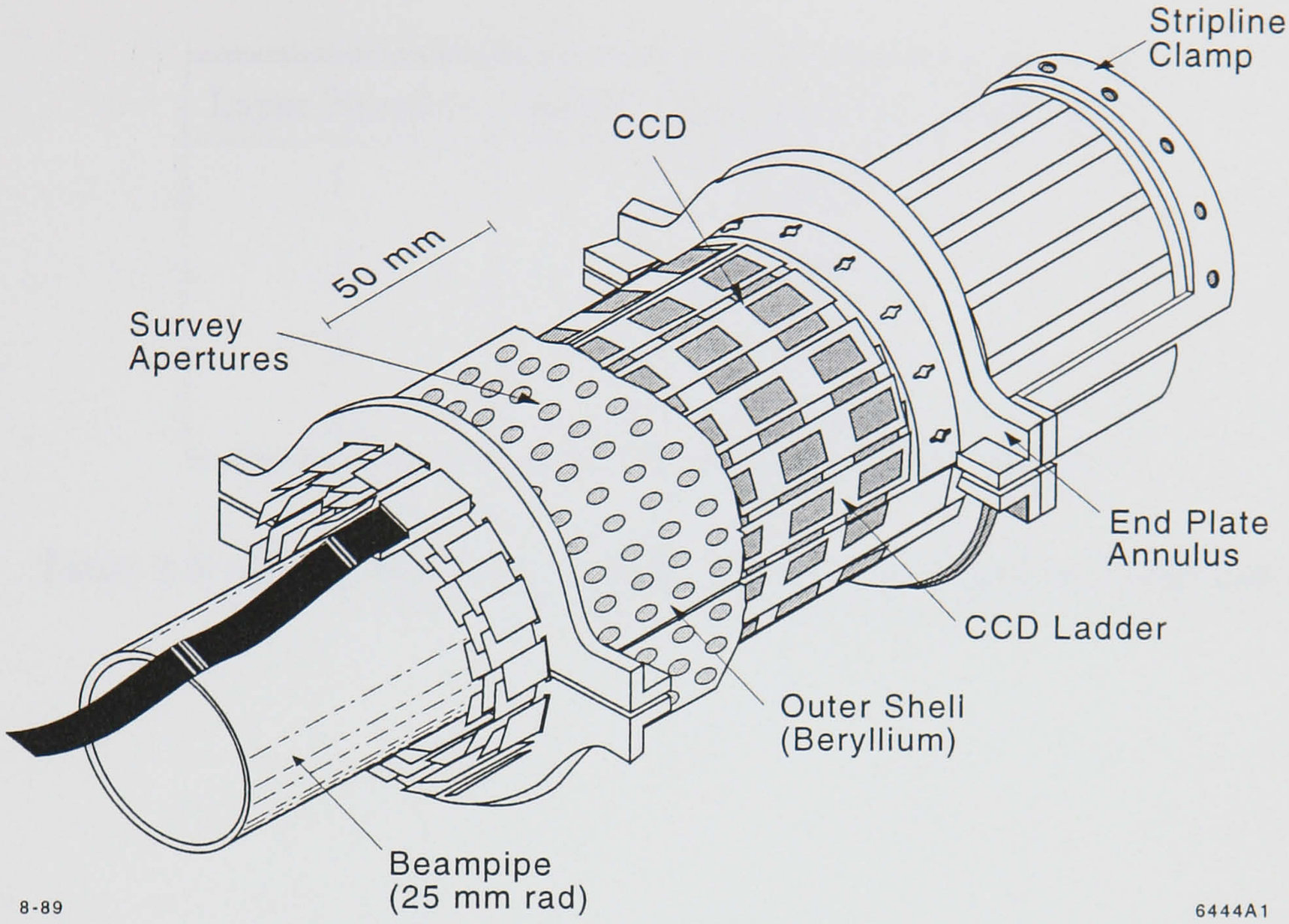

Figure 2.5: Schematic view of VXD2.

The VXD2 is constructed from sixty 9.2 cm long ladders arranged in four concentric cylinders, Table 2.3 and Figure 2.6, which are held in place by a beryllium shell.

Each of the ladders consists of eight small CCDs attached to complex motherboards. The motherboard is a ceramic (alumina) substrate, on each side of which there is a two-layer trace pattern plus a ground plane, patterned using thick film technology. CCDs are attached to the motherboard using thermoplastic adhesive. The overall thickness of each layer is 1.15% X_0 (radiation length). Electrical contact to the CCDs is made by wirebonds to the motherboard, and to the end of the ladders by custom made micro-connectors. To minimise the electrical interference, the drive pulses are fed to one end of each ladder, and the analogue biases and signal outputs were read out through the other end.

The two inner layers are made up from 13 ladders and the two outer layers consist of 17 ladders. Since each layer only covers $\sim$ 60% of the ϕ angle, Figure 2.6, layer

Layer Number	Radius (cm) from the beam line
1	2.9625
2	3.3625
3	3.7625
4	4.1625

Table 2.3: Radial distances of each VXD2 layer from the beam line

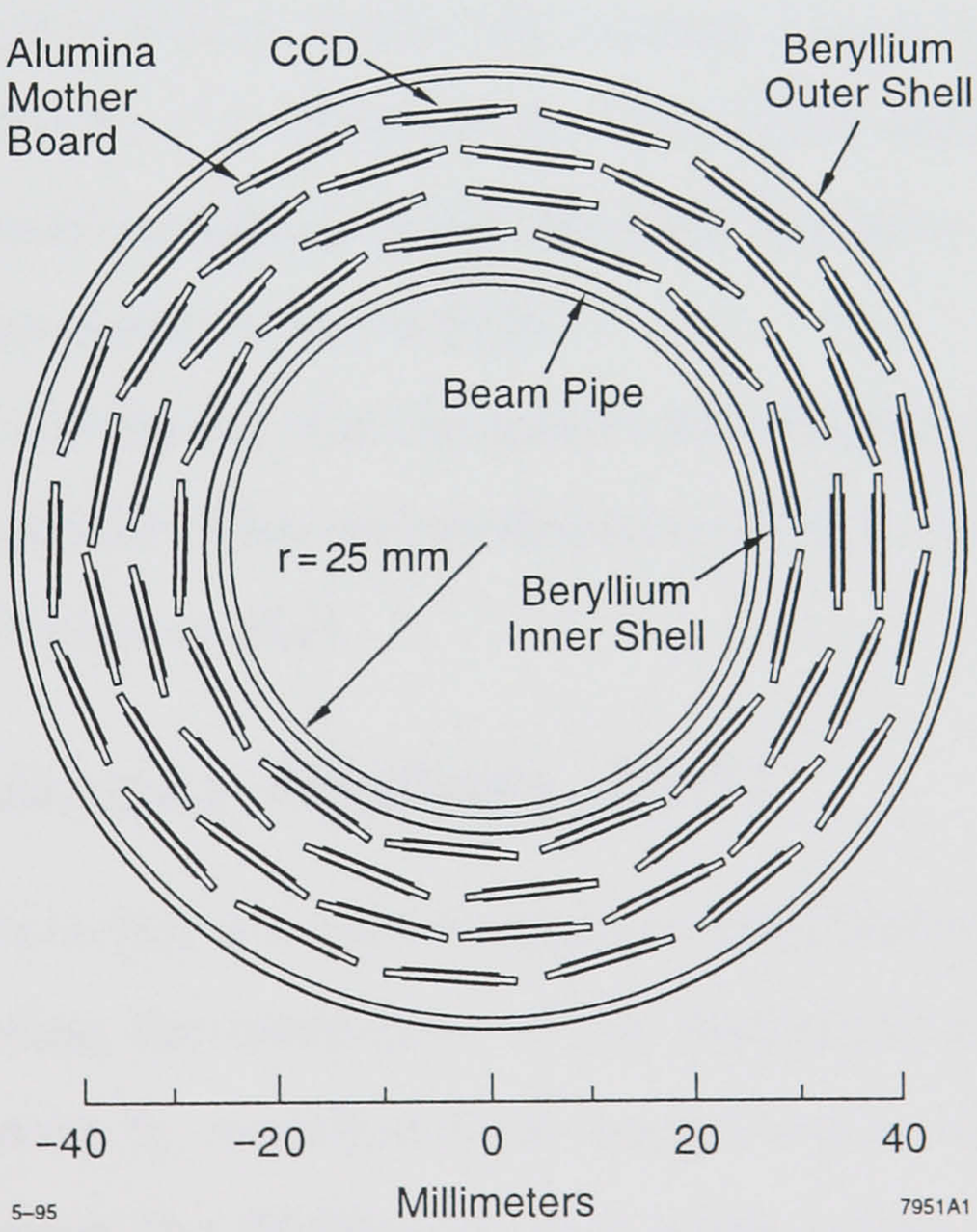

Figure 2.6: The four barrel layout of VXD2.

two is orientated to cover the gaps in layer one and similarly for the outer layers. The average number of VXD2 hits per radial track is 2.3. At least two hits are possible for any track within $|\cos\theta| < 0.75$.

Each CCD is approximately 1cm square, and contains 385 $\times$ 578 pixels, each 22 μm square. Each pixel has a depletion depth of 5 μm. Charge collection occurs over the whole depth of the epitaxial layer ($\sim$ 15 μm) which allows excellent position resolution even for tracks passing through the detector at large dip angles.

The detector is operated at 190K to suppress dark current and the loss of charge transfer efficiency due to radiation damage [55]. It is housed in a very low mass cryostat, and cooled with liquid nitrogen, which is piped to and from the detector by means of vacuum jacketed pipes.

The vertex detector and the cryostat make up the R20 module which is clamped to each end of the CDC, by means of a pair of aluminium support cones. (The R20 module is shown in Figure 4.1)

The readout rate of VXD2 is 2MHz, the shaping time of approximately 300ns giving a noise performance of $< 100e^{-}$(rms). The VXD2 anologue output is read out on striplines to local electronics which transmit the data via twisted pairs to analogue-to-digital converters on top of SLD.

Immediately after installation, 2 of the ladders were found to be dead due to inaccessible connection problems. This was confirmed to be due to the micro connectors after VXD2 was removed from SLD.

2.4.3 The Luminosity Monitors, LUM

The luminosity monitors [56] are silicon-tungsten calorimeters arranged in a pad configuration surrounding the beam-pipe. Their purpose is to measure the absolute integrated luminosity by recording small angle Bhabha scattering events. The luminosity monitor covers the 28-68mrad polar angle range. There are 23 layers of tungsten each with a radiation length of 1% X_0 (3.5mm thick), separated by 8mm. The silicon diode detectors, which provide the readout, are mounted on semi-circular printed circuit motherboards, and are sandwiched between the tungsten.

Electromagnetic showers which develop in the tungsten liberate electrons in the fully depleted silicon detectors, which are segmented radially into pads. The pads are arranged into a projective tower geometry. Each tower is divided longitudinally into an EM1 section and an EM2 section.

2.4.4 The Drift Chambers, CDC and EDC

The drift chambers [57] provide momentum and position measurements of charged particles. There are five drift chamber systems, the Central Drift Chamber (CDC) located in the central barrel region and four Endcap Drift Chambers (EDC), see Figure 2.4. The CDC is constructed in the form of a cylindrical annulus of inner radius 20cm, outer radius 1m, and length 2m. The active elements are 5120 sense wires interspersed throughout the chamber volume.

The sense wires are arranged into 80 layers which are organised into 10 superlayers of 8 sense wires. At 4mm from the sense wire plane are guard wires held at a voltage of $\sim$ 3kV and at 30mm on either side are field wires held at a voltage of $\sim$ 5kV, Figure 2.7. Several additional guard and field wires at the top and bottom of the cell complete the field shaping. These guard and field wires shape the potential and create the field necessary for amplifying the charge. A unit of sense and associated field wires is called a cell.

The superlayers alternate between Axial (A), and stereo orientations, (U and V), of $\pm$ 41 mrad with respect to the beam axis, in the arrangement AUVAUVAUVA, Figure 2.8. The field shaping and guard wires consist of 150 μm diameter gold plated aluminium wires and the sense wires are 25 μm diameter gold plated tungsten wires.

The gas mixture was chosen to provide maximum precision on the drift distance measurement. The gas mixture is CO_2 (75%), Ar (21%), Isobutane (4%), and H_2O (0.2%).

Electrons produced by the ionising particles crossing the CDC drift under the force of the electric field onto the sense wires, where they are amplified by an avalanche mechanism in the gas. The resulting signals are read out, preamplifiers providing further gain for the signal. Both ends of each sense wire are instrumented.

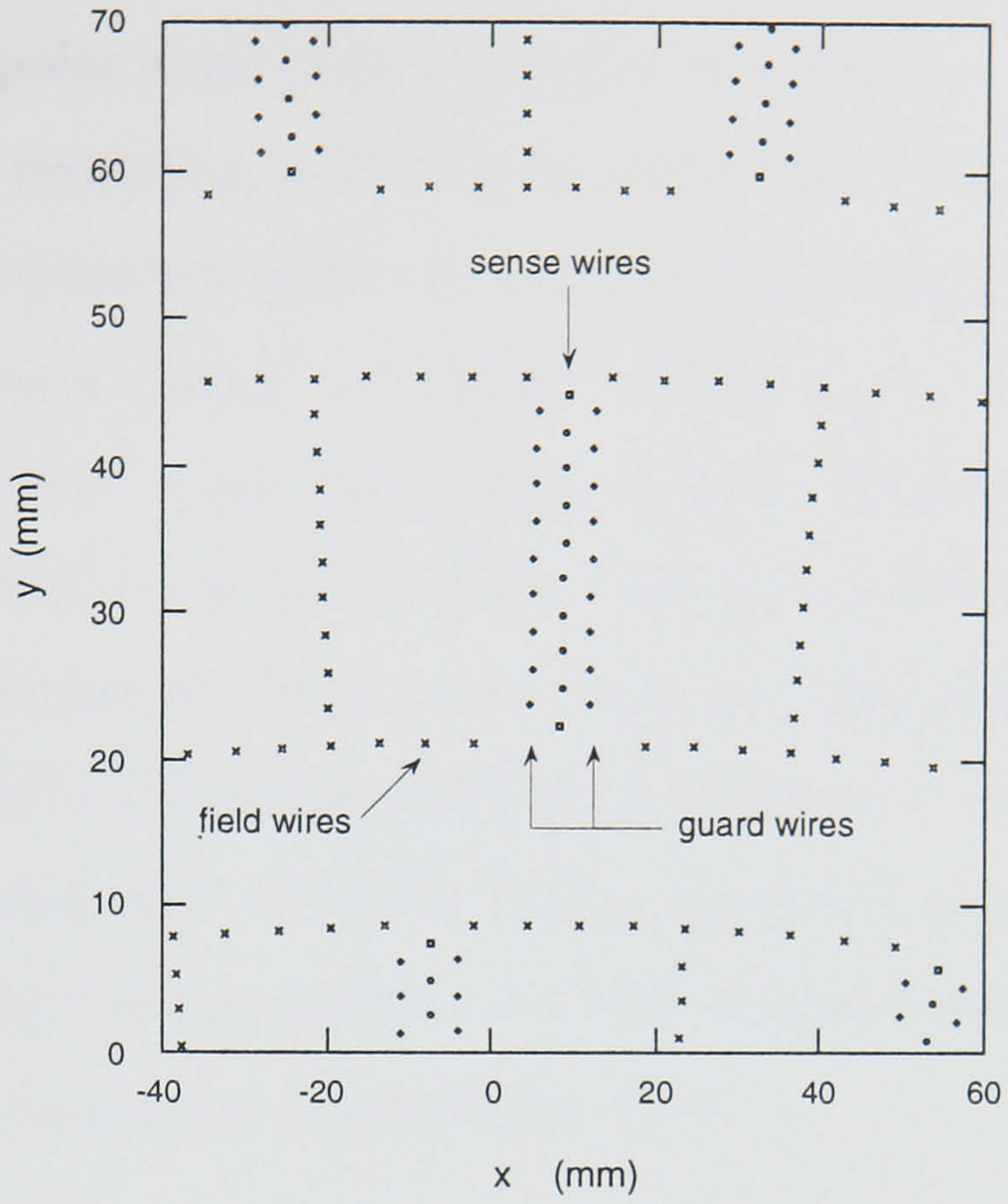

Figure 2.7: Schematic of the CDC showing the positions of the different types of wires.

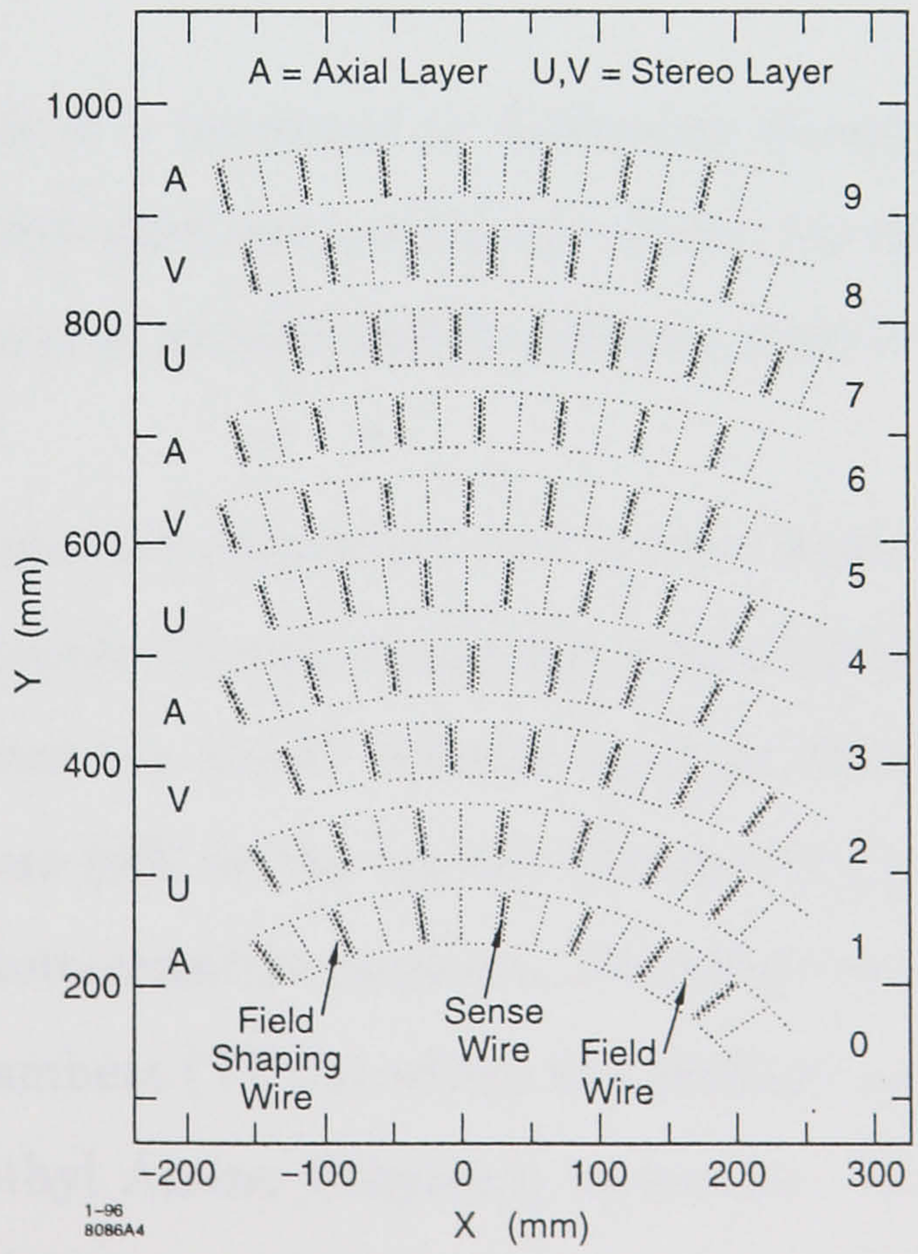

Figure 2.8: Systematic of the CDC showing the AUVAUVAUVA structure.

enabling charge division [58] to be used to extract the z co-ordinate of the hit. The measurement of the polar angle comes from the stero layers.

An intrinsic drift resolution of 55-110μm in the region of uniform field has been achieved [57]. This resolution gives rise to a momentum resolution which is characterised by the formula $(\sigma/p_t)^2 = 0.0050^2 + (0.010/p_t)^2$. Where p_t is the track momentum perpendicular to the beam axis in GeV/c. The first term is the effect of measurement error, and the second is due to multiple scattering.

The endcap drift chambers consist of two sets of endcap detectors located in the forward region ($\theta > 45°$). The inner EDCs are situated at $z = \pm$ 1.2m, whereas the outer EDCs are situated at $z = \pm$ 2.0m. Each chamber is constructed from only 3 superlayers. At the time of this analysis the SLD reconstruction code has not been sufficiently tuned to reconstruct tracks in the EDC.

2.4.5 The Čerenkov Ring Imaging Detectors, CRID

The Čerenkov Ring Imaging Detector (CRID) [59] was designed to allow particle identification over a wide range of momenta. It can be used to separate charged $\pi/K/p$ and e/π.

To identify a particle it is necessary to determine directly or indirectly the rest mass of the particle. With particles moving at relativistic speeds, it is necessary to measure the momentum of a particle and its velocity, thereby determining the mass directly.

In order to achieve particle separation over a wide momentum range, the CRID has two radiators to generate Čerenkov photons, a liquid (C_6F_{14}) and a gas (C_5F_{12}). Figure 2.9. Photons from the liquid radiator impinge directly on the drift boxes, while a system of mirrors (480 in the barrel) focuses the photons from the gas radiator back onto the photo-sensitive medium. The photo-sensitive medium consists of Time Projection Chambers (TPCs) where the photons cause photo-ionisation of TMAE (Tetrakis Dimethyl Amino Ethylene) molecules. The electrons are drifted in a uniform field of 400 V/m to wire chambers where the charge is read out.

The position of the photo-ionisation is reconstructed using a combination of the

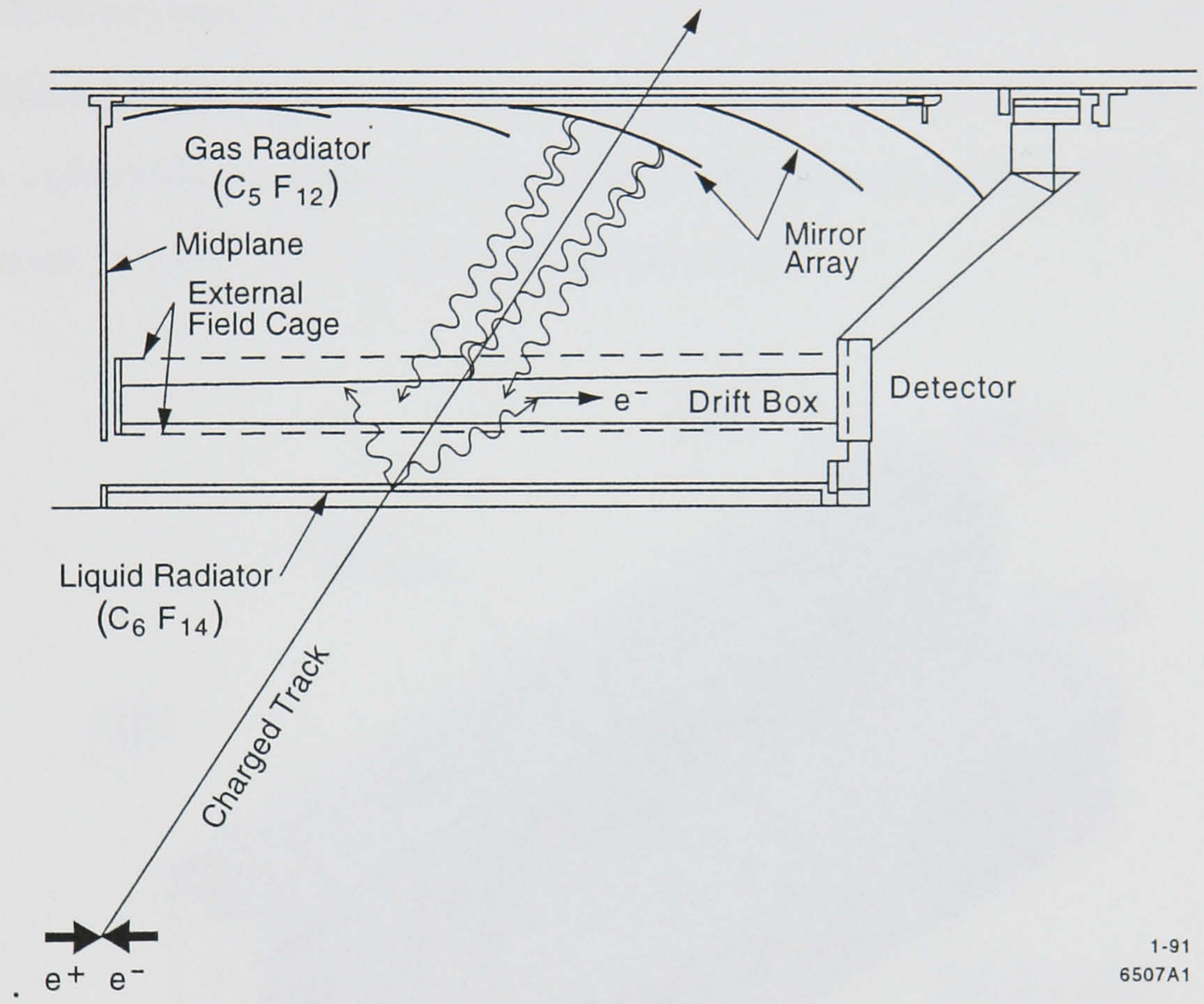

Figure 2.9: A schematic diagram illustrating the principle of the CRID operation. A charged particle entering the liquid radiator emits Čerenkov photons which impinge on the drift boxes containing a photo-sensitive medium. Čerenkov photons from the gas radiator are focussed back onto the photo-sensistive medium for detection.

drift time, wire address, and charge division on the readout wire. A ring is fitted to the data and finally the radius of the ring is used to assign a log-likelihood of the associated charged track with its measured momentum, being a particular particle type.

2.4.6 The Liquid Argon Calorimeter, LAC

The LAC [60] is a sampling calorimeter whose basic module consists of lead plates immersed in liquid argon. The argon is the active medium, as it is ionised by charged particles passing through the calorimeter. The lead serves to induce particle showers and as the collection medium for the charge liberated in ionising the argon. The basic structure of the LAC is shown in Figure 2.10.

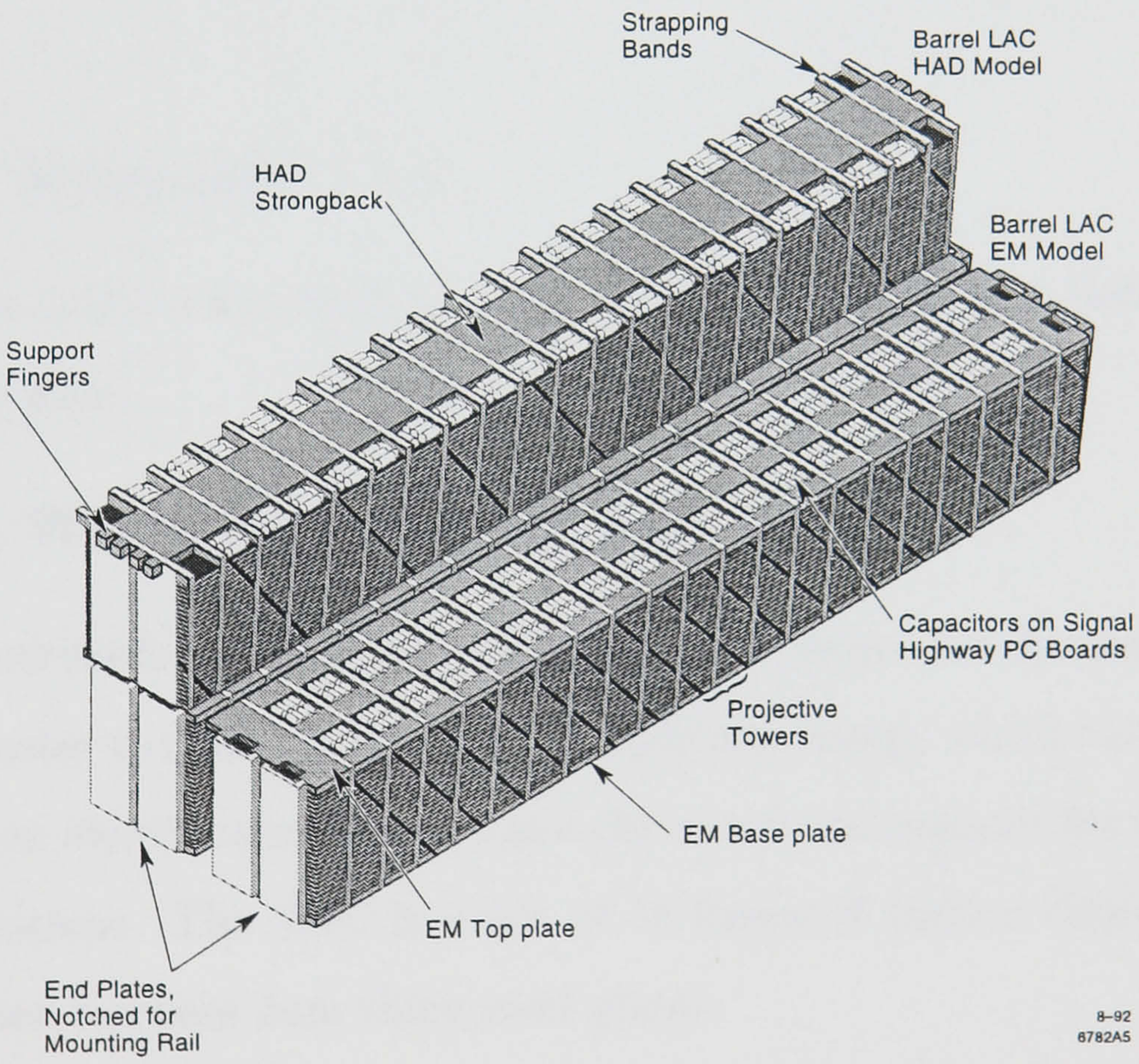

Figure 2.10: Electromagnetic and hadronic modules of the LAC barrel.

The layers of lead are broken up into alternating grounded plates and tiles held at $\sim$ 2kV; it is here that the charge collection occurs. As the lead is stacked, the tiles are arranged into projective towers whose longitudinal depth depends on how many layers have been ganged together for readout.

The LAC is segmented into two layers, the electromagnetic (EM) and the hadronic (HAD) sections. The EM section is formed from 2mm thick lead plates separated by 2.75mm of liquid argon, and is subdivided longitudinally into two layers, EM1 (6% X_0, 0.24 interaction lengths (λ_0)) and EM2 (20% X_0, 0.6λ_0). The HAD section is formed with 6mm thick lead plates, but the 2.75mm argon gap is maintained. The HAD section is also subdivided into HAD1 (13.9% X_0, 1λ_0) and HAD2 (13.9% X_0, 1λ_0). The EM towers subtend one quarter of the solid angle of the HAD towers, so that each set of four EM towers is backed by a single HAD tower. The EM section contains approximately 99% of the energy from a 45 GeV electron, while the LAC as a whole contains 85-90% of the total energy in a hadronic Z^0 decay. The energy resolutions for the LAC have been measured [61] using $e^+e^- \longrightarrow e^+e^-$ and $Z^0 \longrightarrow q\bar{q}$ events to be $12\%/\sqrt{E}$ and $65\%/\sqrt{E}$ for the EM and HAD sections respectively.

2.4.7 The Solenoidal Coil

Surrounding the LAC is the SLD solenoid. It provides a uniform field of 0.6 Tesla along the beam axis.

2.4.8 The Warm Iron Calorimeter WIC

The WIC [62] serves four functions within SLD: flux return for the magnetic field, a backing calorimeter to measure the residual hadronic energy which has leaked out of the LAC, a muon identification system and the structural support for the rest of the detector sub-systems. The WIC is made of 18 layers of Iarroci (limited-streamer) tubes sandwiched between 5cm thick steel plates.

The tubes are instrumented with square pad readout for calorimetric purposes and long strips for reading out the individual tubes in order to use the WIC as a muon tracker. The WIC geometry is shown in Figure 2.11 The WIC strips which provide the muon tracking information are arranged in two separate arrays 90° from each other to enable the trajectory of a muon to be determined in two dimensions.

The endcap chambers in particular have half of the strips oriented vertically and

half horizontally.

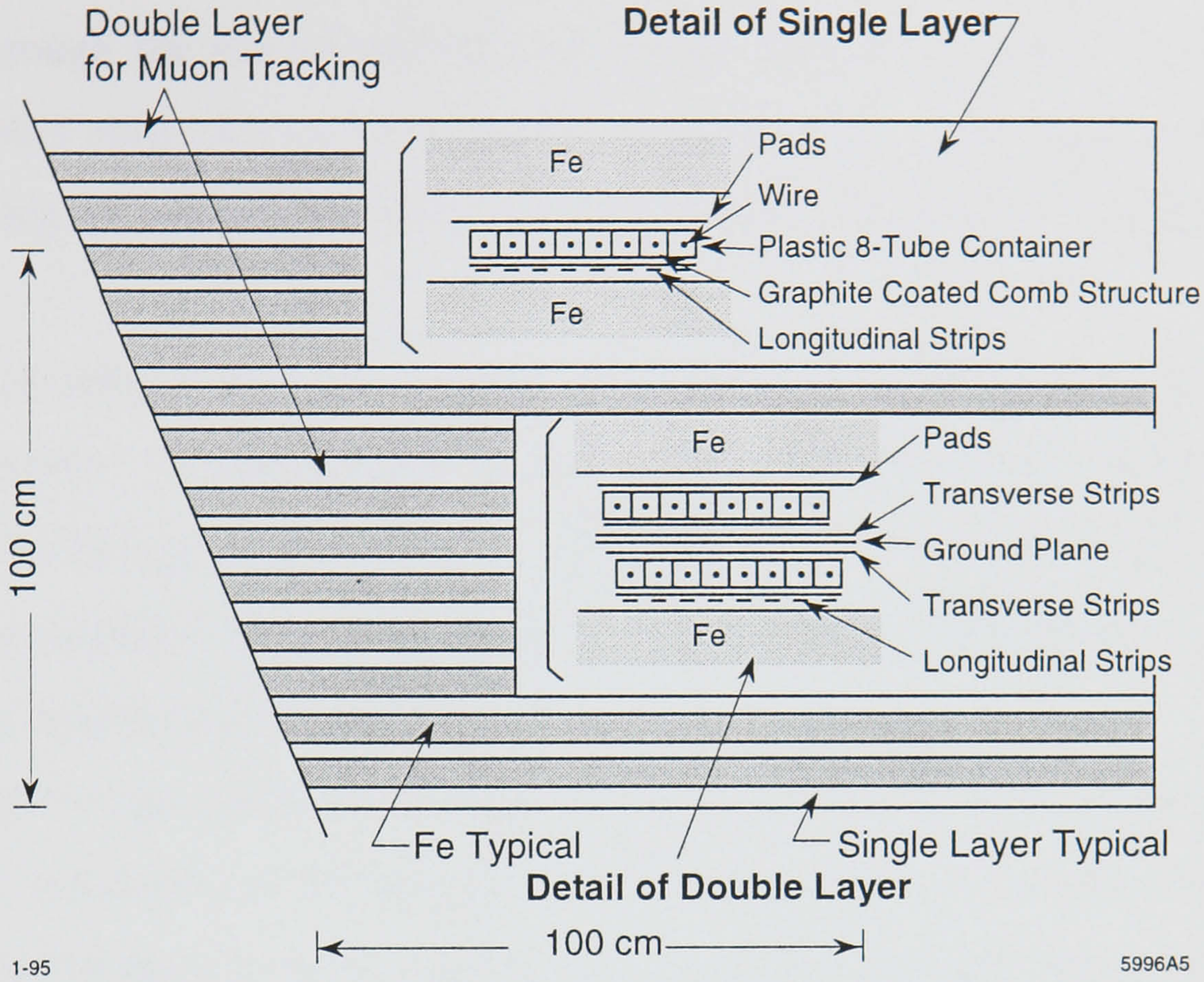

Figure 2.11: The WIC structure, showing the single layers containing longitudinal strips for muon tracking as well as pad tower readout. Also shown are the double layers with crossed strips for tracking in the other plane.

2.5 Tracking Performance

The SLD tracking system consists of two elements, the CDC and the VXD. The reconstruction of tracks in these two subsystems is briefly described in the following sections.

2.5.1 CDC Track Reconstruction

The reconstruction of a track in the CDC is a complicated procedure which can be split into four stages, raw hit finding, vector hit finding, pattern recognition and track fitting.

The first stage involves finding the positions of hits in the CDC. The z position was determined by the charge division from the double ended readout of each wire.

Simple cuts were applied to remove common noise sources, such as synchrotron radiation. These hits are characterised by proximity in time to the beam crossing (no drift through the gas is involved), small pulse height and total charge.

The second stage is to identify segments of the tracks called vector hits. These are sets of four or more hits within a cell that are consistent with belonging to the same helix.

The third stage is pattern recognition [63] which combines vector hits to form candidate tracks. Combinations of vector hits on the axial layers of the chamber are formed by fitting them to circles. The vector hits are added to the axial track segment depending on whether the angle of the stereo hit matches the track at the appropriate longitudinal position.

The fourth stage, track fitting, starts with the estimated track parameters from the pattern recognition. It then swims a helical trajectory through the detector material, modifying it to take into account the effects of energy loss, multiple scatterings and local variations in the magnetic field. A χ^2 is formed, and its derivatives with respect to each of the five track parameters (the curvature, the dip angle, the azimuthal angle and the two position parameters) are estimated. The second derivatives are formed into a matrix. The χ^2 is iteratively minimised using the derivatives. Hits can be added or removed at each iteration to improve the hit finding rate and the χ^2. When the fit has converged the second derivatives are inverted to form the error matrix for the track parameters.

2.5.2 VXD Reconstruction

To improve the overall tracking performance the reconstructed CDC tracks are linked to VXD hits. The CDC track parameters are extrapolated in towards the vertex detector. When the track intercepts the surface of a CCD on the outer layer of the detector, a primary search area is established. This elliptical search area is momentum dependent ranging from 0.5-4mm in $r-\phi$ and from 5-25mm in z. When the hits have been found, the extrapolated track is constrained to go through the candidate and a search is made to find other hits on the inner barrels. This secondary

search area is 100μm in both the $r-\phi$ and z directions. A combined fit, taking into account the multiple scattering [64] is then performed. All track candidates with two or more hits at different radii and that have a good χ^2 are said to be "linked".

Due to the dead ladders, tracks where there was only one VXD hit had to be recovered. The extrapolated track was constrained to go through the interaction point and a search area of $1\times5\text{mm}^2$ was used to detect candidate hits.

The linking efficiency was measured to be 96% [65].

2.5.3 Impact Parameter

The impact parameter of a track is defined as the distance of closest approach of the extrapolated track to the interaction point, Figure 2.12

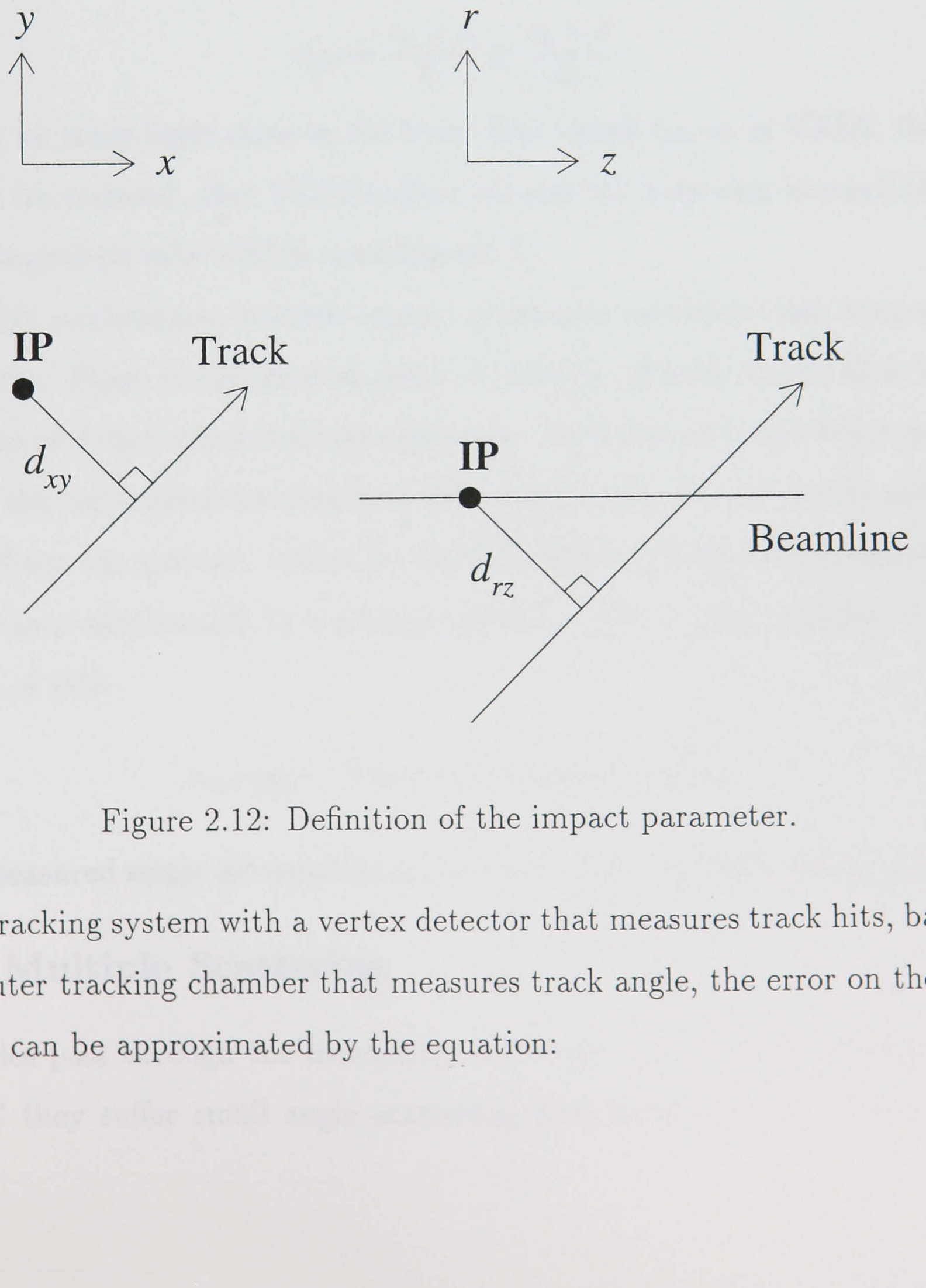

Figure 2.12: Definition of the impact parameter.

For a tracking system with a vertex detector that measures track hits, backed up with an outer tracking chamber that measures track angle, the error on the impact parameter can be approximated by the equation:

$$\sigma_d = \sigma_{int} \oplus \frac{\sigma_{scatt}}{p \times \sin^{\frac{2}{3}}\theta} \tag{2.2}$$

where σ_{int} is the intrinsic resolution of the tracking devices, σ_{scatt} is the multiple scattering term, θ is the track polar angle, and p is the momentum of the particle in GeV/c. These contributions are described below.

2.5.4 Intrinsic Detector Resolution

The intrinsic resolution is the uncertainty due to detector resolution on the position of track hits contributing to the track fit. For a pair of hits with a precision σ at distance r_1 and r_2 from the primary vertex position with distance δ_r between them, the intrinsic resolution is given by:

$$\sigma_{int} = \frac{r_1 \times \sigma}{\delta_r} \oplus \frac{r_2 \times \sigma}{\delta_r} \tag{2.3}$$

By having an inner layer close to the beam-line (small r_i), as in VXD2, this uncertainty can be reduced. But VXD2 suffers because its lever arm is small (δ_r). This has been improved with VXD3, see Chapter 3.

The high momentum, intrinsic impact parameter resolution was measured from $\mu^+\mu^-$ events. These events provide pairs of isolated collinear tracks that have high momentum and minimum multiple scattering. Since the primary vertex position is not used, the uncertainty coming from this is removed. The $\mu^\pm$ tracks should each originate from the primary vertex so any difference between the measured origins of the tracks is attributable to tracking resolution. The μ-pairs indicate an intrinsic resolution of [65]:

$$\sigma_{int}(xy) = 11\mu m \text{ and } \sigma_{int}(rz) = 38\mu m$$

The measured single hit resolutions are 5 μm in the xy plane and 6 μm in z [65].

2.5.5 Multiple Scattering

As particles pass through the material of the beam pipe, vertex detector, cryostat and CDC they suffer small angle scattering from Coulomb interactions with the

nuclei. The multiple scattering term for the impact parameter resolution term is a function of momentum. To measure this term, the tracks from hadronic Z^0 decays are split into bins of momentum and $\cos\theta$ and a Gaussian core fit is done to the impact parameter distribution. This is then corrected for tracks that do not come from the interaction point, for example, tracks from B decays [66].

2.5.6 Impact Parameter Resolution

The intrinsic and multiple scattering contributions to the impact parameter resolution is given by [65]:

$$\sigma_d^{r\phi} = 11 \oplus \frac{70}{p \sin^{\frac{3}{2}}\theta} \mu m \tag{2.4}$$

$$\sigma_d^{rz} = 38 \oplus \frac{70}{p \sin^{\frac{3}{2}}\theta} \mu m \tag{2.5}$$

where p is the momentum of the particle and θ is the polar angle of the track with respect to the beam direction. The impact parameter resolution as a function of momentum at $\cos\theta = 0$ is shown in Figure 2.13 [74].

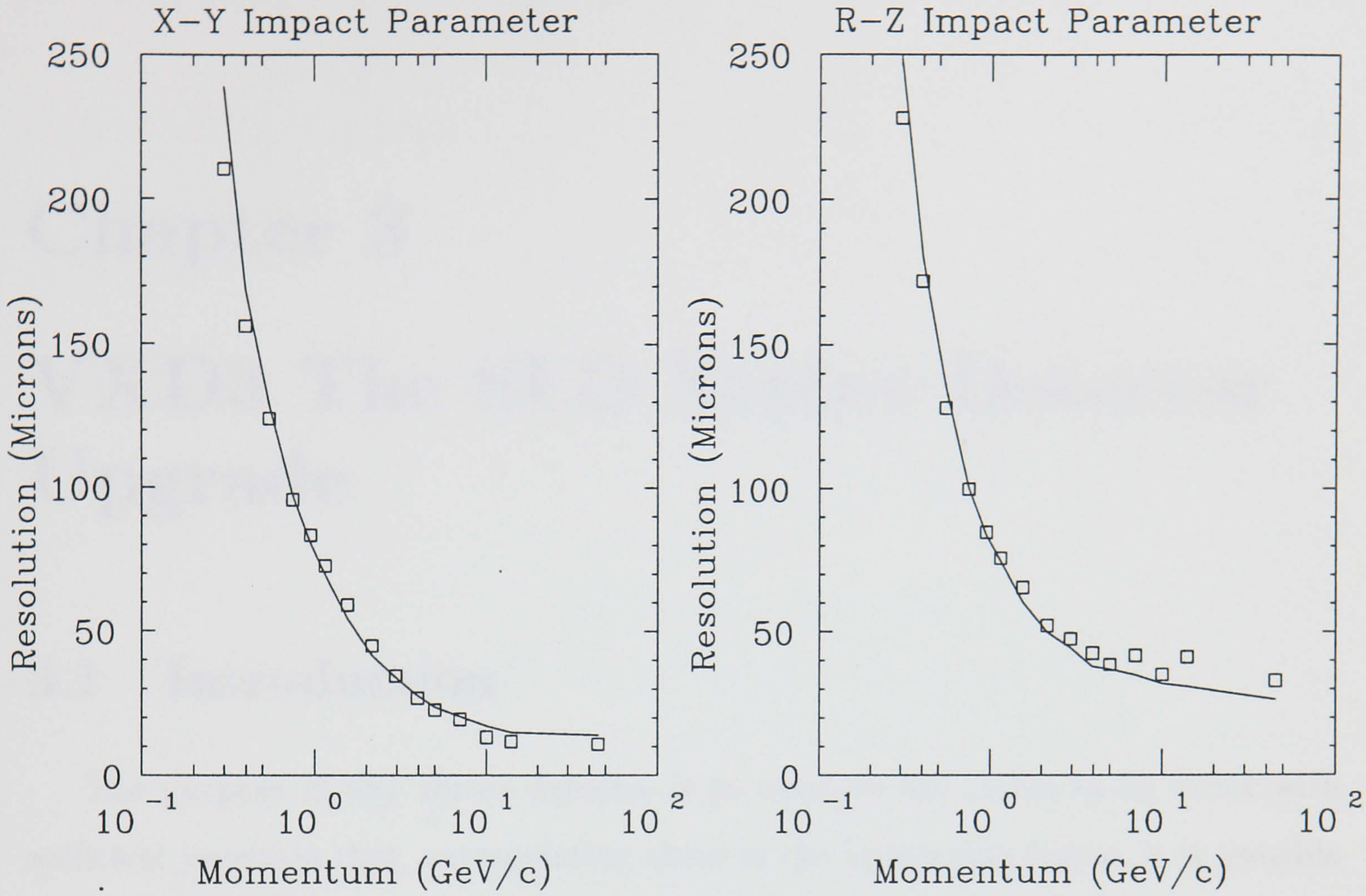

Figure 2.13: VXD2 impact parameter resolution. The squares are data and the solid line is the simulation [74].

Chapter 3

VXD3 The SLD Vertex Detector Upgrade

3.1 Introduction

The purpose of any vertex detector is to measure the tracks in an event with sufficient precision that, extrapolating them to the interaction region, it is possible to distinguish between those from the primary vertex and those from secondary or tertiary vertices due to the decay of particles containing heavy quarks (bottom or charm), or tau leptons. In practice, the majority of the tracks have rather low momentum, so that the measurement precision at the interaction region is limited by multiple scattering in the material of the vertex detector, rather than by its intrinsic measurement precision. In these circumstances, the usefulness of the detector for physics is dependent on achieving a small inner layer radius, a spacing between layers similar to that radius (allowing a good lever-arm for extrapolation to the interaction region) and the smallest possible amount of material. In this chapter the motivation for the upgrade vertex detector will be given, along with details of the design and construction of this new detector, called VXD3.

3.2 VXD2 and its Limitations

VXD2 was a four layer detector, Figure. 2.6. The detector elements (8-CCD ladders) had to be redistributed because the planned radius of the beam pipe was increased from 10 mm to 25 mm while VXD2 was being built.

Hence barrel 1 covered only a little more than 50 % of the azimuth, leaving barrel 2 to fill the gaps. Barrel 3 covered not much more than 50 % of the azimuth with 17 ladders, with barrel 4 again covering the gaps. Therefore VXD2 could only guarantee two hits per track (an average of 2.3 hits per track), with sometimes a radial separation of only 4mm between them. Thus the lever arm was poor, and, as explained in Section 2.5.3, the impact parameter resolution suffers because of this.

The detector was operated in a background environment of predominantly electromagnetic radiation (a broad X-ray spectrum resulting from multiple bounces of synchrotron radiation photons, and fluorescence). This can lead to two types of radiation damage. The first is oxide damage, this is caused when electromagnetic radiation generates electron-hole pairs in the gate oxide, leading to flat-band voltage shifts, which makes it necessary to change the operating biases. These effects were observed in VXD2 only at a very small level. The second is bulk damage. This is where higher energy electromagnetic radiation causes displacement damage in the silicon crystal. This leads to a degradation in the charge transfer efficiency (CTE). This was seen in VXD2 as signal reduction of 10% on the inner facing CCDs of barrel 1, or an effective CTI of $\sim 1.7 \times 10^{-4}$.

The space point precision on each point was ~ 5 μm, but as a result of the poor lever arm between measurements, the impact parameter resolution at the IP for a track of momentum p (in GeV/c), and polar angle θ with respect to the beam line was limited, Equations 2.4 and 2.5.

3.3 VXD3 Improvements

The ideal SLD vertex detector would have the following improvements.

- *Full Three Hit Azimuthal Coverage:* Full azimuthal coverage in each of the three barrels, to achieve a self-tracking capability independent of the CDC, and hence improved overall tracking efficiency.

- *Coverage Out To $|cos\theta| < 0.85$:* The CDC requires a minimum of four of the ten superlayers to be used for efficient tracking pattern recognition and

reasonable momentum measurement. This limits the CDC coverage to $|\cos\theta| < 0.85$. Hence the new vertex detector should have three hit coverage to at least $|\cos\theta| < 0.85$ to provide full coverage of the CDCs useful tracking volume.

- *Improved Impact Parameter Resolution:* The impact parameter resolution can be improved in two ways. The first is to improve the level arm of the detector, by increasing the radial distance between the layers, covering $|\cos\theta| < 0.85$. Hence longer ladders are needed. Secondly, multiple scattering must to reduced. This can be achieved by reducing the radiation length of detector material i.e. the ladders. This is very important because most of the tracks coming from heavy quark decays come from low momentum tracks.

To summarise, an improved detector must have longer and thinner ladders that provide three hit azimuthal coverage out to $|\cos\theta| < 0.85$. This detector became known as VXD3 and its design and construction are described below.

3.4 VXD3 CCD Design

In order to construct longer ladders without increasing the complexity of the ladder design and without increasing the number of CCDs per ladder, larger CCDs were needed. A description of a CCD is given in Appendix B.

A number of advances in CCD technology had allowed the possibility of CCDs to be produced to customer specification and with large active areas, hence the upgrade became a reality. It was possible to produce four CCDs with an active area of $80 \times 16\text{mm}^2$, and a number of test devices (of smaller area) on one five inch wafer, see Figure 3.1. The devices used for VXD3 are known as CCD32-60.

Figure 3.3 is a schematic of a CCD32-60. The devices were split into quadrants for readout purposes, hence decreasing by a factor of four the amount of time needed to readout the device. The two stage output circuits, Figure 3.2, could be run at 10MHz, but in VXD3 the CCDs were read out at 5MHz to reduce clock feedthrough into the analog output. An increase in the number of outputs operated at higher speed, without overloading the limited space available for local electronics, was the

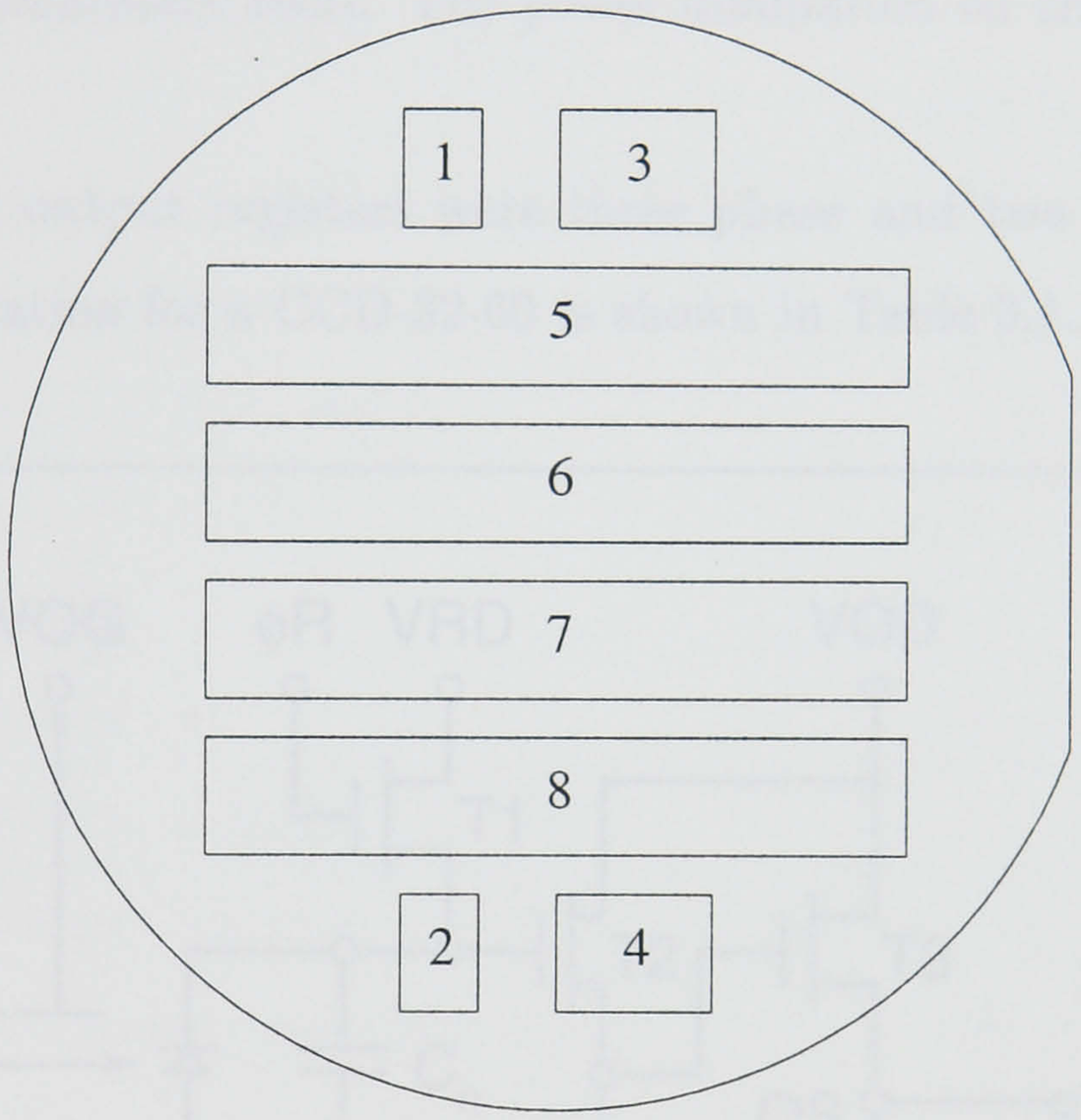

Figure 3.1: Wafer Layout for CCD32. Devices 1,2 were designated CCD32-00, used to setup the wirebonder. Devices 3,4 were designated CCD32-10, used for radiation tests. Devices 5-8 were designated CCD32-60, used for VXD3.

key to achieving a larger detector. The node capacitance was minimised to achieve the highest responsivity. The various circuit capacitances were adjusted to give both sufficient bandwidth and adequate damping with the system load capacitance C_L of 40pF. The second stage load resistor R3 (3.3KΩ) is off chip, on the front-end electronics board, to minimise power dissipation inside the detector cryostat. Both the first and second stage transistors were surface channel devices.

The CCD output node capacitance is approximately 40fF which, together with a voltage gain of 1.75, gives an overall resonsivity of about 3μV/electron. The output impedance is approximately 260Ω. The power dissipation on chip for each channel is $\sim$ 45mW.

The image and output registers were three phase and two phase respectively. The design specification for a CCD-32-60 is shown in Table 3.1.

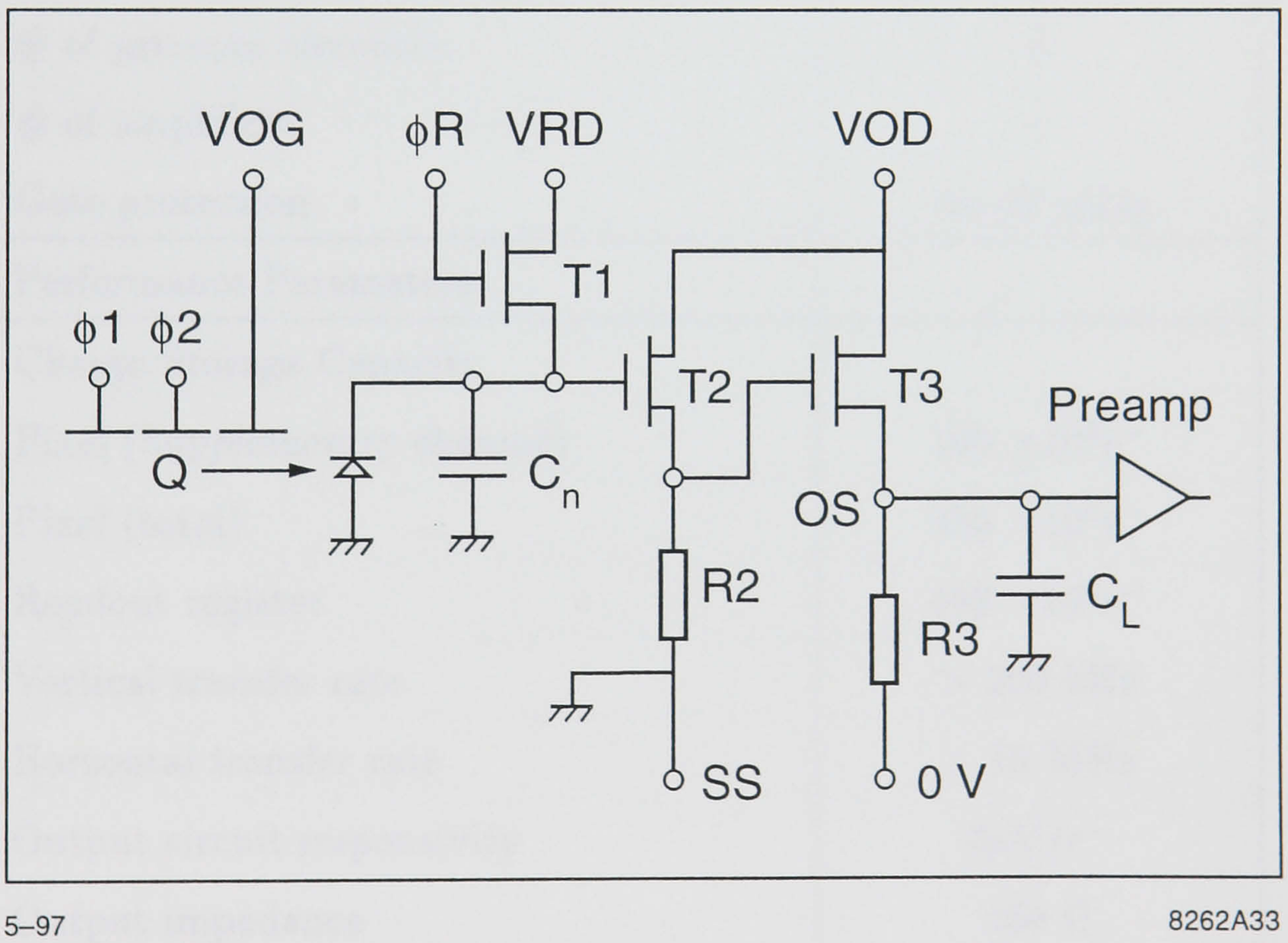

Figure 3.2: Schematic of the two stage output circuit used for CCD32-60.

Basic Design Features	
Substrate resistivity	< 20 mΩcm
Epitaxial layer resistivity	20 Ωcm
Format	4 quadrant full frame
# of pixels	800 Hor $\times$ 4000 Vert
Pixel size	20 $\times$ 20 μm
Sensitive area	$\leq$ 16 mm $\times$ 82.8 mm
Inactive edge spacing	< 300 μm
Thickness	150 $\pm$ 20 μm
Passivation	2 μm polyimide
Image area clock type	3-phase
Readout register clock type	2-phase
# of pre-scan elements	6
# of amplifiers	4
Gate protection	On all gates
Performance Parameters	
Charge Storage Capacity	
Pixel (Supplementry channel)	$100 \times 10^3 e^-$
Pixel (total)	$350 \times 10^3 e^-$
Readout register	$400 \times 10^3 e^-$
Vertical transfer rate	$>$ 200 kHz
Horzontal transfer rate	$>$ 10 MHz
Output circuit responsivity	$3\mu V/e^-$
Output impedance	260 Ω
Power Dissipation (on-chip)	
Image section (10 V clocks at 200 kHz)	1.3W
Readout register (10 V clocks at 10 MHz)	25 mW
Each output amplifier	45 mW

Table 3.1: CCD design specification [67].

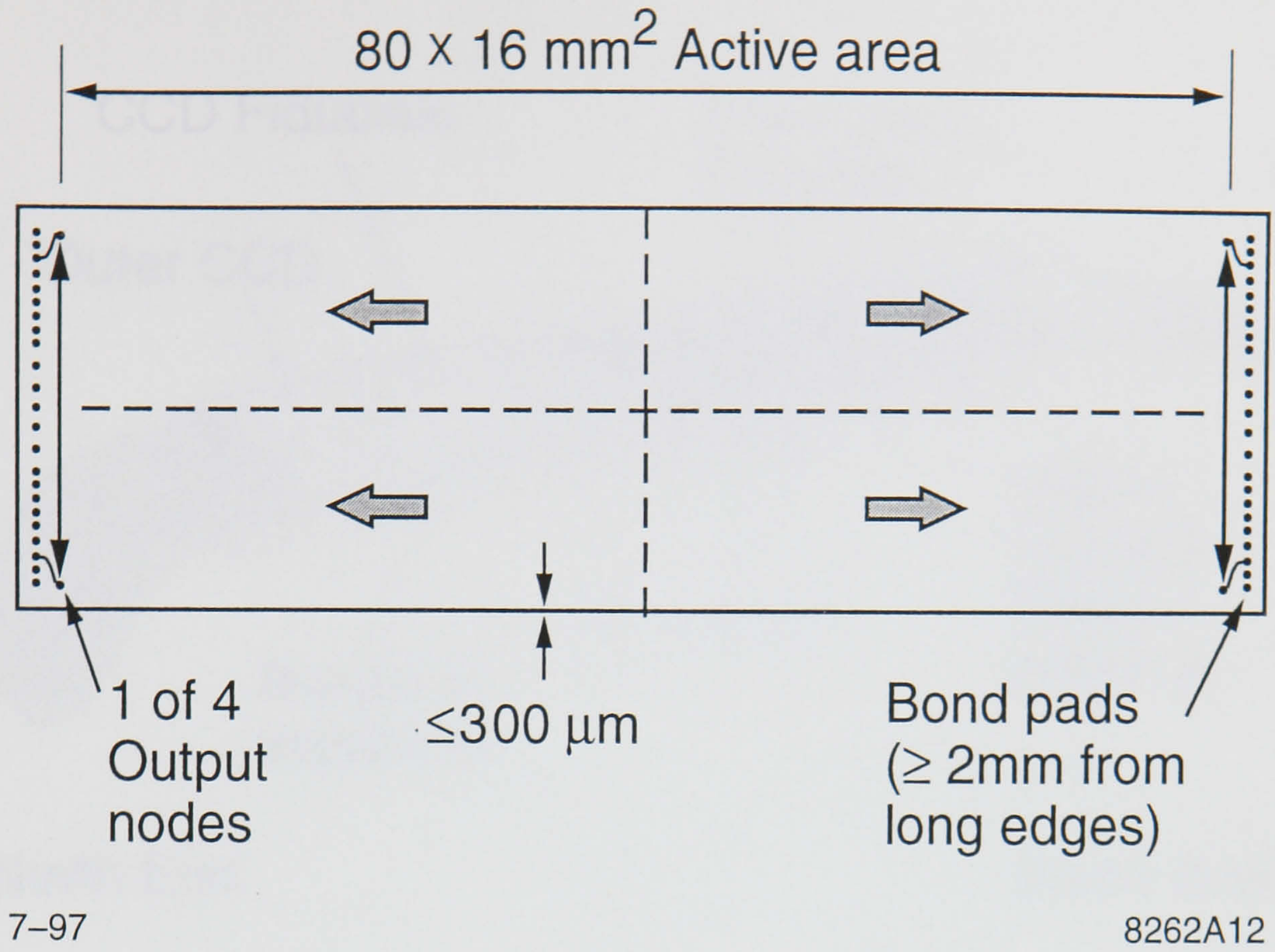

Figure 3.3: Schematic view of CCD32-60.

3.5 The 3-Barrel Layout

The size of the motherboards was set by the size of the CCDs. One CCD was mounted on each side of the motherboard forming a 2-CCD ladder as the basic detector component having an active length of 16cm, 1.7 times longer than the VXD2 8-CCD ladder. Figure 3.4 shows a schematic of a ladder. The active region extended across the whole ladder width and covered almost the whole length of the ladder as the two CCDs had a small overlap in the centre.

The wirebonds protruded out of the ladder surface along the short edge. This feature permitted adjacent ladders in the same barrel to be placed in a shingled layout with a small cant angle of 9-10°, thus providing azimuthal coverage overlap in the range of 300μm to 1mm, depending on layer and CCD location on the inner or outer surface of the ladder. This layout not only established complete azimuthal coverage for each barrel, but also provided important assistance in the tracking-based alignment, by using the tracks passing through the overlap regions, establishing direct constraints between the adjacent ladders.

The mean radii of the three layers was chosen to be 28.0, 38.2 and 48.3 mm with

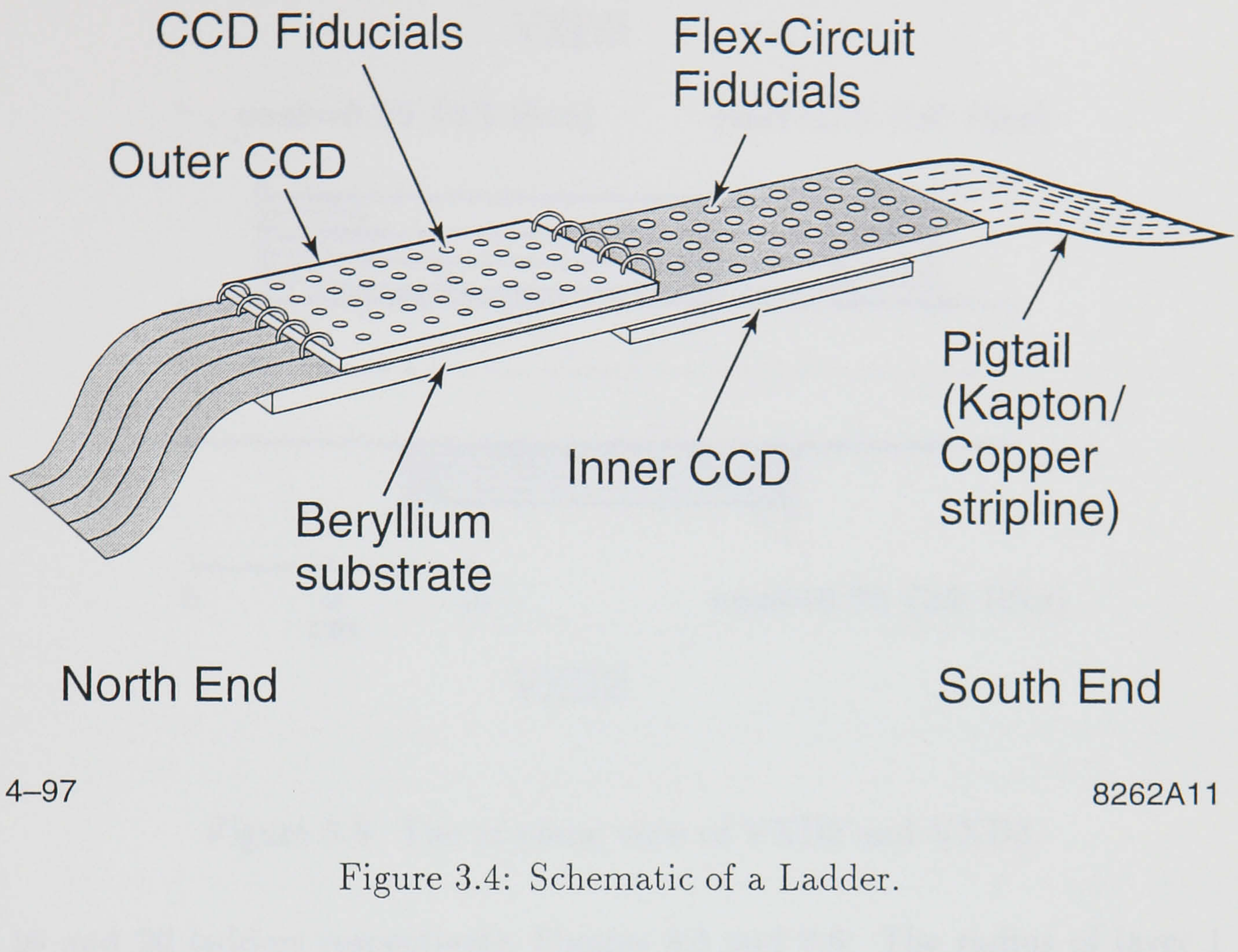

Figure 3.4: Schematic of a Ladder.

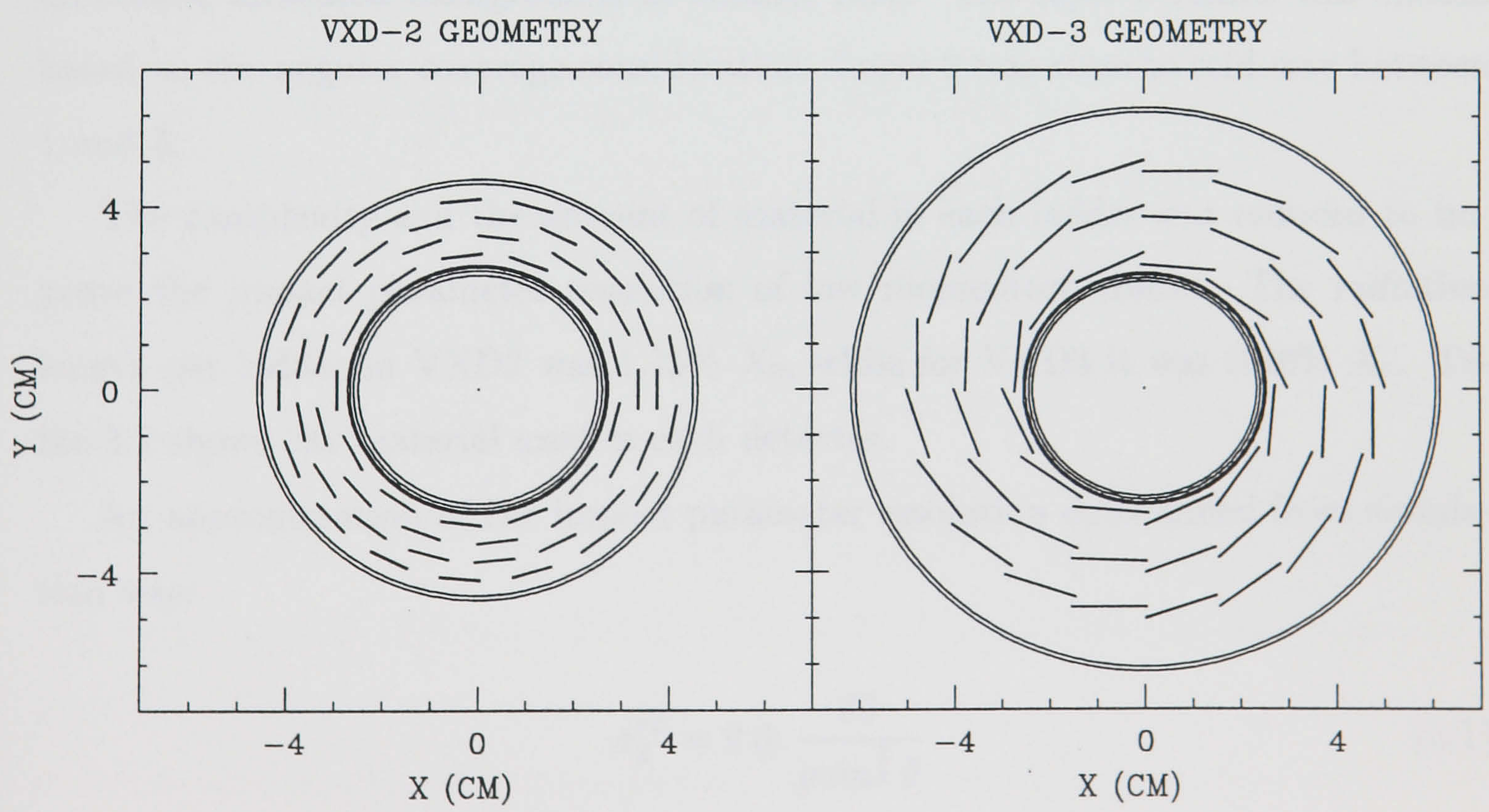

Figure 3.5: The xy plane view of VXD2 and VXD3.

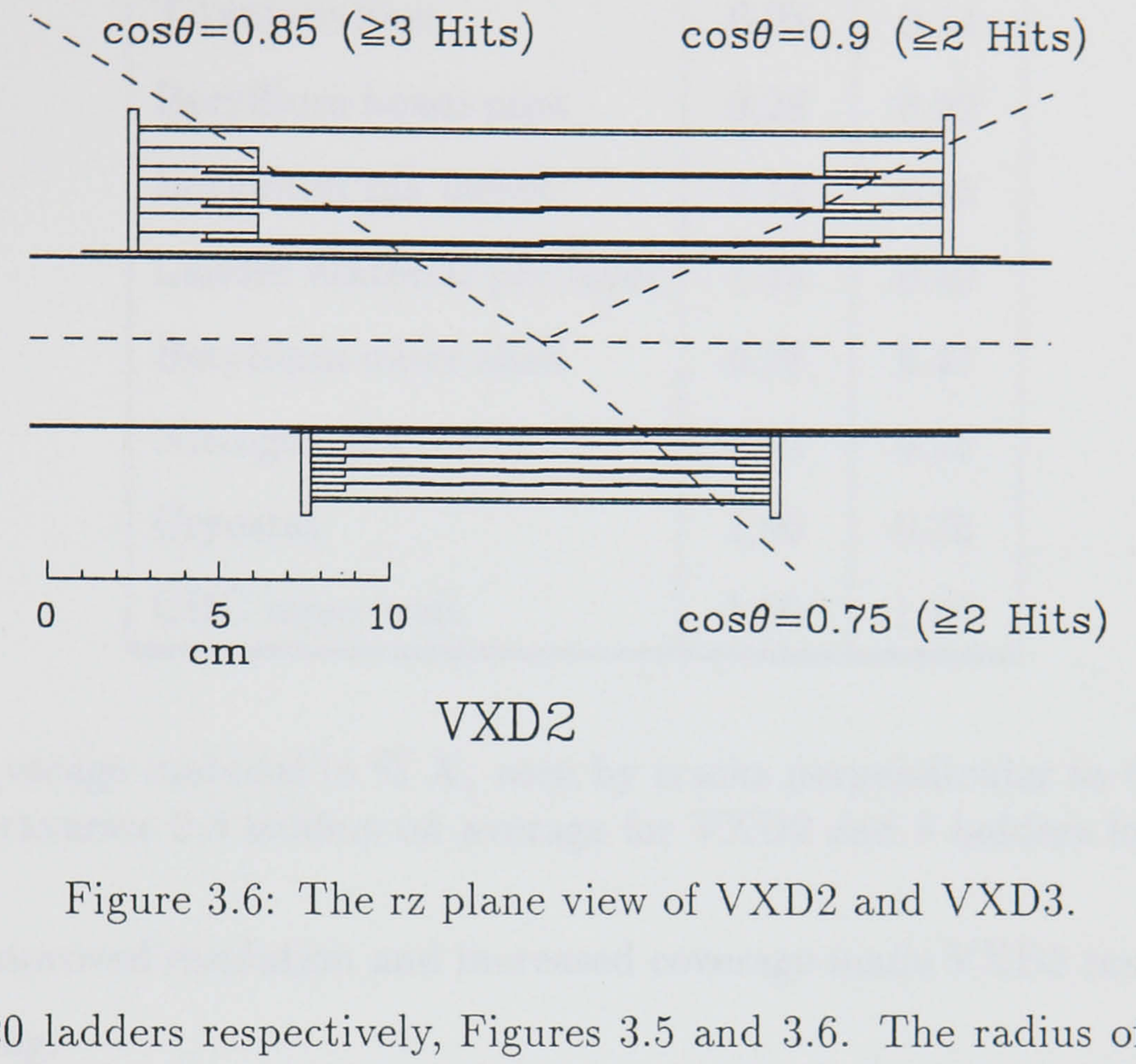

Figure 3.6: The rz plane view of VXD2 and VXD3.

12, 16 and 20 ladders respectively, Figures 3.5 and 3.6. The radius of layer 1 was constrained by the beam-pipe radius of 23.2 mm. It was decided not to risk the inevitable increased backgrounds at smaller radii. The layer 3 radius was chosen based on the angular coverage consideration. Layer 2 was close to mid-way between 1 and 3.

The complexity and the amount of material in each ladder was reduced to improve the impact parameter resolution of low momentum tracks. The radiation length per ladder in VXD2 was 1.15% X_0, while for VXD3 it was 0.40% X_0. Table 3.2 shows the material used in each detector.

An approximation of the impact parameter resolution determined from simulation was:

$$\sigma_d^{r\phi} = 9 \oplus \frac{33}{p \sin^{\frac{3}{2}} \theta} \tag{3.1}$$

$$\sigma_d^{rz} = 17 \oplus \frac{33}{p \sin^{\frac{3}{2}} \theta} \tag{3.2}$$

Figure 3.7 shows the expected impact parameter resolution as a function of momen-

	VXD2	VXD3
Titanium liner	0.28	0.14
Beryllium beam-pipe	0.28	0.22
Beryllium gas jacket	0.14	0.16
Ladder Material per layer	1.15	0.40
Beryllium outer shell	0.28	0.47
Nitrogen gas	0.05	0.05
Cryostat	1.90	0.70
CDC inner wall	1.80	1.80

Table 3.2: Average material in % $X_\circ$ seen by tracks perpendicular to the beamline. Each track traverses 2.3 ladders on average for VXD2 and 3 ladders for VXD3.

tum. This improved resolution and increased coverage made VXD3 much better for flavour tagging.

3.6 Design Overview

The detector operating conditions required the placement of 96 flexible thinned CCDs, or 48 ladders in a cryogenic environment (operating temperature $\sim$ 220K). It was important for multiple scattering and alignment reasons that the detector was low mass but had a high mechanical stability.

The CCDs were attached to thin beryllium substrates (Section 3.7), forming ladders, Figure 3.4. These ladders were attached to a series of three concentric beryllium annuli, which were clamped to the overall beryllium support stucture, which consisted of a closed cylinder external to the detector barrels, Figures 3.5 and 3.6. This structure was made from beryllium [75]. The support structure could be split to allow the two complete half-detectors to be assembled around the SLC beam-pipe. To obtain a high level of geometrical repeatablity of the support structure at the assembly, all mating surfaces were lapped flat and all adjacent components were match drilled, reamed and pinned. This extremely rigid support

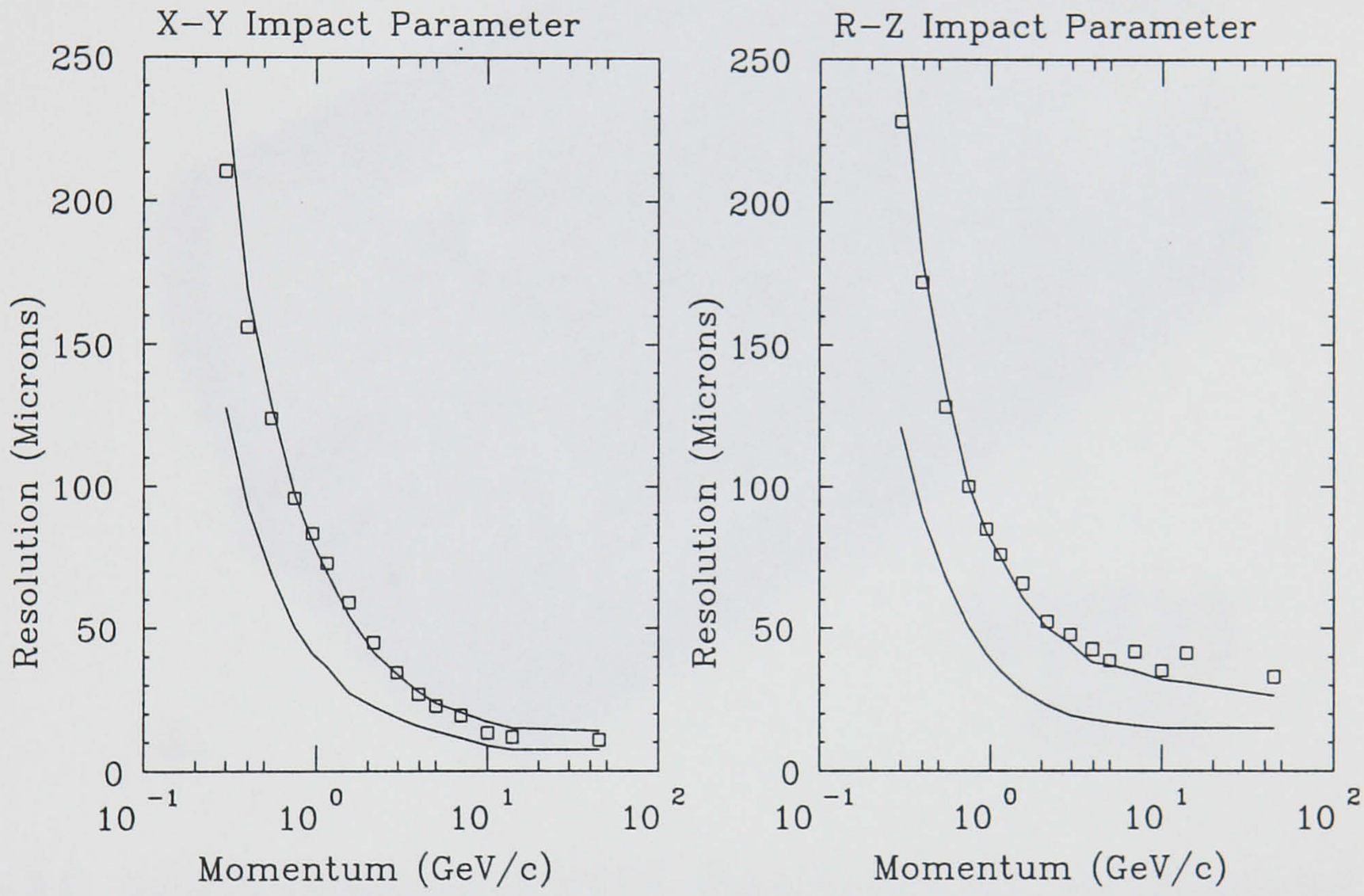

Figure 3.7: A comparison of the impact parameter resolution as a function of momentum for tracks at $\cos\theta = 0$ for VXD2 and VXD3. The measured resolution from VXD2 data are shown as squares, and agree well with the data. The second curve, without data points, is the VXD3 simulaton [74].

structure transformed the 48 flexible ladders into a highly stable 3-barrel assembly. This demountable structure permitted a succession of assemblies with one barrel at a time, allowing a full optical survey of the CCD geometery to be built up layer by layer. A mesh construction of the support shell permitted the survey of each installed barrel from the outside, Figure 3.8.

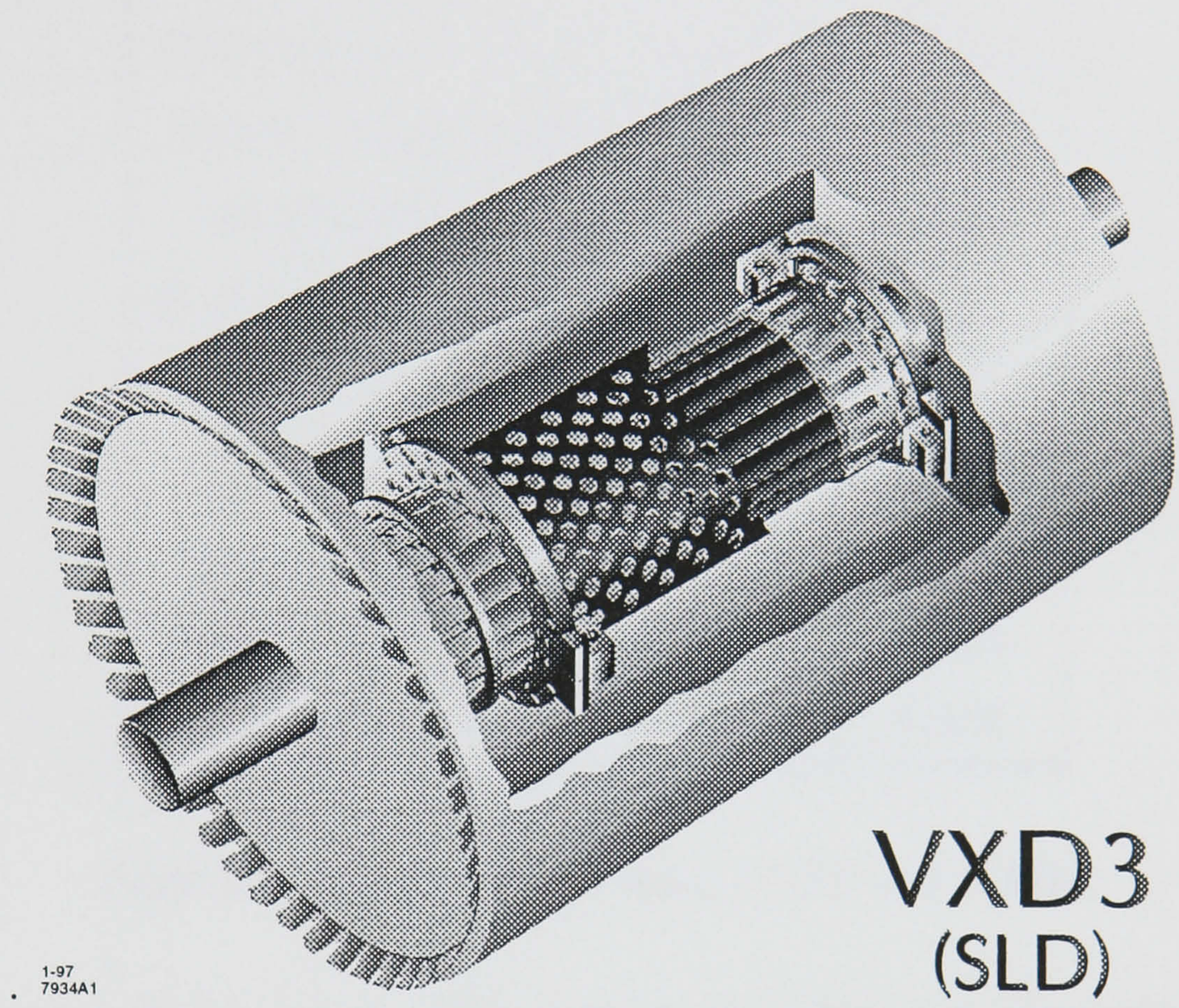

Figure 3.8: Artist's impression of VXD3. Showing the detector, surrounded by the mesh through which the detector survey was done, in the middle of the cryostat.

The VXD support structure when fully assembled consisted of a rigid cylinder which was mounted to the beam-pipe by means of a low-stress, three point kinematic mount. This assured that the detector shape during the survey (when the detector was mounted on a short dummy beam-pipe) would be identical to that in the final assembly on the real SLD beam-pipe.

Table 3.3 shows a comparison between VXD2 and VXD3.

In SLD, the vertex detector has to be cooled down so it is contained within a low mass foam cryostat. The inner section of the beam-pipe on which it is mounted is mechanically isolated from the SLC final focus system by means of an atmospher-

Parameter	VXD2	VXD3
# of layers	4	3
# of ladders	60	48
# of CCDs	480	96
# of pixels ($\times 10^6$)	110	306
CCD active size (cm)	1.3 × 0.9	8.0 × 1.6
Active z length (cm)	9.2	15.9
<# Hits/Track>	2.3	3.2
% of ϕ Covered/Layer	60	100
2 Hit $\cos\theta_{max}$	0.74	0.90
3 Hit $\cos\theta_{max}$	-	0.85
Readout rate (MHz)	2	5
Readout time (msec)	160	< 100
X_0 per layer	1.15%	0.36%

Table 3.3: Comparison between VXD2 and VXD3.

ically balanced bellows system. This reduces (but does not eliminate) occasional disturbances due (for example) to alignment adjustments to the final focus. Despite the fact that the vertex detector is hidden within the cryostat, any positional variations can be accurately inferred by monitoring with a capacitive wire position monitor, see Chapter 4. Within stable epochs, the position of VXD3 relative to the CDC (global alignment) is deduced by tracking, see Chapter 5. Tracking is also used to determine residual corrections to the internal detector geometry, in order to account for effects beyond the precision of the optical survey.

3.7 The Ladder

The basic support structure was a thin beryllium beam, 21cm × 1.6cm × 0.381mm having an initial flatness after machining (as measured by the sagitta when held at

one end on edge) of less than 100μm. Onto this was bonded, in one operation for both sides, a pair of Kapton/copper flex circuits: 13μm Kapton, carring $\frac{1}{2}$ ounce (17.8μm) rolled, annealed copper traces, passivated by a Kapton cover layer. These circuits ran the full length and width of the ladder, with pigtail extentions to carry the electrical traces to microconnectors, $\sim$ 5cm beyond each end of the ladder. An acrylic thermoplastic adhesive was used to attach the flex-circuits to the mother-boards under pressure, at a temperature of 350K. The CCDs were attached to the ladders by adhesive pads, and wirebonded from each end of the CCD to gold-plated pads Figure 3.9 shows an exploded view of the ladder assembly. Table 3.4 lists the contributions to the ladder thickness of 0.40% $X_\circ$ in the active volume of the detector.

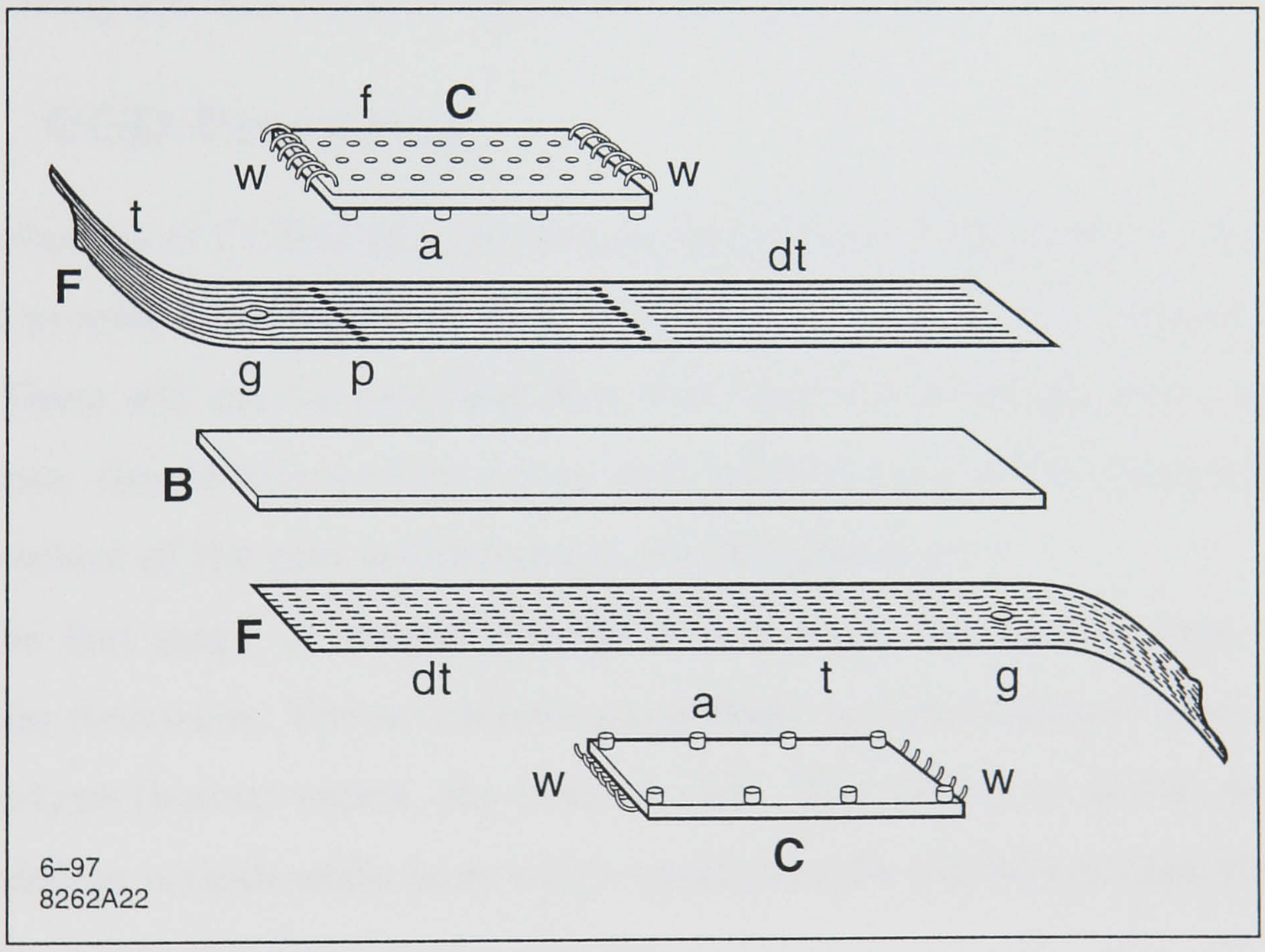

Figure 3.9: Exploded view of a Ladder. Where C is CCD, f is fiducial pad, a is adhesive, w is wirebond, F is flex cicuit, B is beryllium beam, p is bond pad and t is trace.

3.8 Ladder Production

The ladders were produced at EEV [68], and involved a complex and lengthy process of production and testing. Figure 3.10 shows a flow diagram of the whole process.

Component	Thickness (X_0)
Beryllium motherboard	1.08×10^{-3}
CCD + Adhesive	1.60×10^{-3}
Kapton + Adhesive (Both sides)	0.47×10^{-3}
Metal Traces (17.8μm) (average both sides)	0.90×10^{-3}
Total	4.05×10^{-3}

Table 3.4: Contributions to the ladder thickness. The bond pads in the central region (7.6μm gold on a 3.8μm nickel barrier layer) are very small (1mm $\times$ 0.25mm each) and contribute negligible additional material.

The following sections describe each of the steps in detail.

3.8.1 CCD Processing

The production of CCD32-60s, the devices used for the VXD3 detector, was a complicated process involving more than 100 steps and $\sim$ 40 Quality Assurance (QA) steps. These will not be described here, but they can be broken down into three main areas: the definition of the active area, the formation of the column isolation, the deposition of the gate structures and the metallization.

In the first stage, an n-type (phosphorous dopant) was used to form the gate protection structures. The active area was defined by surrounding it with a heavily doped p-type (boron) region, the channel stop. The periphery of the device was surrounded by a thick oxide layer which minimised the polysilicon capacitance and helped to reduce the risks of short circuits.

During the second stage, the gate oxide was deposited. The n-channel was implanted and the image area was divided into columns by the p-type channel stops. The nitride passivation was then added.

The third fabrication stage was the production of three polysilicon phases. The polysilicon was deposited, etched, phosphorous doped and then oxidised to form an insulation layer. This was repeated for each of the electrodes. Boron was implanted

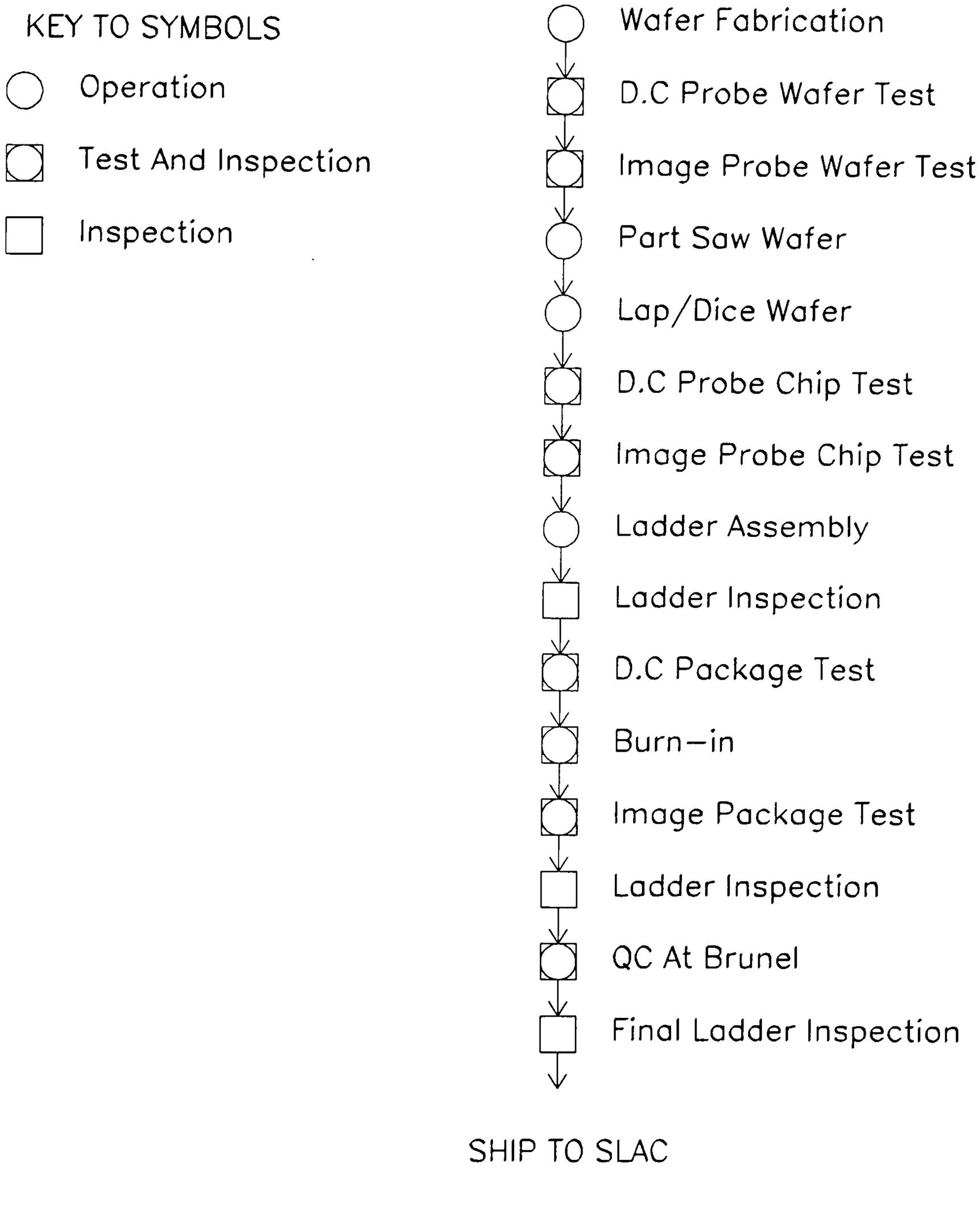

Figure 3.10: Flow diagram showing the steps in the production of VXD3 at EEV.

into the output register to prevent charge being re-injected into the image area and to insure the charge is transported down the centre of the register. A passivation layer of low temperature oxide was then deposited across the whole device except over the bond pads and fiducial pads (used in the ladder/detector survey). Finally aluminium metallization was deposited to form the bond pads and contacts.

All three stages included repeated use of: furnace for oxidation, annealing, deposition and doping; photolithography, which was used to produce accurately aligned resist masks by a step and repeat technique; etching; ion implantation for doping the various stages. For details of each of these processes see [69].

3.8.2 Wafer D.C. Tests

After fabrication was complete, the devices were tested while still on the wafer. Contact to the bond pads was made possible with the use of a probe station. The D.C. characteristics of the devices were checked, to allow the pre-selection of devices for the ladder assembly. Due to the large size of the CCD32-60 devices it was necessary to probe each end of a device separately.

During testing, one pad of the structure under test was connected to a programmable current sink, which was set to a predetermined current, while the other pin was connected to a voltage source. The test voltage was set to a certain value depending on the type of test being carried out, and the voltage across the two pins was measured.

Table 3.5 shows the tests that were performed and the pass/fail criteria are shown in Table 3.6. Sixty tests were performed on each end of each of the devices, the notation RD4/1 means that RD4/RD1 was tested when the top/bottom of the CCD was probed. The numbers in brackets are the bond pad numbers.

In tests 1-5 the Silicon Substrate (SS) through resistance was measured. The current source was set at 10mA, the voltage to 25V, and the equivalent impedance should be no more than 100Ω. The device was classified a fail if the voltage between the two pins was greater than 1V. In tests 6-8 the resistance of the polysilicon gates was measured. The current sink was set to 10mA, and the voltage to 25V, and

Test	High	Low	Test	High	Low
1	SS(5)	SS(8)	31	Rϕ2/1(12)	Rϕ1/2(13)
2	SS(5)	SS(11)	32	Rϕ1/2(13)	OG4/1(10)
3	SS(5)	SS(14)	33	Rϕ1/2(13)	OG3/2(15)
4	SS(5)	SS(17)	34	OG4/1(10)	Rϕ4/1(4)
5	SS(5)	SS(20)	35	OG3/2(15)	Rϕ3/2(21)
6	Iϕ1(1)	Iϕ1(24)	36	OD4/1(7)	Iϕ1(1)
7	Iϕ2(2)	Iϕ2(23)	37	OD3/2(18)	Iϕ1(1)
8	Iϕ3(3)	Iϕ3(22)	38	OD4/1(7)	Iϕ2(2)
9	SS(5)	RD4/1(6)	39	OD3/2(18)	Iϕ2(2)
10	SS(5)	RD3/2(19)	40	OD4/1(7)	Iϕ3(3)
11	SS(5)	OD4/1(7)	41	OD3/2(18)	Iϕ3(3)
12	SS(5)	OD3/2(18)	42	OD4/1(7)	Rϕ4/1(4)
13	SS(5)	OS4/1(9)	43	OD3/2(18)	Rϕ3/2(21)
14	SS(5)	OS3/2(16)	44	SS(5)	Iϕ1(1)
15	RD4/1(6)	SS(5)	45	SS(5)	Iϕ2(2)
16	RD3/2(19)	SS(5)	46	SS(5)	Iϕ3(3)
17	RD4/1(6)	Iϕ1(1)	47	SS(5)	Iϕ1(24)
18	RD3/2(19)	Iϕ1(24)	48	SS(5)	Iϕ2(23)
19	RD4/1(6)	Iϕ2(2)	49	SS(5)	Iϕ3(22)
20	RD3/2(19)	Iϕ2(23)	50	SS(5)	ϕR4/1(4)
21	RD4/1(6)	Iϕ3(3)	51	SS(5)	ϕR3/2(21)
22	RD3/2(19)	Iϕ3(22)	52	SS(5)	Rϕ2/1(12)
23	RD4/1(6)	ϕR4/1(4)	53	SS(5)	Rϕ1/2(13)
24	RD3/2(19)	ϕR3/2(21)	54	SS(5)	OG4/1(10)
25	RD4/1(6)	OG4/1(10)	55	SS(5)	OG3/2(15)
26	RD3/2(19)	OG3/2(15)	56	Iϕ2(2)	SS(5)
27	Iϕ1(1)	Iϕ2(2)	57	Rϕ2/1(12)	SS(5)
28	Iϕ1(1)	Iϕ3(3)	58	Rϕ1/2(13)	SS(5)
29	Iϕ2(2)	Iϕ3(3)	59	OG4/1(10)	SS(5)
30	Iϕ3(3)	Rϕ2/1(12)	60	OG3/2(15)	SS(5)

Table 3.5: D.C. Probe tests.

Tests	Functions Tested	Test Current	V_{min}	V_{max}
1-5	SS Through Resistance	10mA	–	1V
6-8	Polyresistance	10mA	–	200Ω/□
9-14	Forward Diodes	1mA	0.2V	1.5V
15-16	Reverse Diodes	50μA	24V	–
17-26	Drain-Gates	50μA	24V	–
27-35	Gate-Gate	30μA	14V	–
36-43	Drain Gates	30μA	19V	–
44-60	Gate Protection	30μA	19V	27V

Voltage Limit = 25V (28 for the gate protection tests and 15V for the gate-gate test.)

Table 3.6: D.C. Probe test limits.

the equivalent inpedance should be less than 200Ω/□. In tests 9-14 the forward diode characteristics of the junction formed by the p-type substrate and the n-type implants in the drains and sources of the output circuits were checked. The current sink was set to 1mA, the voltage to 25V, and the equivalent impedance should be greater than 200Ω and less than 1.5kΩ. The device was classified a fail if the voltage drop between the two pins was less than 0.2V or greater than 1.5V. In tests 15-16 the reverse diode characteristics of the RD to substrate are checked, and in tests 17-26 the presence of shorts between various drains and gates are checked for. The current sink was set to 50μA, the voltage to 25V, and the equivalent impedance should be greater than 480Ω. The device was classified a fail if the voltage drop between the two pins was greater than 24V. In tests 27-35 the oxide integrity of the interphase oxides was checked for shorts. The current sink was set to 30μA, the voltage to 15V, and the equivalent impedance should be greater than 467kΩ. The device was classified a fail if the voltage drop between the two pins was less than 14V. In test 36-60 the device is checked for shorts between various drains and gates, the oxide integrity of the gate oxides are checked for shorts and the gate protection

structures are tested. The current sink was set to 30μA, the voltage to 28V, and the equivalent impedance should be greater than 643kΩ and less than 900kΩ. The device was classified a fail if the voltage between the two pins was less than 19V or greater than 27V. These tests also measured the average voltage at which the gate protection structures turn on.

The results of these tests were printed out and stored in the batch folder, so that suitable devices could be picked for further testing, lapping and ladder assembly.

3.8.3 Wafer Image Tests

After wafer D.C. probe tests, the devices on the wafer were then image probed. The device was run and an image (grid) was projected onto the surface of the CCD. By observing the quality of the image, devices could be rejected or selected for dicing and lapping. Whist the chips would not be used in the standard TV imaging mode, testing the chips this way but using a slightly different acceptance criteria provided a means of selecting good chips.

A device used for TV imaging could not have dark columns (caused by blocked columns) but for VXD3 this was acceptable, since a loss of 0.25% (i.e 2 blocked columns) coverage on one device represents a small loss in the total detector coverage. On the other hand white defects would cause a problem if still present when the device was cooled down. The signals from the particles are small in comparison to that of the white spot or column, for example, 1600 e^- from a particle but 3 $\times$ 10^5 e^- from a white spot. The electronics was designed to cope with small signals from particles and it would be saturated by the signal from white spots, making it impossible to detect particle signals.

The charge transfer efficiency (CTE) is important; because small signals were being handled, any inefficiency would have a significant effect on the signal. The CTE could not be quantified during the image test but the operator could check visually for smearing of the image at high and low light levels.

The defect specification for the cold tests at SLAC were:

- With a 200ms integration time, no pixels $>$ 5000 e^- spurious signal.

- With a 200ms integration time, no more than two pixels with up to 5000 ϵ^- spurious signal.
- No more than two blocked columns.
- Limits noted for CTI, potential pockets, general leakage current.

Note, that these tests were caried out at SLAC with the devices at their operating temperature. Hence any devices with white spots/columns that EEV thought would freeze out could have be packaged and sent to SLAC for testing. No such devices were packaged.

As with the D.C. wafer probe tests a probe station was used to make contact with the bond pads on one end of the device. The optical system was setup to project a test grid onto the device via a shutter and a zoom lens. Each output of the device (two at each end) was displayed on a monitor and all four images were assessed by the operator. The results of the tests were recorded on a wafer map and stored with the wafer D.C. test results.

Devices that passed both the D.C. wafer probe and the image probe were selected for dicing and lapping.

3.8.4 Lapping and Sawing

The CCDs were part sawn to a depth of 200μm. The sawing is done along a scribe channel, defined during the metallization stage of the CCD production.

The back of the wafers were then lapped or thinned until they were 200μm thick. A detailed description of the EEV lapping procedure can be found in [70]. Once the wafer has been lapped, the individual CCDs can be carefully separated from the rest of the wafer.

3.8.5 Die D.C. Probe Tests

Once the wafers had been sawn and lapped into individual chips, the chips that passed the wafer D.C. probe and the image probe were D.C. tested again. These

tests were done to ensure that any devices damaged during the sawing and lapping procedure, were not used for the ladder assembly.

The chip D.C. probe tests were the same as the wafer D.C. probe tests. The test results were then printed out as before and stored in the batch folder. Good devices were selected for chip imaging testing.

3.8.6 Chip Image Probe Tests

The chip image tests were the same as the wafer image probe. If the device passed the tests, the images from the four quadrants of the device were stored on disc. Hence the images from marginal devices could be inspected by RAL/SLAC personnel where a final decision could be made, as to whether the device should be packaged.

Devices that passed all the tests were then safely stored until they were used for ladder assembly.

3.8.7 Die Attachment

The die attachment is the proceduce for attaching two CCDs to the motherboard, and hence producing a ladder. The CCDs needed to be positioned accurately onto the motherboard for a number of reasons:

- The CCDs had to overlap in the centre of the motherboard, so that the whole length of the ladder was covered by active area.
- The CCDs had to be positioned so that they ran parallel to the edge of the motherboard i.e. the CCD does not hang over the edge of the CCD, which might have caused problems when the detector was assembled.
- The CCD bond pads had to be adjacent to the equivalent bond pads on the motherboard, otherwise the wire bonding would become non-trivial.

In addition to the positioning, the adhesive pads used to attach the CCDs to the motherboard had to be uniform, so that they would contract (when cooled) in a uniform manner.

This required the development of a well defined and easy to follow assembly procedure. The procedure adopted was one that involved the use of a jig with various attachments and templates for the different stages of the assembly.

The ladder was positioned on the jig with the aid of positioning pins and spring loaded 'nudgers'. The ladder was then held in position by a vacuum hold down. 'Spacers', 250μm thick stainless steel shims, were then pulled across the motherboard in the region where the CCD would be attached. Gaps were left where the adhesive was applied. The shims were used to help form uniform adhesive pad heights. The adhesive template was then positioned (again with positioning pins) above the area where the CCD was to be attached. There were eight holes in the template indicating the positions for the adhesive pads. The adhesive [71] was administered to the motherboard using an automated adhesive dispenser. The adhesive template was then replaced by the die attach template, which was again positioned with the aid of positioning pins. The die attach template had a hole the same size and shape as the CCDs, into which a CCD was placed onto of the adhesive pads. The CCD was then flattened using a flat 100 gm weight, with a piece of filter paper in-between to protect the CCD. The weight was left in place until the adhesive had cured (24 hours at room temperature). This device was then wire bonded to the motherboard (Section 3.8.8). The ladder was then removed from the jig and the procedure was repeated on the other side. (There was a recess in the jig where the first CCD could sit without being damaged.)

3.8.8 Wire Bonding

Wire bonding was needed to make contact between the CCD and the motherboard, and thence to the external electronics. The bond wire was 25μm thick 99%Al/1%Si. (Alloying strengthens the aluminium, which otherwise would easily break.) and was ultrasonically bonded to the bond pads on the CCDs and the motherboards. Figure 3.11 shows the wire bonding procedure.

The first bond is formed on a CCD bond pad. The wire is brought into contact with the CCD bond pad and put under a load by the bonding-wedge and an ultra-

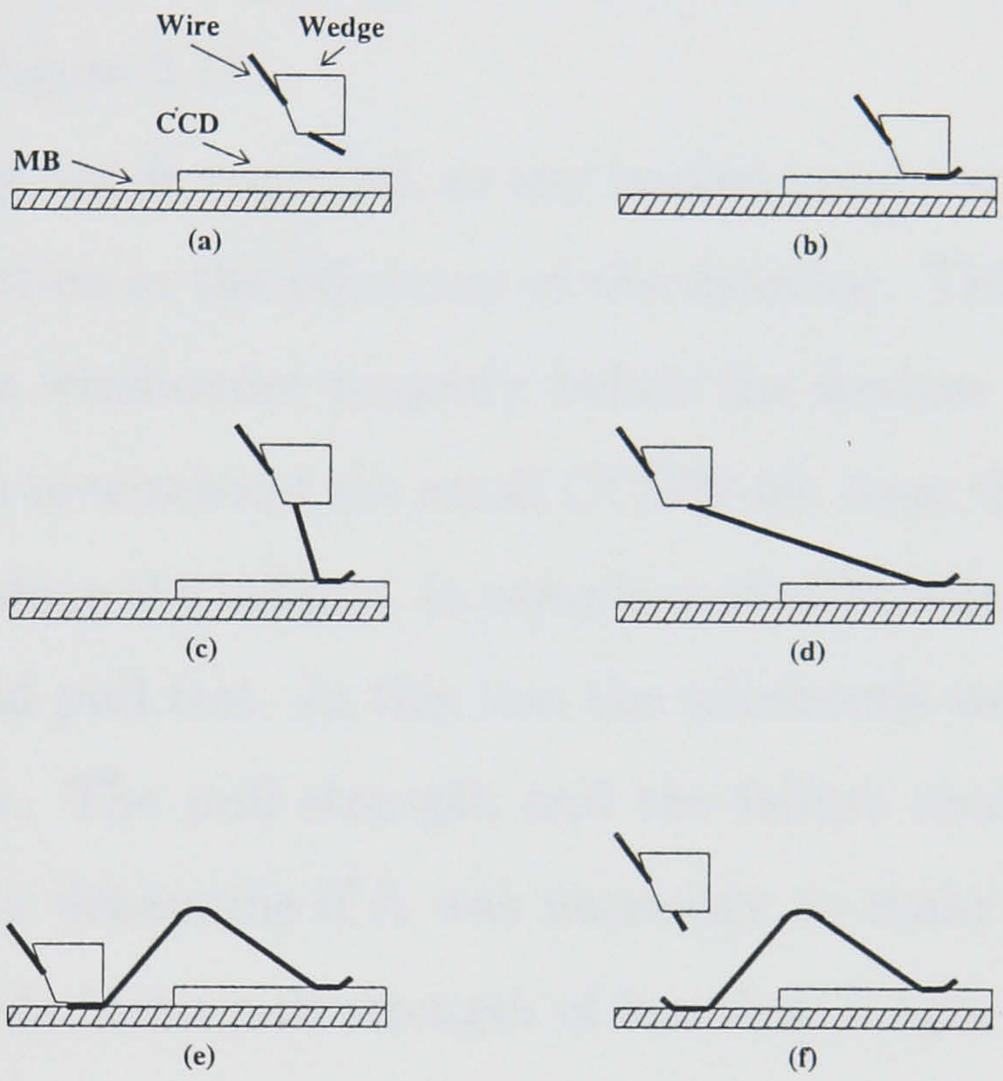

Figure 3.11: Wire bonding procedure. (a) The wire is first threaded through the wedge. (b) The wire is brought into contact with the CCD and a load is applied as well as an ultrasonic pulse, producing the first bond. (c) The wedge is raised. (d) The wedge is stepped back. (e) The second bond is formed on the motherboard. (f) The wedge is raised and the wire is broken.

sonic pulse of energy is applied to the wedge. The ultrasonic energy first softens the material. This, combined with the load, causes the material to flow, breaking up surface oxides and exposing the material which will be bonded. A wave then propagates through the wire to the wire bond pad interface. This causes a cutting action in the bond pad. As a result of this process the surfaces are cleaned and pressure is imposed on the bonding surfaces. The shape and size of the resulting contact area is a function of time, energy of the ultrasonic pulse and the load applied [73]. The bond pad on the motherboard, directly opposite the bond pad on the CCD is then bonded, as shown in Figure 3.11.

Making good strong bonds was vital, as any broken bonds could result in the loss of a CCD, and a reduction in the efficiency of the detector. This meant that it was important to setup the wirebonder properly before the devices were attached. The procedure adopted was to wirebond the small CCD32-00, from the same wafer as the devices selected to produce the ladders, to sample motherboards, and then carry out a destructive wire bond pull test. In this test the wirebonds were pulled vertically, using a fine wire hook. The pull strength and the failure mode [70] are recorded and the results used to determine if it was necessary to make adjustments to the wirebonder. If the bonds had a pull strength of less than 3.5gm the wirebonder had to be re-set. Figure 3.12 shows a histogram for all the tests carried out. The mean strength was 9.8g with a standard deviation of 1.3gm. As can be seen there are no points below 3.5g.

3.8.9 D.C. Package Test

When two CCDs had been die attached, wire bonded to the motherboard and placed in the ladder box, the ladder was D.C. tested again. The tests were similar to the D.C. probe tests except the probe station was no longer needed, and instead the devices were connected to the test equipment using the ladder pigtails and appropriate transition boards. Table 3.7 shows the 43 tests carried out on each device, and Table 3.8 shows the pass/fail criteria. A description of the test can be found in Section 3.8.2. Both devices had to pass these tests for the ladder to pass.

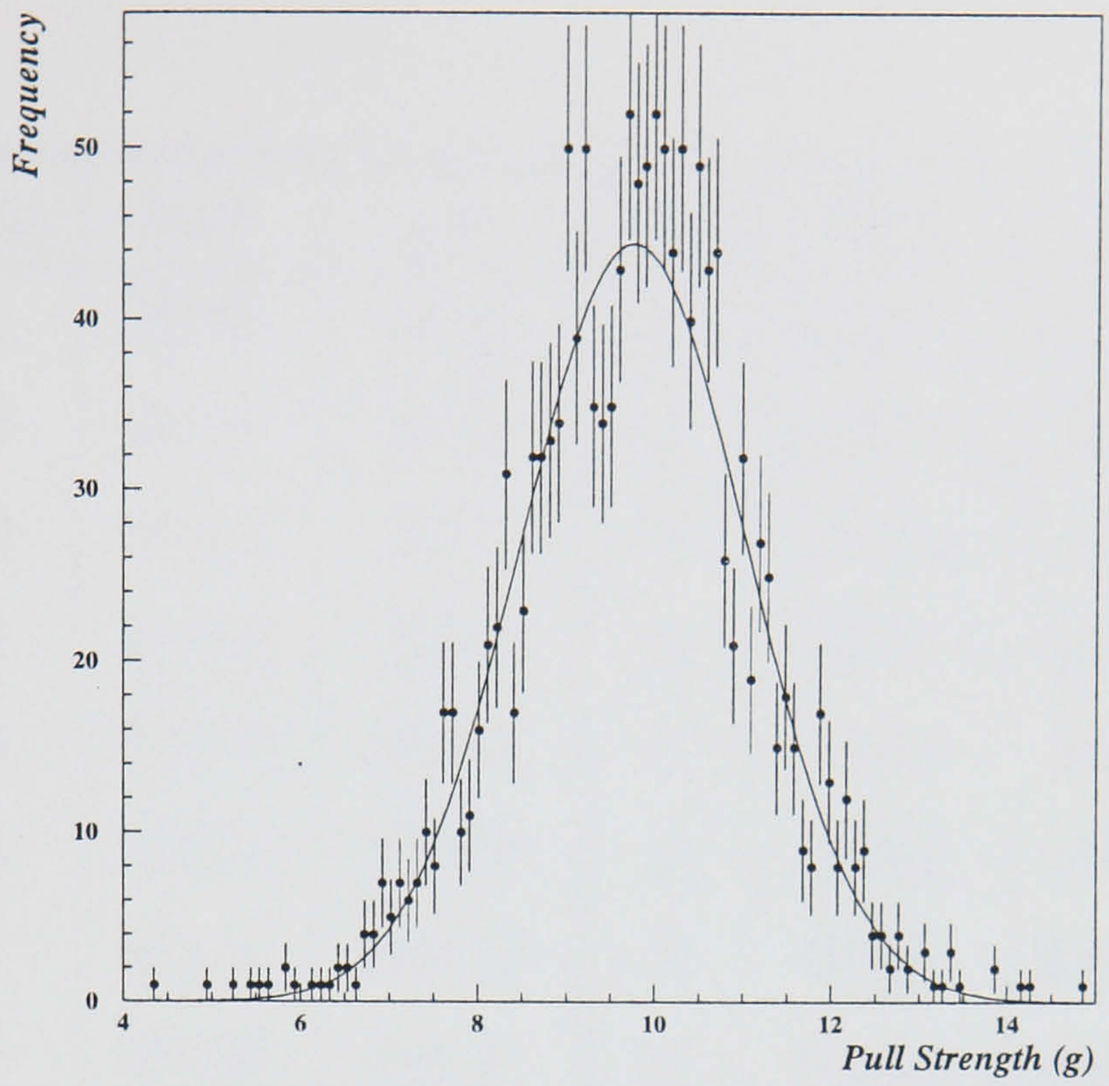

Figure 3.12: The pull strength of the wirebonds. The points are the data and the curve is a guassian fit with a χ^2 per degree of freedom of 0.95.

If one or both of the devices failed then the ladder had to be reworked.

3.8.10 D.C. Burn-in

When both of the CCDs on the ladder had passed the D.C. package test, the ladders were burnt-in. The purpose of the test was to prevent devices with potential reliability problems from being installed in SLD. The loss of one CCD would cause a loss in tracking coverage, and there would be no way of replacing the device. It was therefore important that the probability of a device failing was reduced as far as possible. The burn-in screen was therefore essential.

During burn-in the devices were screened for weak interpoly (the oxide layers between the polysilicon gates) and gate oxides. A static voltage of -14.6V was applied to each phase in turn, whilst holding the others at ground, Table 3.9. The voltage was applied to each phase for one hour, this meant that gate oxides were stressed for one hour, while the interpoly oxides were stressed for two. If a short

Test	High	Low	Test	High	Low
1	SS(10)	SS(2)	23	Rϕ1(20)	Rϕ2(19)
2	SS(10)	SS(6)	24	Rϕ2(19)	OG(23)
3	SS(10)	SS(5)	25	OG(23)	ϕR(24)
4	SS(10)	SS(7)	26	OD(3)	Iϕ1(12)
5	SS(10)	SS(18)	27	OD(3)	Iϕ2(1)
6	SS(10)	SS(21)	28	OD(3)	Iϕ3(11)
7	SS(10)	RD(16)	29	OD(3)	Rϕ1(20)
8	SS(10)	OD(3)	30	OD(3)	Rϕ2(19)
9	SS(10)	OS1(8)	31	OD(3)	OG(23)
10	SS(10)	OS2(4)	32	OD(3)	ϕR(24)
11	SS(10)	OS3(22)	33	SS(10)	Iϕ1(12)
12	SS(10)	OS4(17)	34	SS(10)	Iϕ2(1)
13	RD(16)	SS(10)	35	SS(10)	Iϕ3(11)
14	RD(16)	ϕR(24)	36	SS(10)	Rϕ1(20)
15	RD(16)	OG(23)	37	SS(10)	Rϕ2(19)
16	RD(16)	Iϕ1(10)	38	SS(10)	ϕR(24)
17	RD(16)	Iϕ2(1)	39	SS(10)	OG(23)
18	RD(16)	Iϕ3(24)	40	Iϕ2(1)	SS(10)
19	Iϕ1(12)	Iϕ2(1)	41	Rϕ1(20)	SS(10)
20	Iϕ1(12)	Iϕ3(11)	42	Rϕ2(19)	SS(10)
21	Iϕ2(1)	Iϕ3(11)	43	OG(23)	SS(10)
22	Iϕ3(11)	Rϕ1(20)			

Table 3.7: D.C. Package tests.

Tests	Functions Tested	Test Current	V_{min}	V_{max}
1-6	SS Through Resistance	10mA	–	1V
7-12	Forward Diodes	1mA	0.2V	1.5V
13	Reverse Diodes	50μA	24V	–
14-18	Drain-Gates	50μA	24V	–
19-25	Gate-Gate	30μA	14V	–
26-32	Drain Gates	30μA	19V	–
33-43	Gate Protection	30μA	19V	27V

Voltage Limit = 25V (28 for the gate protection tests and 15V for the gate-gate test.)

Table 3.8: D.C. Package test limits.

circuit was present an LED lit up, providing the current exceeded 30μA.

Both devices on the ladder were burnt-in at the same time. The CCDs were connected to the custom made burn-in headboards via the pigtails and transition boards. The burn-in voltages were supplied through the burn-in head-boards via the burn-in slave units. The timing of the switches (i.e phases) were controlled by the burn-in timer unit. During testing the ladders were placed into light tight boxes.

Before the burn-in was performed the stress voltages were manually applied by the operator one at a time to check for any failures. This discovered devices that failed the screen immediately. After burn-in the process was repeated in order to identify failures that had occured during the screen, as these were not recorded by the system. This information was recorded in the ladder test traveller.

If a device failed the burn-in, it was D.C. package tested again to determine the fault. The bad device was then removed from the ladder and replaced with a working one, and the new device put through all the package tests (D.C. and burn-in).

North CCD	Poly Level	South CCD	Poly Level	Burn-in Voltage
PCB GND	-	PCB GND	-	GND
-	-	-	-	-
-	-	-	-	-
VSS	-	VSS	-	GND
VOS1	-	VOS4	-	GND
VSS	-	VSS	-	GND
Rϕ2	2,1	Rϕ1	3,1	X1
VSS	-	VSS	-	GND
VOS4	-	VOS1	-	GND
ϕR	2	ϕR	2	X1
Iϕ2	2	Iϕ2	2	X2
-	-	-	-	-
-	-	-	-	-
VOS3	-	VOS2	-	GND
VSS	-	VSS	-	GND
Rϕ1	3,1	Rϕ2	2,1	X2
VSS	-	VSS	-	GND
VOS2	-	VOS3	-	GND
VSS	-	VSS	-	GND
VOD	-	VOD	-	GND
VSS	-	VSS	-	GND
Iϕ3	3	Iϕ3	3	X3
Iϕ1	1	Iϕ2	1	X1

Burn-in Operating Conditions X1 = -14.6V (Switch 1) X2 = -14.6V (Switch 2) X3 = -14.6V (Switch 3)

Table 3.9: Burn-in test voltages.

Dimension	Mean	Standard Deviation
CCD Length	82.560mm	0.0027mm
CCD Width	16.675mm	0.0016mm
CCD Thickness	194μm	12μm
Adhesive Pad Height	309μm	16μm
Adhesive Pad Diameter	905μm	109μm

Table 3.10: Summary of the ladder Q.C. measurements.

3.8.11 D.C. Package Image Test

The aim of this test was to check that the CCDs were not damaged during the ladder assembly. During packaging the CCDs could have been physically damaged, or damaged by static during the handling. Static damage causes white spots, which would be picked up in the image test.

The ladder inside the ladder box was placed where the wafer would have been during the image probe tests, and was connected to the test system via a number of modifications to the probe system. The tests were carried out in a similar manner to the image probe test.

3.8.12 Q.C. Measurements at Brunel

After the tests had been performed the ladders that passed were taken to Brunel for Q.C. (Quality Control) measurements on the coordinate measuring machine. The physical dimensions of the motherboard and CCDs were measured and are shown in Figure 3.13. The adhesive pad dimensions were also measured and are shown in Figure 3.14. A summary of the measured dimensions is shown in Table 3.10.

After Q.C. measurements at Brunel the ladders were returned to EEV for a final visual inspection before being shipped to SLAC.

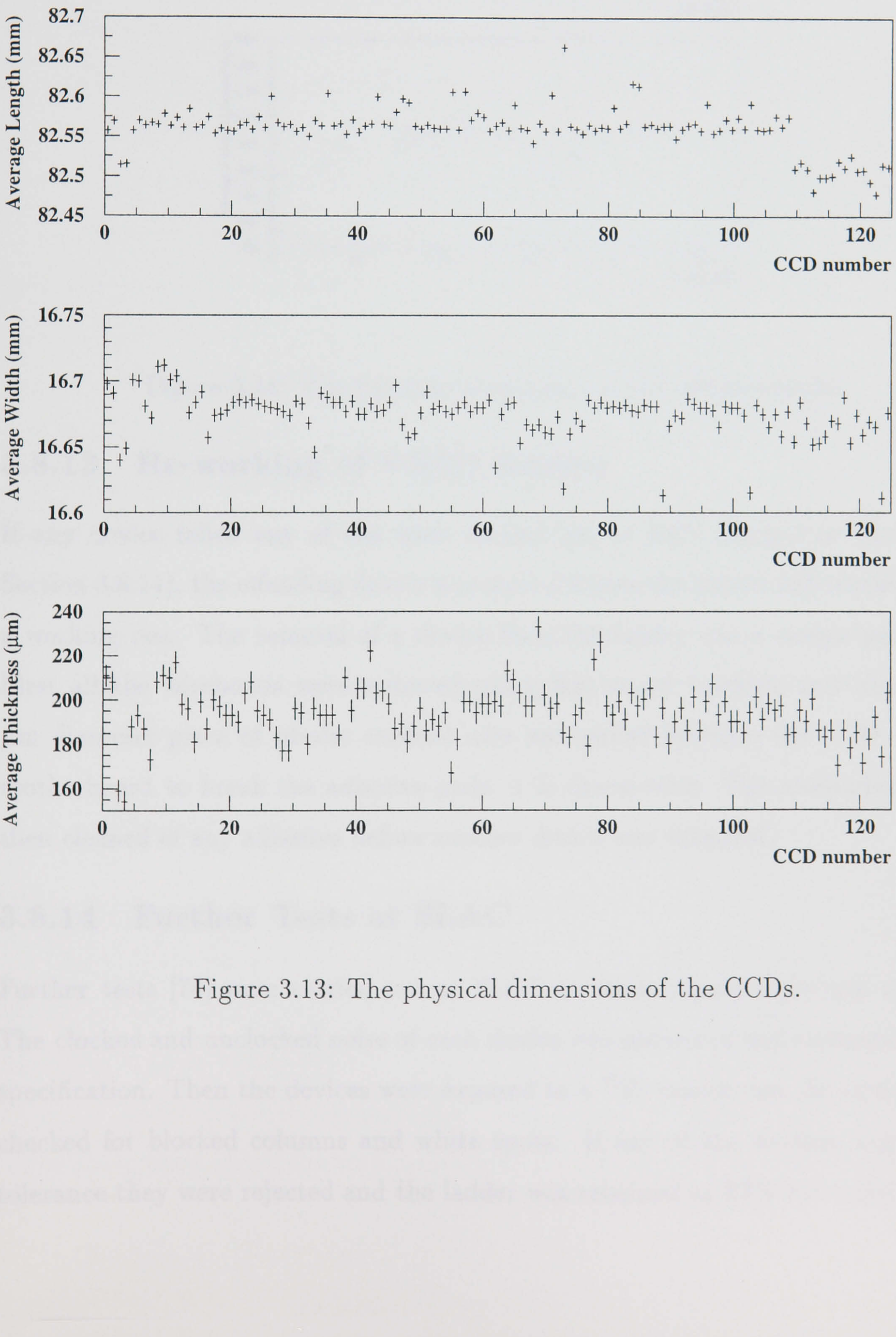

Figure 3.13: The physical dimensions of the CCDs.

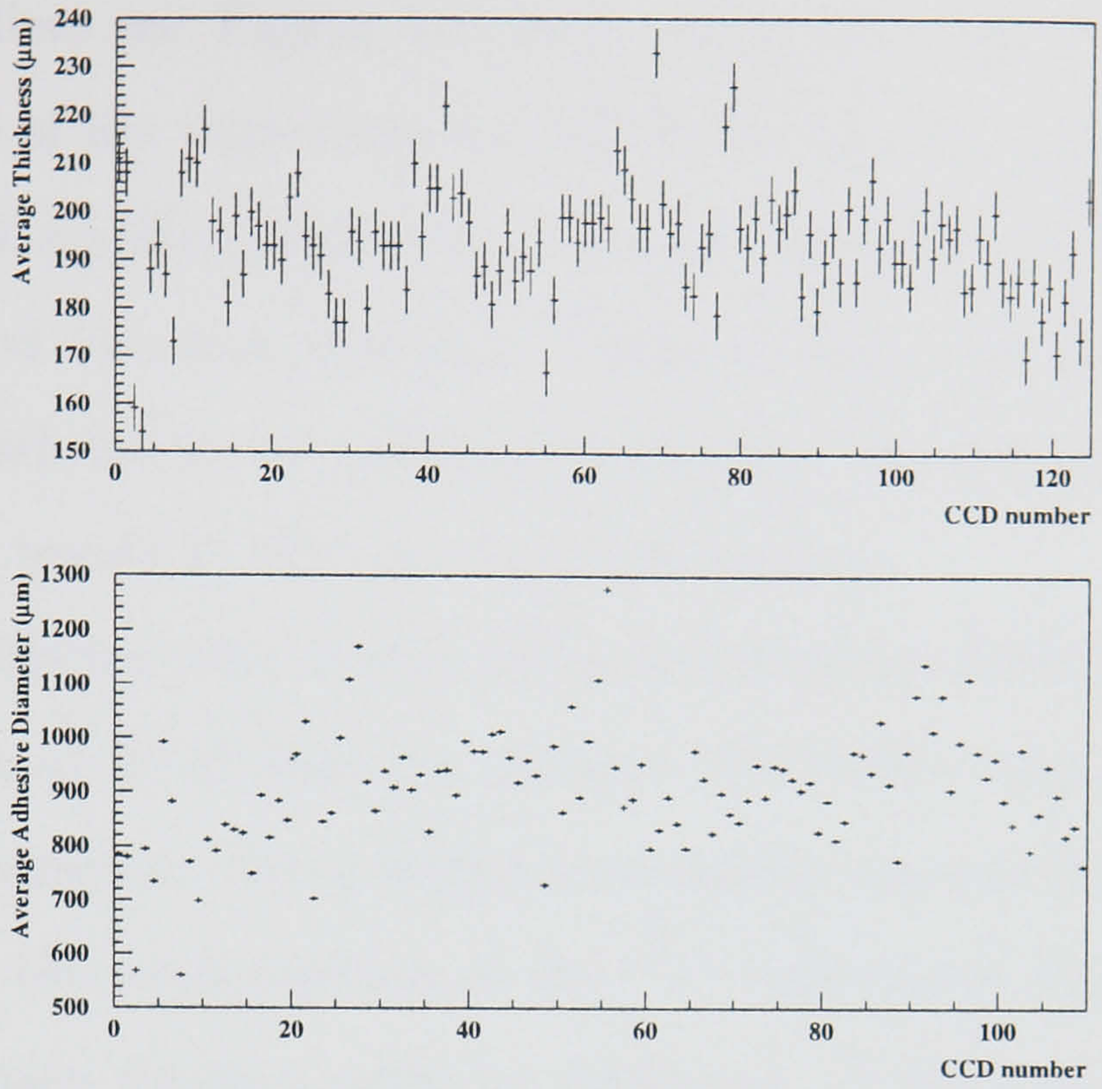

Figure 3.14: The physical dimensions of the adhesive pads.

3.8.13 Re-working of VXD3 ladders

If any device failed any of the tests carried out at EEV, Brunel or SLAC (see Section 3.8.14), the offending device was removed from the ladder and replaced with a working one. The removal of a device from the ladder was a simple procedure. First all the wirebonds were removed using thin nosed tweezers and then a 200 μm diameter piece of plastic covered wire was pulled between the CCD and the motherboard to break the adhesive pads, *à la* cheese-wire. The motherboard was then cleaned of any adhesive before another device was attached.

3.8.14 Further Tests at SLAC

Further tests [74] were carried out at SLAC at room temperature and at 220K. The clocked and unclocked noise of each device was measured and compared to the specification. Then the devices were exposed to a ^{55}Fe source and the devices were checked for blocked columns and white spots. If any of the devices were out of tolerance they were rejected and the ladder was returned to EEV for rework.

3.8.15 Radiation Damage Tests

As indicated earlier, see Figure 3.1, each wafer also contained 2 CCD32-10 devices. These were of the same type as CCD32-60s but were shorter in the I register (CCD32-60 had 6 middle sections and two end sections, CCD32-10 had only one middle section and two end sections). These devices, one from each batch, were used to qualify each batch for radiation hardness. The devices were attached to a motherboard and tested at EEV in the usual manner.

At SLAC the devices were tested before and after irradiation with a ^{60}Co source, up to a total dose of 10-15 krad per device. The CCDs were held at their normal operating bias throughout the irradiation to mimic normal operating conditions.

By measuring the peak position of the ^{55}Fe calibration source, the loss of CCD gain due to radiation damage could be measured. A linear loss of gain with accumulated dose was observed, with a median value of 0.6% per krad. The radiation-induced shifts of the effective bias voltages of the CCD were also determined, by measuring the threshold voltage of the reset gate voltage, ϕR, for the transmission of a test pulse on the VRD line. The shift was measured to be $\sim$ 100mV/krad on all devices. The specification stated that the flatband voltage shift should be less than 0.15 V/krad and that the CTI (charge transfer inefficiency) degradation should be less than 5×10^{-5}. These figures were well within the specification. The CCDs were also checked for the formation of new hot spots due to radiation induced defects in the silicon. No significant formation of hot spots was observed.

3.9 Production

During the wafer fabrication a number of problems were encountered.

Throughout the prototype and production phase, some devices at SLAC were found to have potential traps. These traps could swallow part or all of the ^{55}Fe signal charge of approximately 1600e^-. As a result, signals from below the position of the trap (i.e. closer to the R register) would show a normal cluster charge distribution, while those from above the trap position would be degraded or completely missing.

These traps could not be seen during image tests at EEV because they were filled with dark current at room temperature. The ladders with affected CCDs were returned to EEV for rework. A few of the worst devices were inspected under a high magnification microscope at RAL and the problem was diagnosed, to be due to localised overetching, which transformed the nominal overlap between the gates into a ragged gap. This exposed the buried channel to fixed charges in the gate oxide, interface oxide or polyimide passivation. This charge could create a local disturbance to the channel potential, which could block or trap small signals. EEV later recognised the problem as being associated with a recent change from a negative to a positive resist for some of the processing steps.

The first few batches had a low yield, the reasons for which were unknown. The D.C. probe test results were analysed and it was found that the major contributer to the fails was a poor oxide layer. Figure 3.15 shows pie charts of type of failures for the first three batches (One batch consists of 10 wafers).

After investigations in the wafer fabrication area it was discovered that the HF (Hydro-Fluoric acid, used to clean the wafers before fabrication begins) was being diluted by water, hence an inferior oxide layer was being grown due to unclean wafers.

The production of the 52 ladders proceeded smoothly once good quality devices were being produced. Figure 3.16 shows the output of ladders compared with the schedule. The production of ladders was achieved in a very intensive 14-week period. Only 9 ladders were rejected at SLAC, mainly because of the charge trap problem.

3.10 Cold Survey

An optical survey of VXD3 was performed at MIT, in order to determine the internal geometry of the detector to an accuracy sufficient for beam related tracks to be used for the final internal alignment. A secondary goal of the survey was to measure aspects of the geometry which would be difficult to determine accurately from the tracks, such as the complex shapes of the CCDs themselves and the gravitational sag of the ladders. These two aspects of the project were important factors in achieving

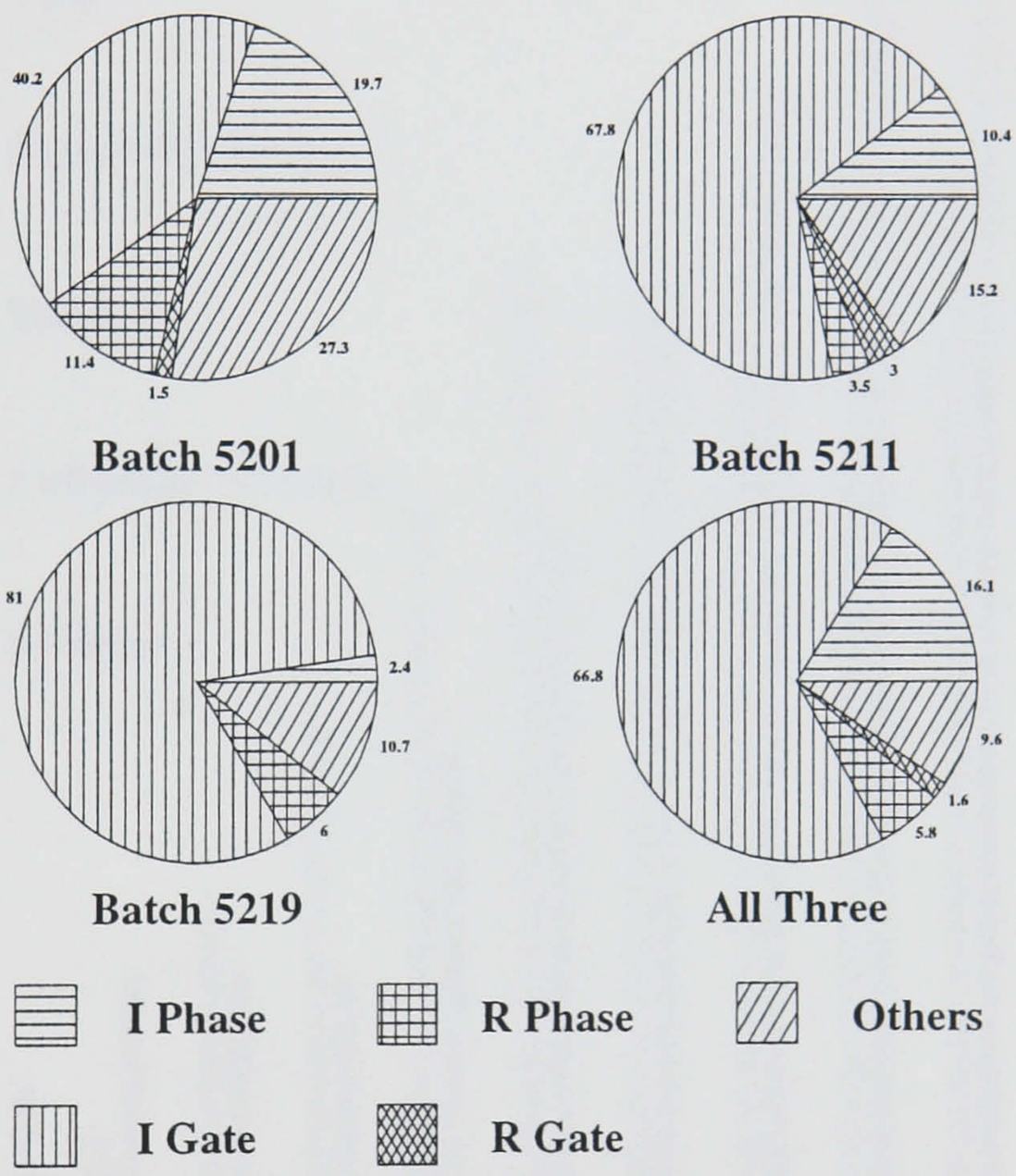

Figure 3.15: Charts showing the distribution of D.C. fails for three of the production batches.

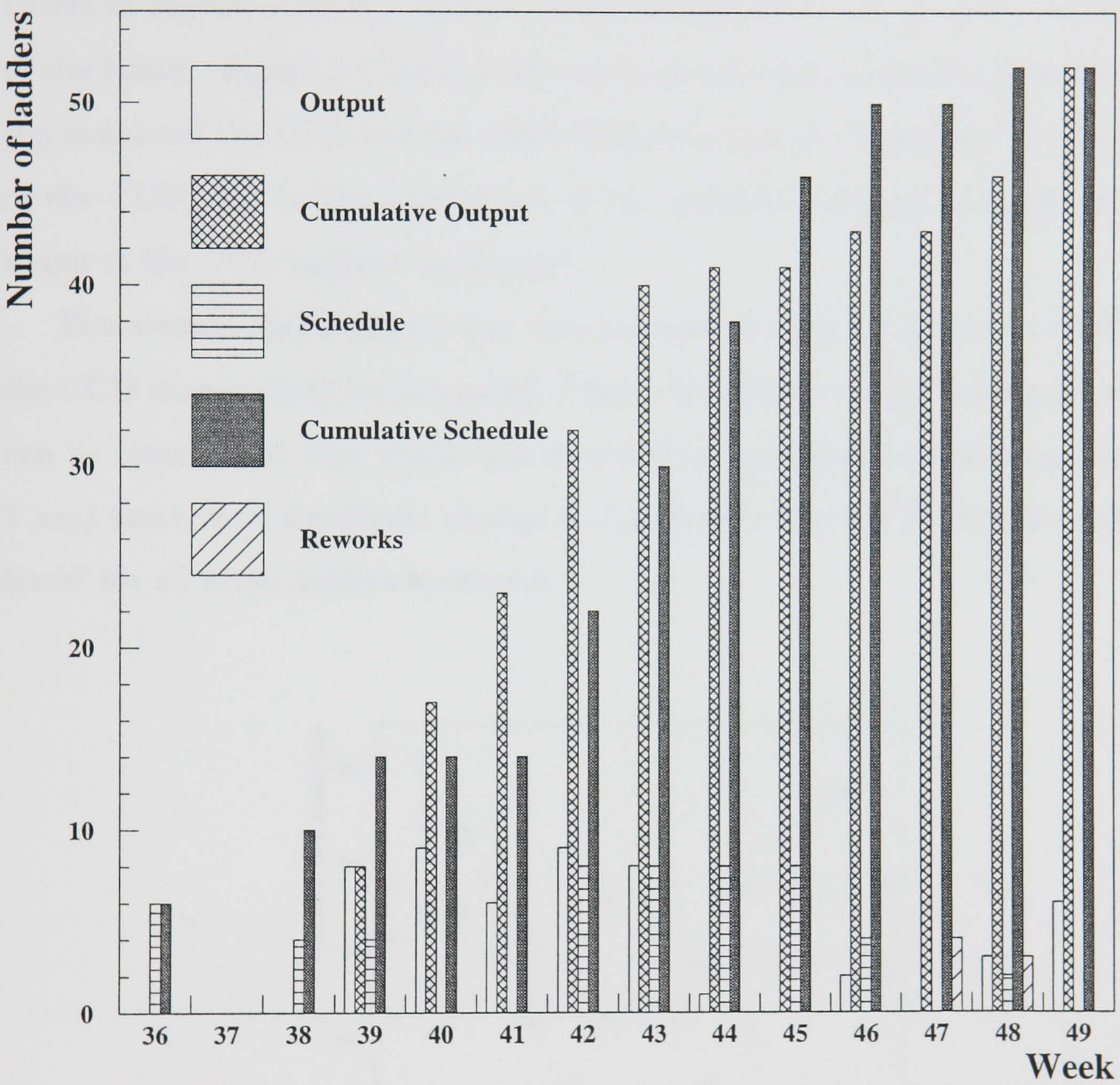

Figure 3.16: Number of ladders produced compared with the schedule and the reworks.

the overall precision required. The details of the survey will not be given here. For details see [74].

The survey of the detector was carried out at room temperature. To determine if the shape of the CCDs changed considerably when the ladders were cooled down to the operating temperature, measurements were carried out at Brunel on three sample ladders. Measurements were made along the long edge of the motherboard and the CCDs at regular intervals, both at room temperature and at 220K, on both sides of the ladder. Figure 3.17 shows the raw measurements of the distance between the top surface of the CCD and the motherboard for one of the ladders. A displacement of the CCD, due to the contraction of the adhesive columns is apparent, but the shape of the CCD appears unchanged.

The average displacement was then subtracted from the points at 220K so that the CCD shapes could be compared. Figure 3.18 shows the CCD shapes overlaid. It can be clearly seen that within the errors of the coordinate measuring machine ($\pm$ 5 μm) there is no significant change to the shape of the CCD. Similar results were found for all three ladders measured.

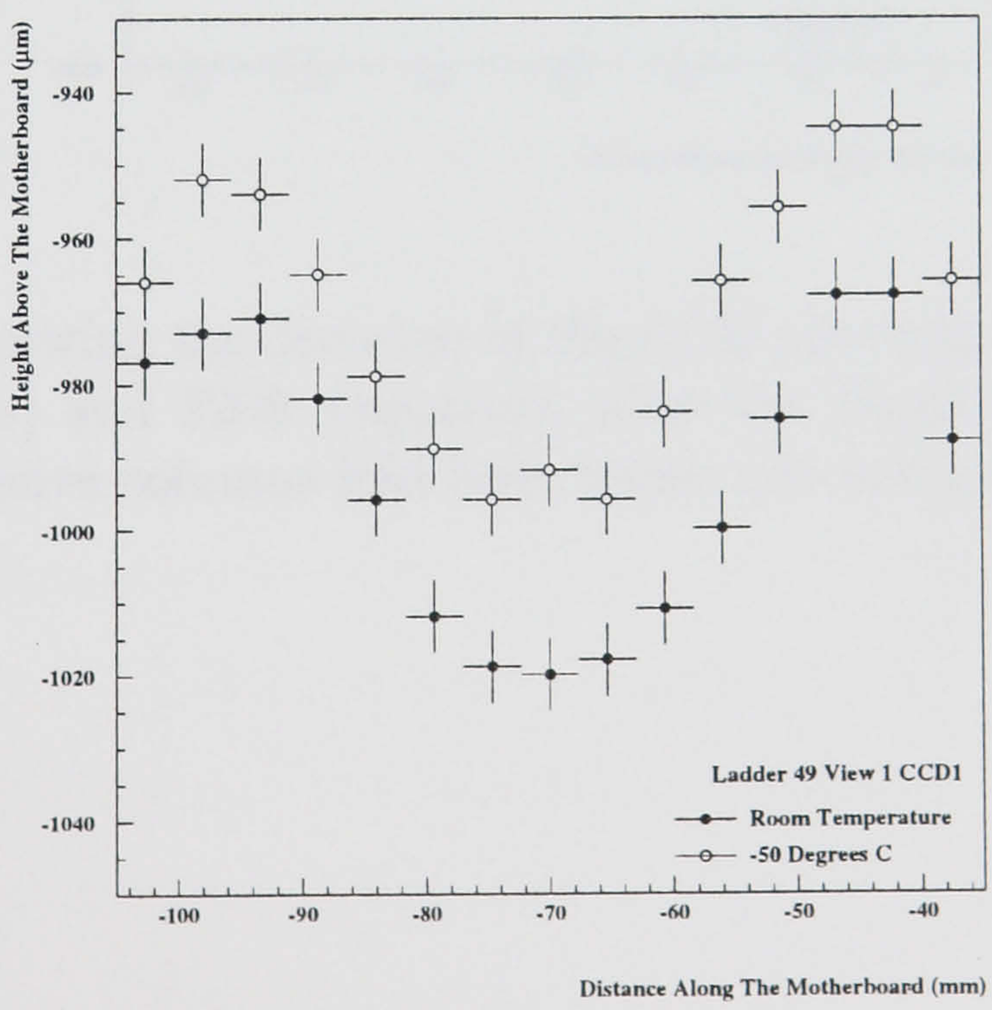

Figure 3.17: Plot showing the distance of the CCD above the motherboard at room temperature (circles) and 220K (squares).

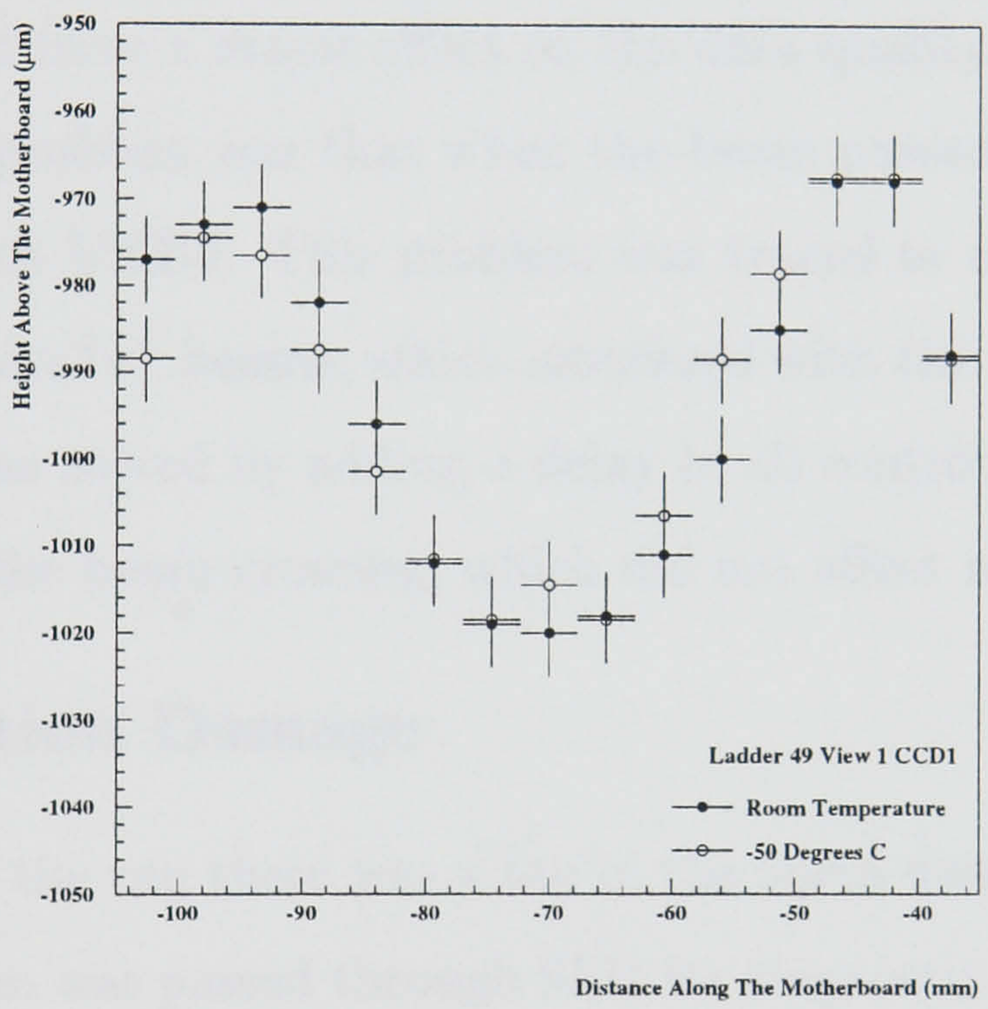

Figure 3.18: Plot showing the distance of the CCD above the motherboard at room temperature (circles) and 220K (squares), after the displacement due to the contraction of the adhesive columns had been taken into account.

3.11 VXD3 Performance

VXD3 was installed in SLD, replacing VXD2, in January 1996. The detector was commissioned during the 1996 SLD physics run. 50,000 Z^0 were collected using VXD3. This section gives a brief description of how VXD3 performed.

3.11.1 Hardware

There were a number of minor problems with the local electronics or A/D boards. These included charge smearing, stuck ADC bits and imperfect optical links between the local electronics and the FASTBUS system. These were all fixed during or after the run, and did not have a major effect on the data quality.

A more serious problem was that when the beam passed through the detector, contact was lost with VXD3. This problem was traced to magnetic fields induced by the passage of the e^+e^- beams, which interfered with the electronics on the A/D boards [74]. This was solved by adding a delay to all control commands sent to the A/D board during the beam crossing, which did not affect readout operations.

3.11.2 Radiation Damage

At the beginning of the run there was a fire in the north damping ring. This meant that undamped beam was passed through SLD for diagnostic purposes, for extensive periods of time. In addition, the solenoid was turned off, which allowed low energy $e^{\pm}$ backgrounds to reach the detector, particles which would normally be curled up by the solenoid field. Hence VXD3 suffered more radiation damage than VXD2 (Section 3.2). The damage was worst in Layer 1, where an efficiency loss at the end of the I register of $\sim$ 15 % was observed, and negligible in Layer 3.

The damage was discovered by a drop in the 3-hit efficiency in the high ϕ region.

The detector was operated at a temperature of 220K during the 1996 run. This was warmer than for VXD2. However, it has been shown that by lowering the temperature to 185K the efficiency of layer 1 can be restored to its pre-irradiation level. This effect is caused by increasing the relaxation time of the traps caused by the radiation damage [55]. In the future the detector will be operated at the lower

temperature. In addition, no beam will be allowed through SLD unless the solenoid is turned on.

3.11.3 Detector Alignment

The survey of the detector at MIT produced a first level detector geometry. This included CCD shapes from the ladder survey data, together with temperature scaling and gravity sag corrections. This first level geometry was then improved using a tracking based internal-alignment. The internal alignment was a lengthy and complex procedure which will not be described here; see [74] for details. The internally aligned detector was then taken as a rigid body and aligned globally with respect to the CDC using tracks from hadronic Z^0 decay events, see reference [76] and Chapter 5.

3.11.4 Tracking Efficiency

The linking routine used for VXD3 was the same as for VXD2 (Section 2.5.2). The tracking efficiency for high momentum tracks was measured using good quality $e^+e^- \rightarrow \mu^+\mu^-$ events. The all-link rate ($\geq$ 2 hits) was >99.8% and the $\geq$3 hit rate was 97%. Figure 3.19 shows the linking rate as a function of momentum measured using Z^0 hadronic decays. The main source of the efficiency loss in the 3-hit linking was the radiation damage referred to in Section 3.11.2. Problems with the electronics also had a small effect. By correcting the electronics problems and running the detector at a lower temperature, these efficiency losses will be eliminated in future.

3.11.5 Impact Parameter Resolution

As already shown in Section 2.5.2 the miss-distance of two back-to-back $\mu^+\mu^-$ measures the intrinsic impact parameter resolution, independent of the interaction-point. After the detector was fully aligned $Z^0 \rightarrow \mu^+\mu^-$ events were reconstructed and the miss-distance determined. Figure 3.20 shows the mu-pair miss distance in the $r\phi$ and rz projections. A single track intrinsic impact parameter resolution of 14μm in $r\phi$ and 26.5μm in rz was obtained.

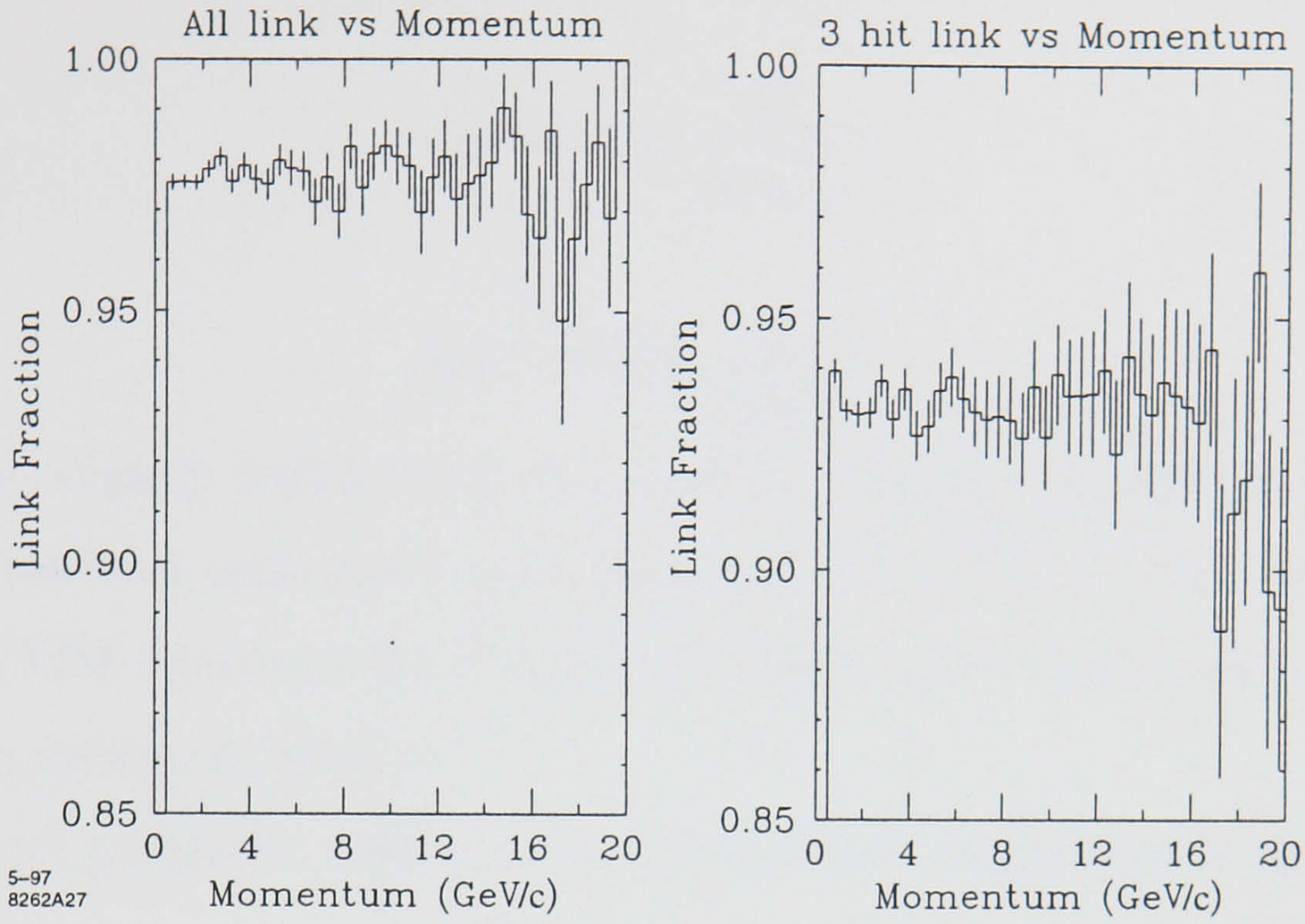

Figure 3.19: Quality CDC track VXD linking rate, as a function of track momentum, for all links and 3-hit links [74].

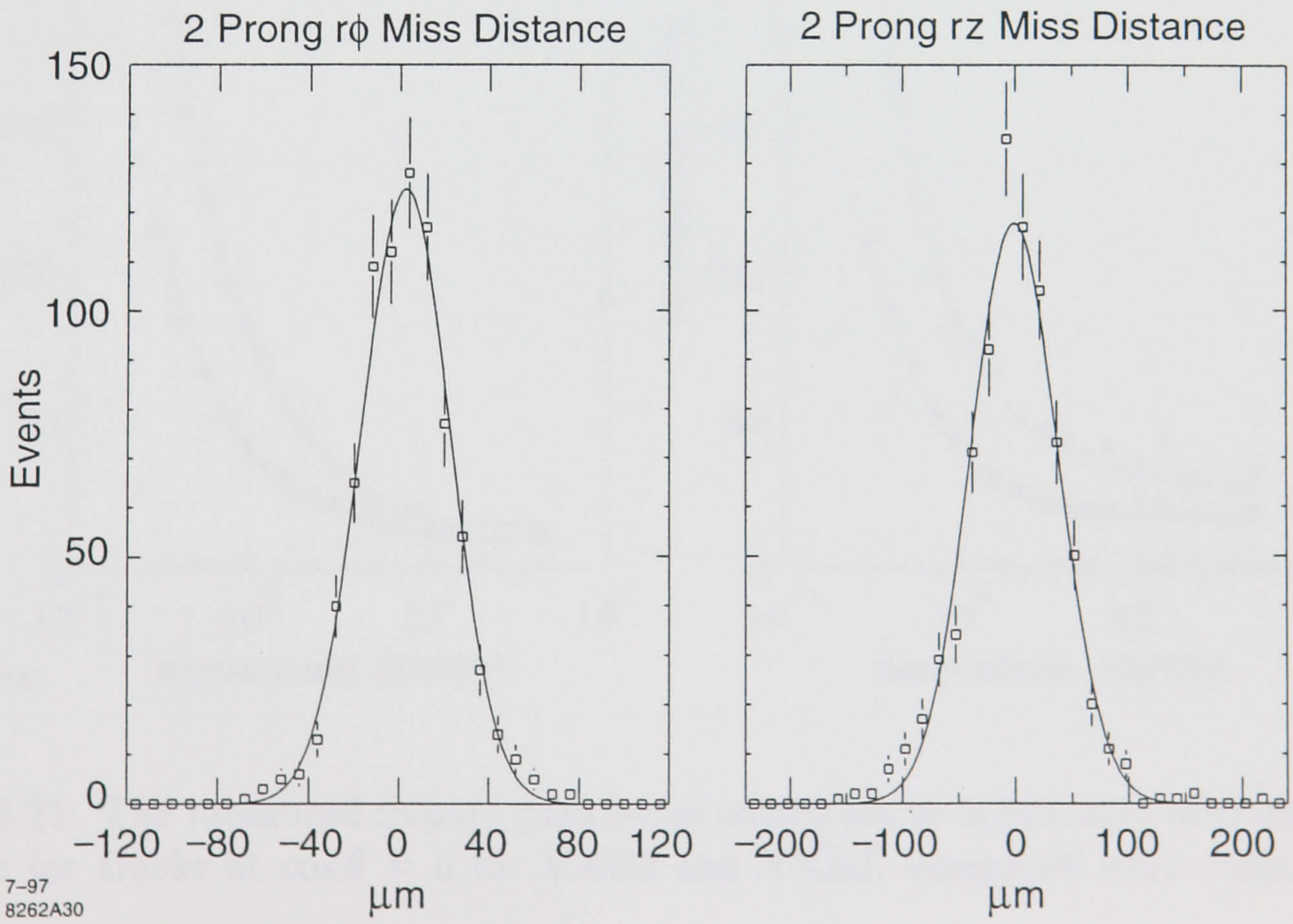

Figure 3.20: Mu-pair miss distance in $r\phi$ and rz projections [74].

The multiple scattering term was also calculated in the same manner as VXD2 (Section 2.5.5). The total measured impact parameter resolution was [74]:

$$\sigma_d^{r\phi} = 14 \oplus \frac{33}{p \sin^{\frac{3}{2}} \theta} \tag{3.3}$$

$$\sigma_d^{rz} = 26.5 \oplus \frac{33}{p \sin^{\frac{3}{2}} \theta} \tag{3.4}$$

These are slightly higher than the expected numbers, particularly for the rz plane. This has been understood as a problem with the CDC tracks in the combined fit. If only VXD3 vectors are used for the calculation of the resolution, the constant term 26.5μm reduces to 15.9μm.

The impact parameter resolution as a function of momentum is shown in Figure 3.21.

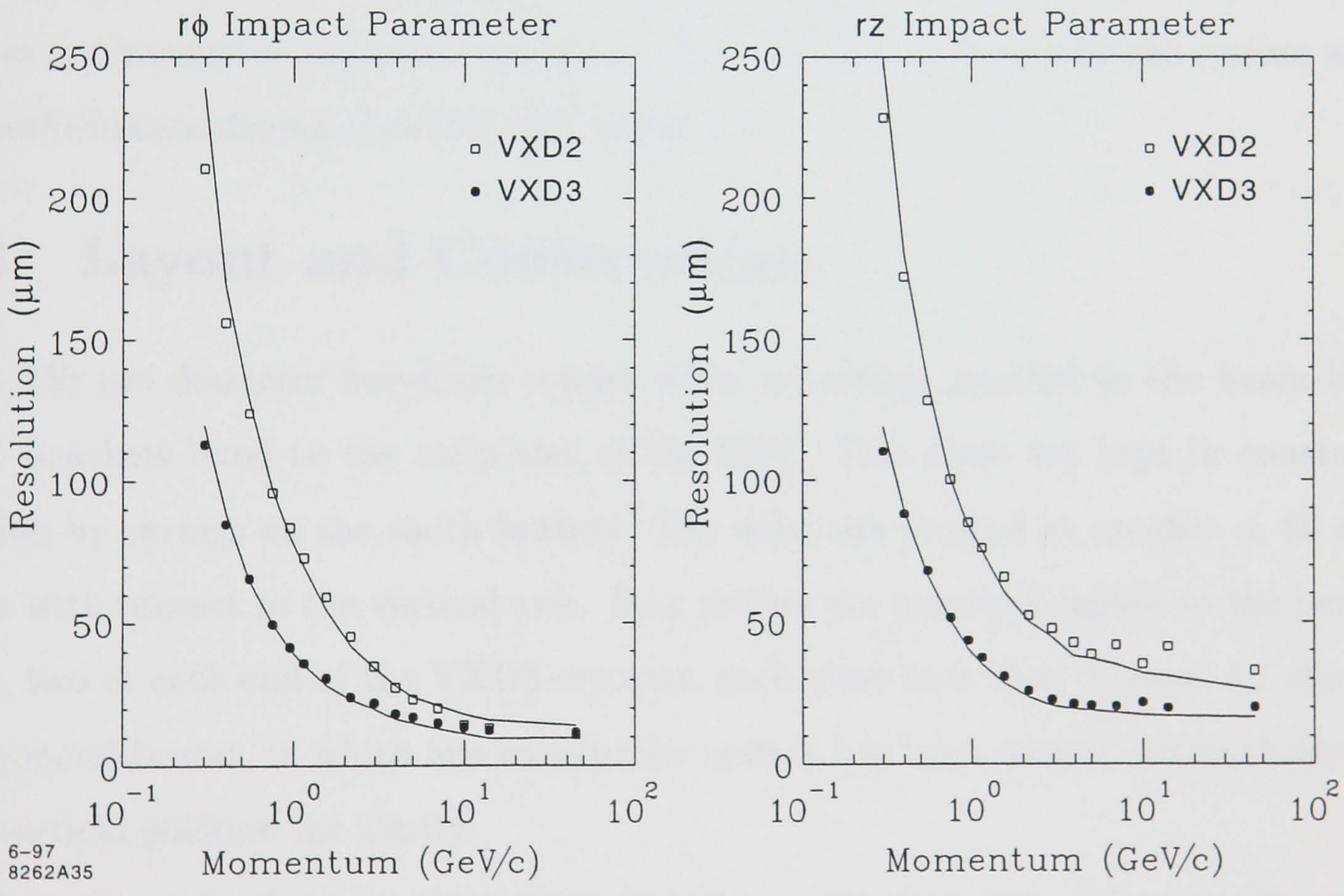

Figure 3.21: The measured impact parameter resolution as a function of track momentum for tracks at $\cos\theta = 0$ for VXD2 and VXD3, compared with simulation [74].

Chapter 4

The Capacitive Wire Position Monitor

4.1 Introduction

The capacitive wire position monitor is a real-time system to monitor the position of the R20 module, hence VXD3, with respect to the CDC. It is vital that any VXD3 moves are known for alignment purposes. This Chapter will describe the system and its performance during the 1996 SLD physics run.

4.2 Layout and Construction

Two 250 μm diameter beryllium-copper wires are strung parallel to the beam-line from brackets fixed to the endplates of the CDC. The wires are kept in constant tension by springs on the south brakets. The wires are located at roughly $\pm$ 60 degrees with respect to the vertical axis. Four probes are mounted rigidly to the beam pipe, two at each end of the VXD3 cryostat, each close to a wire. Figure. 4.1 shows the general layout, in which one wire/probe system has been rotated azimuthally to the vertical position for clarity.

A probe comprises an aluminium housing supporting two, 9.5 mm diameter capacitive plates arranged such that the plates are orthogonal. The probes are mounted so that one plate is parallel to the horizontal plane, the other is parallel to the vertical plane, and both are parallel to the beam-line. Hence these plates form a local x (horizontal axis) y (vertical axis) coordinate system for the wires.

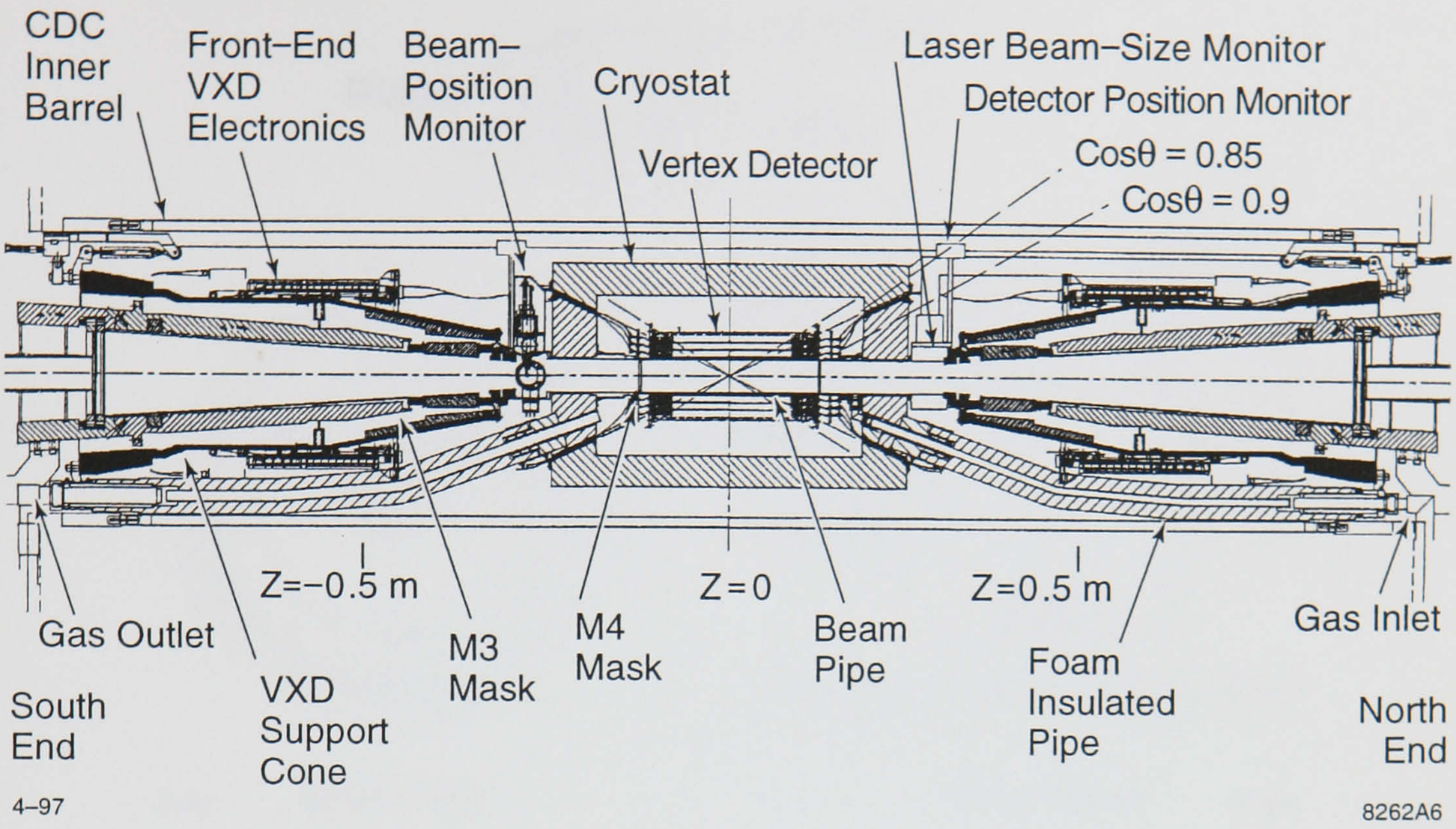

Figure 4.1: The R20 module showing the positions of the capacitive wire position monitor system.

Each wire is strung so as to pass approximately through the geometric centre of the x-y fiducial formed by the two plates. A schematic of the configuration is shown in Figure. 4.2.

Both wires are connected to a common ground. A constant excitation signal is applied separately to each plate at a frequency of 15 kHz and the required voltage is monitored continually using a CAMAC-based slow readout system with data transfer to a computer. The probes and signal source units were obtained from a commerial manufacturer [77]. Since each probe and nearby wire form a system whose capacitance depends on the distance of the wire from the plates, this distance can be inferred from the measured signal voltages. Since the wires are mounted rigidly with respect to the CDC and the probes with respect to the VXD3, changes in the monitored voltages indicate relative displacements between VXD3 and the CDC. The configuration yields four measurements of the transverse (x-y) displacements permitting VXD3 global translations, tilts, or rotations about the beam-line to be determined. The system is not sensitive to relative translations along the beam-line.

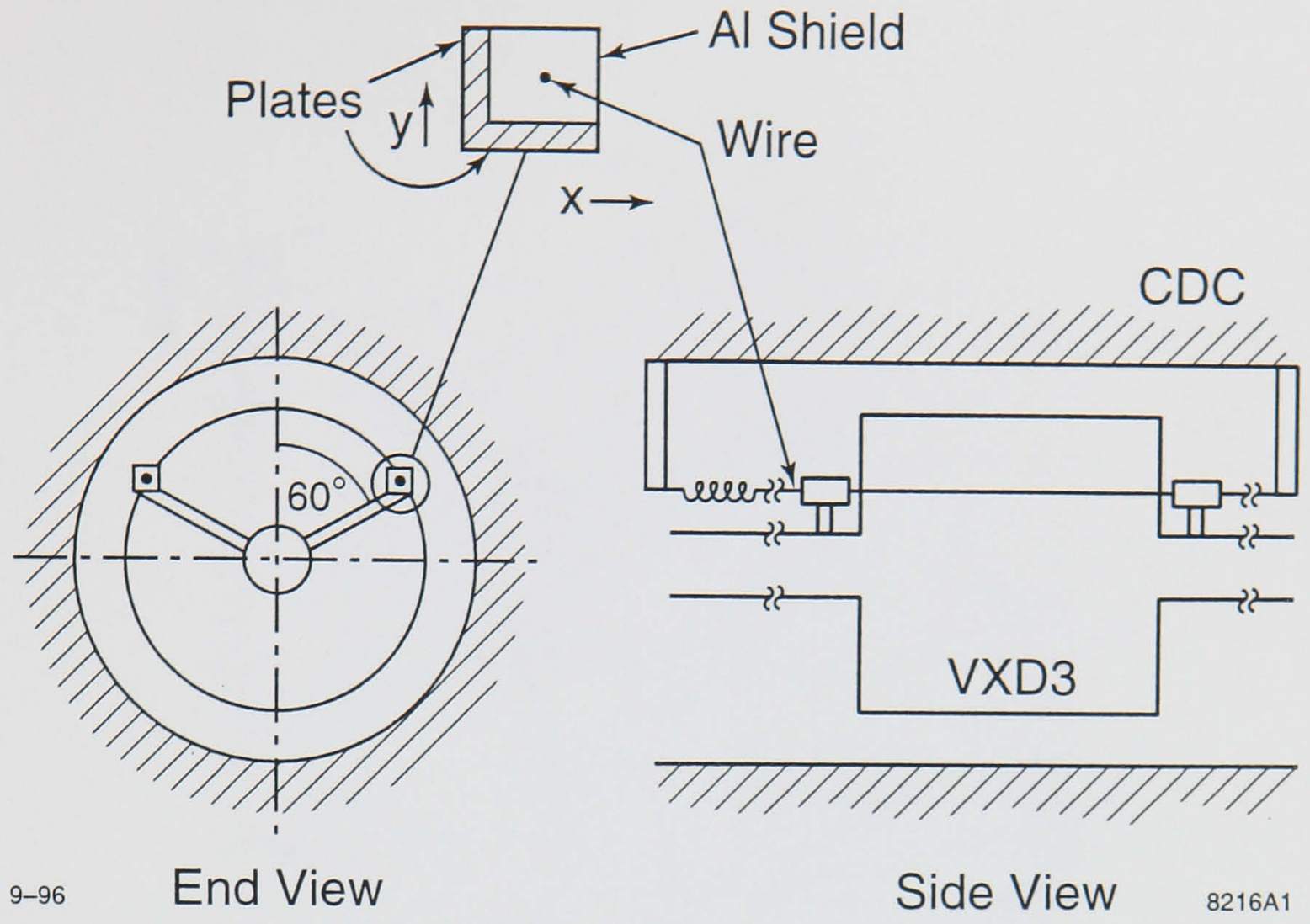

Figure 4.2: Schematic of the capacitive wire position monitor configuration.

4.3 Calibration

The voltage-distance calibration for each probe was measured prior to installation in the detector. Initially the gain and offset of the amplifier in each signal source was adjusted to obtain a voltage response in the range $0 < V < 10V$ for a corresponding separation, s, in the range $0 < s < 1cm$. In the test setup a probe was mounted on a granite table and a wire was strung through the fidual volume. After an initial adjustment of the wire parallel to, and just in contact with, both plates, the displacement was measured with a micrometer. At each position the voltages applied to both the horizontal plate, V_y, and the vertical plate, V_x, to maintain constant currents, were recorded. Hence, the response of all the probes to wire positions across the x-y plane was measured. As the probes have a circular geometry, V_x and V_y depend both on the x and the y coordinates of the wire. Measurements were taken every $\sim$ 2 mm in the horizontal plane and $\sim$ 0.5 mm in the vertical plane. The measurements from one of the probes are shown in Figure. 4.3. The voltage can be seen to be smoothly varying but non-linear, especially close to, and far from the plate.

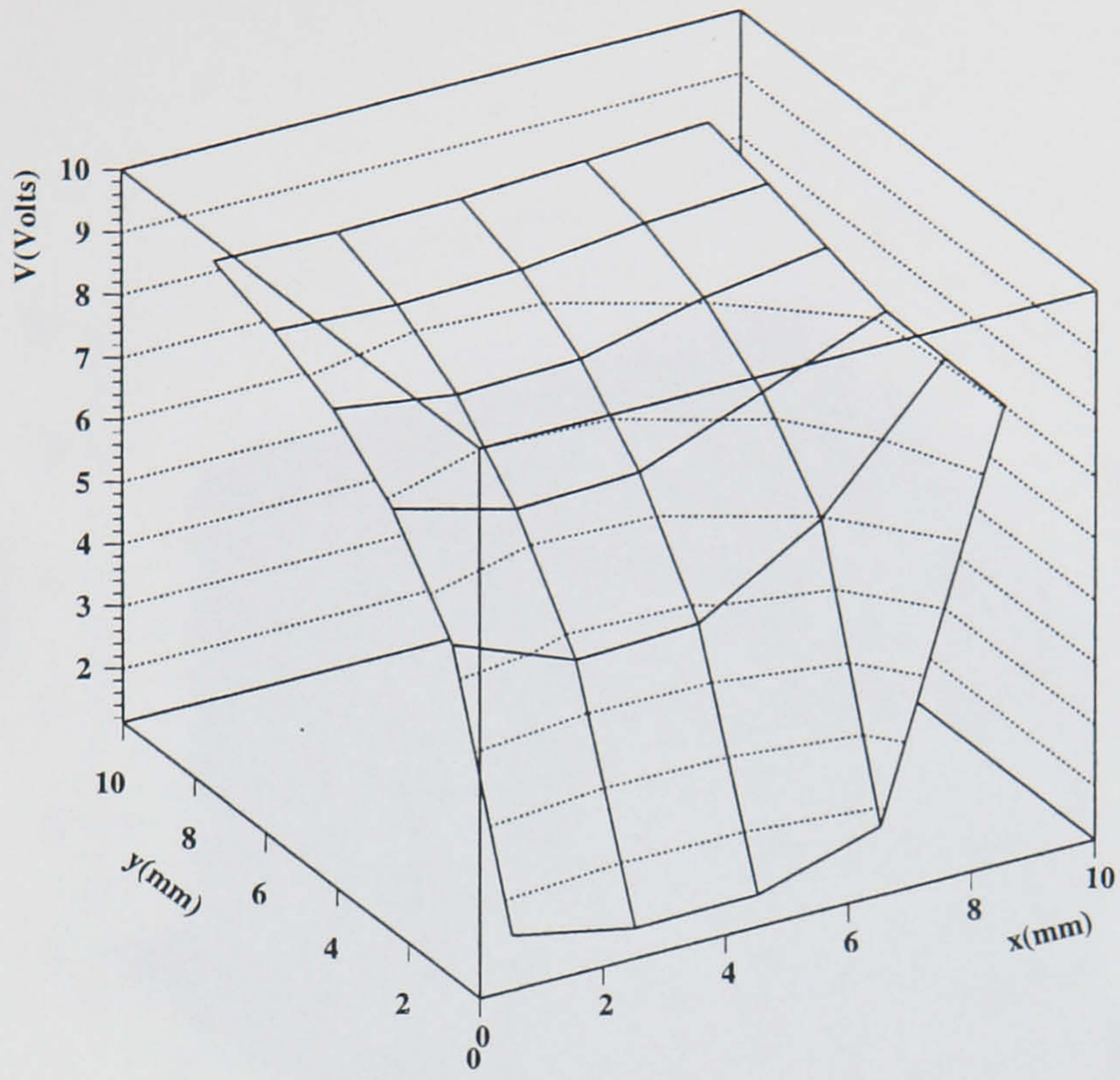

Figure 4.3: The calibration measurements from one of the probes.

4.3.1 Fits to the Calibration Data

A convenient parameterisation of V_x and V_y for each of the four probes was obtained by fitting *ad hoc* polynomial functions of x and y to the calibration data:

$$V_x = A_1 + B_1x + C_1x^2 + D_1x^3 + E_1x^4$$

$$+(F_1 + G_1x + H_1x^2 + J_1x^3 + K_1x^4) \times ln(y)$$

$$+(L_1 + M_1x + N_1x^2 + O_1x^3 + P_1x^4) \times y$$

$$+(Q_1 + R_1x + S_1x^2 + T_1x^3 + U_1x^4) \times y^2$$

$$V_y = A_2 + B_2y + C_2y^2 + D_2y^3 + E_2y^4$$

$$+(F_2 + G_2y + H_2y^2 + J_2y^3 + K_2y^4) \times ln(x)$$

$$+(L_2 + M_2y + N_2y^2 + O_2y^3 + P_2y^4) \times x$$

$$+(Q_2 + R_2y + S_2y^2 + T_2y^3 + U_2y^4) \times x^2$$

An example is shown in Figure. 4.4 for one of the probes. The corresponding residuals i.e data-fit, are shown in Figure. 4.5 in terms of voltage.

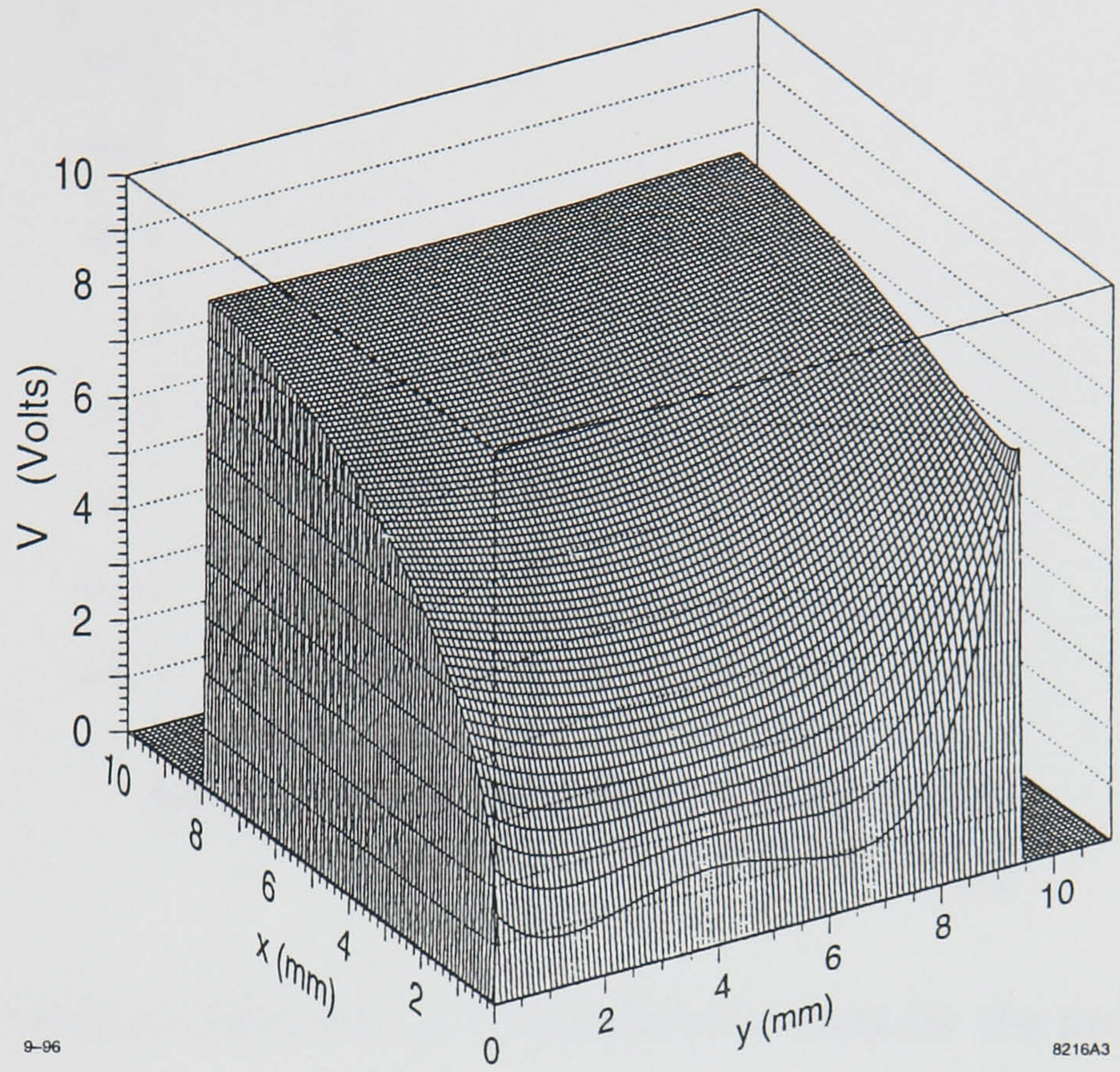

Figure 4.4: Parameterised surface, showing the voltage-distance characteristic of a probe.

4.3.2 Voltage to Distance Conversion

Using an iterative procedure the effective position (x_i,y_i) of a wire, at a time i, with respect to a probe could be determined from the measured voltages V_x^i, V_y^i.

$$V_x(x_i, y_i) = V_x^i$$

$$V_y(x_i, y_i) = V_y^i$$

Displacements between time i and a chosen reference time are then readily obtained by comparing the two solutions. The residuals from Figure. 4.5 are shown in Figure. 4.6 in terms of mm.

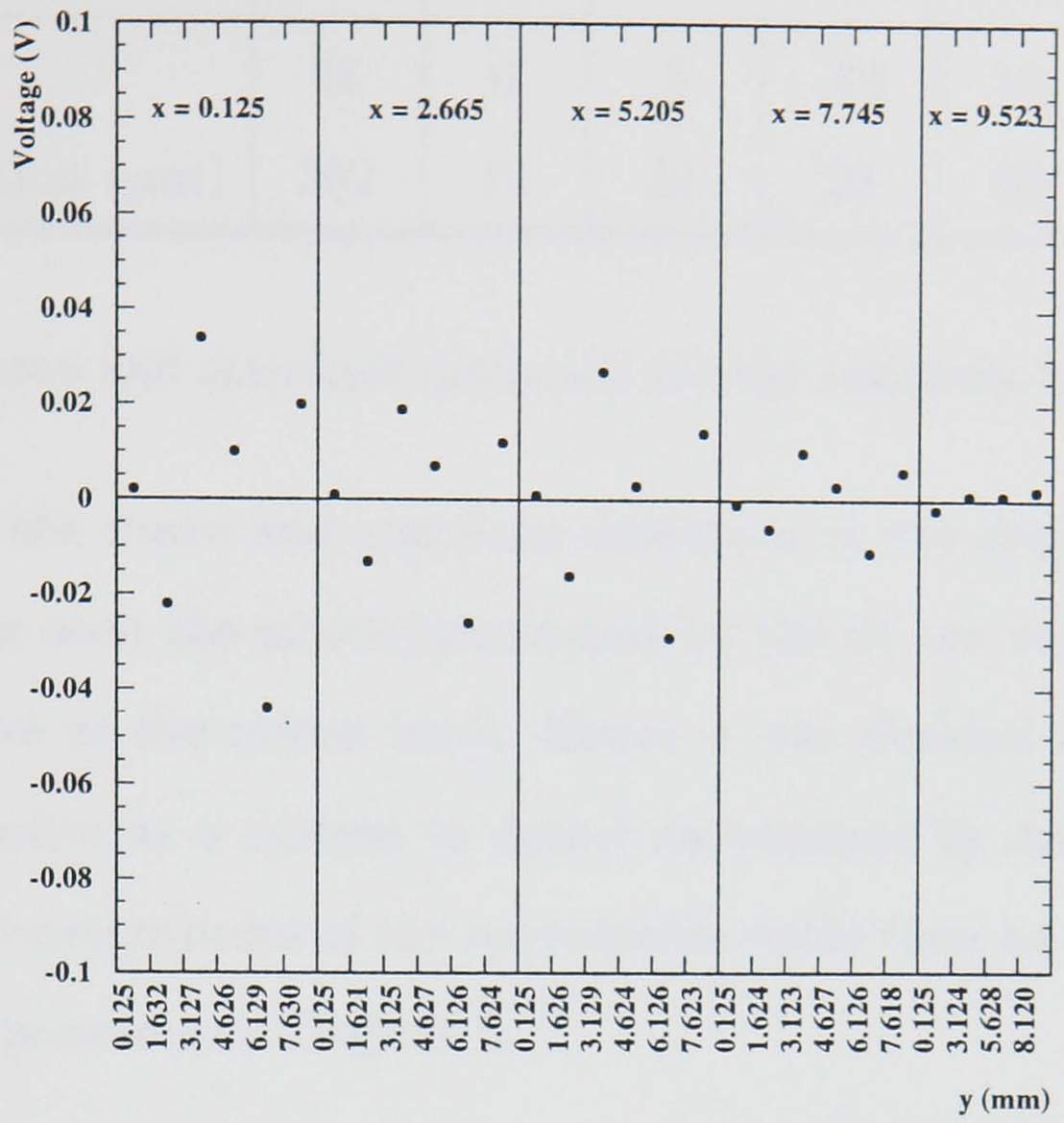

Figure 4.5: The residuals from a fit to the calibration data for the probe in Figure. 4.4 in volts.

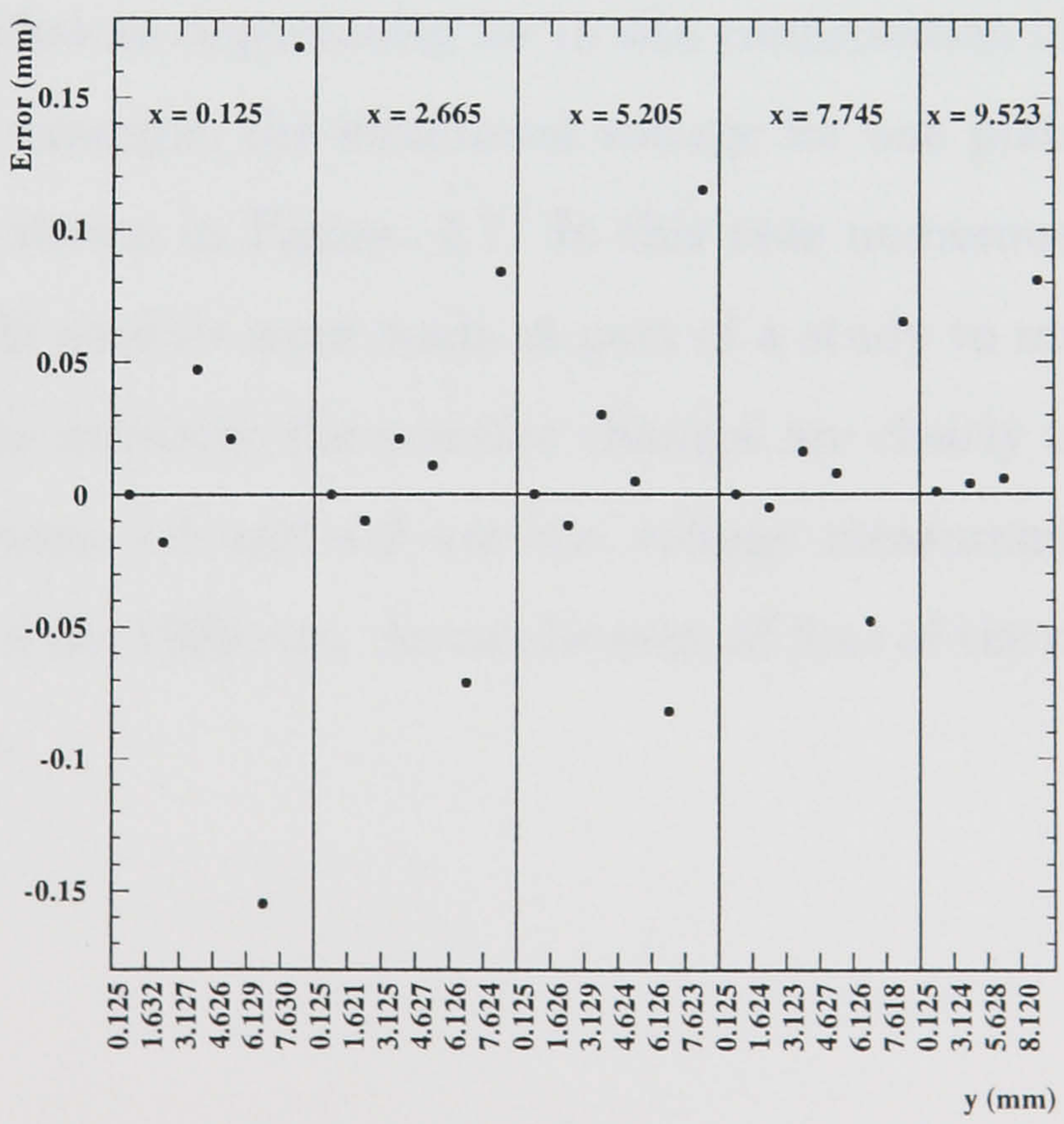

Figure 4.6: The residuals from a fit to the calibration data for the probe in Figure. 4.4 in mm.

Probe	NLX	NLY	NUX	NUY	SLX	SLY	SUX	SUY
Mean (μm)	58	0	5	-83	10	-95	-61	-10
Standard Deviation (μm)	352	18	34	29	60	419	378	37

Table 4.1: The mean and standard deviation for the residuals for each of the probes.

Table. 4.1 shows the mean and standard deviation of the residuals for each of the probes. As can be seen the errors introduced by the fit are very large. The system should be sensitive at the micon level. Hence it was desided to use the capacitive wire position monitor as a system to detect movements by monitoring the voltage outputs only. The magnitudes of the movements could then be determined from the global alignment procedure, Chapter 5.

4.4 Performance

During the 1996 SLD run the system performed well and no unexpected displacements were observed. Four controlled movements of the R20 module with respect to the CDC provided an opportunity for in situ confirmation of the monitoring performance. As an example, the monitored voltage for one plate for the duration of one movement is shown in Figure. 4.7. In this case numerous systematic position changes of the R20 module were made as part of a study to minimise beam related backgrounds in the detector; the position changes are clearly tracked by the data.

Shown in Figures. 4.8 and 4.9 are the voltage measurements from all probes during the whole of the 1996 run. As can be seen all four of the controlled movements are clearly visible.

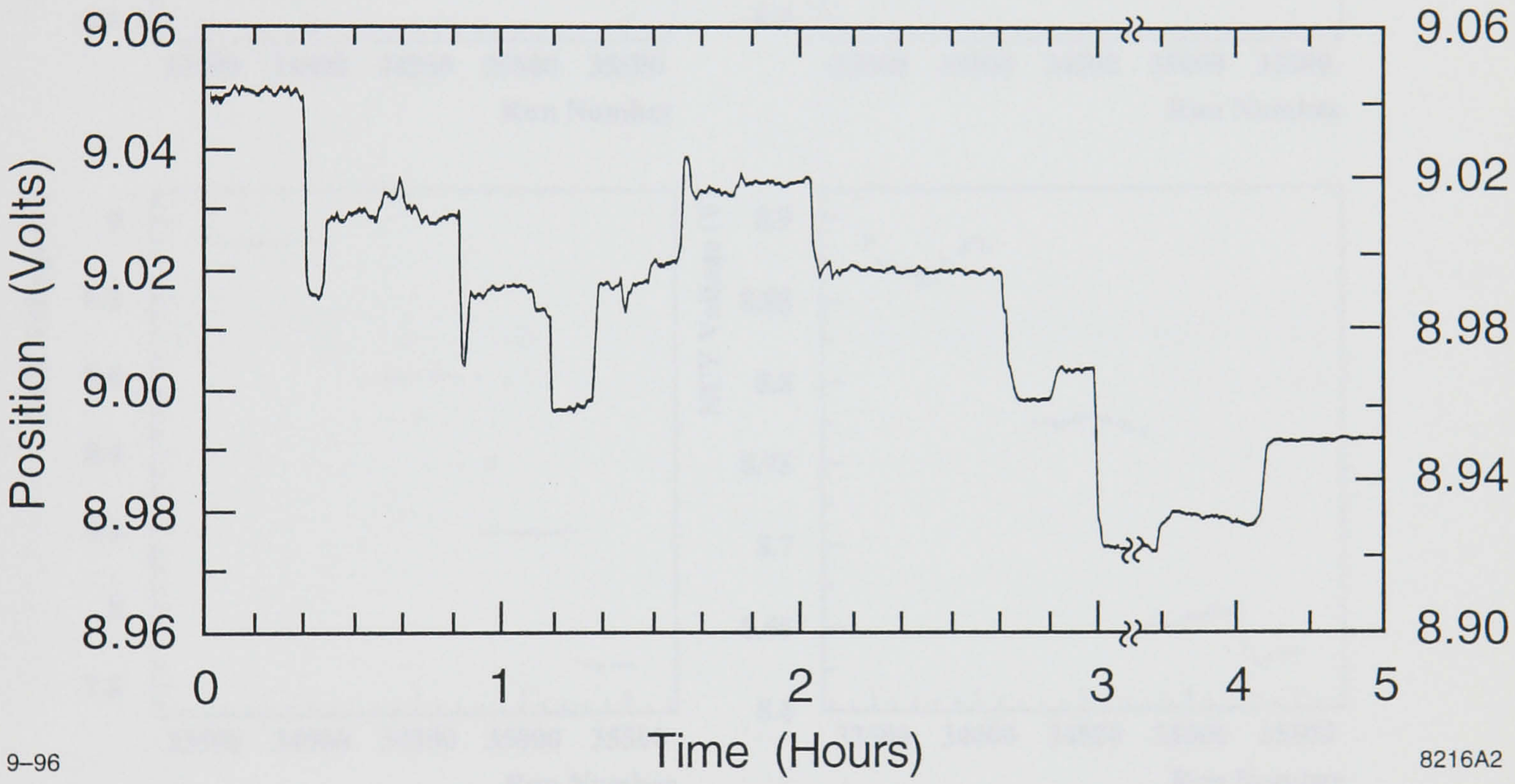

Figure 4.7: Controlled movements of the R20 as seen by one of the probes (1mV $\sim$ 1μm).

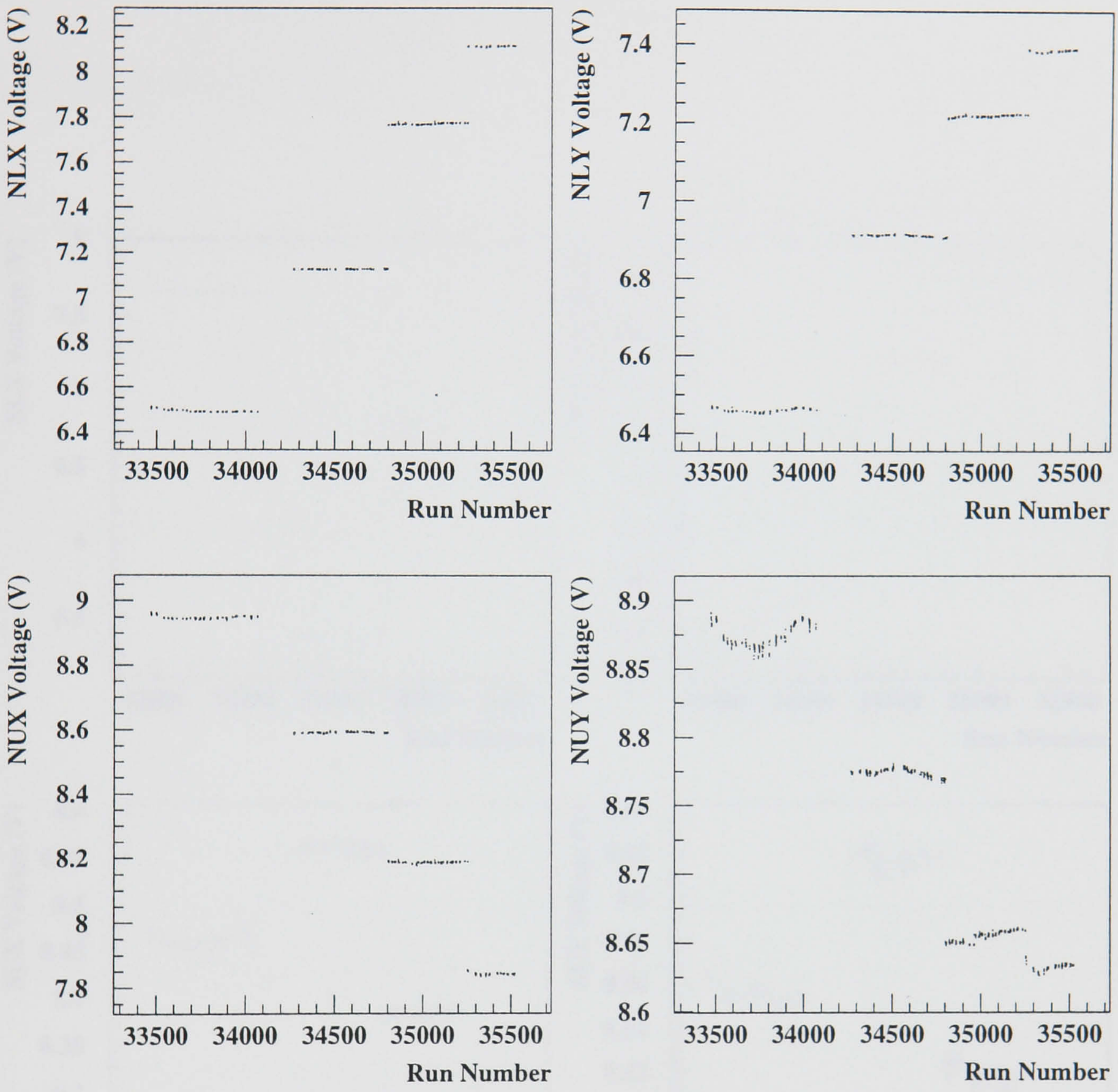

Figure 4.8: The voltages read from each of the north probes over the whole 1996 SLD run.

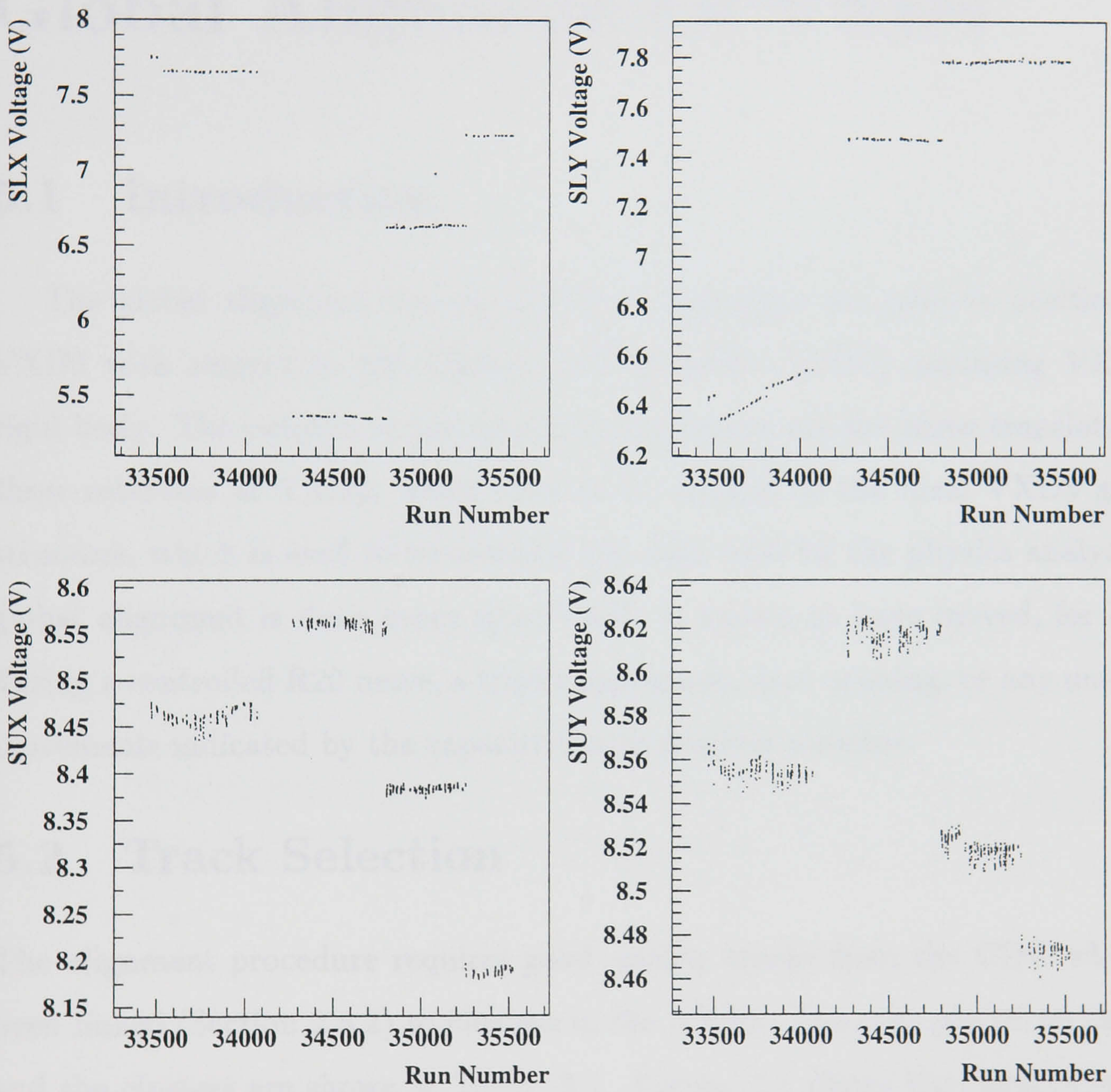

Figure 4.9: The voltages read from each of the south probes over the whole 1996 SLD run.

Chapter 5

Global Alignment Of VXD3

5.1 Introduction

The global alignment is a procedure to determine the relative position of the VXD3 with respect to the Central Drift Chamber (CDC) assuming VXD3 is a rigid body. The outputs of the alignment procedure are the three translations and three rotations of VXD3, which need to be applied to the ideal VXD3 geometry structure, which is used to reconstruct the data used for the physics analyses. The global alignment is done every time VXD3 is known to have moved, for example during a controlled R20 move, a triplet movement, door opening, or any unexpected movements indicated by the capacitive wire position monitor.

5.2 Track Selection

The alignment procedure requires good quality tracks from the CDC which have been linked (Section 2.5.2) to clusters in the VXD3. The cuts placed on the tracks and the clusters are shown in Table 5.1. Figure. 5.1 shows the clusters in VXD3, from a typical hadronic event, before linking to tracks. Figure. 5.2 shows the same event, however only the clusters linked to tracks extrapolated from the CDC are plotted.

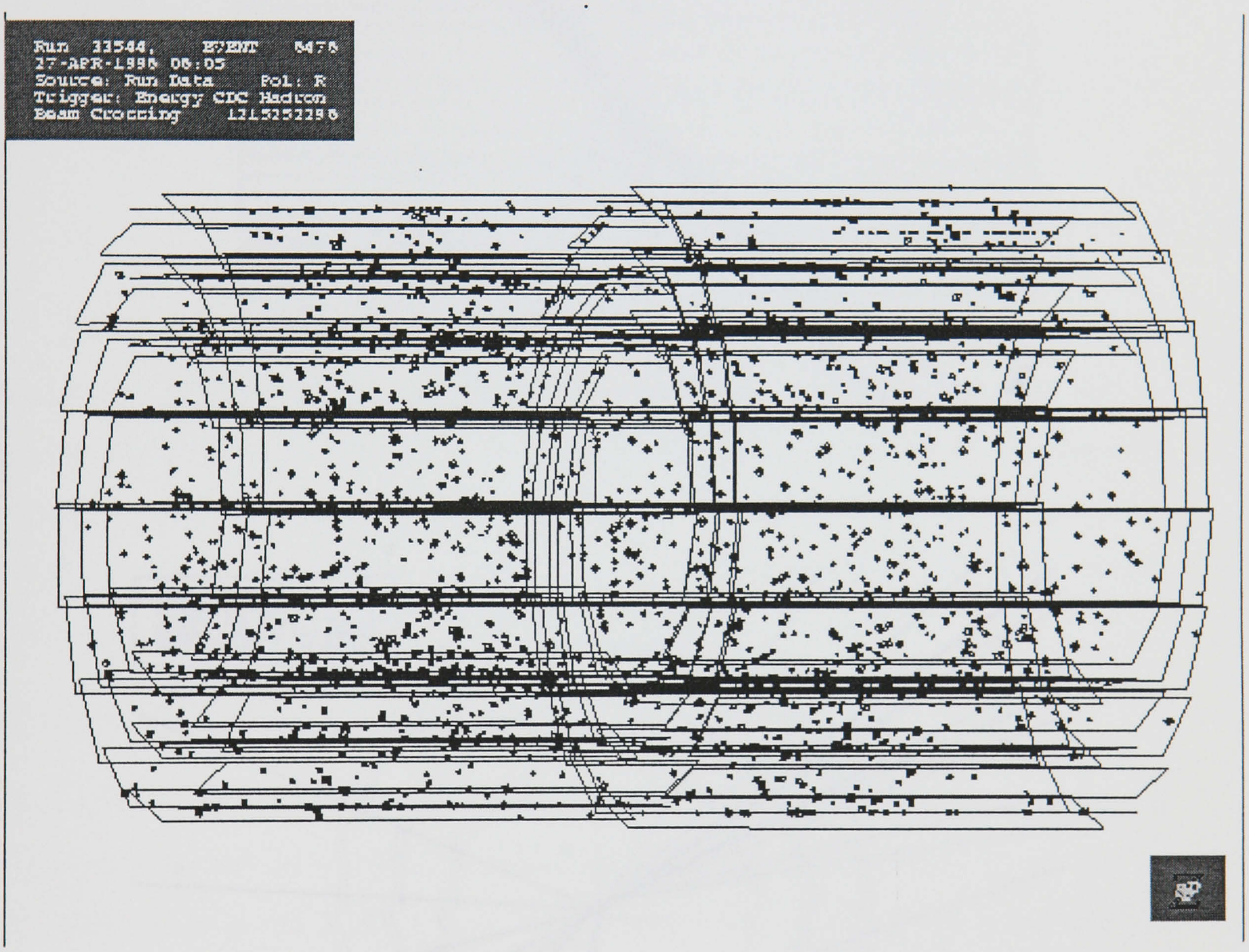

Figure 5.1: Side view of VXD3, showing clusters in a typical hadronic event, where most of the clusters are noise. Note the three layer cylindrical structure.

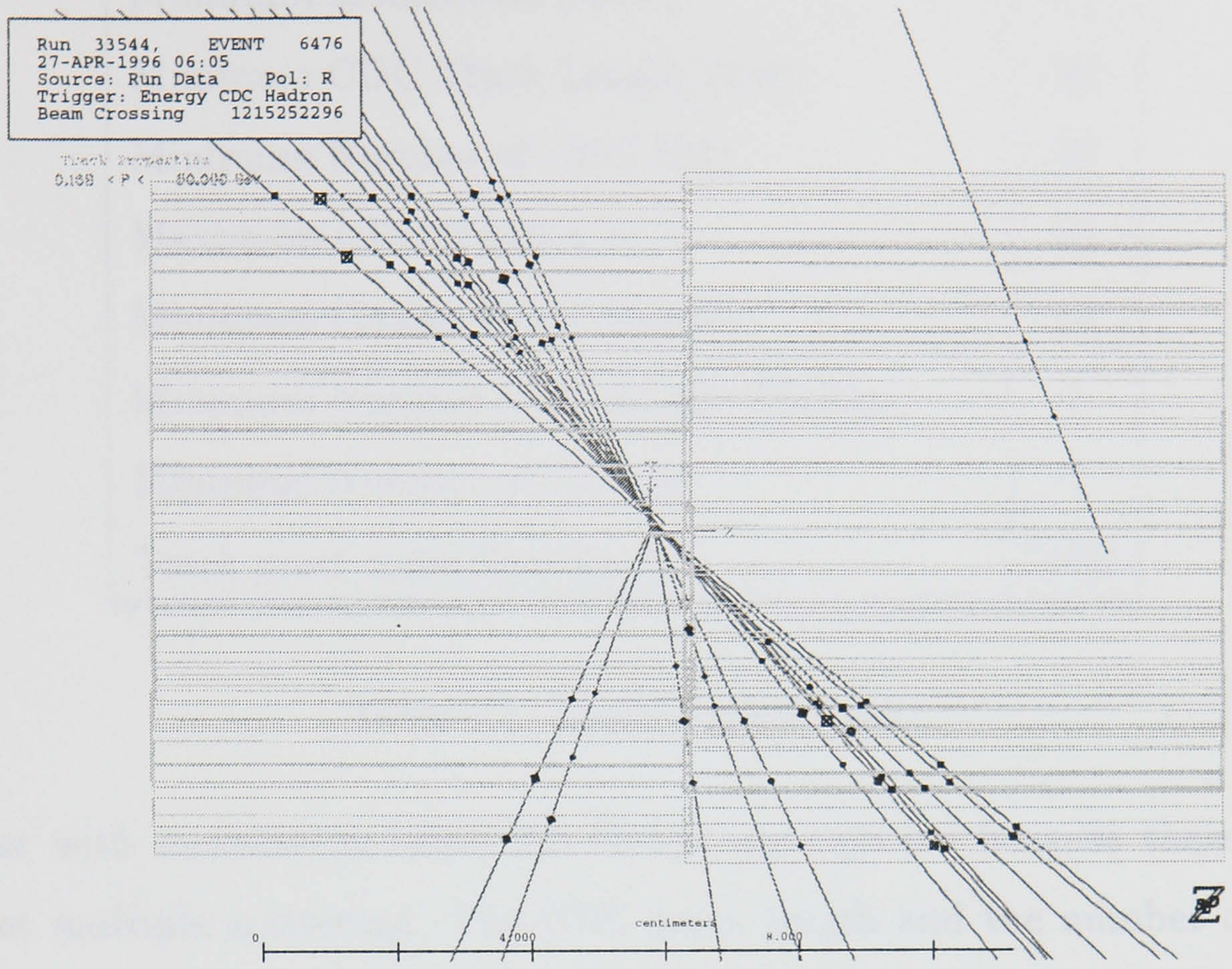

Figure 5.2: Side view (top) and front view (bottom) of VXD3. The lines are tracks extrapolated from the CDC, plotted with their associated VXD3 clusters.

Minimum Momentum (GeV)	0.5
Minimum CDC Track Length (cm)	50
Minimum Number of CDC Hits	50
Maximum CDC Track χ^2	10
Minimum Cluster Pulse Height	20
Minimum Number of Pixels per Clusters	1
Minimum Number of Clusters	2
Track must come from the IP	YES

Table 5.1: Quality track cuts.

Tracks with momentum below 0.5 GeV/c are rejected because these undergo significant multiple scattering. The CDC track length and the number of hits requirements selects tracks that have gone through a large volume of the the drift chamber, while the χ^2 requirement eliminates tracks that have been reconstructed badly. Demanding that the track must come from the Interaction Point (IP) ensures that tracks similar to the one on the right of Fig. 5.2 are rejected.

5.2.1 Residual Calculation

The CDC tracks are then extrapolated inwards and the point at which the track intersects the surface of a CCD is recorded. The residuals are formed by calculating the difference, in the x and z direction, between the track intercept point and the cluster center (Figure. 5.3).

Fig. 5.4 shows plots of the residuals before the alignment is performed. Notice the double peak in the dη residuals, indicating a misalignment of the VXD3 with respect to the CDC. To understand this structure the detector can be split into zones as schematically drawn in Fig. 5.5. The residual plots for dη for each of the zones are shown in Fig. 5.6.

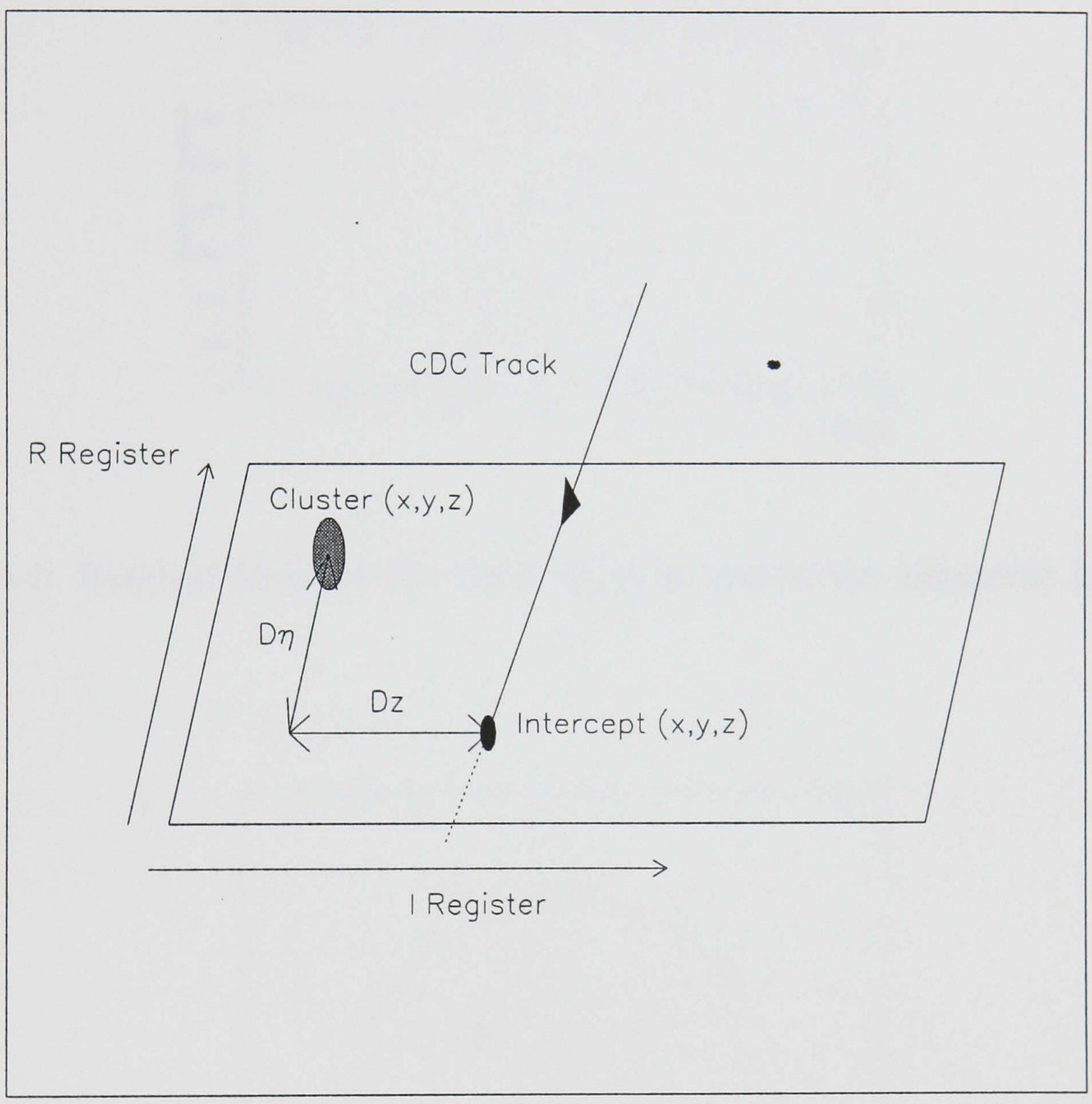

Figure 5.3: One CDC track extrapolated back onto the surface of a CCD, plotted along with the intercept point and the residuals between that point and the associated VXD cluster. The residual dz is along the CCD I register (z) and dη is the residual along the CCD R register (rϕ).

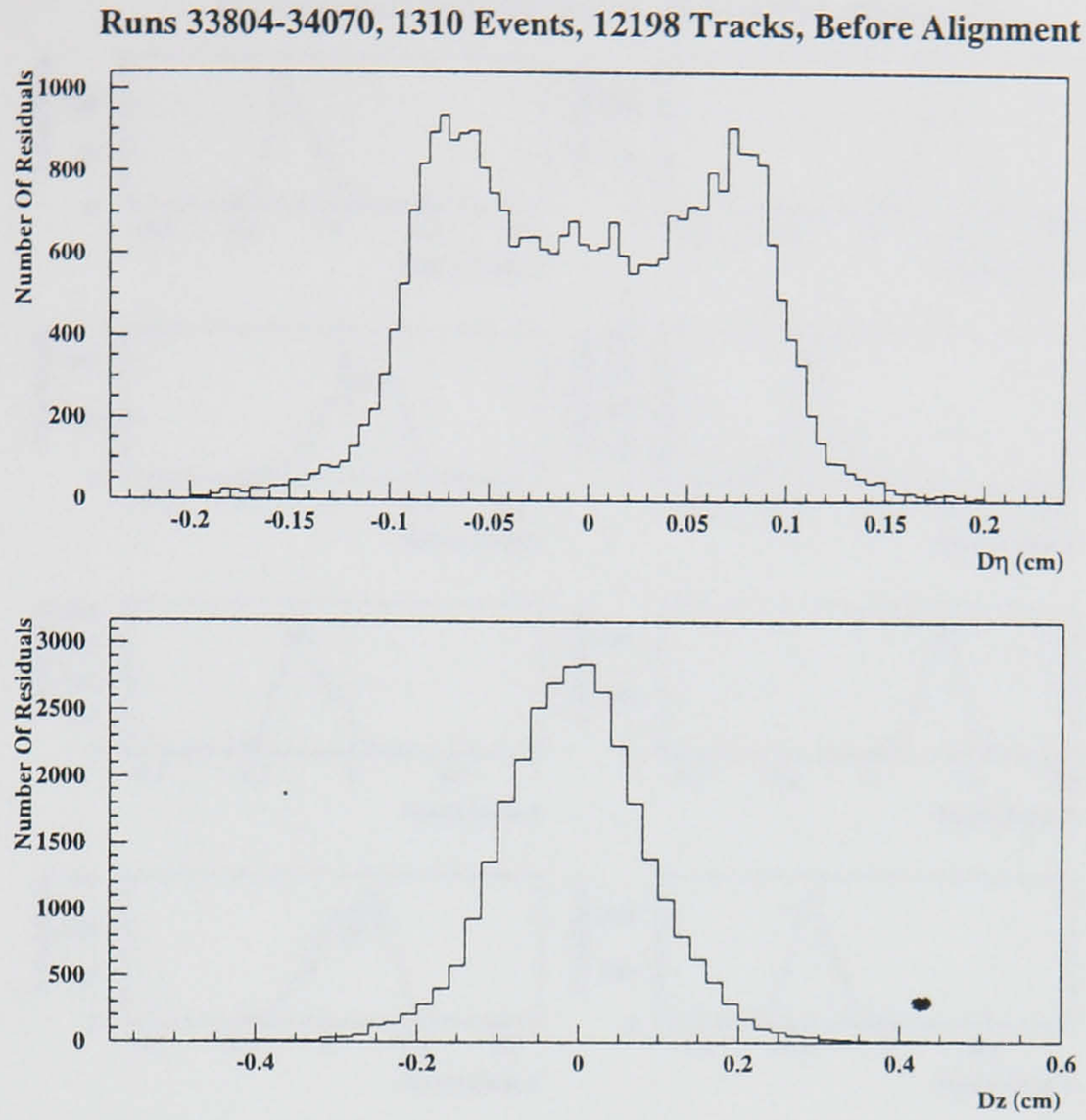

Figure 5.4: Residual plots for the whole detector, before the alignment is carried out.

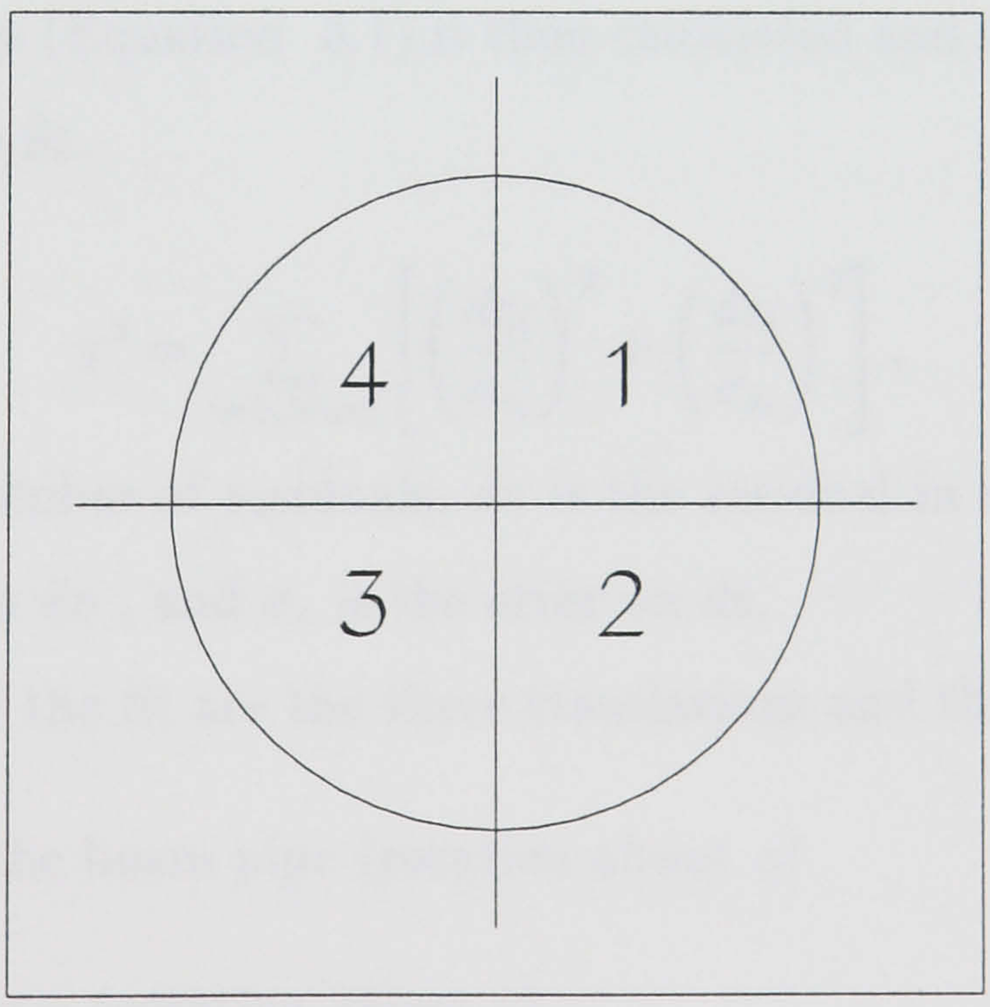

Figure 5.5: VXD3 can be split into eight zones, four in the North and four in the south.

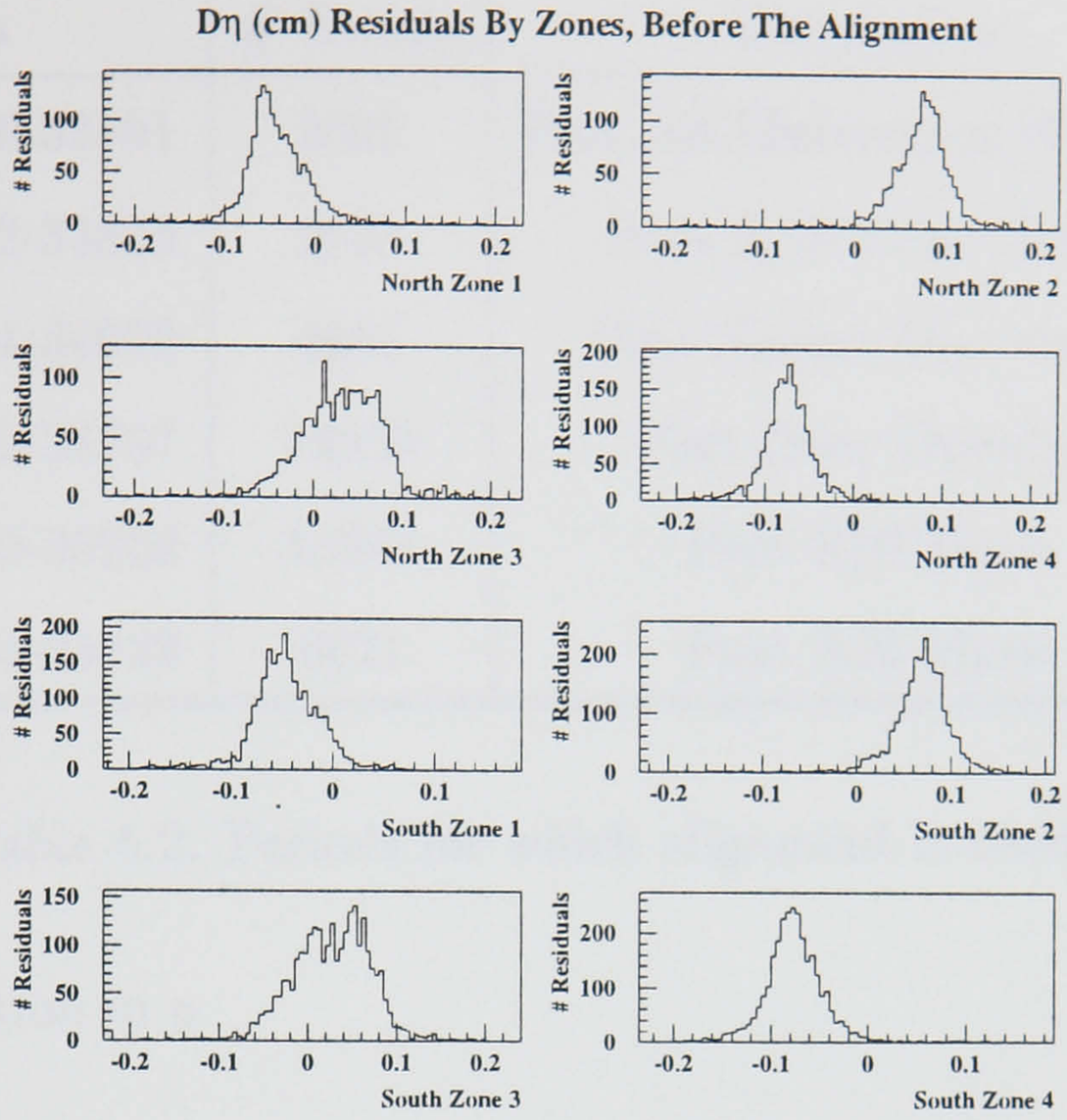

Figure 5.6: dη residual plots for different zones of the detector, before the alignment is carried out.

5.2.2 χ^2 Minimisation Fit

The following function (Equation 5.1) is then calculated and fed into MINUIT [79] for a χ^2 minimization fit.

$$\chi^2 = \sum_{i=1,Num} \left[\left(\frac{d\eta_i}{\sigma_{\eta_i}} \right)^2 + \left(\frac{dz_i}{\sigma_{z_i}} \right)^2 \right], \tag{5.1}$$

Where Num is the number of residuals, $d\eta$ is the residual in $r\phi$, dz is the residual in z, σ_η is the error on dη , and σ_z is the error on dz.

The parameters of the fit are the three translations and three rotations:

- α : Roll about the beam pipe (rotation about z)
- β : Horizontal yaw (rotation about y)
- γ : Vertical Pitch (rotation about x)
- dx : Translation in x

Runs	# Events	Description
33470-33591	2608	Post All Electronics Working
33592-33803	2935	Post A/D Fiber Swap
33804-34070	6681	Post Triplet Movement
34270-34797	13859	Post Door Opening
34800-35253	15985	Post R20 Move
35254-35522	6621	Post R20 Move

Table 5.2: Periods for which alignment is needed.

- dy : Translation in y
- dz : Translation in z

Those parameters are the changes from the geometry files used to reconstruct the tracks and the clusters.

The above procedure is repeated for the different run periods where the R20 was stationary. The boundaries of these stationary periods are defined by data from the capacitive wire position monitor (Chapter4). The translations and rotations are then incorporated into the geometry files used to reconstruct the data. Hence there is a geometry file for each period.

The different periods for which geometry files were generated for the 1996 SLD physics run are shown in Table 5.2. When the internal alignment is added to the geometry file, these files were used to resconstruct the data used for physics analysis.

5.2.3 Cross Check

After the χ^2 minimisation the residuals are recalculated. Fig. 5.7 and Fig. 5.8 show the residuals of Fig. 5.4 and Fig. 5.6 after the alignment has been carried out. Clearly the double peak structure has gone and the distributions are now nicely centered on zero, as one would expect.

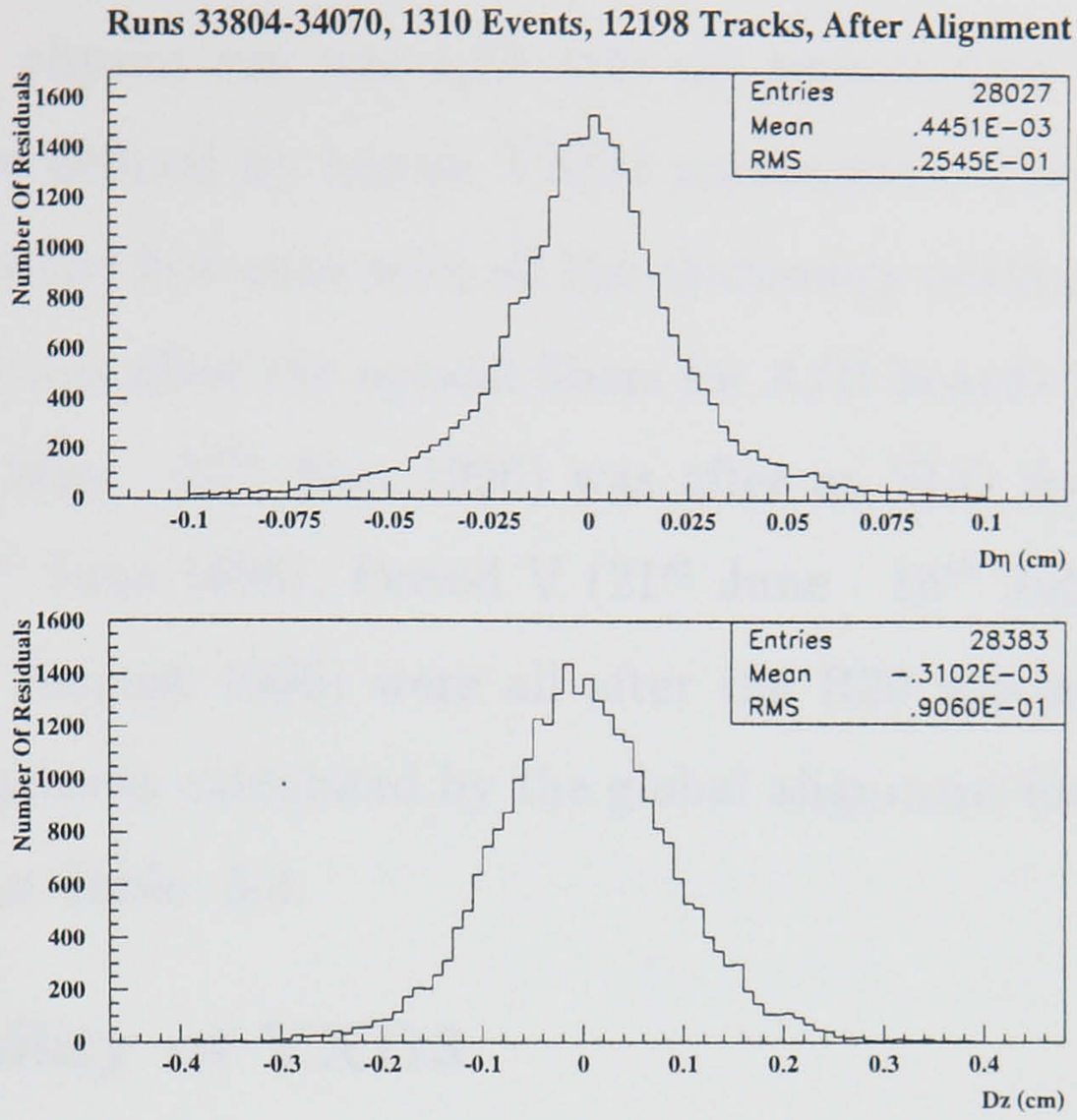

Figure 5.7: Residual plots for the whole detector, after the alignment is carried out.

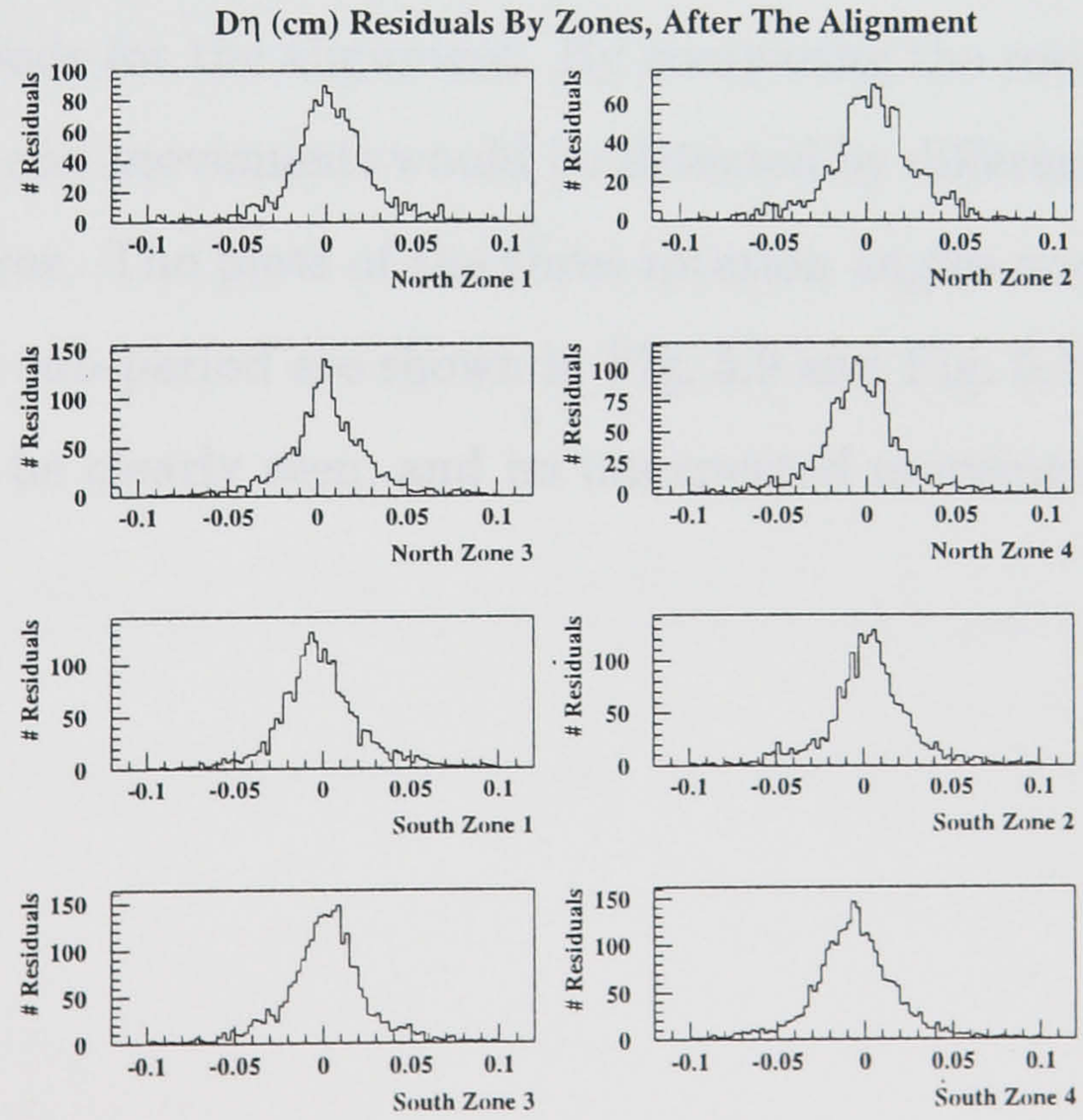

Figure 5.8: dη residual plots for different zones of the detector, after the alignment is carried out.

5.3 The Constants for the 1996 run

The SLD 1996 physics run was split into six periods (see Table 5.2). where the boundaries were defined by known VXD3 movements. Period I (23^{rd} April - 29^{th} April 1996) were the first runs with all the electronics working. Period II (29^{th} April - 9^{th} May 1996) was after the optical fibers for A/D boards 9 and A were swapped. Period III (9^{th} May - 25^{th} May 1996) was after an SLD door opening. Period IV (25^{th} May - 21^{st} June 1996), Period V (21^{st} June - 16^{th} July 1996) and Period VI (16^{st} July - 1^{st} August 1996) were all after the R20 was moved, to better center VXD3. The constants calculated by the global alignment for the SLD 1996 physics run are shown in Table 5.3.

5.3.1 Stability of VXD3

A concern one might have is that the VXD3 moves unexpectedly during the run, and hence goes un-noticed. Two ways were used to check for any movement. The first is monitoring the capacitive wire position monitor (Chapter 4). During the SLD 1996 physics run, no unexpected movements were seen. The second way was to use the sub-periods for the alignment. By comparing the results of the alignment of the sub-periods any movements would be detected by differences not consistent with the expected error. The plots of the three rotation angles and three translations for each period and sub-period are shown in Fig. 5.9 and Fig. 5.10. Where the expected movements can be clearly seen, and no unexpected movements are detected.

Parameter	Period I (4/23-4/29)	Period II (4/29-5/9)	Period III (5/9-5/25)
α (mrad)	-2.33 $\pm$ 0.03	-2.19 $\pm$ 0.06	-2.11 $\pm$ 0.02
β (mrad)	-4.77 $\pm$ 0.10	-4.68 $\pm$ 0.16	-4.90 $\pm$ 0.07
γ (mrad)	1.88 $\pm$ 0.10	1.99 $\pm$ 0.15	1.99 $\pm$ 0.06
δx (μm)	594 $\pm$ 2	593 $\pm$ 3	556 $\pm$ 2
δy (μm)	2310 $\pm$ 2	2311 $\pm$ 3	2283 $\pm$ 2
δz (μm)	5557 $\pm$ 10	5566 $\pm$ 16	5558 $\pm$ 6

Parameter	Period IV (5/25-6/21)	Period V (6/21-7/16)	Period VI (7/16-8/1)
α (mrad)	-1.62 $\pm$ 0.02	-1.55 $\pm$ 0.03	-1.30 $\pm$ 0.05
β (mrad)	-4.84 $\pm$ 0.05	-1.59 $\pm$ 0.07	0.58 $\pm$ 0.13
γ (mrad)	1.73 $\pm$ 0.05	0.55 $\pm$ 0.07	0.64 $\pm$ 0.13
δx (μm)	-122 $\pm$ 1	-117 $\pm$ 1	-77 $\pm$ 3
δy (μm)	1881 $\pm$ 1	2120 $\pm$ 1	2131 $\pm$ 2
δz (μm)	5475 $\pm$ 6	5513 $\pm$ 8	5487 $\pm$ 13

Table 5.3: Global Alignment Constants for the 1996 run. The errors are from the fit.

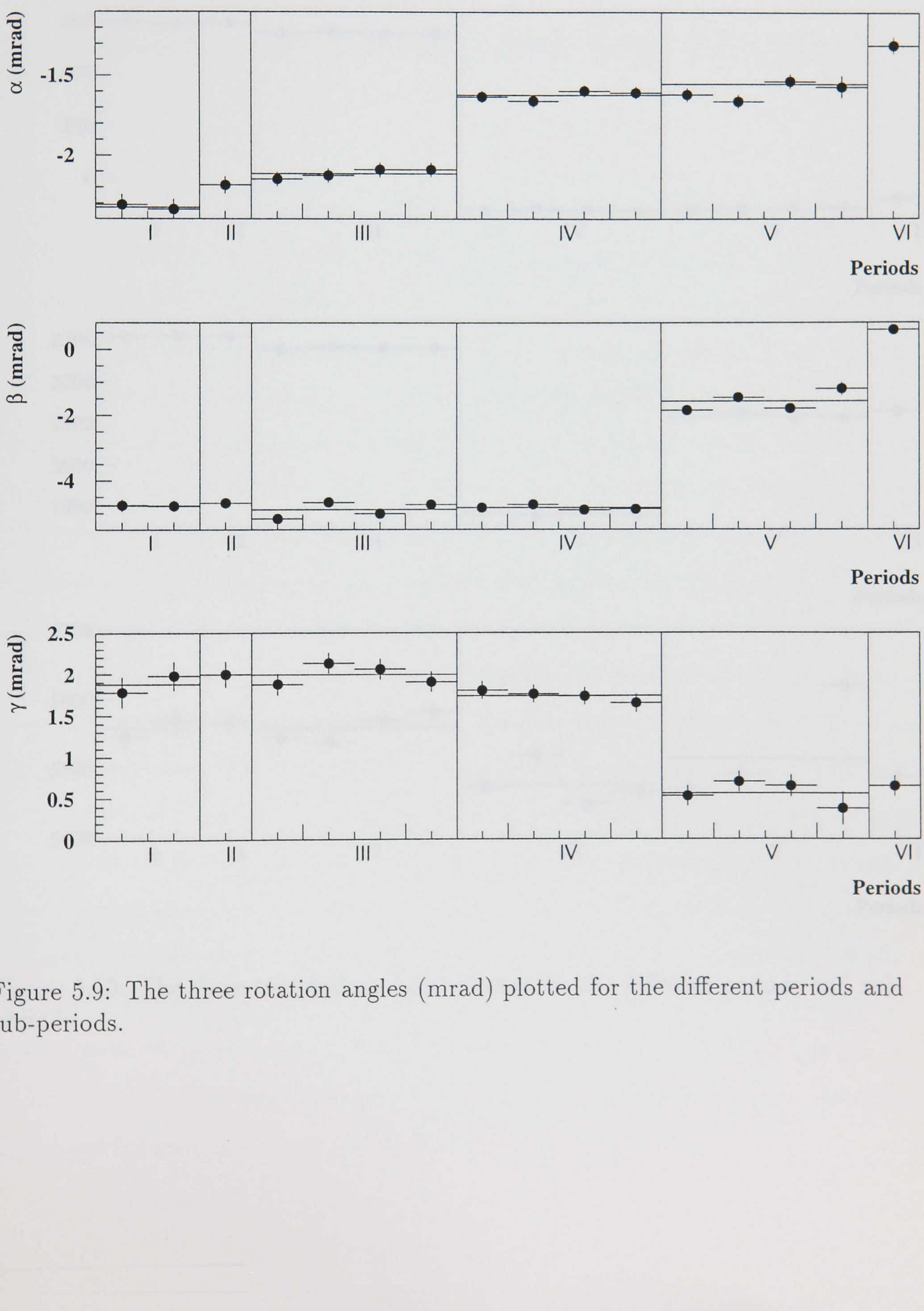

Figure 5.9: The three rotation angles (mrad) plotted for the different periods and sub-periods.

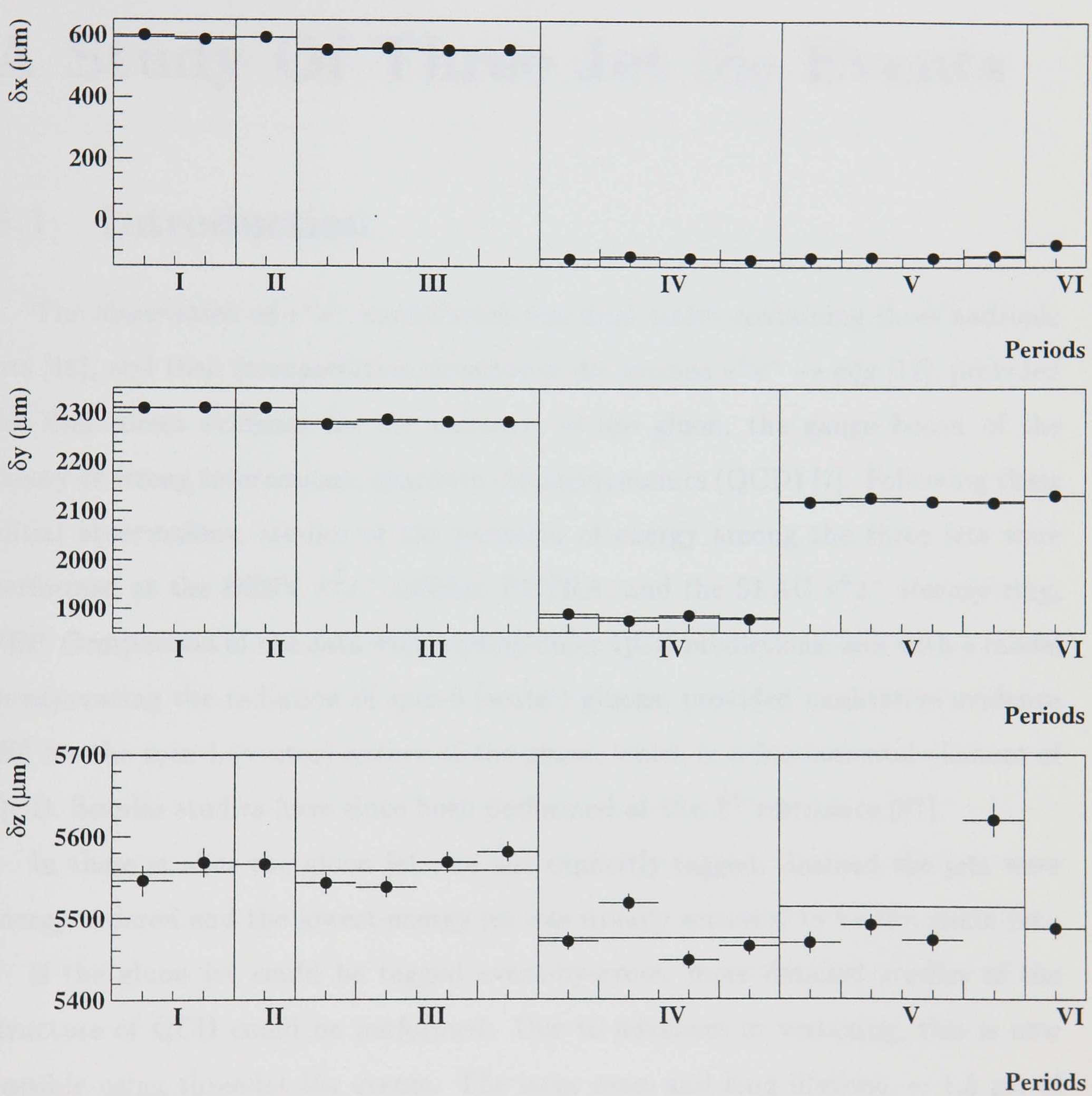

Figure 5.10: The three translations (μm) plotted for the different periods and sub-periods.

Chapter 6

A Study Of Three Jet $b\bar{b}g$ Events

6.1 Introduction

The observation of e^+e^- annihilation into final states containing three hadronic jets [16], and their interpretation in terms of the process $e^+e^- \rightarrow q\bar{q}g$ [17], provided the first direct evidence for the existence of the gluon, the gauge boson of the theory of strong interactions, quantum chromodynamics (QCD) [7]. Following these initial observations, studies of the partition of energy among the three jets were performed at the DESY e^+e^- collider, PETRA, and the SLAC e^+e^- storage ring, PEP. Comparison of the data with leading-order QCD predictions, and with a model incorporating the radiation of spin-0 (scalar) gluons, provided qualitative evidence [80] for the spin-1 (vector) nature of the gluon, which is a fundamental element of QCD. Similar studies have since been performed at the Z^0 resonance [81].

In these studies the gluon jet was not explicitly tagged. Instead the jets were energy ordered and the lowest-energy jet was usually assumed to be the gluon jet.

If the gluon jet could be tagged event-by-event, more detailed studies of the structure of QCD could be performed. Due to advances in vertexing, this is now possible using three-jet $b\bar{b}g$ events. The large mass and long lifetime, $\sim$ 1.5 ps, of B hadrons [1] lead to decay signatures which uniquely distinguish them from charm and light quark decays. Using the SLD CCD vertex detector it is possible to identify in each event the jets containing the B hadrons, and hence to tag the gluon jet. A similar technique has been used recently by the OPAL Collaboration, to investigate differences between quark and gluon jets [82].

The Standard Model has provided a remarkably successful description of almost all available data involving the electroweak interaction. Recently, however, some measurements of the quantities R_b and A_b have been reported [83] which are in mild disagreement, at the 2-3 standard deviation level, with Standard Model expectations. Since, on general grounds, one expects new high-mass scale dynamics to couple to the massive third-generation fermions, these measurements in the b-quark sector have aroused considerable interest and speculation. This provides additional motivation to study the strong-interaction dynamics of the b-quark via $Z^0 \rightarrow b\bar{b}g$ events.

The chromomagnetic moment of the bottom quark is induced at the one-loop level in QCD and is of the order α_s/π. One can also write down an *ad hoc* Lagrangian [84] with a $b\bar{b}g$ coupling modified via anomalous chromoelectric and chromomagnetic moments:

$$\mathcal{L}^{b\bar{b}g} = g_s \bar{b} T_a \{\gamma_\mu + \frac{i\sigma_{\mu\nu}k^\nu}{2m_b}(\kappa - i\tilde{\kappa}\gamma_5)\} b G_a^\nu \tag{6.1}$$

where g_s is the strong charge, T_a are the $SU(3)_c$ generators, m_b is the bottom quark mass, k is the outgoing gluon momentum, $\sigma_{\mu\nu} = \frac{i}{2}[\gamma^\mu, \gamma^\nu]$ and κ and $\tilde{\kappa}$ parameterize the anomalous chromomagnetic and chromoelectric moments, respectively, which might arise from physics beyond the Standard Model. The values of κ and $\tilde{\kappa}$ are zero in the Standard Model. The effect of the former on three-jet observables has been calculated recently [84, 85]. The latter is CP-violating, and in this analysis we have not attempted to discriminate between the b and $\bar{b}$ jets and are hence insensitive to non-zero values of $\tilde{\kappa}$. Non-zero values of κ would modify the gluon energy distribution in $b\bar{b}g$ events.

6.2 Hadronic Event Selection

6.2.1 The SLD Trigger

The triggers are described in detail in Ref [86]. Only a brief description will be given here. There were six main classes of triggers. If an event passes any of these triggers

the whole of SLD is read out:

- *Total energy trigger*: The energy trigger required a minimum total energy of 8 GeV, where the sum is taken only over those EM (HAD) calorimeter towers containing more than 60 ADC counts (120 ADC counts) of deposited energy, which corresponds to an energy threshold of 250 MeV (1.3 GeV) per tower.

- *Charged track trigger*: The charged track trigger was based on a pattern map of the cells that might be hit as a charged track of momentum greater than 250 MeV/c passed through the CDC. A hit cell was defined as a cell where pulses consistent with hits from tracks fired a discriminator on 6 of the possible 8 wires. Events containing two tracks passing through at least 9 superlayers of the CDC and lying roughly 120 degrees apart were accepted by this trigger.

- *Hadron (HAD) trigger*: The HAD trigger required one charged track of 9 or more superlayers and a large energy deposition in the LAC. It was expected that most Z^0 events ($\sim 90\%$) would satisfy this trigger.

- *Wide-angle-Bhabha (WAB) trigger*: The WAB trigger was designed to ensure that all wide-angle e^+e^- pairs were recorded, even those at angles where the track stubs in the CDC were not long enough to satisfy the track trigger requirements.

- *Muon pair trigger*: The muon trigger required a combination of a charged track in the CDC and hits in the opposite WIC octants, as this would be the signature for a $Z^0 \rightarrow \mu^+\mu^-$ event.

- *Random trigger*: This trigger recorded data every 20 seconds, regardless of the detector status, to provide information for background studies.

6.2.2 The Hadronic Event Filter

The event filter is run offline to eliminate events which clearly have no analysis use. The first stage EIT pass-1 filter, selects events using calorimetry information only, as it is much faster to process compared to the tracking information. EIT

pass-1 requires that the event is relatively spherical and has good forward-backward momentum balance. It is based on three LAC quantities:

- NEMHI, the number of LAC EM towers with signals above 60 ADC counts (This is equivalent to ~250 MeV from minimum ionising particles (min-I))

- EHI, the sum of the energy deposited in all EM (HAD) towers with signals greater than high thresholds of 60 (120) ADC counts. (This is equivalent to 250 MeV (1.3 GeV) min-I)

- ELO, the sum of the energy deposited in all EM (HAD) towers with signals greater than low thresholds of 8 (12) ADC counts. (This is equivalent to 33 MeV (130 MeV) min-I)

The filter requires that each event satisfy:

1. NEMHI $\geq$ 10
2. EHI $>$ 15 GeV min-I
3. ELO $<$ 140 GeV min-I
4. $2 \times$ EHI $> 3 \times$ (ELO-70)
5. The north and south hemispheres of the detector must each have NEMHI > 0

Cuts three and five tend to remove beam-wall events. After applying the EIT pass-1 filter, 207460 events remain from the 1993-1995 data samples.

6.2.3 Hadronic Event Selection Cuts

In order to select a sample of hadronic events useful for the physics analysis, cuts are applied to select events contained within the fiducial region of the SLD detector. Since charged tracks are the basis for the analysis, this restricts us to the barrel region of the SLD, as the CDC starts to lose tracking efficiency for $|\cos\theta| > 0.8$. (The SLD reconstruction code has not been sufficiently tuned for the EDC, hence the end-caps drift chambers are not used.) The energy flow of the event must also

be well contained within the fiducial region so as to guarantee that large parts of the event are not lost in the detector endcaps. All but one of the event cuts are based on charged tracks, the one exception is that based on the thrust [14] (Section 1.4.3), where energy clusters in the LAC are used.

Since most of the event cuts are based on charged tracks, we must first define a 'well measured' charged track, which is any track satisfying:

- $|\cos\theta| < 0.8$ (θ is the polar angle of the track.)
- Distance of closest approach to the IP in the xy plane $doca_{xy}^{IP} < 5$cm.
- Distance of closest approach to the IP in the rz plane $doca_{rz}^{IP} < 10$cm.
- Transverse momentum relative to the beam axis $p_\perp > 150$ MeV/c.

The $doca_{xy}^{IP}$, $doca_{rz}^{IP}$ and $p_\perp$ cuts reject tracks that have low momentum and have interacted with detector material. The selected events are required to satisfy:

- ≥ 5 charged tracks. This is to eliminate leptonic Z^0 decays, which have a lower track multiplicity.
- $|\cos\theta_{Thrust}| < 0.71$. Reconstructed from calorimeter clusters, is required to lie well within the CDC acceptance.
- $E_{vis} > 20$ GeV, where E_{vis} is calculated from the charged tracks, assuming all tracks to be pions. This cut also eliminates $\gamma\gamma$ events and leptonic Z^0 decays, especially $\tau^+\tau^-$.
- VXD2 fully operational. This ensures that the events selected can be used for flavour tagging.

The efficiency for selecting hadronic events was estimated to be above 96% [27]. The background in the selected event sample was estimated to be 0.3 ± 0.1 %, dominated by $Z^0 \rightarrow \tau^+\tau^-$ events.

Figure 6.1 shows the data sample, with the hadronic event simulation overlayed. The agreement between the data and the simulation is not very good for the number

of tracks and E_{vis}. This is due to a simplified simulation of the dependence of the CDC hit efficiency and resolution on the position within a CDC cell. The correction for this is described in Section 6.7.1. Table. 6.1 shows the efficiency for the different event flavours to pass these selection cuts for each period of data used in the analysis. Any small flavour bias in event selection will be corrected in the analysis, but, as can be seen, this bias is very small.

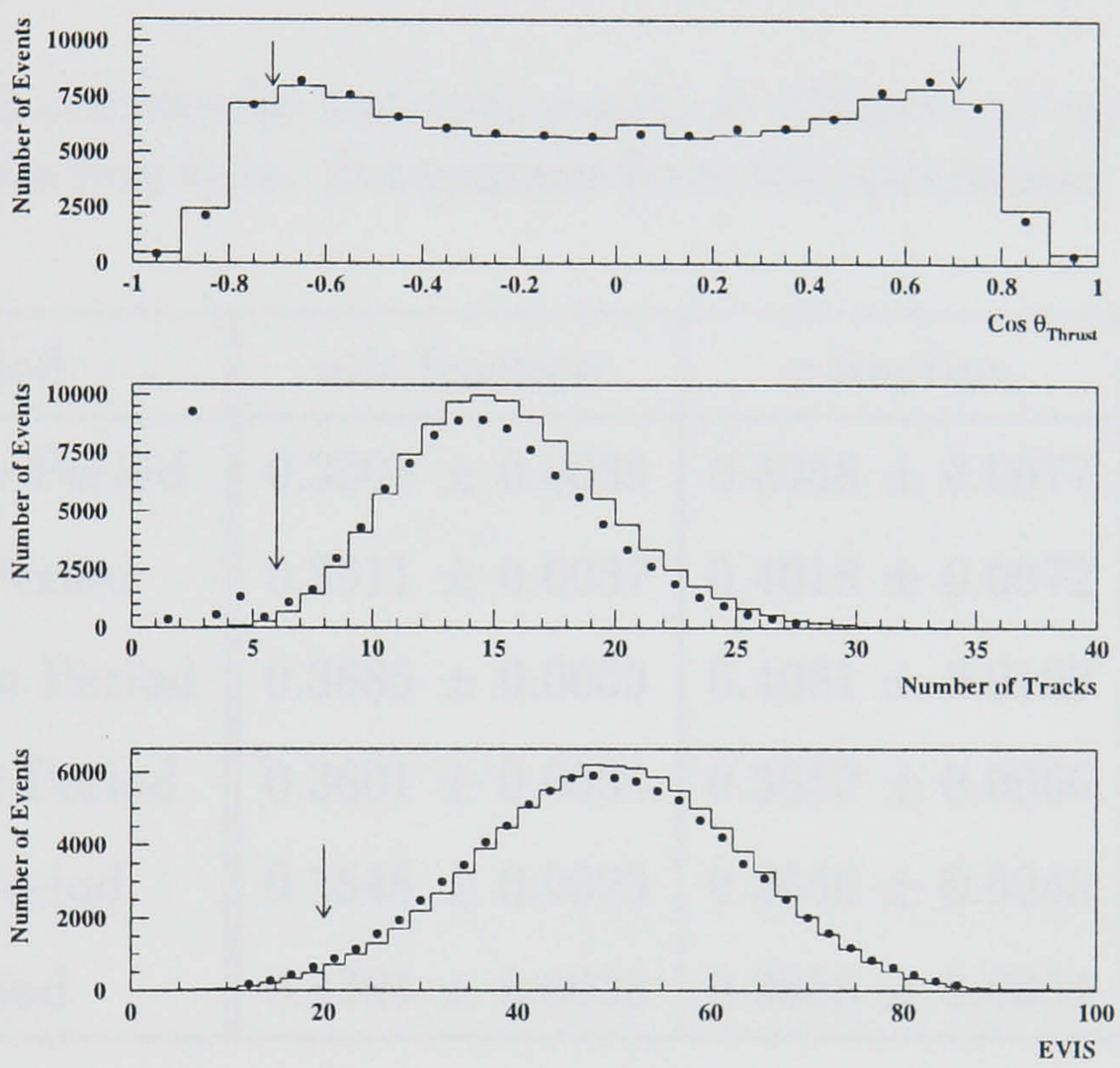

Figure 6.1: Distributions of the hadronic event selection variables, comparing data (points) and MC (histogram). To make each plot, all of the other cuts have been applied except for the ones being plotted. The arrows indicate the values of the cut on each of the variables.

6.2.4 Three-Jet Event Selection

This analysis required three-jet events. The jets are defined using the JADE jet finding algorithm [39] with a y_{cut} of 0.02. Only three jet events are selected, and each of the jets must be well contained within the tracking volume, hence the additional cut:

Run Period	*uds* efficiency	*c* efficiency	*b* efficiency
1993 Pre-Veto Period	0.5989 ± 0.0037	0.6074 ± 0.0070	0.6085 ± 0.0063
1993 Veto Period	0.6168 ± 0.0030	0.6187 ± 0.0058	0.6239 ± 0.0051
1993 Post-Veto Period	0.6219 ± 0.0083	0.6213 ± 0.0094	0.6138 ± 0.0049
1994 Summer Period	0.5668 ± 0.0032	0.5690 ± 0.0061	0.5724 ± 0.0054
1994 Fall Period	0.5553 ± 0.0022	0.5613 ± 0.0043	0.5593 ± 0.0038
1995 Period	0.5972 ± 0.0026	0.6009 ± 0.0050	0.6054 ± 0.0045

Table 6.1: The efficiencies for hadronic events of different primary quark flavours to pass the event selection cuts. Determined from the simulation.

Run Period	*uds* fraction	*c* fraction	*b* fraction
1993 Pre-Veto Period	0.3805 ± 0.0039	0.3958 ± 0.0077	0.3959 ± 0.0069
1993 Veto Period	0.3911 ± 0.0037	0.4018 ± 0.0072	0.4090 ± 0.0065
1993 Post-Veto Period	0.3885 ± 0.0053	0.4081 ± 0.0103	0.4150 ± 0.0093
1994 Summer Period	0.3601 ± 0.0034	0.3652 ± 0.0066	0.3825 ± 0.0061
1994 Fall Period	0.3548 ± 0.0023	0.3656 ± 0.0045	0.3770 ± 0.0041
1995 Period	0.3794 ± 0.0028	0.3858 ± 0.0054	0.3992 ± 0.0050

Table 6.2: The fraction of hadronic events of different primary quark flavours to pass the hadronic event selection and 3-jet selection cuts.

- $|\cos\theta_{jet}| < 0.71$. Where $|\cos\theta_{jet}|$ is the polar angle of the jet with respect to the electron beam direction

was applied. This cut ensures that all of the selected jets are well measured in the VXD and CDC. The fraction of the different event flavours to pass the hadronic event selection cuts and the three-jets cut, are shown in Table. 6.2.

6.2.5 Rescaling

As the charged tracks are used to define the jets and hence the jet energies, about one third of the hadrons are lost, as they are neutral. Hence, the measured jet

energies are approximately two thirds of the true value, Figure 6.2

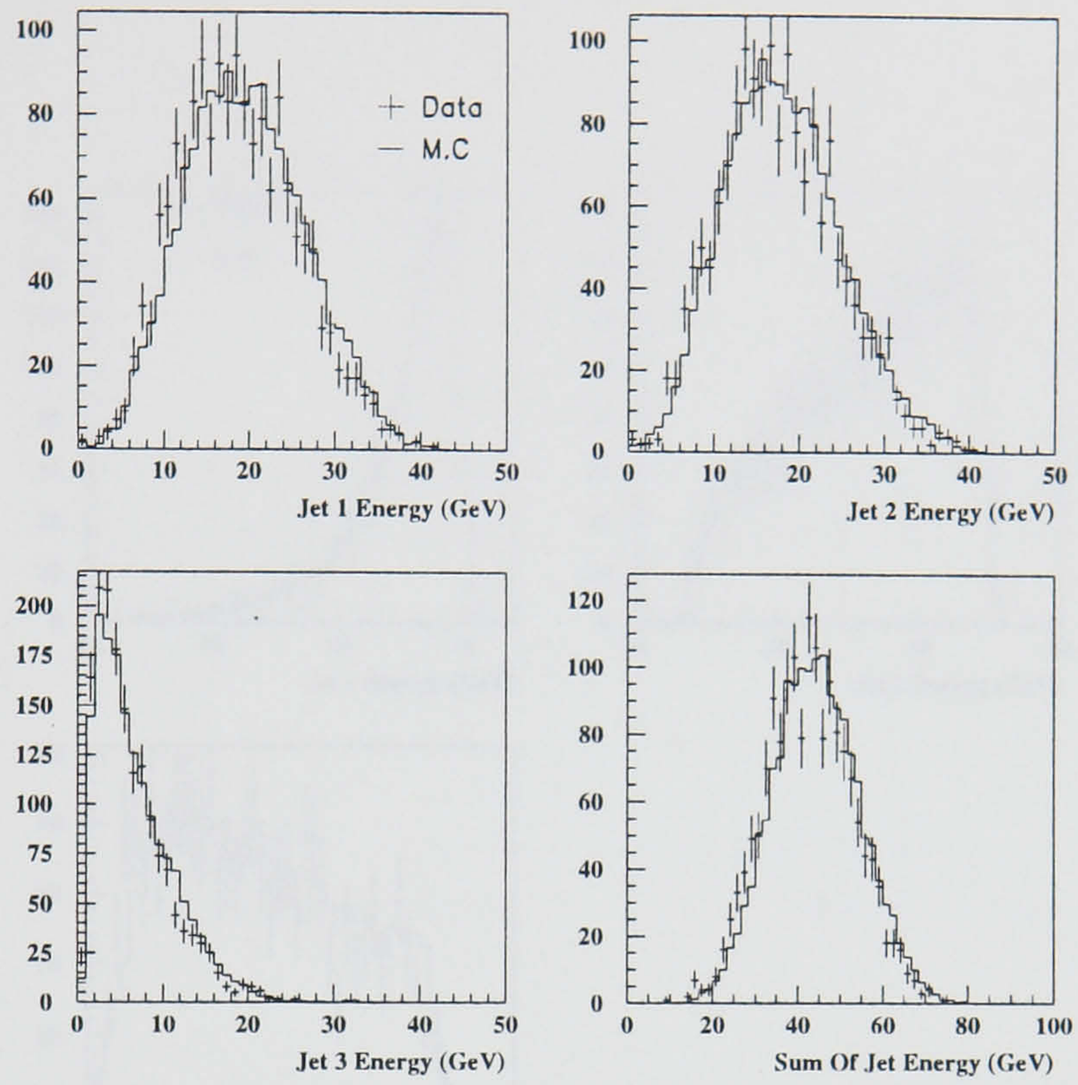

Figure 6.2: The energy of the jets before energy rescaling.

In three-jet events the underlying parton directions are well-reproduced by the jet finding alorithms, while the energies are not. Hence the energies of the jets were kinematically rescaled according to the angles between the jet axes, assuming energy and momentum conservation and massless kinematics. Labelling the jets arbitrarily 1, 2 and 3, and the corresponding inter-jet angles θ_{23}, θ_{13}, θ_{12}, the corrected energy of jet 1 is given by:

$$E_1 = \sqrt{s}\frac{\sin\theta_{23}}{\sin\theta_{12} + \sin\theta_{23} + \sin\theta_{31}} \tag{6.2}$$

The distributions of the jet energies after rescaling are shown in Figure 6.3. Figure 6.4 shows the energy resolutions for each of the jets before and after the rescaling. The energy resolution for jet i $(i = 1, 2, 3)$ is defined as:

$$\text{Resolution}_i = \frac{E_i^{true} - E_i^{recon}}{E_i^{true}} \tag{6.3}$$

where E_i^{true} is the energy of the jet at the parton level and E_i^{recon} is the energy of the jet at the detector level before or after rescaling. Notice the improved resolution. The jets were then ordered in decending energy order, $E_1 > E_2 > E_3$.

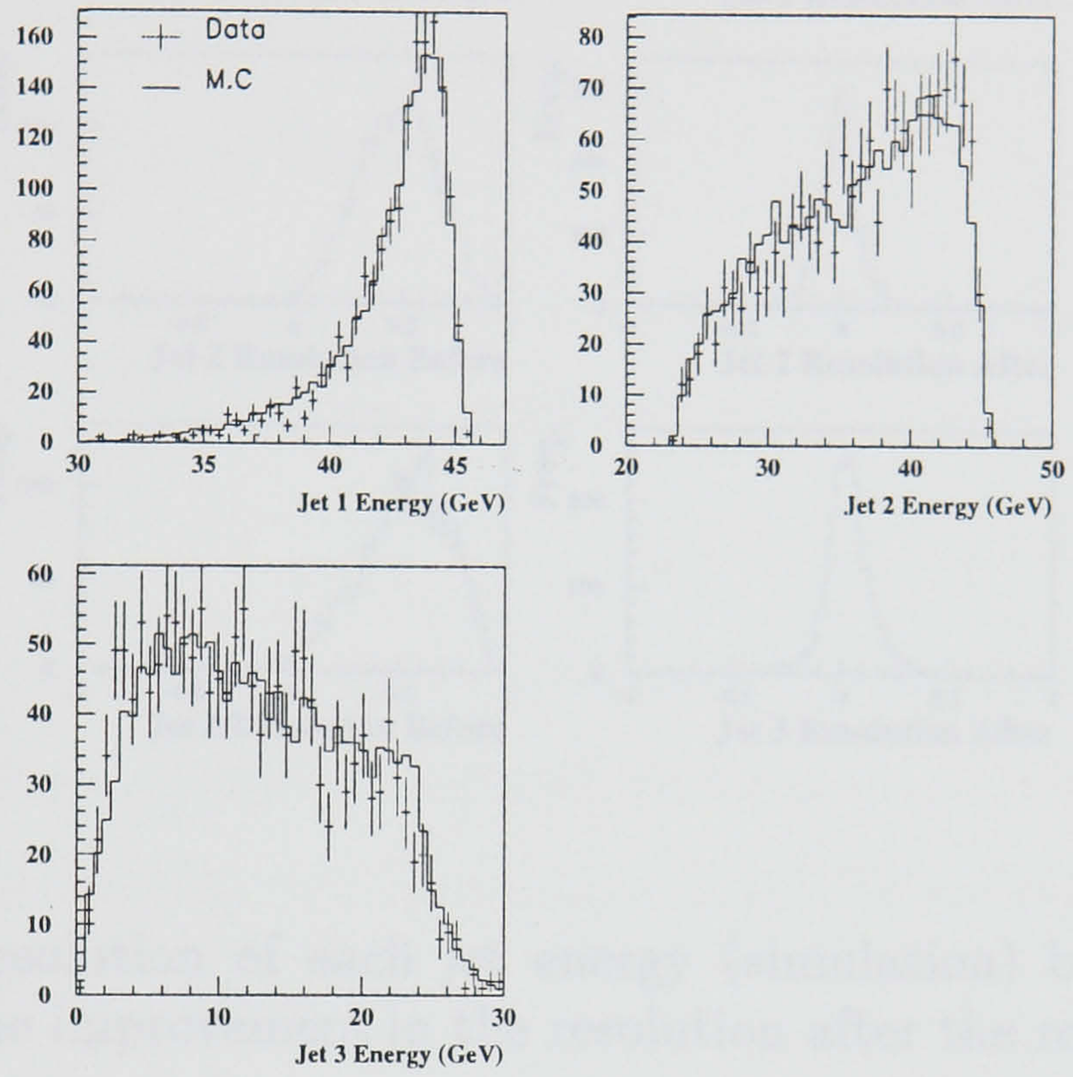

Figure 6.3: The energy of the jets after energy rescaling.

6.3 Flavour tagging

The differences in the lifetimes and the decay multiplicity among the different hadronic species were used to separate events containing different flavours of primary quarks. The tag should be efficient, and should provide maximal purity for the tagged sample. The method used was to look at the number of tracks in each event that miss the IP by a significant distance, as this efficiently separates high purity samples of b events from uds and c events.

6.3.1 Selection of 'Quality' Tracks

As the tag is based on the track multiplicity, it is imperative that the tracks used in the tag are well understood and well measured. To do this, further cuts were

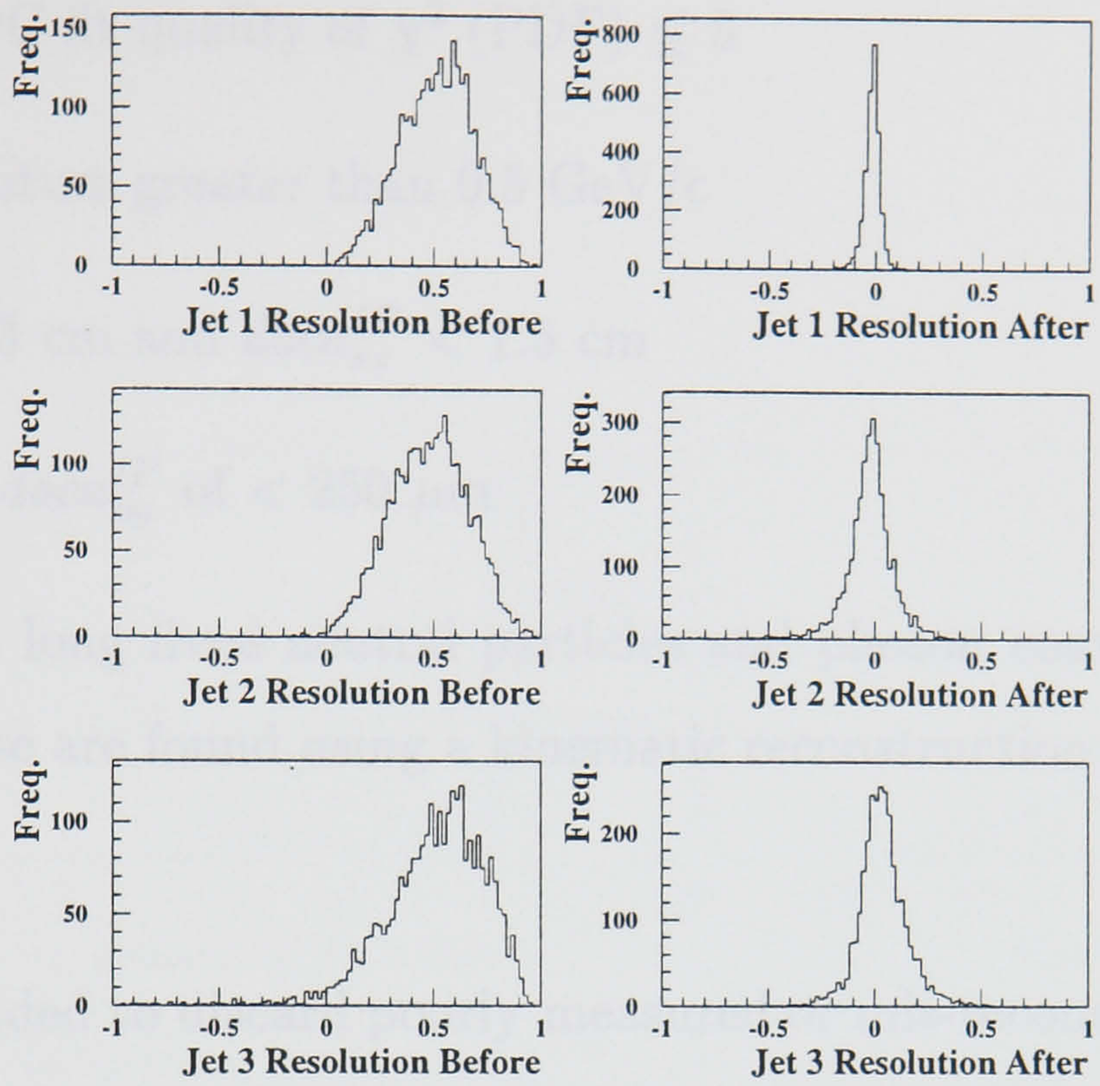

Figure 6.4: The resolution of each jet energy (simulation) before and after the rescaling. Notice the improvement in the resolution after the rescaling.

applied to the charged tracks used in the analysis so as to guarantee that they were well described by the MC. These cuts have the beneficial effect of removing some tracks from light events that carry lifetime information, such as those from K^0 and Λ decays, which can contribute to the light quark contamination in the b sample. The tracks considered as quality tracks must have:

- At least one VXD hit.
- At least 40 CDC hits. Tracks with few hits are likely segments of a kinked track, a track that curved back towards the beam-line before traversing the full radius of the CDC, a track from the decay of a long lived neutral particle or a track that had hits stolen by another track.
- The first CDC hit must have a radius less than 39 cm. As the extrapolation distance increases, the uncertainty on the track parameter increases and becomes more likely to mislink to VXD hits.

- a CDC fit quality of χ^2 (PDF) ≤ 5
- a VXD+CDC fit quality of χ^2 (PDF) ≤ 5
- total momentum greater than 0.5 GeV/c
- $doca_{xy}^{IP} < 0.3$ cm and $doca_{rz}^{IP} < 1.5$ cm
- an error on $doca_{xy}^{IP}$ of < 250 μm
- Tracks from long lived neutral particles and photon conversions (V^0) are rejected. These are found using a kinematic reconstruction of two-track vertices [87].

These cuts tended to discard poorly measured or mis-reconstructed tracks, since they tend to have larger extrapolation errors, fewer hits, and larger IP miss distances than properly reconstructed, well measured tracks. Figure 6.5 shows some of the quantities on which cuts were made.

6.3.2 The Interaction Point

An accurate knowledge of the interaction point is necessary as a reference location to distinguish them from secondary vertices in $b\bar{b}$ events. For a more detailed description of the methods used to determine the interaction point see reference [87]. Only a brief description will be given here.

The beam-beam overlap in the transverse coordinates x and y is much smaller ($\sigma \sim$ 2-3 μm in x and 0.5-1 μm in y) than along the beam direction ($\sigma_z \sim 700$ μm). For this reason, the IP position in x and y is determined from many hadronic events. Whereas, because of the spread of events along the beam direction, the longitudinal position is determined for each event individually.

Transverse Coordinate

The determination of the transverse coordinates of the interaction point uses hadronic events, with cross checks provided by the SLC beam position monitoring and from leptonic events.

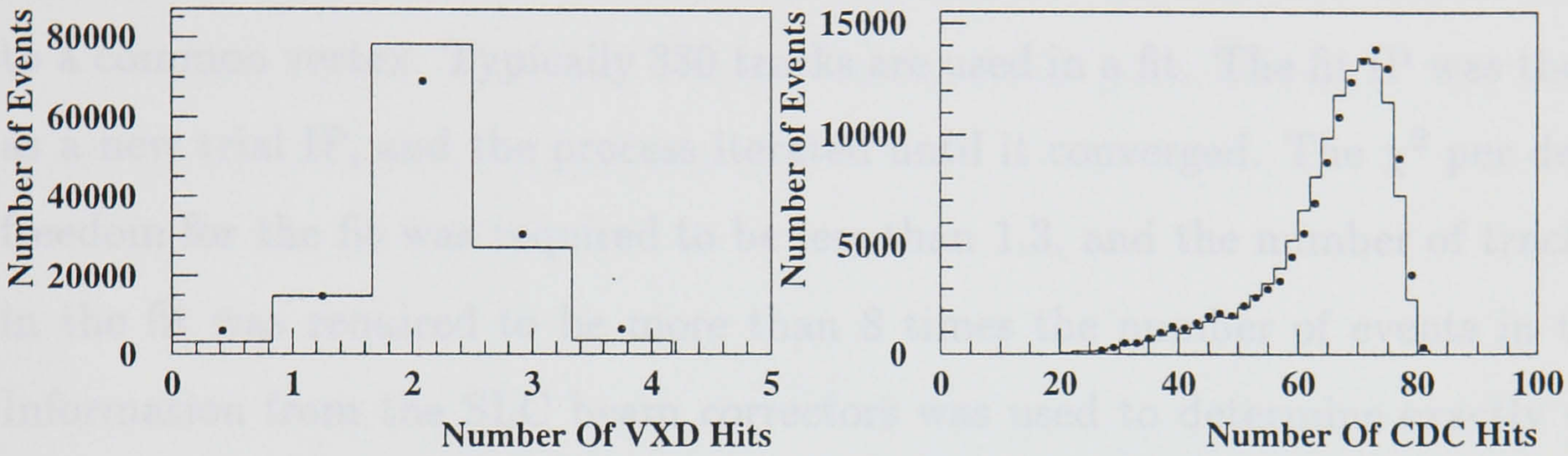

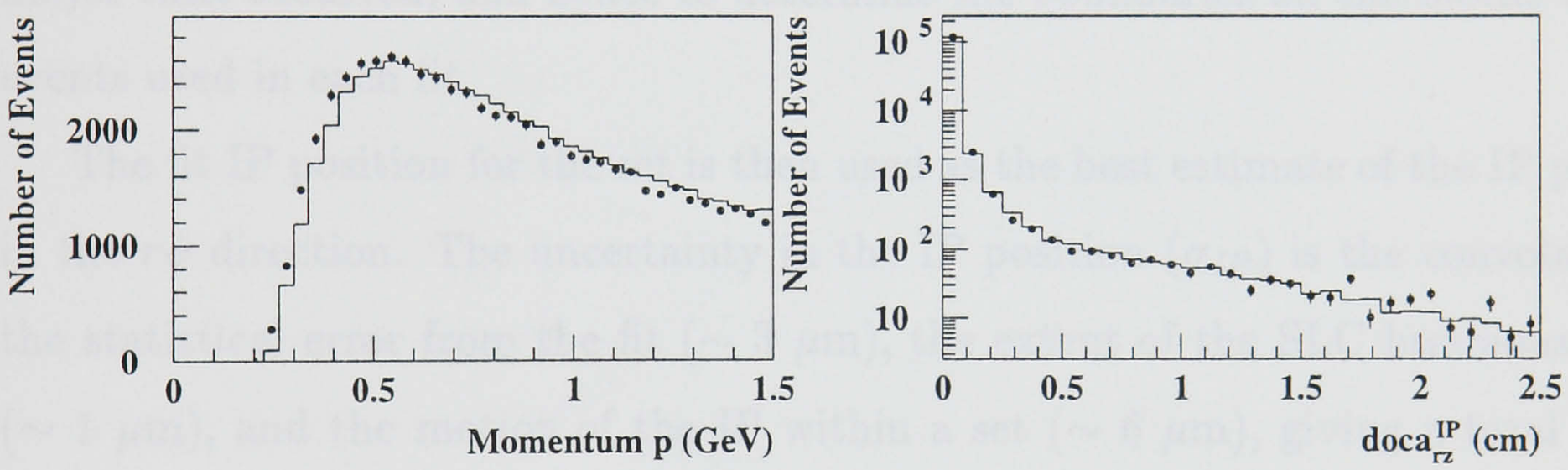

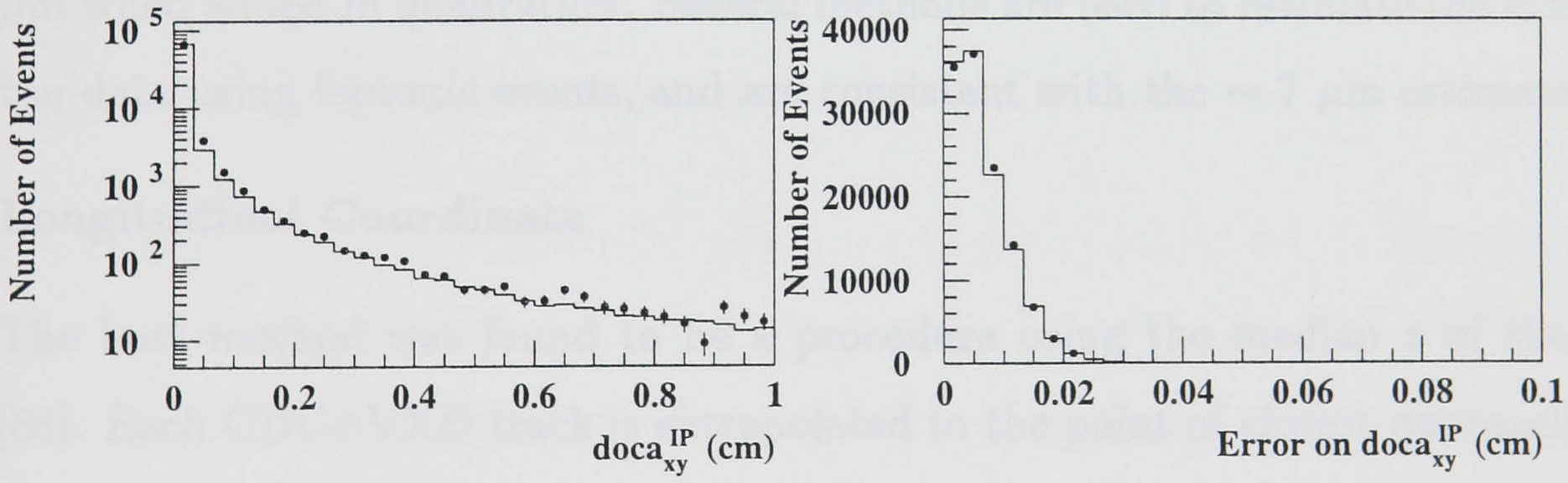

Figure 6.5: Distributions of some of the quantities upon which cuts are placed to select quality tracks, comparing data (points) and MC (histograms). To make each plot, all of the other cuts have been applied except for the ones being plotted.

Beam positions from the SLC feed-back systems suggest that the rϕ position of the luminous region is stable to within 6 μm over a period of many Z^0 events. So it is not necessary to measure the position event by event, which would have large errors along the direction of the event energy flow. Instead the tracks from $\sim$ 30 sequential hadronic events are used.

All tracks which have VXD hits and which come within 3σ of a trial IP are fitted to a common vertex. Typically 330 tracks are used in a fit. The fit IP was then used as a new trial IP, and the process iterated until it converged. The χ^2 per degree of freedom for the fit was required to be less than 1.3, and the number of tracks used in the fit was required to be more than 8 times the number of events in the set. Information from the SLC beam correctors was used to determine exactly when a major shift occurred, and hence to determine the boundaries on the blocks of $\sim$ 30 events used in each fit.

The fit IP position for the set is then used as the best estimate of the IP position in the $r\phi$ direction. The uncertainty in the IP position (σ_{IP}) is the convolution of the statistical error from the fit ($\sim$ 3 μm), the extent of the SLC luminous region ($\sim$ 1 μm), and the motion of the IP within a set ($\sim$ 6 μm), giving a total of $\sim$ 7 μm when added in quadrature. Several methods are used to estimate the error from the data using leptonic events, and are consistent with the $\sim$ 7 μm estimate [88].

Longitudinal Coordinate

The best method was found to be a procedure using the median z of the tracks [88]. Each CDC+VXD track is extrapolated to the point of closest approach to the measured primary vertex position in the plane transverse to the beam and the z coordinate of the track at that point is denoted z_{POCA}. Then the median of the z_{POCA} of those tracks which have an xy distance of closest approach with respect to the measured primary vertex postion less than 500 μm and less than 3σ of its uncertainty are taken as the longitudinal position of the primary vertex. If no CDC+VXD tracks pass these cuts then all the CDC+VXD tracks are used. The resolution is determined from the MC to be $\sim$ 38 μm.

6.3.3 The 2-D Normalised Impact Parameter

The impact parameter, d, is the distance of closest approach to the IP of a charged track. The error on this quantity is defined as σ_d. The basis of the tagging method, originally suggested by Hayes [89], is that tracks from heavy meson decays, mesons containing c and especially b quarks, tend not to extrapolate back to the IP. This is due to two factors, the long meson lifetimes and the significant $p_\perp$ acquired relative to the meson flight direction, a result of the large available energy in the heavy quark decay. Figure 6.6 illustrates this.

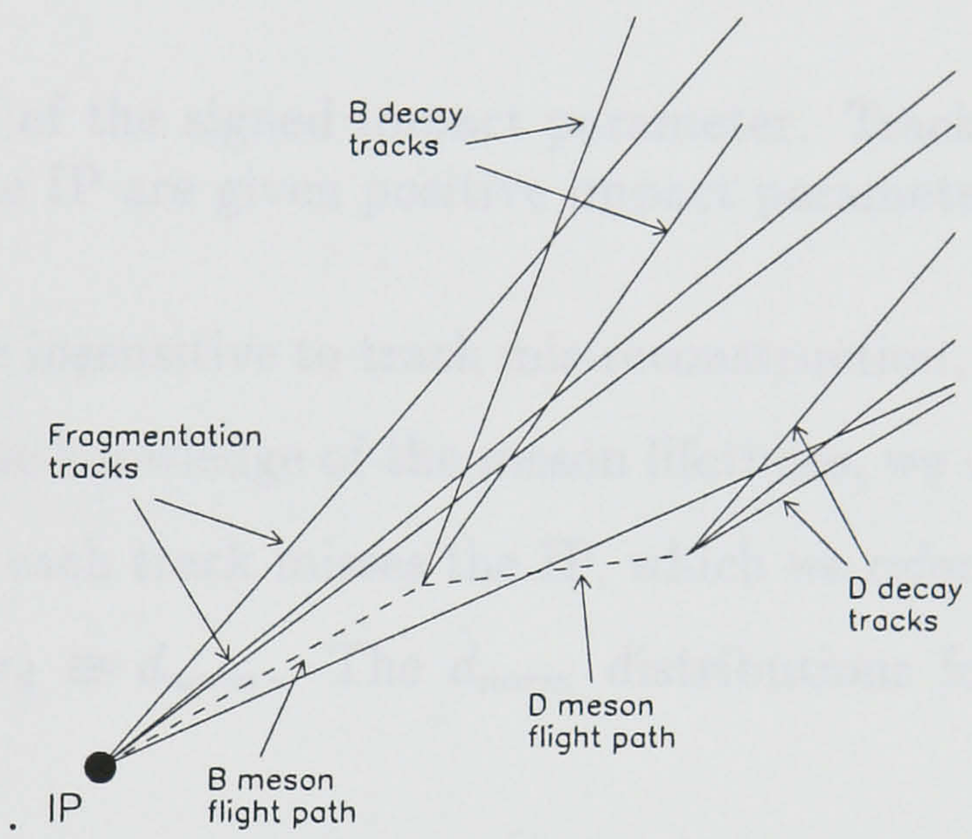

Figure 6.6: Schematic of a B meson decay cascade.

Because of the well known IP position and the excellent vertex detector at SLD (VXD2) we can measure the impact parameters of these tracks well enough to allow a sample of heavy quark events to be selected on the basis of the number of tracks that miss the IP by a certain impact parameter significance.

The Mark II collaboration introduced [90] an improvement to this method, by applying a signed impact parameter, where d is now positive if the track crosses the meson flight direction downstream of the IP, and negative if it crosses the meson flight direction upstream of the IP. The jet axis is used to define the meson flight direction, Figure 6.7. This creates an asymmetric distribution, since the tracks from heavy quarks tend to populate the region of large positive values of d.

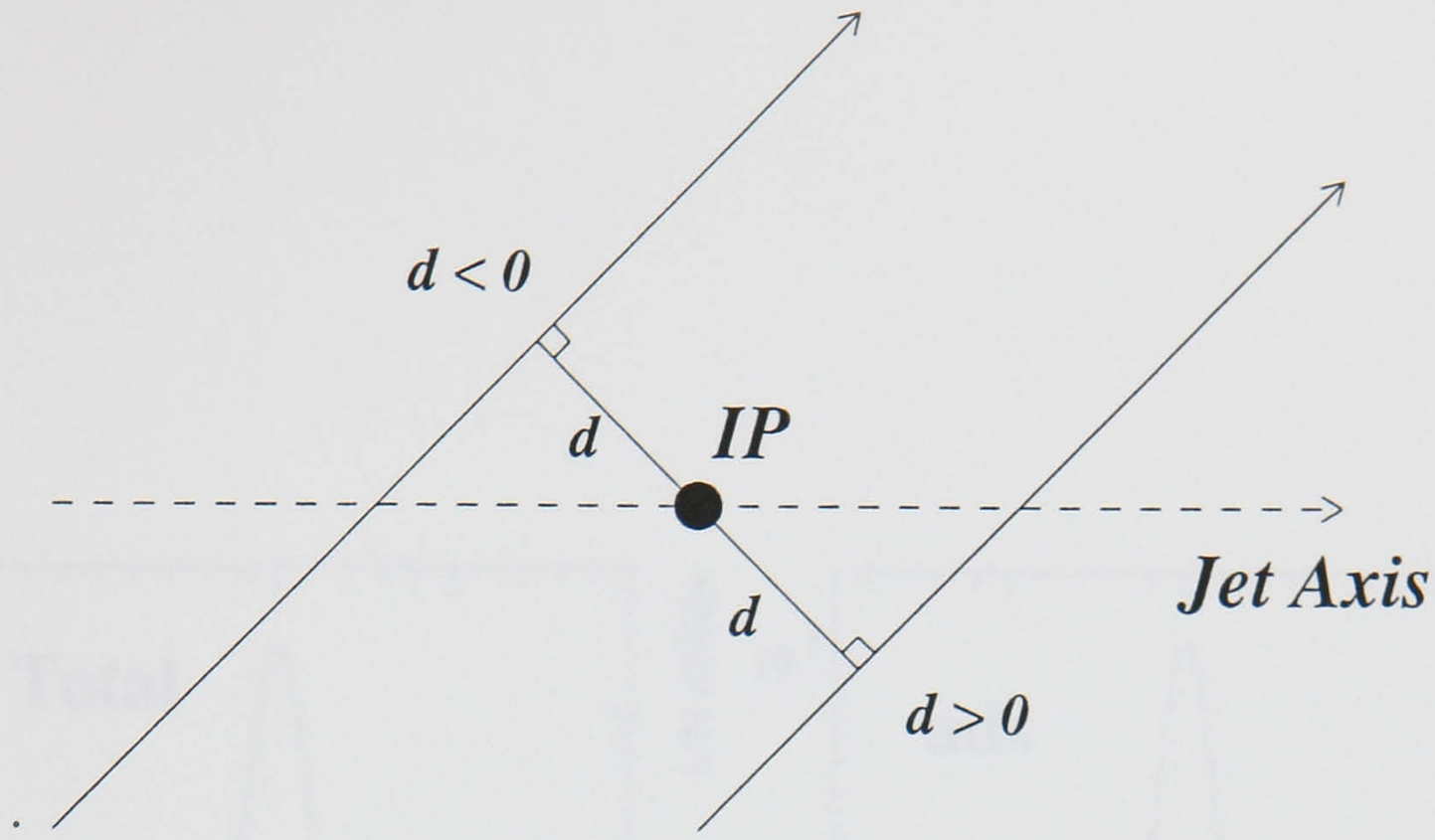

Figure 6.7: Definition of the signed impact parameter. Tracks which cross the jet axis downstream of the IP are given positive impact parameters.

Since we wish to be insensitive to track mis-reconstruction, the absolute distance scale, and our imprecise knowledge of the meson lifetimes, we use the significance of the distance by which each track misses the IP, which we refer to as the normalised impact parameter $d/\sigma_d \equiv d_{norm}$. The d_{norm} distributions for the simulation are shown in Figure 6.8

6.3.4 Definition of Event Flavour Tag

From the d_{norm} distributions one can clearly see that the b and c events have a larger fraction of the tracks that miss the IP by a few sigma with positive impact parameter, than do the uds events. This effect can be used to tag a pure sample of events that contain primary b quarks. The two parameters used in this tag are; the impact parameter significance and the number of tracks that have that significance in each event. Studies have shown that choosing a $d_{norm} \geq 3$ for the track significance effectively separates the events of different primary quark flavour with a good purity [44]. Figure 6.9 shows the distribution of the number of tracks in an event, N_{sig}^{evt}, that have a $d_{norm} \geq 3$, for all events.

The $N_{sig}^{evt} = 0$ bin comprises a very pure sample of uds events (where uds means events containing primary $u\overline{u}$, $d\overline{d}$, or $s\overline{s}$ quarks) while $N_{sig}^{evt} \geq 4$ comprises a pure

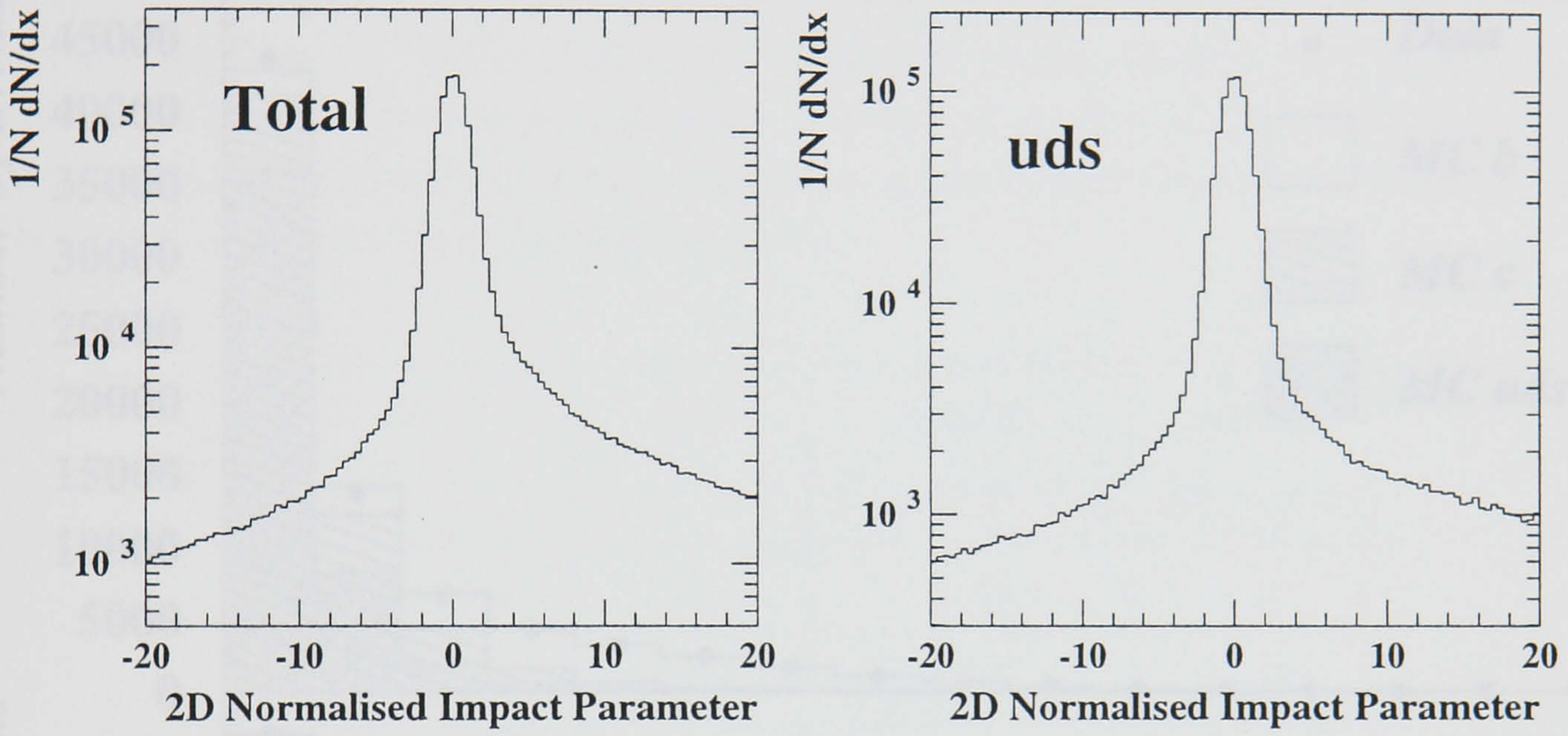

Figure 6.8: The normalised impact parameter distribution for all tracks in hadronic events, and all tracks in *uds*, *c* and *b* events. The long tails at high impact parameters are readily visible in *c* and *b* events. Determined from the simulation.

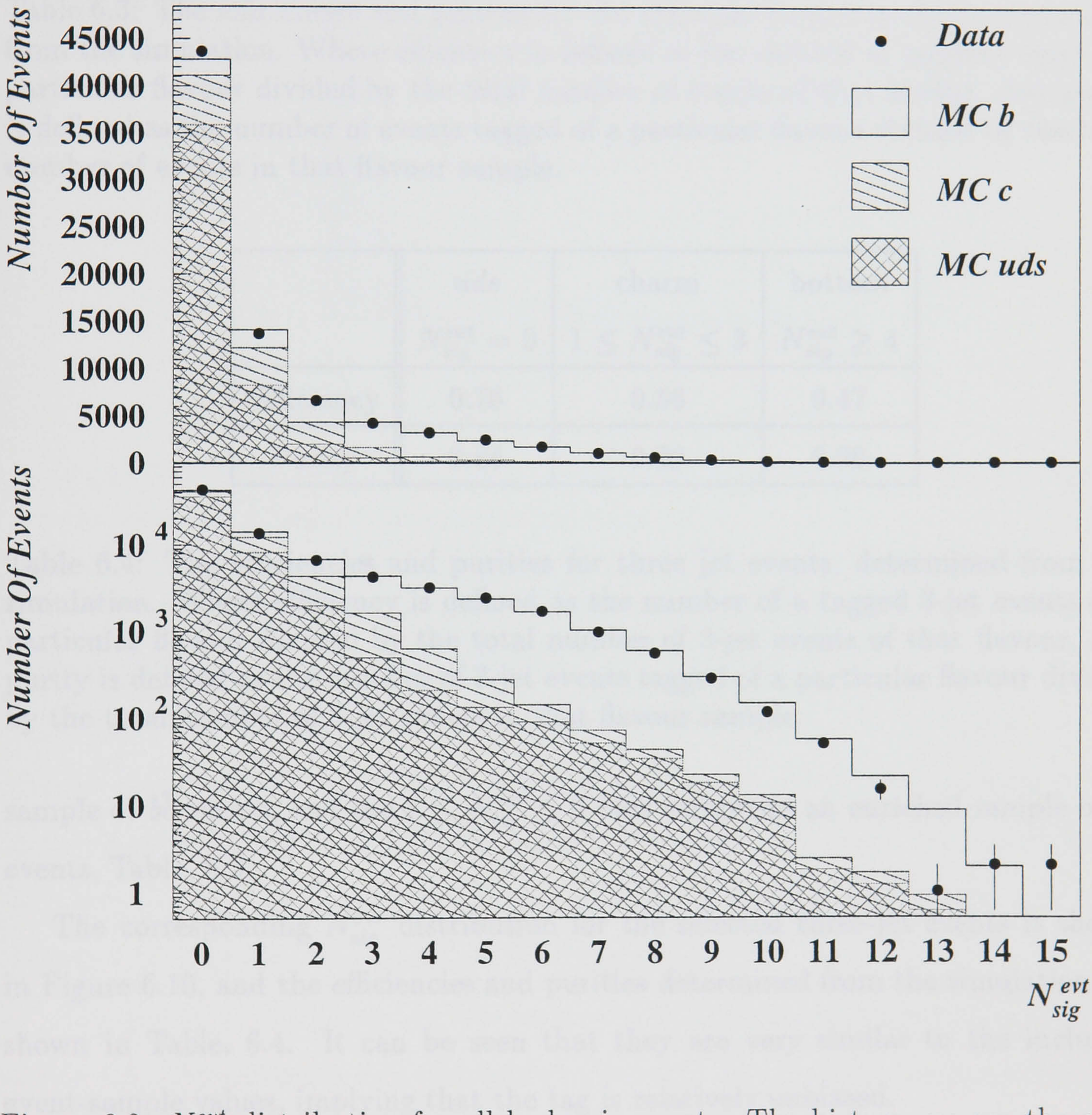

Figure 6.9: N_{sig}^{evt} distribution for all hadronic events. The histograms are the simulation and the points are the data. The lower plot is the same as the upper plot but with a log scale.

	uds $N_{sig}^{evt} = 0$	charm $1 \leq N_{sig}^{evt} \leq 3$	bottom $N_{sig}^{evt} \geq 4$
Efficiency	0.76	0.56	0.48
Purity	0.84	0.30	0.87

Table 6.3: The efficiencies and purities for the different flavour samples, determined from the simulation. Where efficiency is defined as the number of tagged events of a particular flavour divided by the total number of events of that flavour, and purity is defined as the number of events tagged of a particular flavour divided by the total number of events in that flavour sample.

	uds $N_{sig}^{evt} = 0$	charm $1 \leq N_{sig}^{evt} \leq 3$	bottom $N_{sig}^{evt} \geq 4$
Efficiency	0.76	0.56	0.47
Purity	0.84	0.29	0.90

Table 6.4: The efficiencies and purities for three jet events, determined from the simulation. Where efficiency is defined as the number of a tagged 3-jet events of a particular flavour divided by the total number of 3-jet events of that flavour, and purity is defined as the number of 3-jet events tagged of a particular flavour divided by the total number of 3-jet events in that flavour sample.

sample of $b\bar{b}$ events, and the $1 \leq N_{sig}^{evt} \leq 3$ bins comprises an enriched sample of $c\bar{c}$ events, Table. 6.3.

The corresponding N_{sig}^{evt} distribution for the selected three-jet events is shown in Figure 6.10, and the efficiencies and purities determined from the simulation are shown in Table. 6.4. It can be seen that they are very similar to the inclusive event-sample values, implying that the tag is relatively unbiased.

Hence a cut at $N_{sig}^{evt} \geq 4$ is made to select b events.

6.3.5 Definition of Jet Flavour Tag

In addition to selecting a pure sample of $b\bar{b}$ events, we need to tag the jets containing the b or $\bar{b}$. This is done by selecting events that have exactly two jets with an N_{sig}^{jet}

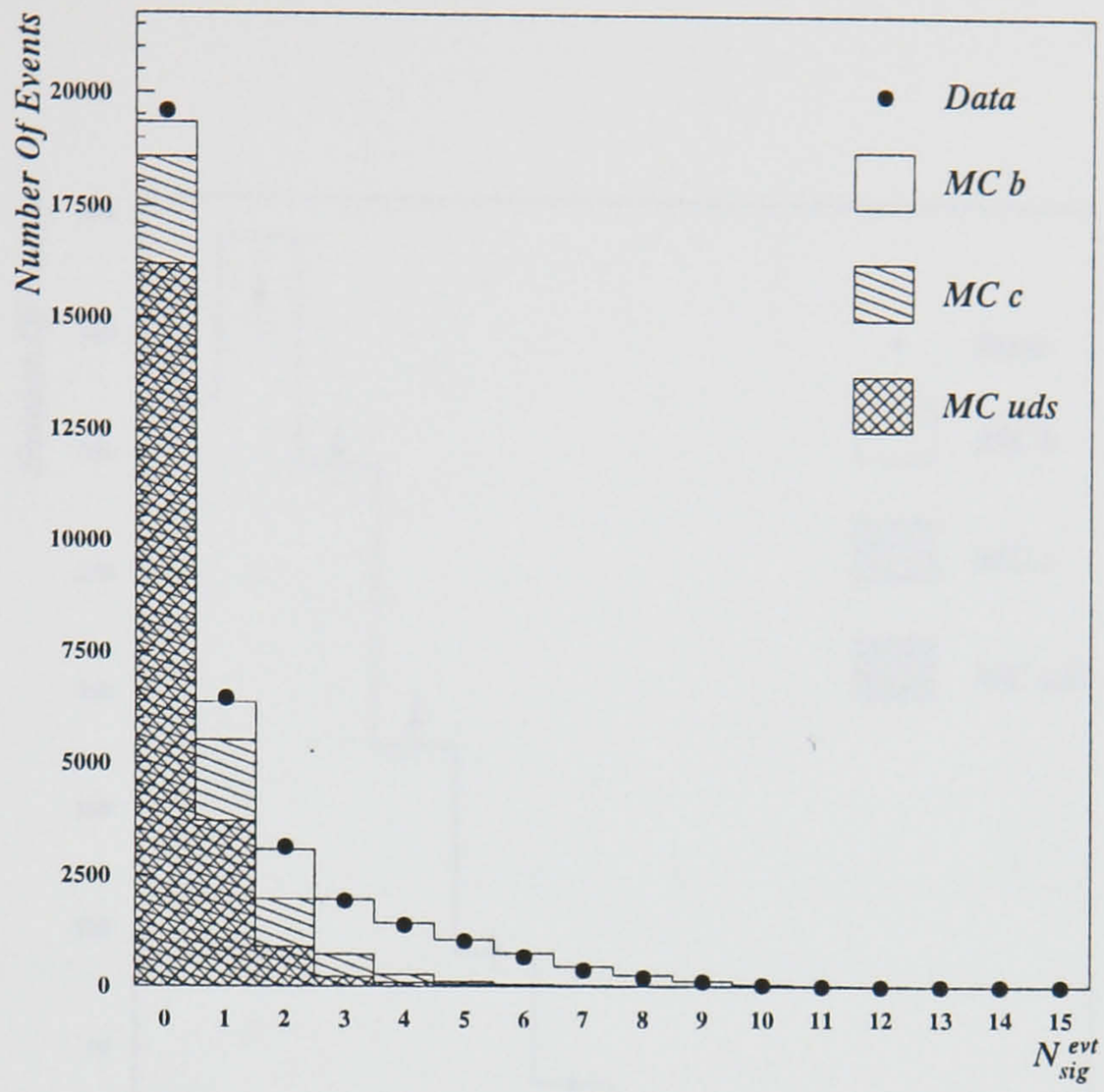

Figure 6.10: N_{sig}^{evt} distribution for selected three-jet hadronic events. The histograms are the simulation and the points are the data.

≥ 2. The N_{sig}^{evt} distribution for these events is shown in Figure 6.11. The number of tagged gluon-jets are shown in Table 6.5.

Figure 6.12 shows the N_{sig}^{jet} distributions separately for jets 1, 2 and 3 in the tagged event sample. The gluon-tagged jets, defined to be those jets with $N_{sig}^{jet} < 2$, are predominantly in the lowest energy jet sample, but there are a substantial number of gluon-jets in the two higher energy jet samples. It can be seen from Figure 6.12 that the M.C describes the data well.

The purity of the gluon tag was estimated from the simulation and is shown in Table 6.5. We estimate that the overall efficiency for correctly tagging a true $b\bar{b}g$ event is 8.25 % (See Section 6.5.4) and the overall purity of the tagged gluon-jet sample is 91 %.

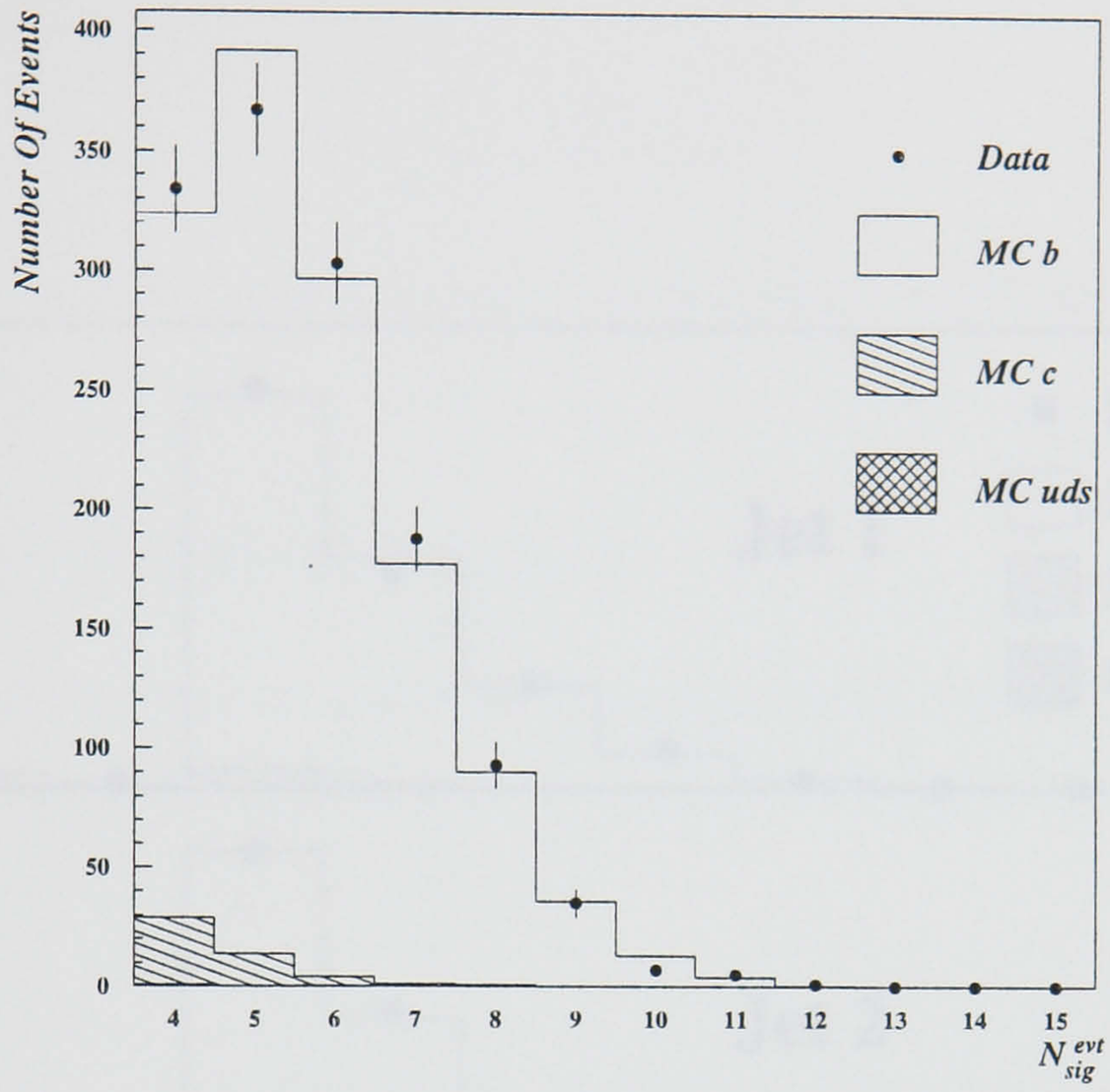

Figure 6.11: N_{sig}^{evt} distribution after the event selection cuts. The histograms are the simulation and the points are the data.

Jet Label	Number of Tagged Gluon-Jets	Purity
3	1155	94.6 %
2	155	83.7 %
1	34	51.8 %

Table 6.5: Estimated purities for tagged gluon-jet samples. The histograms are the simulation and the points are the data.

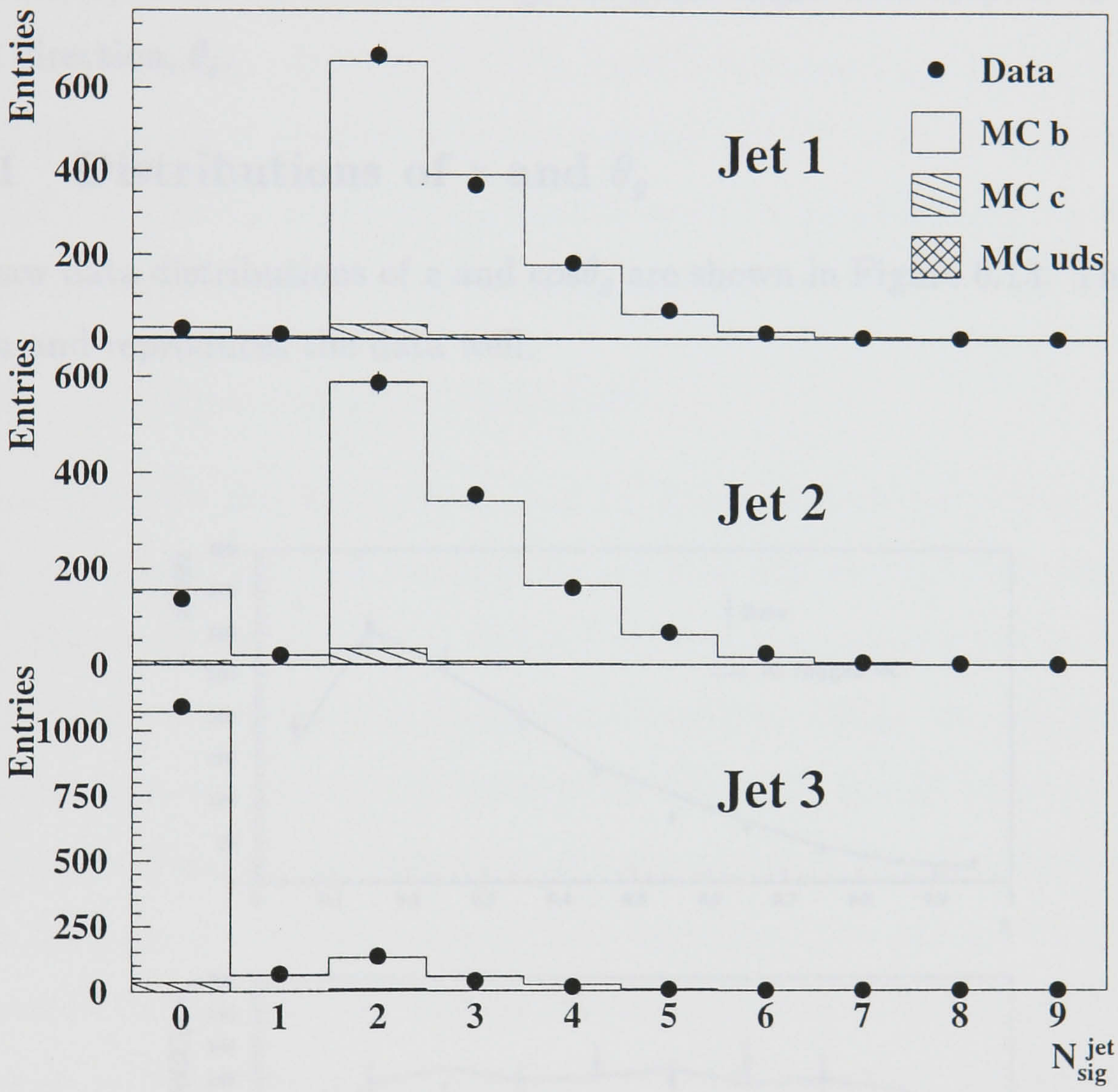

Figure 6.12: N_{sig}^{jet} distribution for the three jet sample. Where the key refers to the event flavour.

6.4 Gluon Jet Observables

We studied two observables in the tagged $b\bar{b}g$ events. The first is the distribution of scaled gluon energy z, where:

$$z = \frac{2E_{gluon}}{\sqrt{s}} \tag{6.4}$$

The second, is the distribution of gluon polar angle with respect to the electron beam direction, θ_g.

6.4.1 Distributions of z and θ_g

The raw data distributions of z and $\cos\theta_g$ are shown in Figure 6.13. The MC is also shown and reproduces the data well.

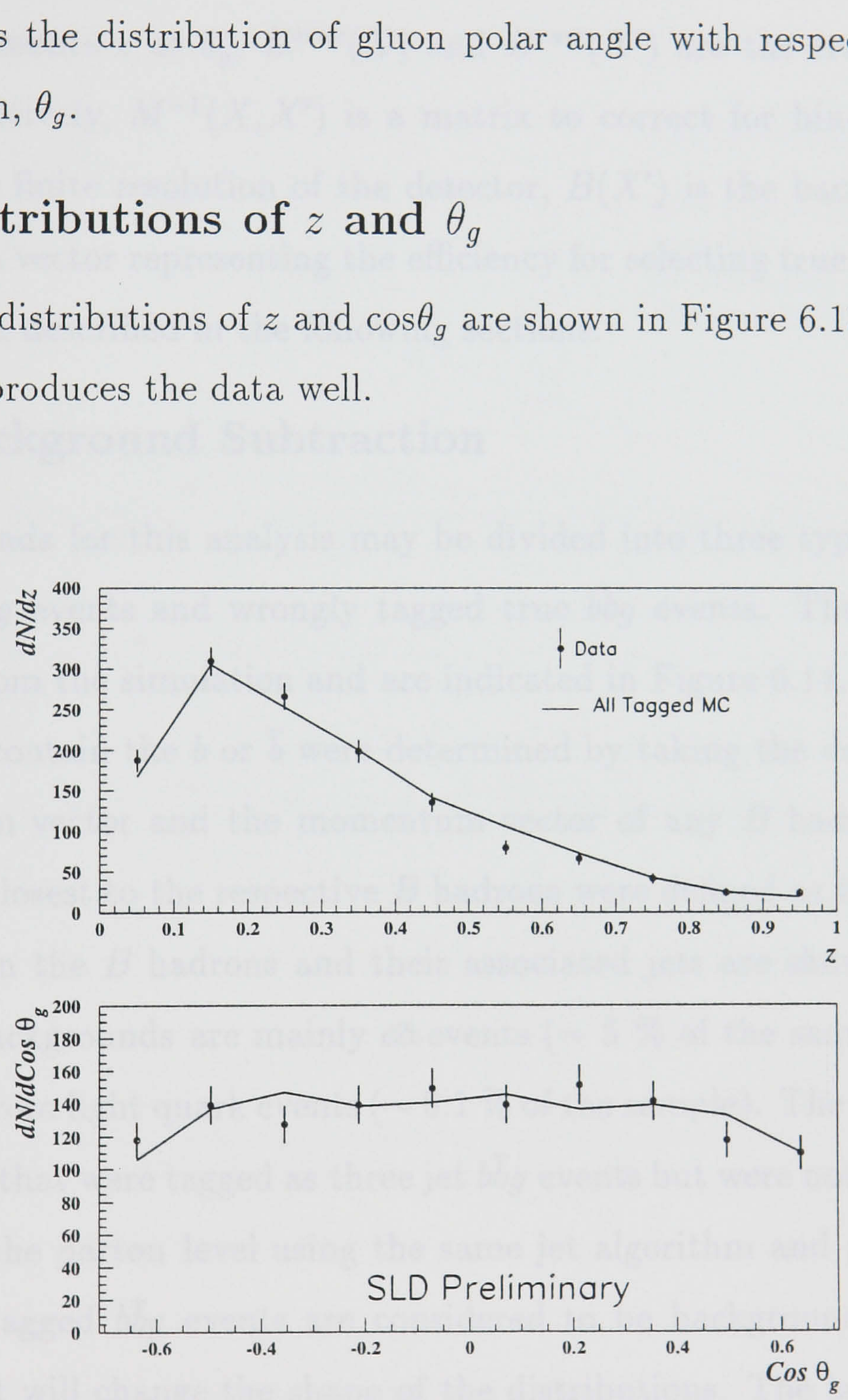

Figure 6.13: Comparision of raw data (points) and simulation (lines joining the bin centres.) for the two observables z and θ_g

6.5 Data Correction

In order to compare these distributions with QCD predictions it was necessary to correct the data, for non-$b\bar{b}g$ backgrounds, detector resolution effects and efficiency:

$$D^{true}(X) = \varepsilon^{-1}(X)M^{-1}(X,X')(D^{raw}(X') - B(X')) \tag{6.5}$$

where X represents z or θ_g, $D^{true}(X)$ and $D^{raw}(X')$ are the true and raw distributions respectively, $M^{-1}(X,X')$ is a matrix to correct for bin-to-bin migrations caused by the finite resolution of the detector, $B(X')$ is the background contribution and ε is a vector representing the efficiency for selecting true $b\bar{b}g$ events. These corrections are described in the following sections.

6.5.1 Background Subtraction

The backgrounds for this analysis may be divided into three types: non-$b\bar{b}$ events, $b\bar{b}$ but non-$b\bar{b}g$ events and wrongly tagged true $b\bar{b}g$ events. The backgrounds are determined from the simulation and are indicated in Figure 6.14. In the simulation the jets that contain the b or $\bar{b}$ were determined by taking the dot product of each jet momentum vector and the momentum vector of any B hadrons in the event. The two jets closest to the respective B hadrons were defined as the b or $\bar{b}$ jets. The angles between the B hadrons and their associated jets are shown in Figure 6.15. The non-$b\bar{b}$ backgrounds are mainly $c\bar{c}$ events ($\sim$ 5 % of the sample), with a small contribution from light quark events ($\sim$ 0.1 % of the sample). The non-$b\bar{b}g$ events are true $b\bar{b}$ events that were tagged as three jet $b\bar{b}g$ events but were not classified as three jet events at the parton level using the same jet algorithm and y_{cut} value. Finally the wrongly tagged $b\bar{b}g$ events are considered to be background as the gluon jet misassignment will change the shape of the distributions. The largest contribution to the background came from tagging true $b\bar{b}$ events as $b\bar{b}g$ events. These three types of background were then subtracted from the raw data, bin-by-bin. The background subtracted distributions are shown in Figure 6.16.

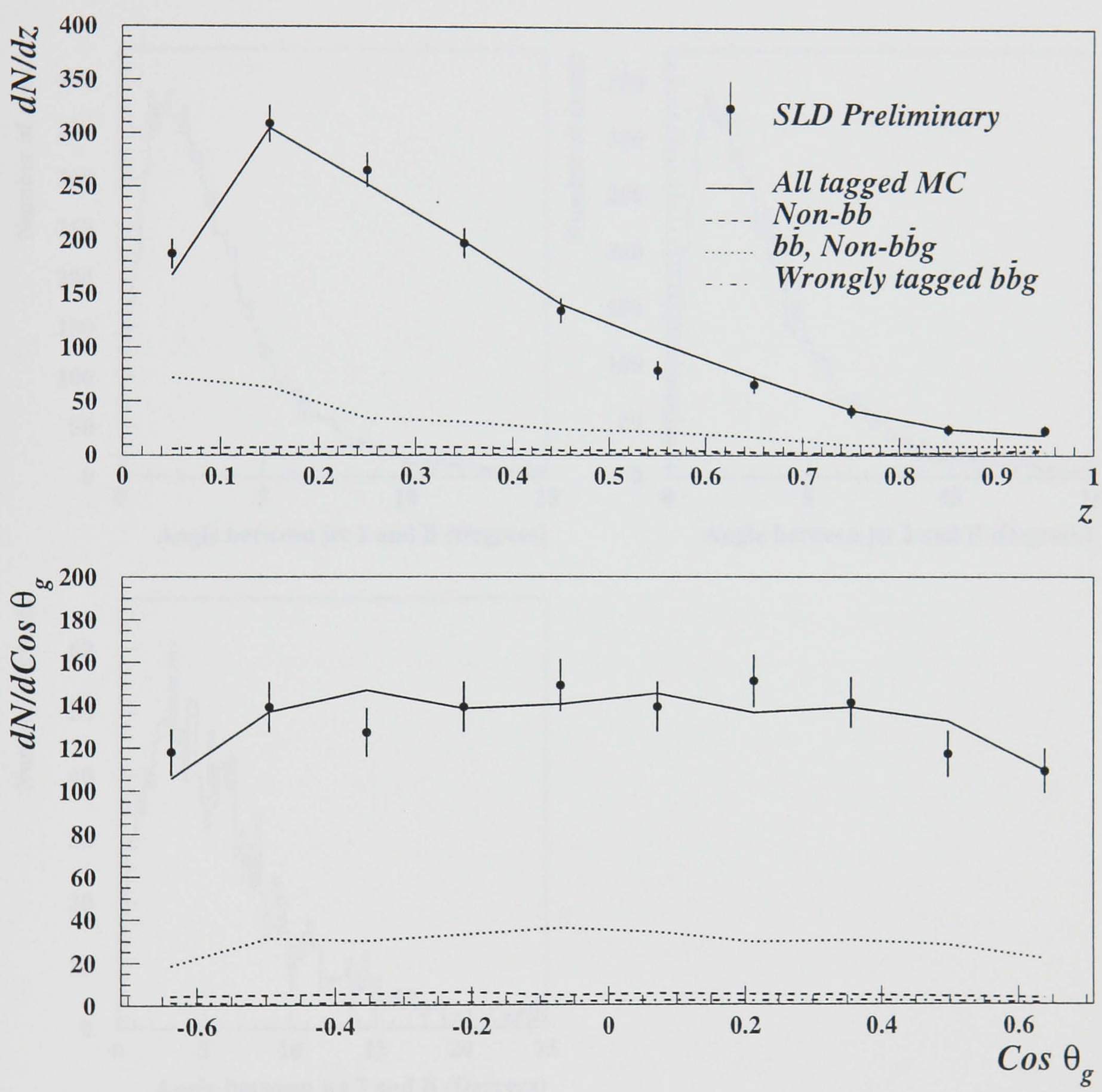

Figure 6.14: The raw (points) distributions and backgrounds (lines jointing bin centres), determined from the simulation.

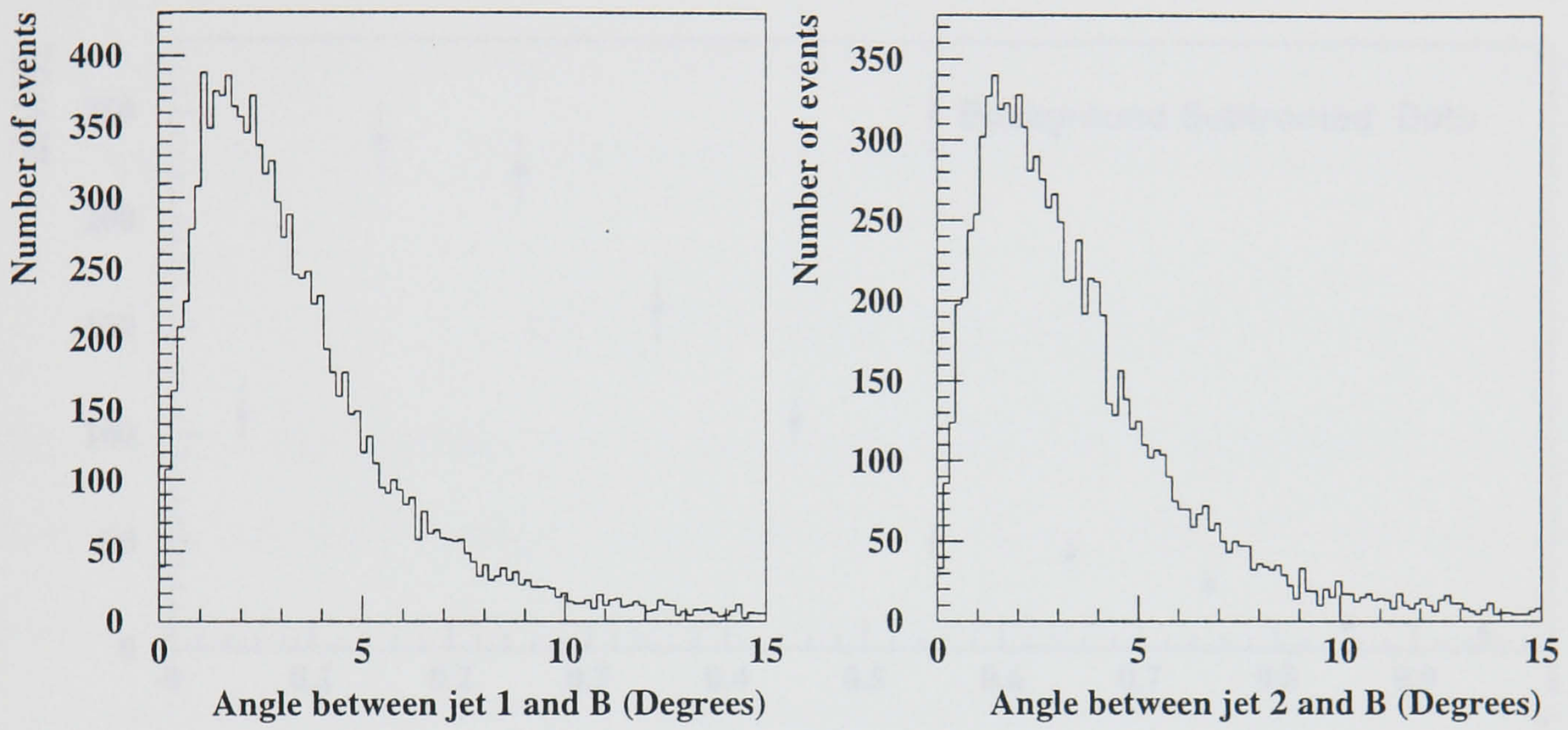

Figure 6.15: Angles between the B hadrons and their associated jets, using the simulation.

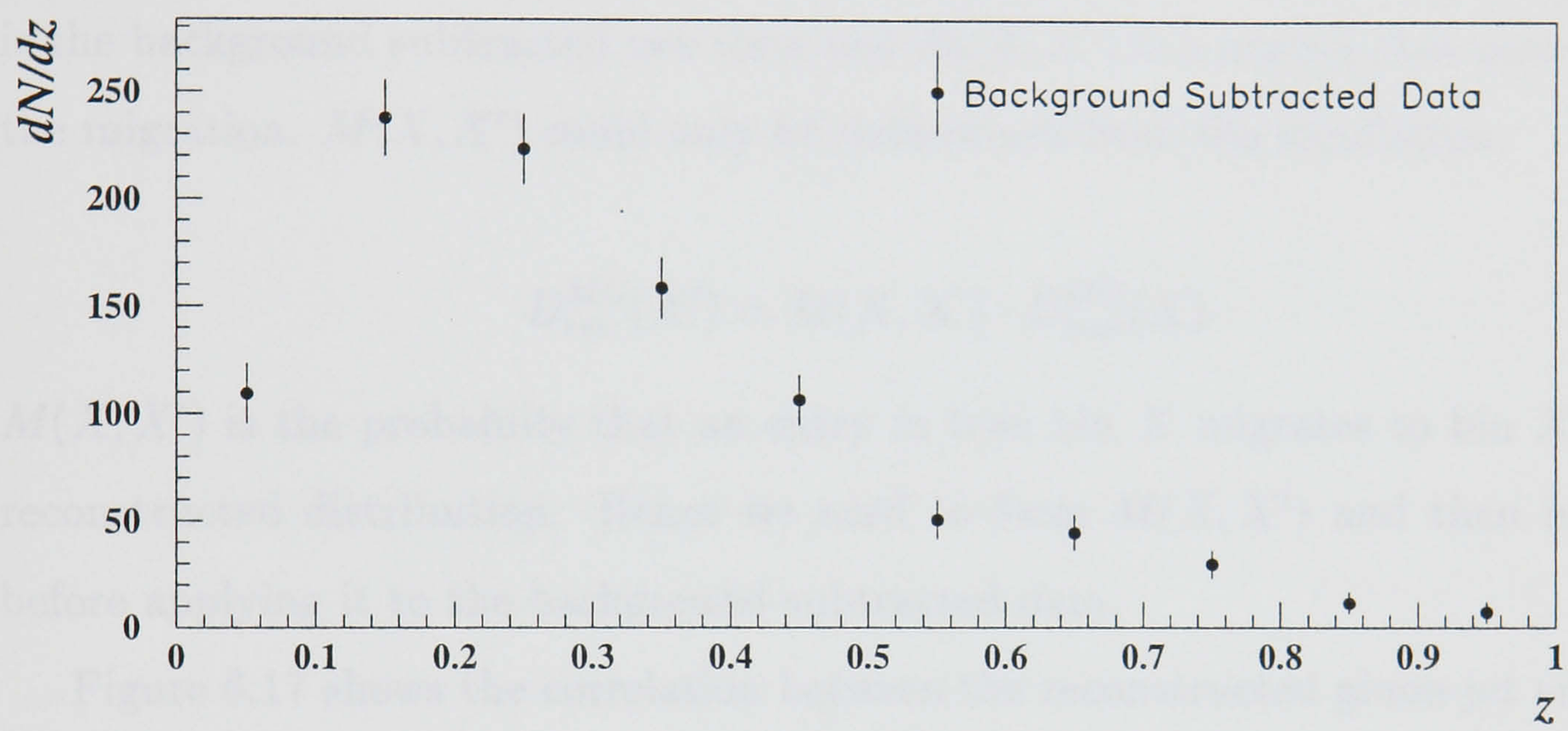

Figure 6.16: The z and θ_g distributions after the background subtraction.

6.5.2 Unfolding Procedures

It was necessary to correct the distributions for the effect of the migration from bins of true gluon energy/polar angle into bins of reconstructed energy/polar angle:

$$D_{rec}^{data}(X') = M(X, X') \cdot D_{true}^{data}(X) \tag{6.6}$$

Where $D_{true}^{data}(X')$ is the true data distribution, determined at parton level, $D_{rec}^{data}(X)$ is the background subtracted raw data and $M(X, X')$ is a matrix that accounts for the migration. $M(X, X')$ could only be determined from the simulation:

$$D_{rec}^{MC}(X') = M(X, X') \cdot D_{true}^{MC}(X) \tag{6.7}$$

$M(X, X')$ is the probablity that an entry in true bin X migrates to bin X' of the reconstructed distribution. Hence we need to form $M(X, X')$ and then invert it, before applying it to the background subtracted data.

Figure 6.17 shows the correlation between the reconstructed gluon-jet energy as measured in the detector and the true gluon-jet energy determined at the parton level, and it also shows the correlations for the gluon jet polar angle. These correlations form the $M(X, X')$ matrices. The matrices were then normalised by the columns to conserve the number of events:

$$normalised_{ij} = \frac{M(X, X')_{i,j}}{\sum_{i=i,j=1,10} M(X, X'_{i,j})} \tag{6.8}$$

where $m_{i,j}$ is the value of the un-normalised matrix element in the i^{th} column and j^{th} row. Figure 6.18 shows the inverted matrices.

Notice that there are negative values in the matrices. These matrices are then applied to the data. The result is shown in Figure 6.19.

It appears that this correction method does not work, as it causes oscillations in the distributions. This is caused by low simulation statistics ($\frac{1}{4}$ million events), and is not a surprising result [91]. Hence given the limited MC size this method cannot be used to correct for the bin-by-bin migrations.

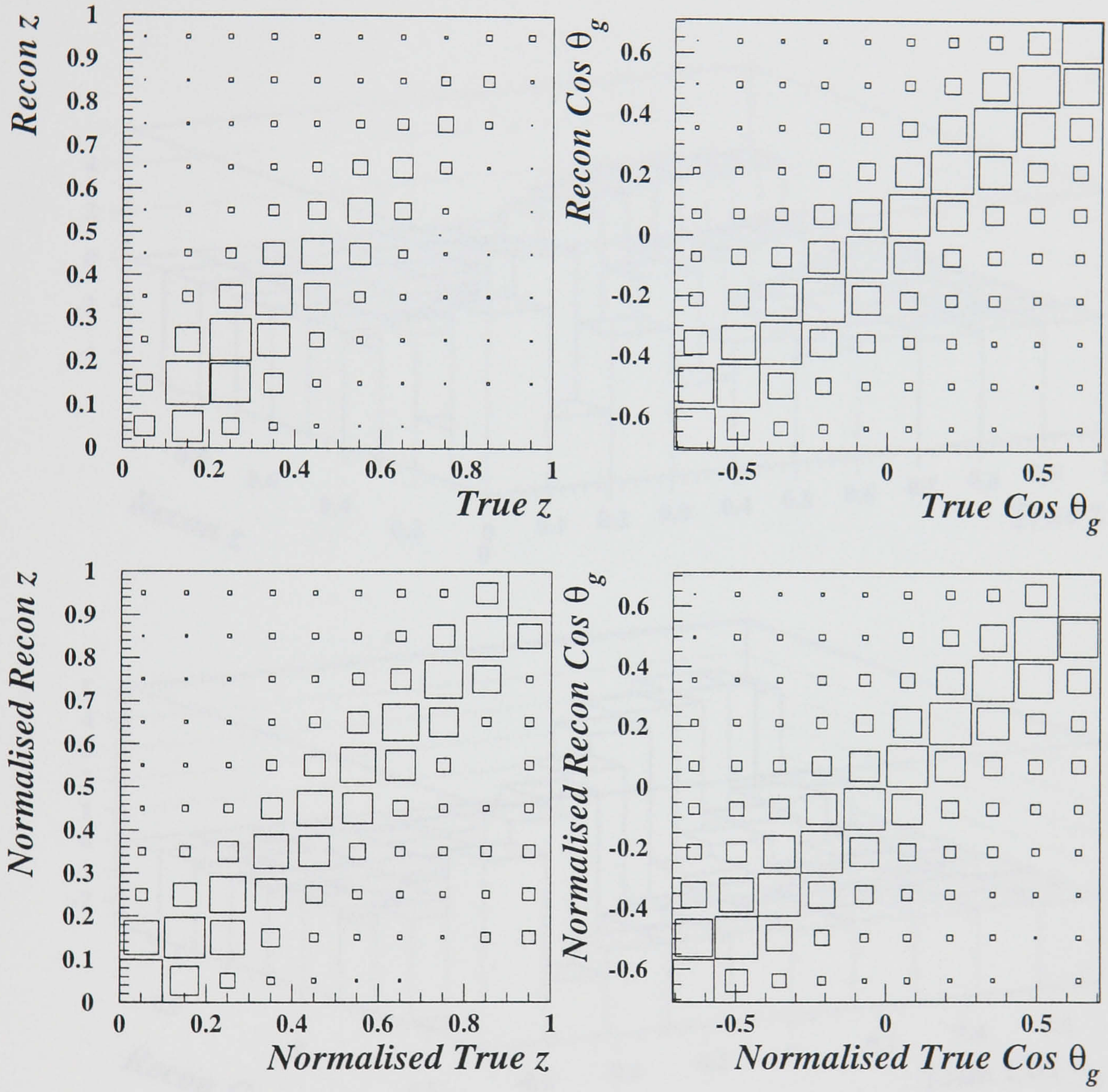

Figure 6.17: The bin migration matrices for the scaled gluon energy and polar angle distributions. The upper plots show the raw values. The lower plot shows the same data after normalisation by the columns. The size of the squares indicate the number of events in that bin. The bigger the square the larger the number of events.

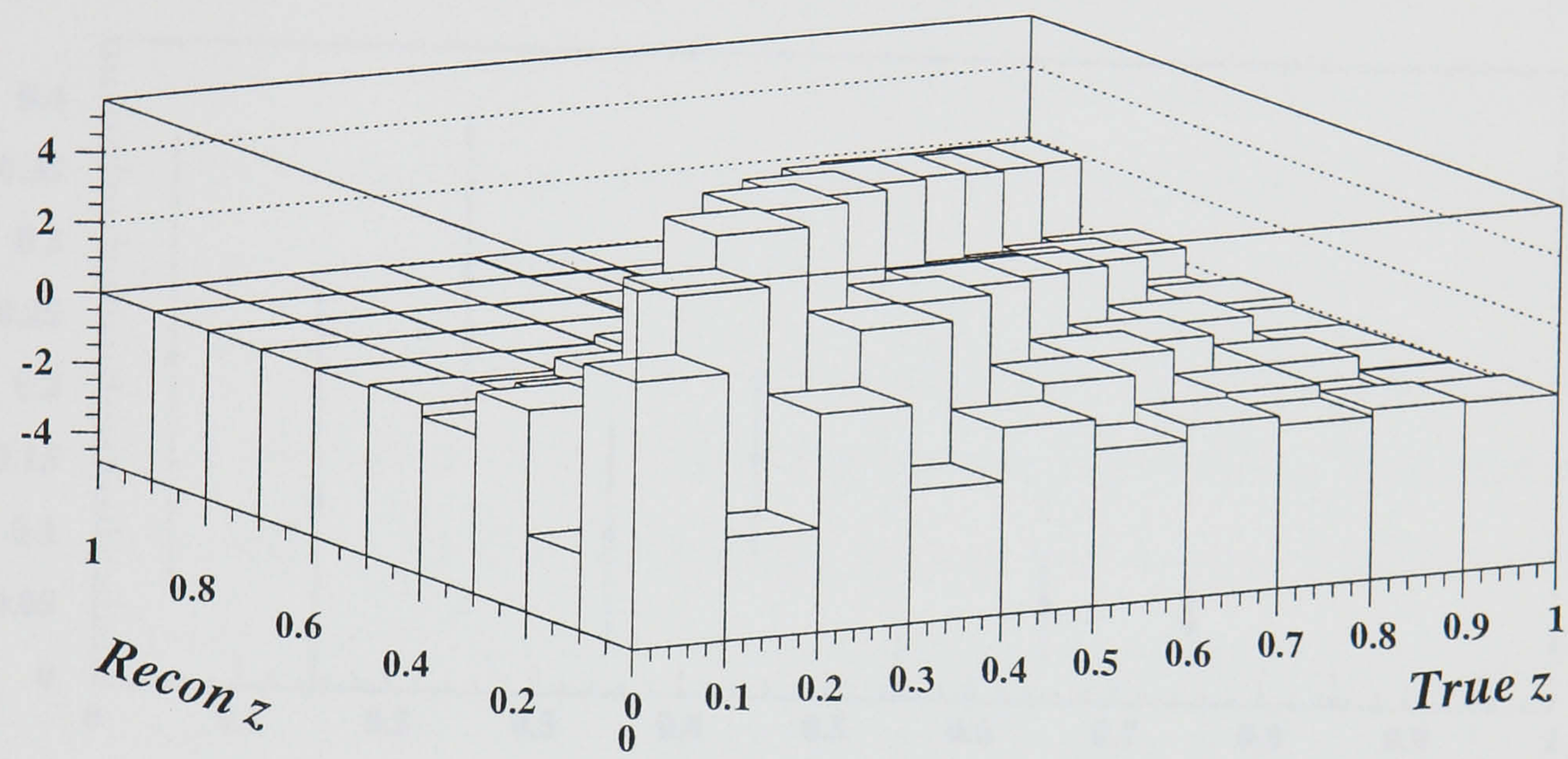

Figure 6.18: The inverted matrices. The vertical column is the number of entries in the bin, hence the matrix element.

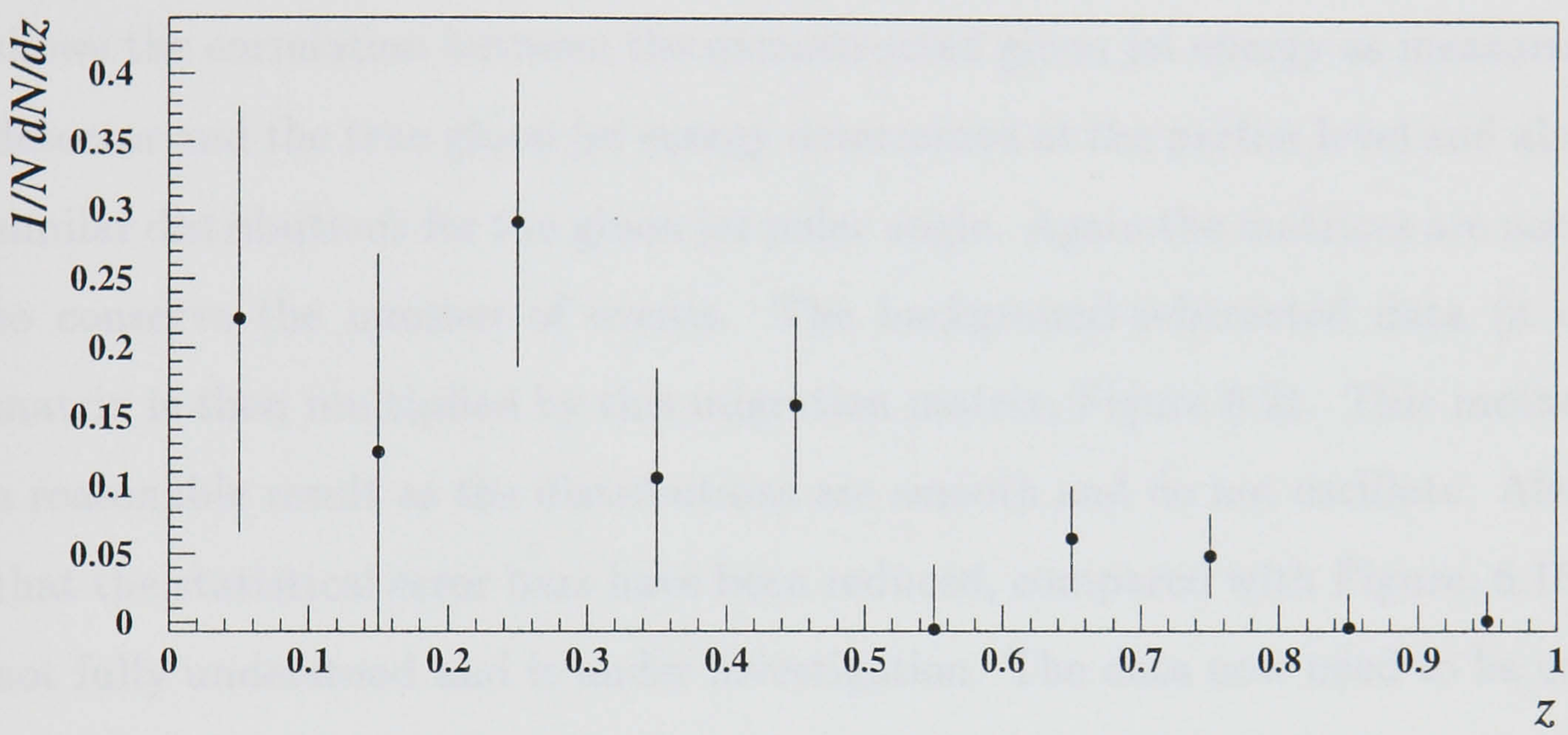

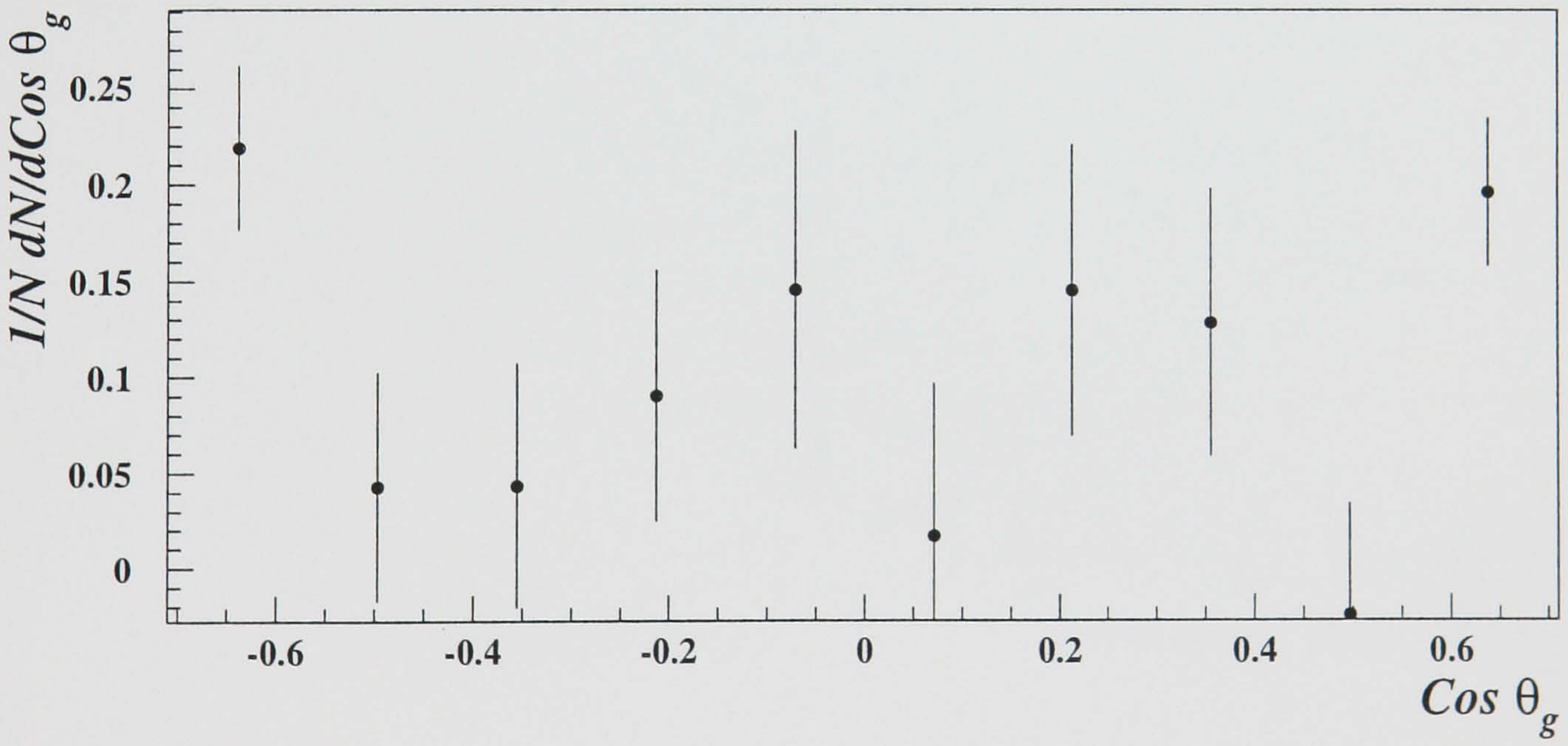

Figure 6.19: Distributions after background subtraction and matrix unfolding.

6.5.3 An Alternative Matrix Unfolding Method

This method is similar to the previous one, but the matrix $M^{'}(X, X')$ is defined as:

$$D^{MC}_{true} = M^{'}(X, X') \cdot D^{MC}_{rec} \tag{6.9}$$

where $M'(X, X')$ is now the probability that an entry in bin X' reconstructed, comes from bin X true. In this method no matrix inversion is necessary. Figure 6.20 shows the correlation between the reconstructed gluon jet energy as measured in the detector and the true gluon jet energy determined at the parton level and also shows similar distributions for the gluon jet polar angle. Again the matrices are normalised to conserve the number of events. The background-subtracted data (a column) matrix is then multiplied by this migration matrix, Figure 6.21. This method gives a reasonable result as the distributions are smooth and do not oscillate. Also notice that the statistical error bars have been reduced, compared with Figure. 6.16, this is not fully understood and is under investigation. The data now need to be corrected for efficiency.

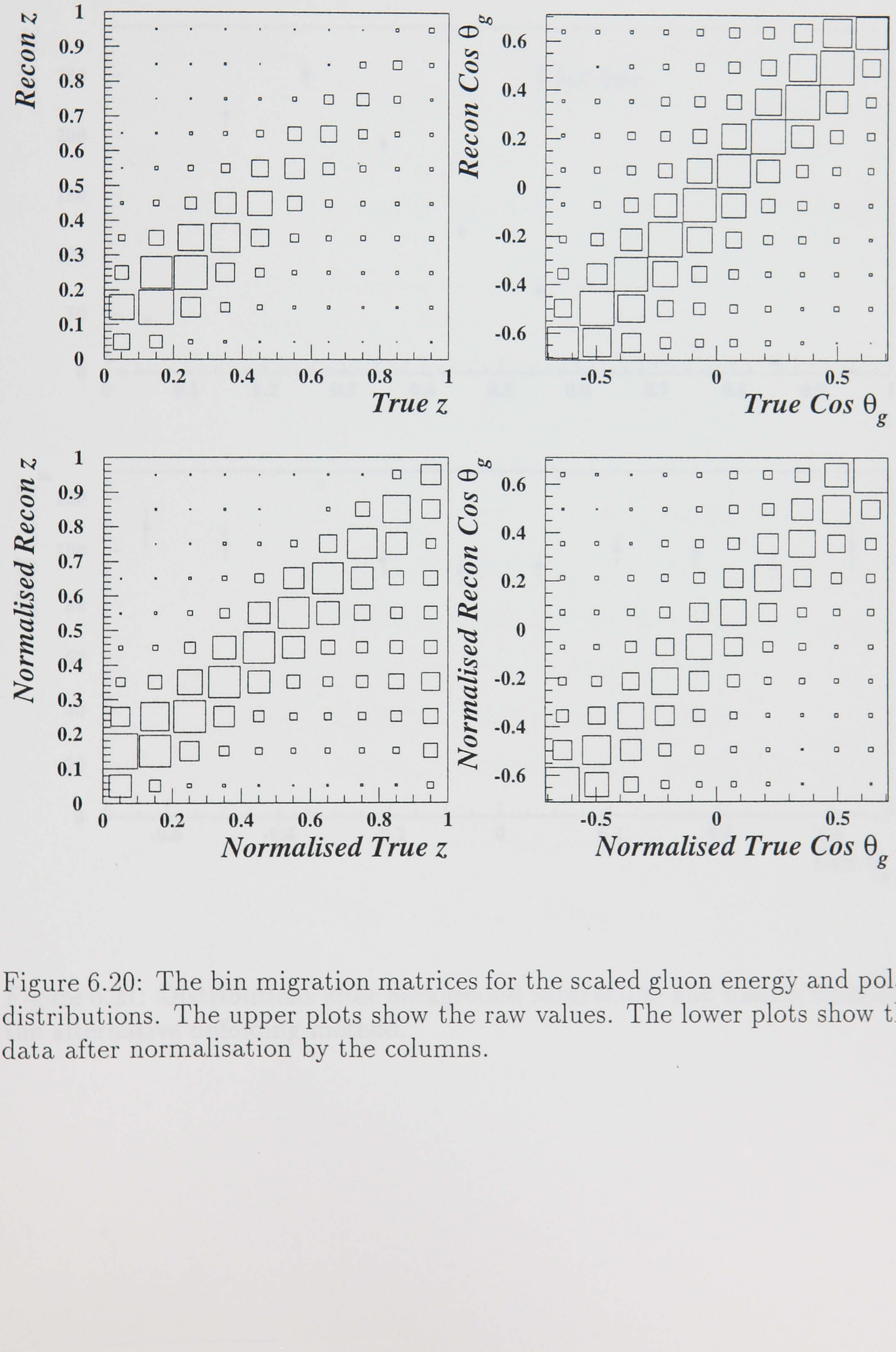

Figure 6.20: The bin migration matrices for the scaled gluon energy and polar angle distributions. The upper plots show the raw values. The lower plots show the same data after normalisation by the columns.

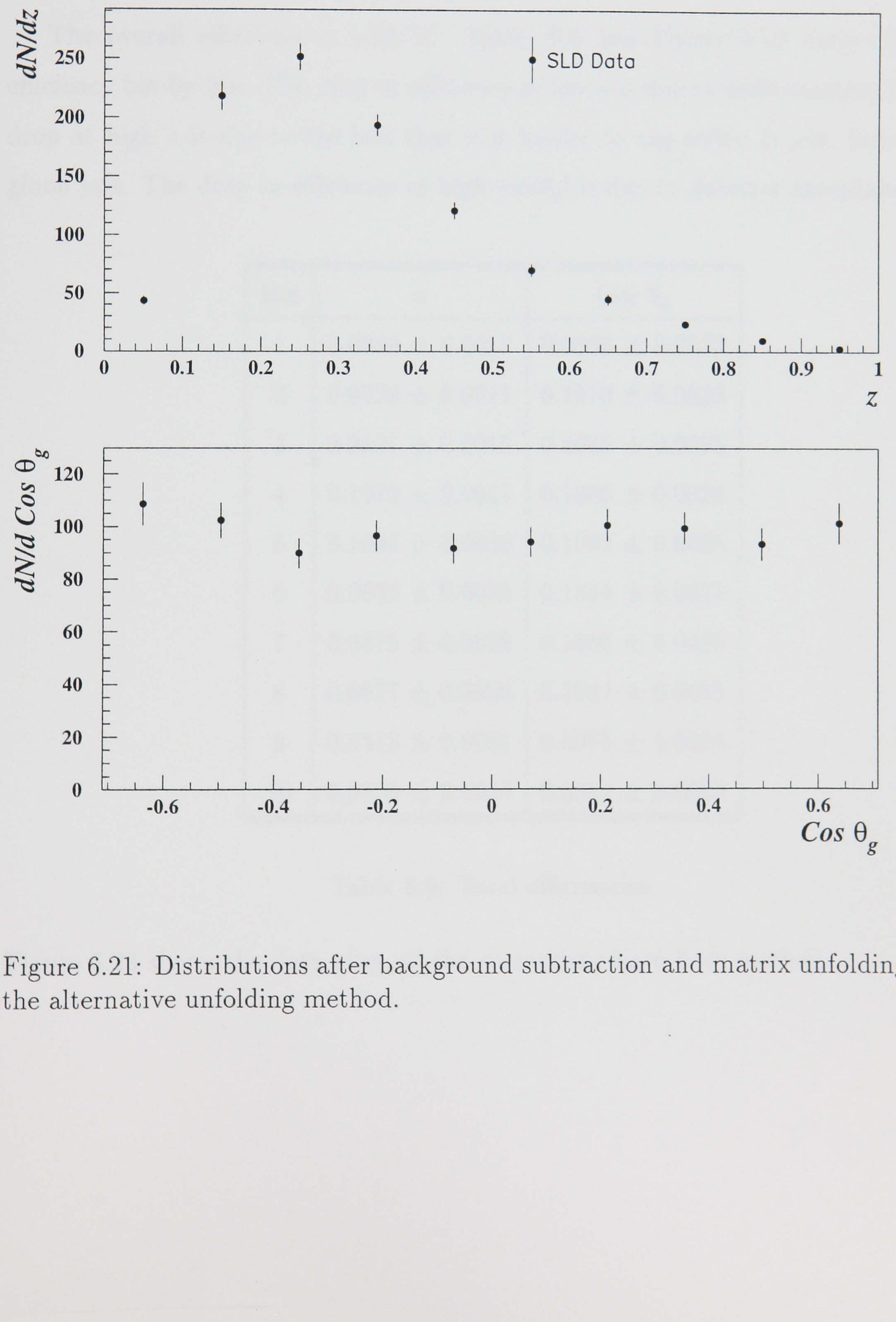

Figure 6.21: Distributions after background subtraction and matrix unfolding using the alternative unfolding method.

6.5.4 Efficiency Correction

A bin-by-bin efficiency correction was applied to the background-subtracted unfolded distributions. The efficiency correction for each bin was defined as, the probability of a true $b\bar{b}g$ event in bin X at the parton-level being tagged. This correction accounts for many effects, such as hadronisation, detector acceptance and tagging and, was determined from the simulation.

The overall efficiency is 8.25 %. Table. 6.6 and Figure 6.22 show the total efficiency bin-by-bin. The drop in efficiency at low z is due to hadronisation and the drop at high z is due to the fact that it is harder to tag softer B jets, hence hard gluon jets. The drop in efficiency at high $|\cos\theta_g|$ is due to detector acceptance.

Bin	z	Cos θ_g
1	0.0349 $\pm$ 0.0012	0.0888 $\pm$ 0.0023
2	0.0729 $\pm$ 0.0011	0.1010 $\pm$ 0.0025
3	0.0101 $\pm$ 0.0015	0.0986 $\pm$ 0.0025
4	0.1075 $\pm$ 0.0017	0.1086 $\pm$ 0.0026
5	0.1007 $\pm$ 0.0020	0.1032 $\pm$ 0.0025
6	0.0958 $\pm$ 0.0023	0.1044 $\pm$ 0.0025
7	0.0875 $\pm$ 0.0026	0.1060 $\pm$ 0.0026
8	0.0677 $\pm$ 0.0028	0.1057 $\pm$ 0.0025
9	0.0513 $\pm$ 0.0031	0.0978 $\pm$ 0.0024
10	0.0410 $\pm$ 0.0047	0.0914 $\pm$ 0.0023

Table 6.6: Total efficiencies.

Figure 6.23 shows the data after all the corrections have been applied.

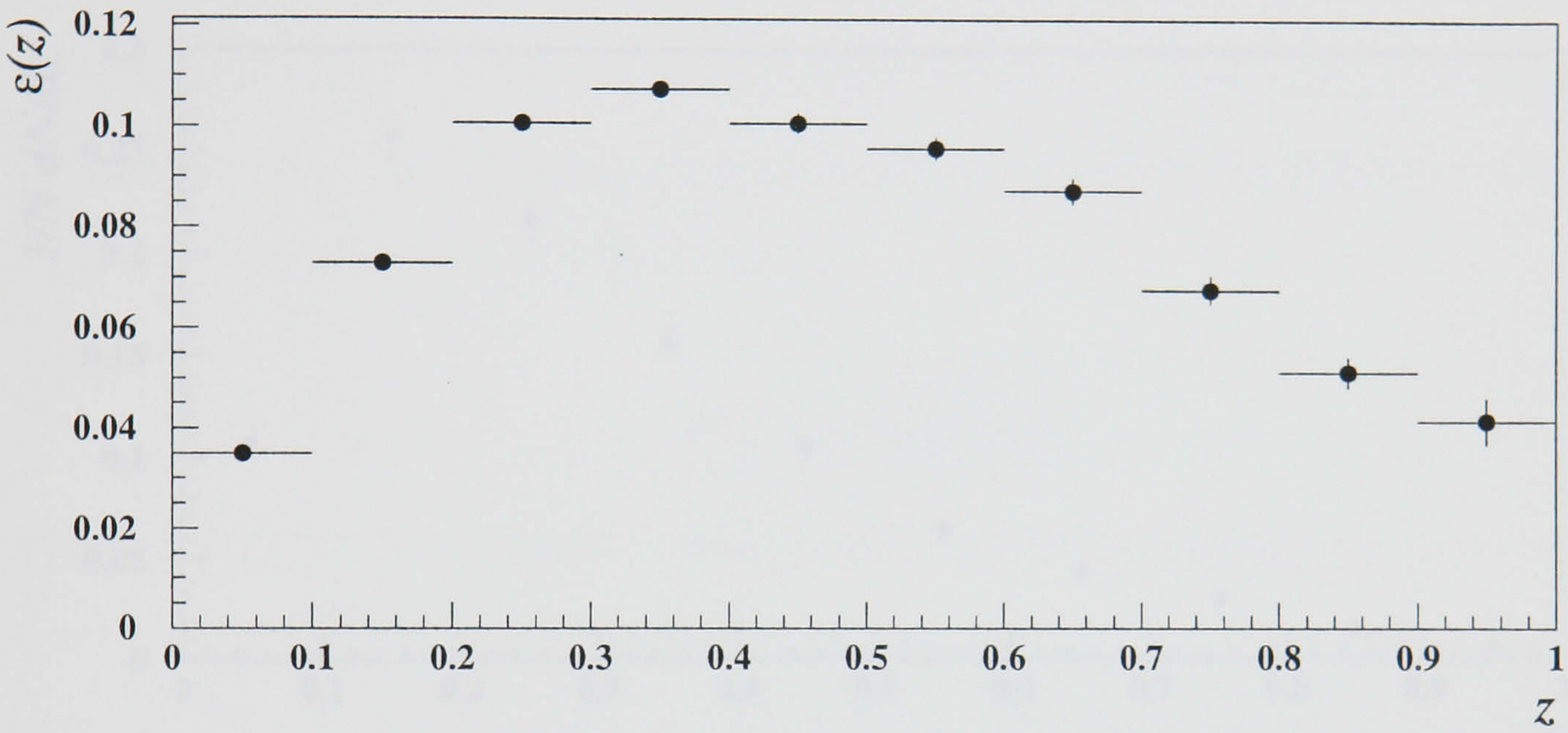

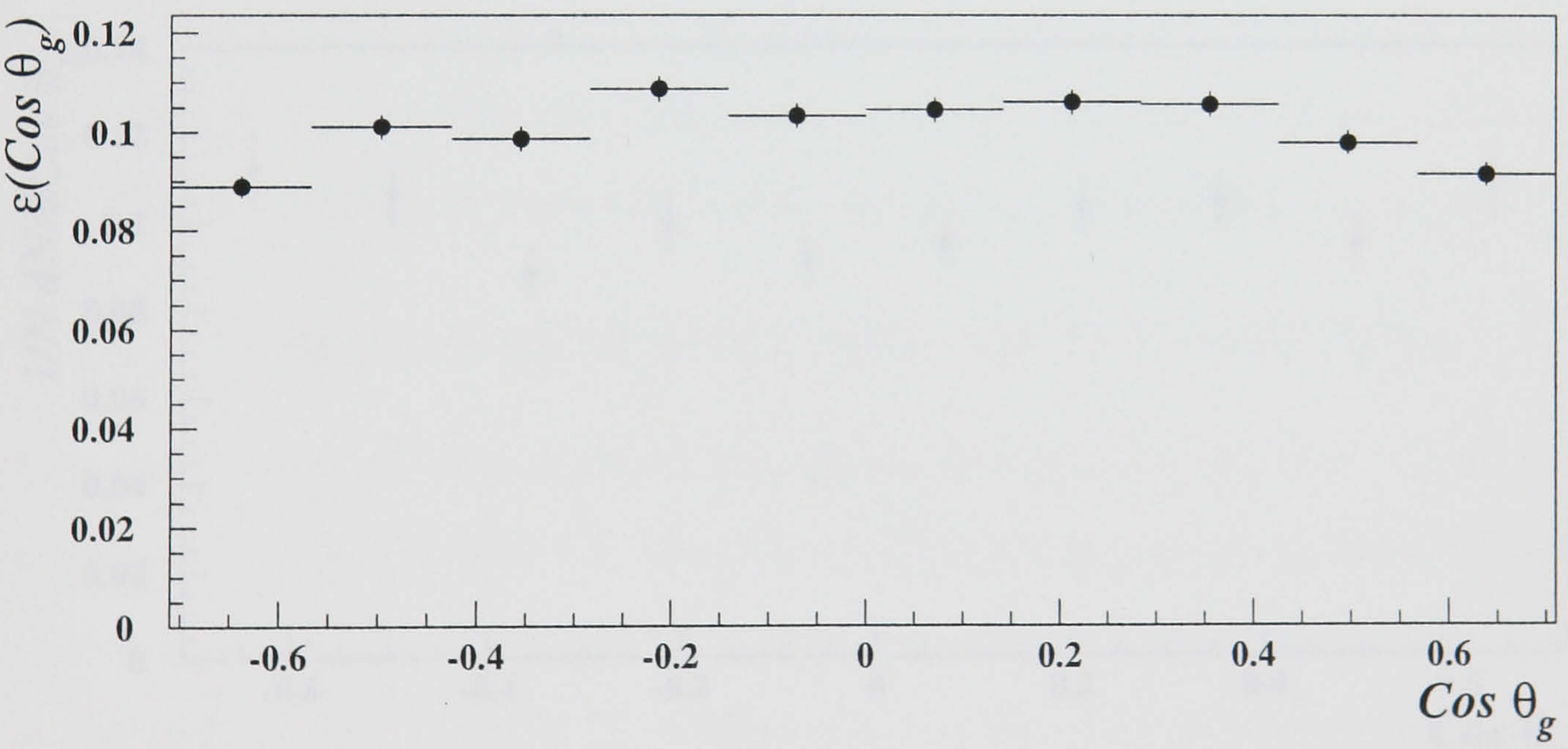

Figure 6.22: The total efficiency (including hadronisation effects, detector acceptance and tagging efficiency) for the two distributions.

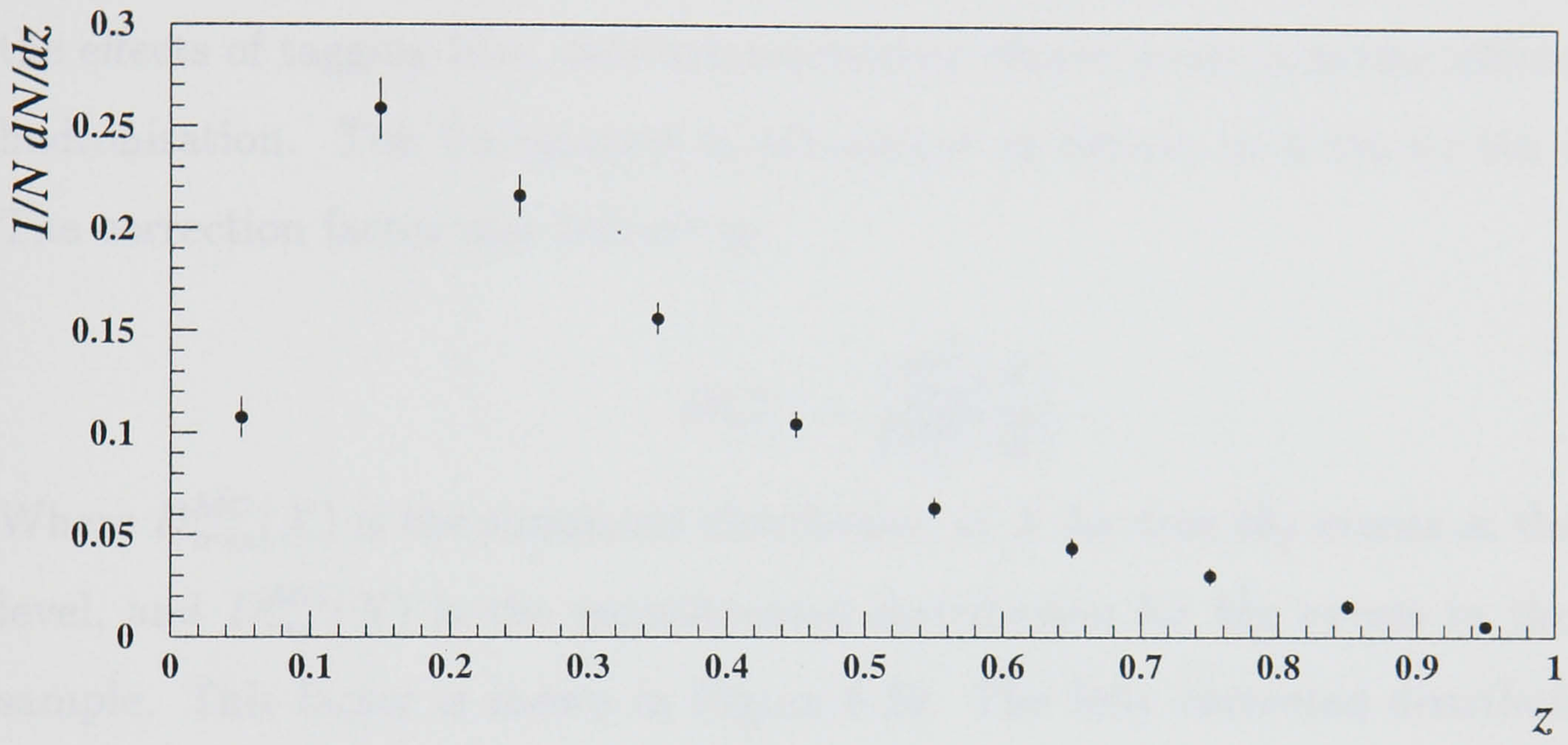

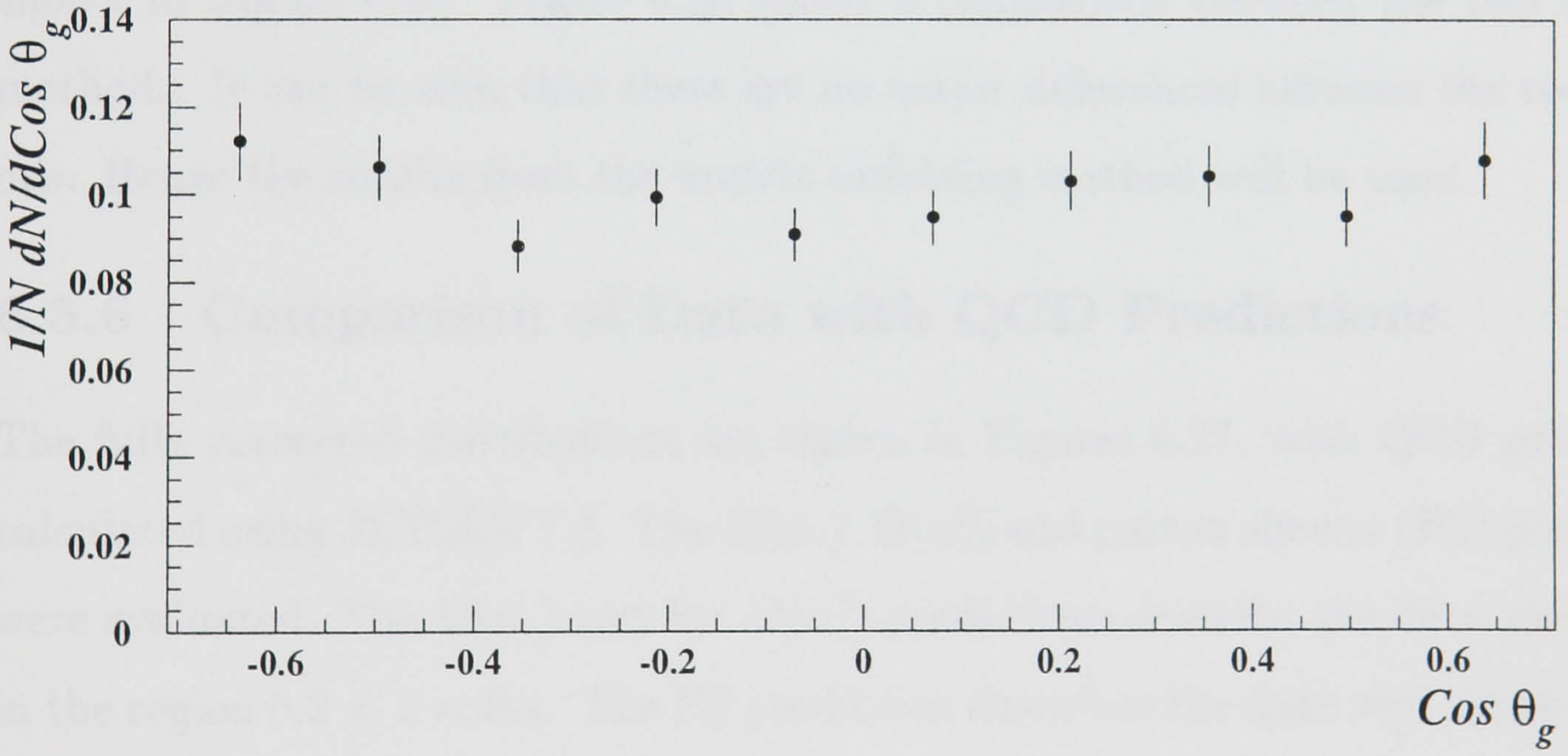

Figure 6.23: The fully corrected data.

6.5.5 Cross Check

As a cross check, a third method of correcting the data was considered:

$$D^{true}(X) = M(X)(D^{raw}(X) - B(X)) \tag{6.10}$$

where X represents z or $\cos\theta_g$, $D^{raw}(X)$ is the raw measured distribution, $B(X)$ is the background contribution, and M(X) is a correction factor that accounts for the effects of tagging bias, detector acceptance effects, event selection efficiency and hadronisation. The background is subtracted as before, in a bin-by-bin method. The correction factor was defined as:

$$M(X) = \frac{D^{MC}_{true}(X)}{D^{MC}_{rec}(X)} \tag{6.11}$$

Where $D^{MC}_{true}(X)$ is the simulated distribution of X for true $b\bar{b}g$ events at the parton level, and $D^{MC}_{rec}(X)$ is the reconstructed distribution for $b\bar{b}g$ events in the tagged sample. This factor is shown in Figure 6.24. The fully corrected distributions are shown in Figure 6.25. Figure 6.26 shows a comparison between the two different methods. It can be seen that there are no major differences between the two methods. Hence the results from the matrix unfolding method will be used.

6.5.6 Comparison of Data with QCD Predictions

The fully corrected distributions are shown in Figures 6.27, with QCD predictions calculated using JETSET 7.4. The $O(\alpha_s)$, $O(\alpha_s^2)$ and parton shower (PS) predictions were evaluated. The $O(\alpha_s)$ and the $O(\alpha_s^2)$ predictions describe the data well except in the region $0.2 < z < 0.4$. The PS prediction describes the data well across the full z range, suggesting that multiple orders of parton radiation are required for a good description. The χ^2 for the comparison of each prediction with the data is given in Table 6.7.

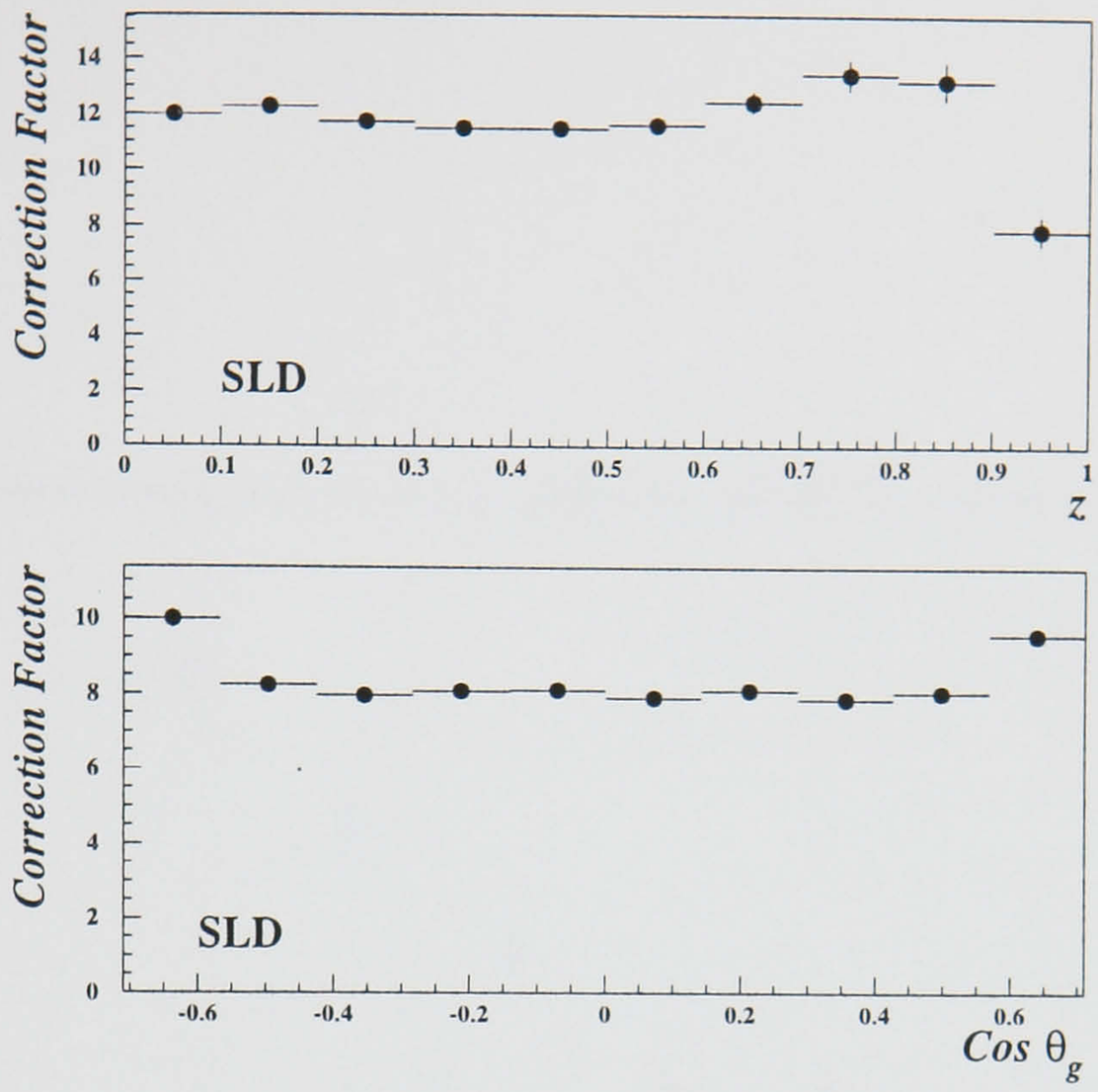

Figure 6.24: The total correction factor for tagging bias, detector effects, event selection and hadronisation (Equation 6.11).

6.6 Study of the Effects of an Anomalous Chromomagnetic Moment

The Lagrangian represented by Eq. 6.1 yields a model that is non-renormalisable. Nevertheless tree-level $O(\alpha_s)$ predictions can be derived [84, 85] and used for a 'straw man' comparison with QCD. In this context we illustrate in Figure 6.28 the effect of an anomalous b chromomagnetic moment on the z spectrum. As the absolute value of κ is increased the gluon energy spectrum gets harder, producing an excess of gluon jets with high scaled energy.

A further difficulty arises in that the $O(\alpha_s)$ QCD calculation does not describe the data as well as the PS calculation, so that the higher-order QCD effects included in the PS prediction could be mimicked in the extended $O(\alpha_s)$ calculation by an artifically large anomalous moment κ. Therefore in each bin i of the z distribution, we parametrised the leading-order effect of an anomalous chromomagnetic moment:

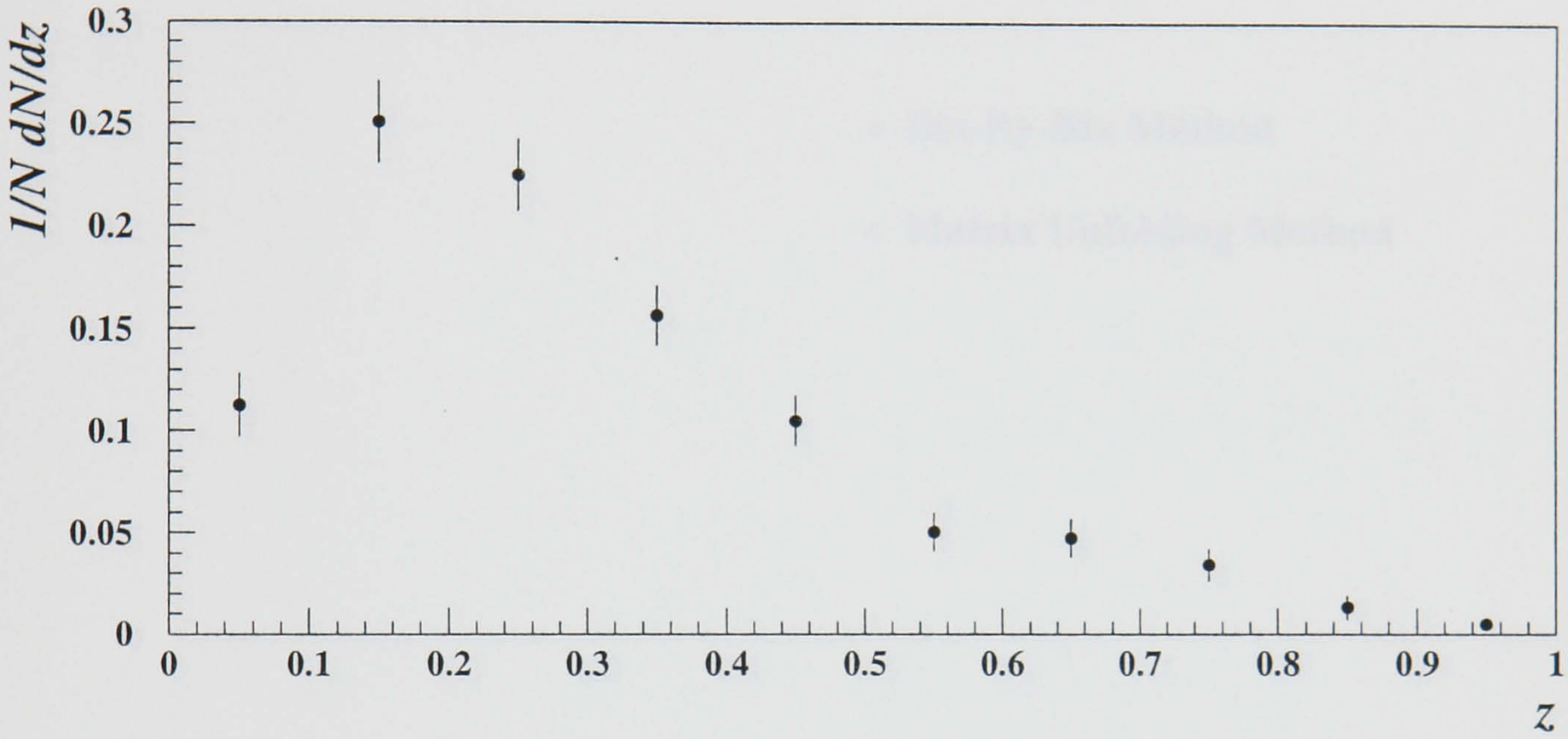

Figure 6.25: Distributions after background subtraction and resolution correction using the bin-by-bin method.

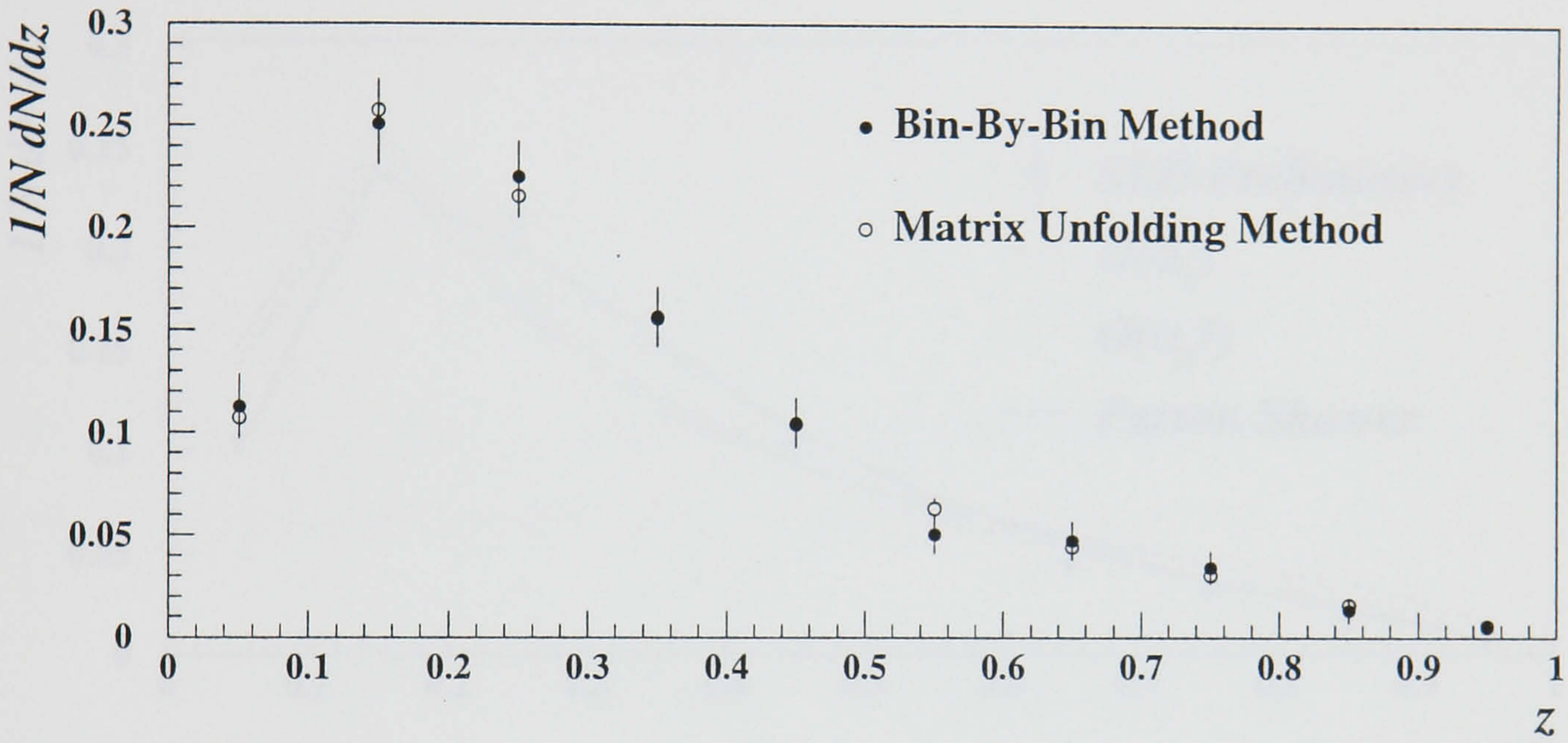

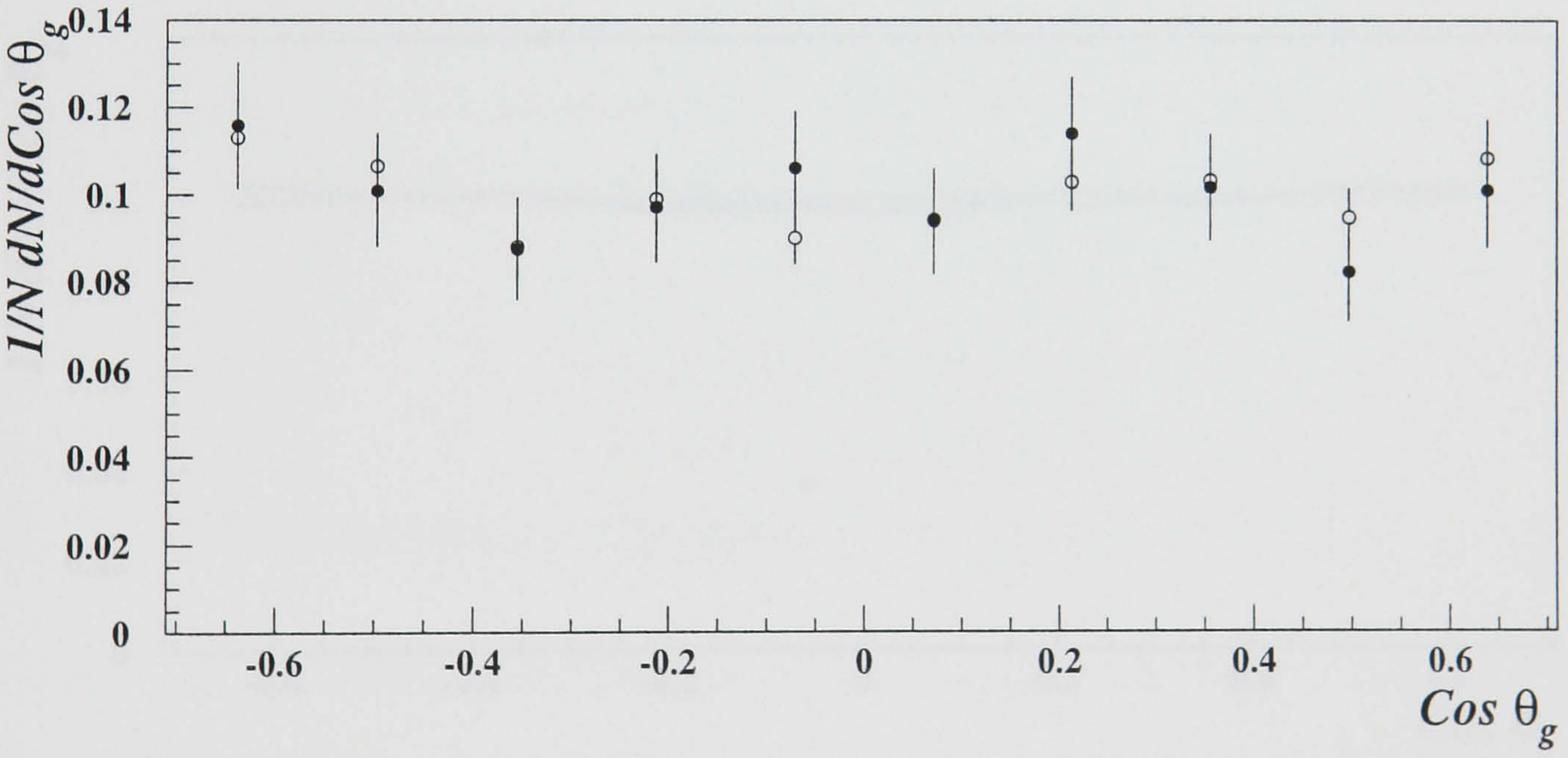

Figure 6.26: Comparison of the results from the bin-by-bin and matrix unfolding correction methods.

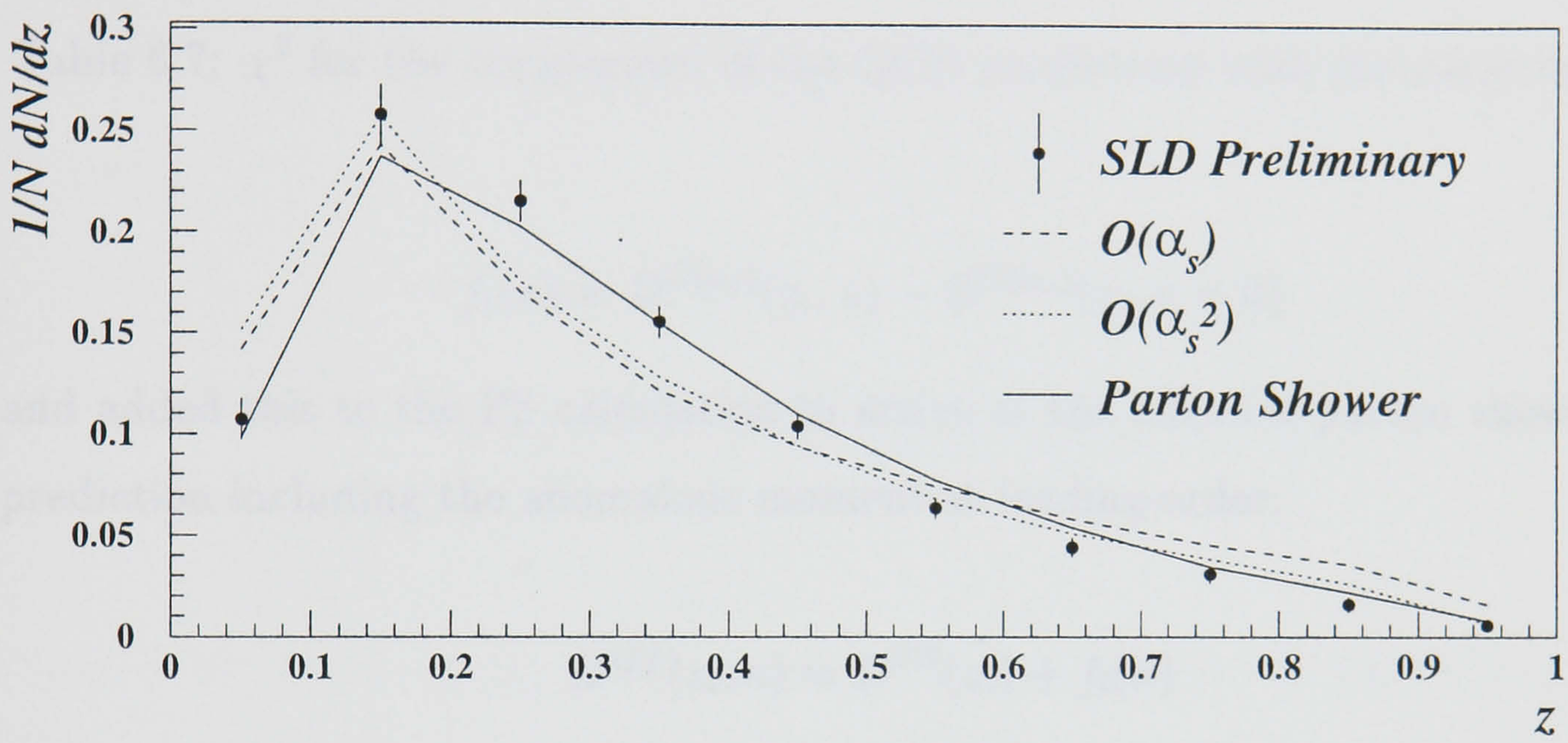

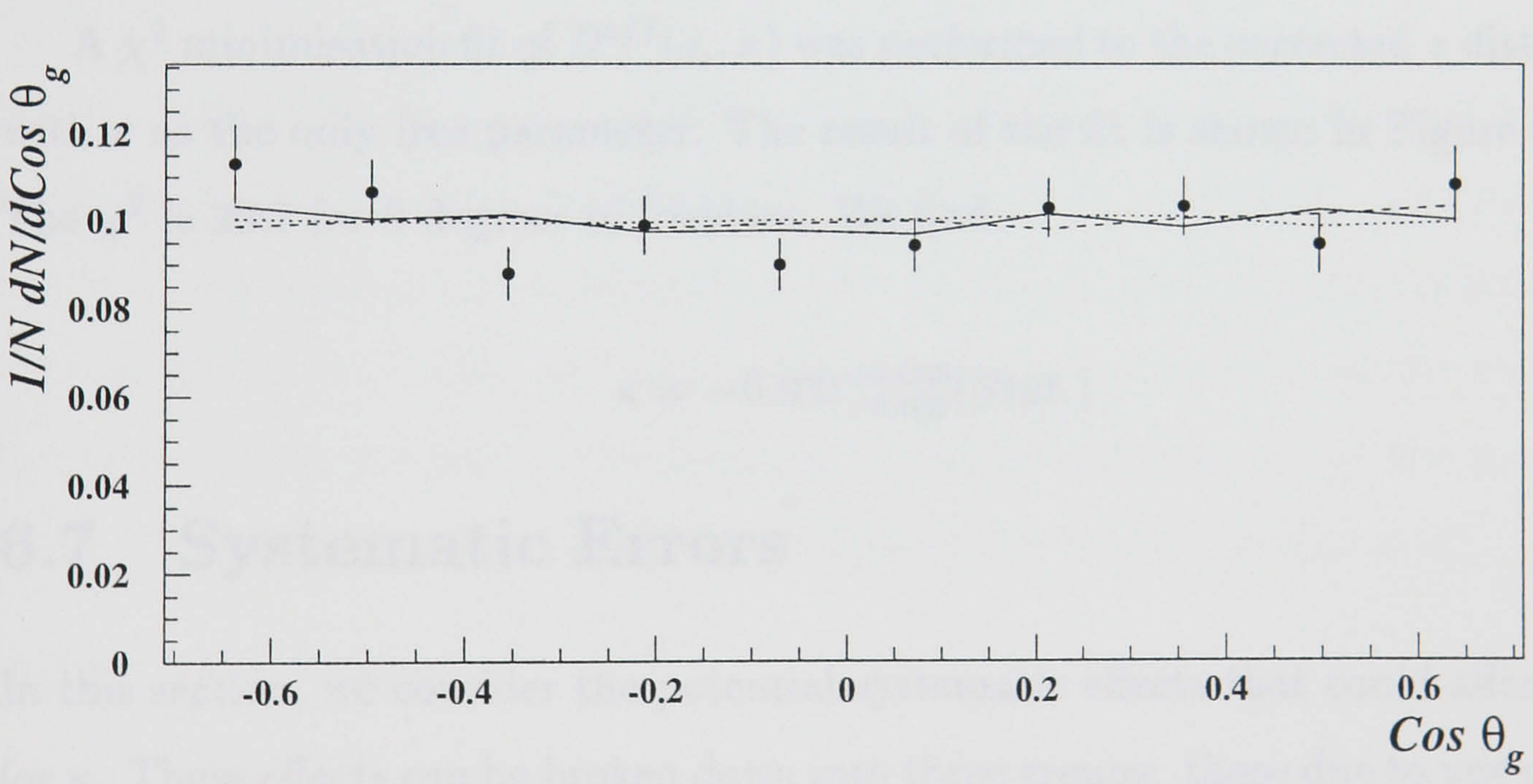

Figure 6.27: A comparison of the corrected distributions with QCD predictions.

	χ^2	
QCD Calculation	z (10 bins)	Cos θ_g (10 bins)
$O(\alpha_s)$	127.2	13.0
$O(\alpha_s^2)$	62.8	11.6
PS	21.3	11.4

Table 6.7: χ^2 for the comparison of the QCD predictions with the corrected data.

$$f_i(\kappa) = D^{O(\alpha_s)}(z_i, \kappa) - D^{O(\alpha_s)}(z_i, \kappa = 0) \tag{6.12}$$

and added this to the PS calculation to arrive at the effective parton shower QCD prediction including the anomalous moment at leading-order:

$$D^{eff}(z_i, \kappa) = D^{PS}(z_i) + f_i(\kappa) \tag{6.13}$$

A χ^2 minimisation fit of $D^{eff}(z_i, \kappa)$ was performed to the corrected z distribution with κ as the only free parameter. The result of the fit is shown in Figure 6.29. The χ^2 is 20.7 for 9 degrees of freedom. We find:

$$\kappa = -0.031^{+0.038}_{-0.039}(Stat.) \tag{6.14}$$

6.7 Systematic Errors

In this section, we consider the potential systematic effects that could affect the fit for κ. These effects can be broken down into three groups: those due to uncertainties in the modelling of B hadron decays, those due to uncertainties in the modelling of D hadron decays, and those due to imperfect detector simulation. The physics errors are due to uncertainties on the experimental measurements that function as input parameters to the modelling of the underlying physics processes. These include such things as errors on the measured values of the total charged multiplicity in B meson decays, the average b lifetime, etc. The MC simulations are tuned using the

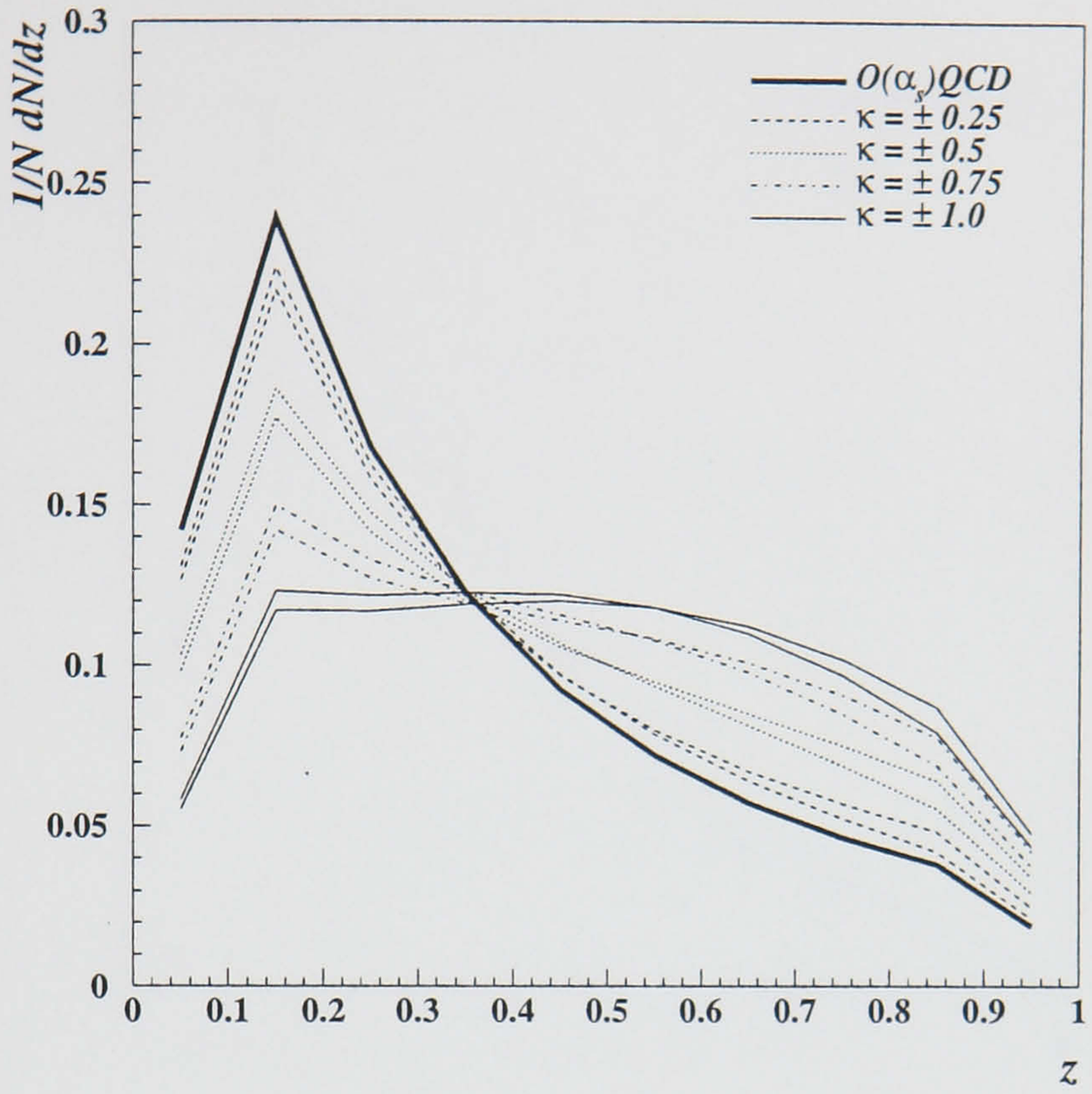

Figure 6.28: Gluon energy spectrum with chromomagnetic moments which are "+" and "-".

world average values, so the possible variation in the experimental results must be considered. Each of these and their effect on the the measurement are described in the following sections. The influence of the various uncertainties on the final results is evaluated in each case by varying the appropriate parameter in the simulation, re-doing the corrections to the data, and performing a new fit on the same data. Table 6.8 summarises the sources of systematic errors that were studied.

Event Re-weighting

Running a new set of MC events through the SLD simulation to evaluate the effects of the variations in each of the parameters governing the production and decay of c and b hadrons would be impossible. Instead, we use an event re-weighting scheme to produce the correct distributions in the simulation. This works as follows: given a normalised distribution D(x) from the default simulation and the desired normalised distribution N(x), one can assign a weight to each event of N(x)/D(x), where the weight is either calculated analytically using the two distributions (e.g. the lifetime)

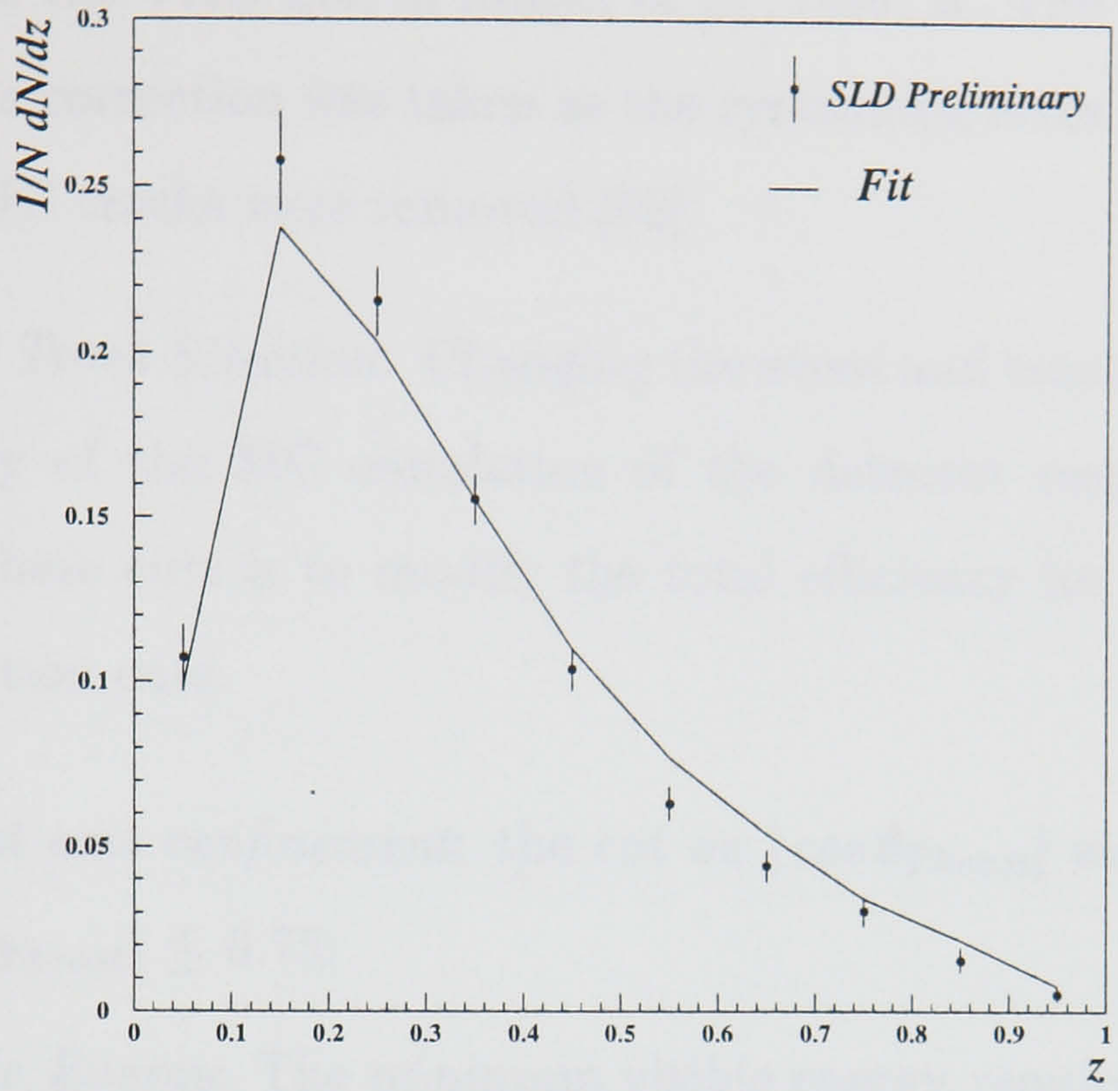

Figure 6.29: Result of the fit of the parton shower calculation including a leading order anomalous chromomagnetic moment contribution.

or is taken from a look-up table for a given bin of x. The total weights of the events are then applied to the default simulation which can then be used to do the corrections to the data.

6.7.1 Errors due to Detector Modelling

- *Tracking Efficiency:* The fraction of tracks passing the quality cuts is different between data and MC. This is due to a simplified simulation of the dependence of the CDC hit efficiency and resolution on the position within a CDC cell. The simulation can be corrected to yield the proper fraction of quality tracks by systematically removing tracks according to the discrepancy between data and MC on the fraction of CDC tracks classified as good and on the CDC to VXD linking rate for the good CDC tracks. The correction is performed by determining the difference between data and MC on the quality track multiplicity fraction in ranges of $p_\perp$, cosθ, ϕ, and the angle with respect to the jet

direction for CDC tracks and in the difference in fraction of good CDC tracks that link to the VXD hits in ranges of $p_\perp$, cosθ, ϕ. The change in κ with and without the correction was taken as the systematic error. In the correction 4.8 % of the MC tracks were removed [92].

- *Event And Track Selection:* Changing the event and track selection cuts checks the validity of the MC simulation of the detector response. The effect of changing these cuts is to modify the total efficiency for an event to pass the event selection cuts.

  - *Thrust axis confinement*: the cut on $|\cos\theta_{Thrust}|$ was varied over $0.67 \leq |\cos\theta_{Thrust}| \leq 0.75$.

  - *Visible Energy*: The minimum visible energy required for an event to be selected was varied in the range $18\text{GeV} \leq E_{vis} \leq 22\text{GeV}$. The effect of this variation is to subtly modify the probablities for a parton-level event to switch assignments between a 2-jet event and a 3-jet event and to change the probability of a parton-level 3-jet event to pass the selection cuts.

  - *Charged track multiplicity*: The number of charged tracks required for an event to pass the selection cuts was increased by unity to check for the effects of allowing some variation in the amount of background in the sample.

6.7.2 Errors due to b-Hadron Modelling

The following b modelling parameters were considered:

- *B Hadron Lifetimes:* As the ease of tagging B hadrons is made possible by the long lifetimes of the B hadron species, any change in the lifetimes will have an effect on the tagging efficiency. The values of the B meson (baryon) lifetimes in the MC are 1.55ps (1.10ps). The B meson lifetime was varied by $\pm$ 0.1ps. and the B baryon liftime by $\pm$ 0.3ps

- *B Fragmentation:* The mean energy fraction $< x_b >$ received by weakly decaying B hadrons was varied by $< x_b > \pm 0.008$. This was done by changing the ϵ parameter of the Peterson fragmentation function [43]. The tag should also be fairly sensitive to the distribution of quark energies. This is easily understood, as softer B's produce decay tracks with smaller total momentum and hence larger extrapolation errors due to multiple scattering, which makes the tracks less likely to miss the IP by a significant amount. Since the B has less boost, it also doesn't travel quite as far before decaying, which also makes it harder to tag the jet.

- *B Hadron Decay Multiplicity:* The mean charged multiplicity in each B hadron decay was varied by ± 0.20 tracks. Any change in the number of tracks in the B meson decay must change the tagging efficiency, because it is easier to tag events with more tracks.

- *B baryon Production Rate:* The rate of B baryon production in B events was varied by $\pm 4\%$. A change in the baryon production rate could affect the B-tagging efficiency due to the low lifetimes measured for the B baryons.

- $R_b = BR(Z^0 \rightarrow b\bar{b})/BR(Z^0 \rightarrow hadrons)$: The tag is sensitive to the fraction of B events hence R_b was varied by $\pm$ 0.0017.

- $B \rightarrow D^+$ *Fraction:* $B \rightarrow D^+$ decays can have a large affect on the tagging efficiency of b events, as the long decay path of the D^+ down stream of the B meson decay point enhances the efficiency for tagging that event.

6.7.3 Errors due to c-Hadron Modelling

The following c modelling parameters were considered:

- $R_c = BR(Z^0 \rightarrow c\bar{c}:)/BR(Z^0 \rightarrow hadrons)$: Since charm events are the main background, the purity is very dependent on the fraction of charm events. R_c was varied by $\pm$ 0.01

- *c Fragmentation:* By making the hadrons containing charm harder, the probability of them being b-tagged increases, and if they are softer, it is harder to tag them. The $< x_c >$ was varied by $\pm$ 0.008.

- $c\bar{c} \rightarrow D^+$ *Fraction:* Due to the long D^+ lifetime, these events could be mistagged as b events. Hence the tag is sensitive to this fraction. The fraction was varied by $\pm$ 0.026

- *D Decay Multiplicity:* The D decay multiplicity was varied by $\pm$ 0.14 tracks. The more tracks there are in the decay, the more probable the event would be tagged as a b event.

6.7.4 Summary of the Systematic Errors.

The individual systematic errors in each bin were defined as the difference between the central value and the new value in that bin for the weighted distribution. The systematic errors for each factor considered are shown in Table 6.8. The overall systematic error is the sum in quadrature of the error from each uncertainty. Figure 6.30 shows the gluon energy and polar angle distributions with the statistical and systematic errors. Tables 6.9 and 6.10 show the same information in tabular format. The systematic error on the value of κ for each uncertainty studied was the difference between the κ from the fit to the central distribution and the κ from the fit to the weighted distribution. The systematic uncertainties were conservatively assumed to be uncorrelated and were added in quadrature to obtain a total uncertainty on κ of $^{+0.003}_{-0.004}$.

Source	Center Value	Variation	$\Delta\kappa$
B PHYSICS			
B decay multiplicity	$<n_{ch}> = 5.39$	± 0.2 trks	$^{+0.0002}_{-0.0001}$
B fragmentation	$<x_b> = 0.702$	∓ 0.008 trks	$^{+0.0017}_{-0.0032}$
B meson life time	$\tau_B = 1.55$ps	± 0.05ps	$^{+0.0001}_{-0.0003}$
B baryon life time	$\tau_B = 1.10$ps	± 0.08ps	$^{+0.0001}_{-0.0001}$
B baryon prod. rate	$f_{\lambda_b} = 7\,\%$	$\pm 4\%$	$^{+0.0003}_{-0.0003}$
$B \longrightarrow D^+ +$ X fraction	0.15	∓ 0.05	$^{+0.0001}_{-0.0003}$
R_b	0.2216	∓ 0.0017	$^{+0.0001}_{-0.0000}$
C PHYSICS			
R_c	0.16	∓ 0.01	$^{+0.0000}_{-0.0000}$
c fragmentation	$<x_c> = 0.484$	± 0.008	$^{+0.0008}_{-0.0005}$
$c\,\bar{c} \longrightarrow D^+ +$ X Fraction	0.231	∓ 0.026	$^{+0.0002}_{-0.0003}$
D decay multiplicity	$<n_{ch}> = 2.39$	± 0.14trks	$^{+0.0002}_{-0.0002}$
$g \longrightarrow c\bar{c}$	2.4	$\mp$ 0.5	$^{+0.0008}_{-0.0006}$
$g \longrightarrow b\bar{b}$	0.13	$\mp$ 0.04	$^{+0.0001}_{-0.0001}$
DETECTOR			
E_{vis}	$E_{vis} > 20$GeV	∓ 2GeV	$^{+0.0000}_{-0.0008}$
cos θ_{Thrust}	$\lvert\cos\theta_T\rvert < 0.71$	∓ 0.04	$^{+0.0005}_{-0.0012}$
n_{trk}	$n_{trk} \geq 5$	$+1$trk	0.0000
Tracking efficiency	–	$^{+4.8}_{-0.0}\%$	$^{+0.0021}_{-0.0000}$
TOTAL			$^{+0.0030}_{-0.0037}$

Table 6.8: Table of systematic errors.

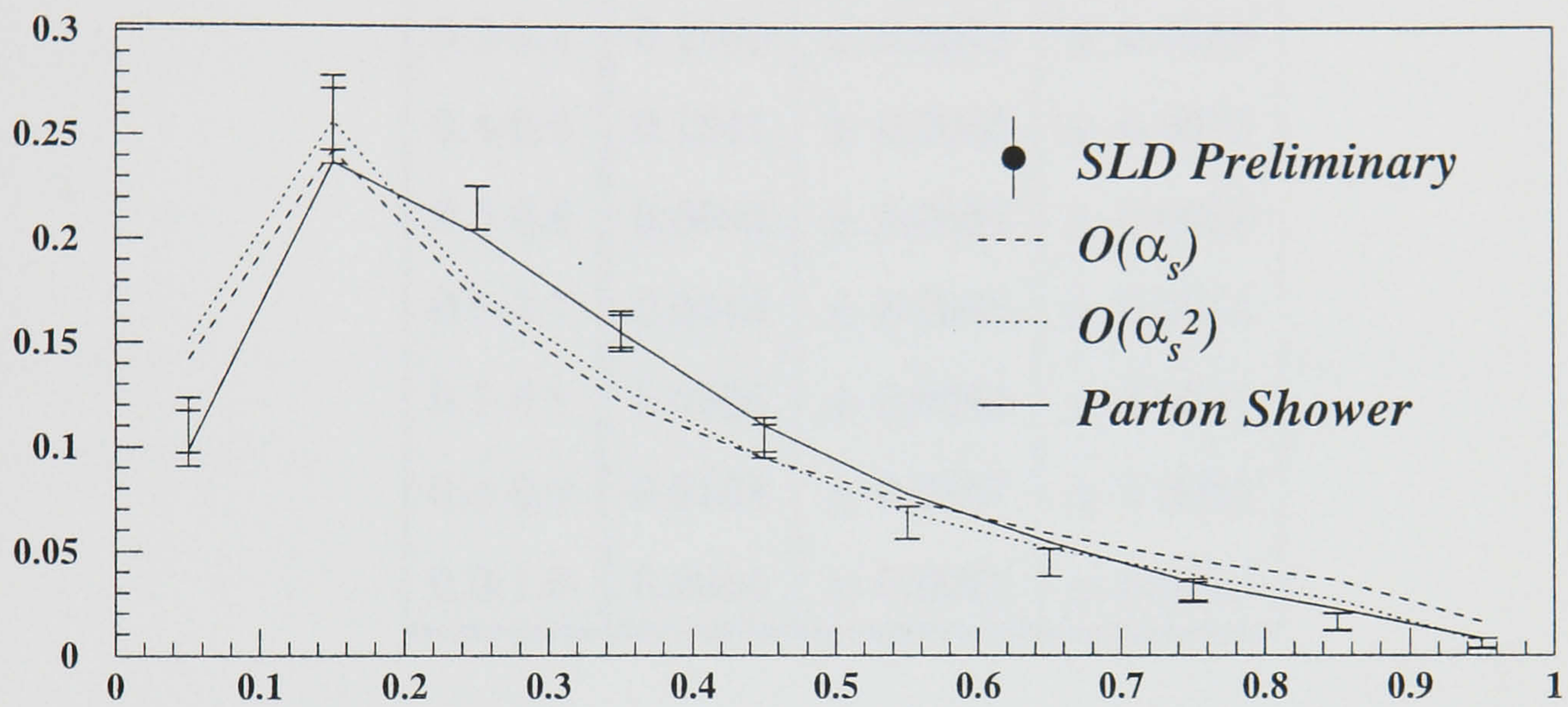

Figure 6.30: The distributions including statistical (inner error bars) and the total error i.e. statistical and systematic errors added in quadrature (outer error bars).

		Errors	
z	$\frac{1}{\sigma}\frac{d\sigma}{dz}$	Stat.	Syst
0.0-0.1	0.1071	± 0.0101	± 0.0131
0.1-0.2	0.2577	± 0.0149	± 0.0150
0.2-0.3	0.2156	± 0.0103	± 0.0028
0.3-0.4	0.1556	± 0.0078	± 0.0059
0.4-0.5	0.1041	± 0.0065	± 0.0073
0.5-0.6	0.0634	± 0.0052	± 0.0058
0.6-0.7	0.0443	± 0.0048	± 0.0044
0.7-0.8	0.0306	± 0.0044	± 0.0034
0.8-0.9	0.0158	± 0.0037	± 0.0023
0.9-1.0	0.0054	± 0.0023	± 0.0012

Table 6.9: Table of values for the gluon energy distribution.

		Errors	
$\cos\theta_g$ bin	$\frac{1}{\sigma}\frac{d\sigma}{dcos\theta_g}$	Stat.	Syst
-0.710 - -0.568	0.1254	± 0.0100	± 0.0045
-0.568 - -0.426	0.1037	± 0.0073	± 0.0027
-0.426 - -0.284	0.0931	± 0.0063	± 0.0019
-0.284 - -0.142	0.0908	± 0.0060	± 0.0015
-0.142 - 0.000	0.0905	± 0.0060	± 0.0025
0.000 - 0.142	0.0921	± 0.0060	± 0.0031
0.142 - 0.284	0.0971	± 0.0063	± 0.0031
0.284 - 0.426	0.0966	± 0.0064	± 0.0033
0.426 - 0.568	0.0974	± 0.0069	± 0.0015
0.568 - 0.710	0.1133	± 0.0093	± 0.0035

Table 6.10: Table of values for the gluon polar angle distribution.

6.7.5 Summary

The precise SLD tracking system has been used to tag $e^+e^- \rightarrow Z^0 \rightarrow b\bar{b}g$ events. The structure of $b\bar{b}g$ events has been studied in terms of the distributions of the scaled gluon energy and the gluon polar angle with respect to the electron beam direction, and it was found that the QCD parton shower predictions agree well with the data. The effect of an anomalous chromomagnetic moment, κ, was investigated. The value of κ was found to be:

$$\kappa = -0.031^{+0.038}_{-0.039}(Stat.)^{+0.003}_{-0.004}(Syst.) \tag{6.15}$$

This value is consistent with the Standard Model, hence no evidence for chromomagnetic moments was found. A 95% confidence-level limit of:

$$-0.106 < \kappa < 0.044 \tag{6.16}$$

was obtained.

Chapter 7

Conclusions

This thesis covers a variety of work, on both hardware development and data analysis. This chapter contains concluding remarks about VXD3, the physics analysis of the structure of $b\bar{b}g$ events using the old vertex detector VXD2, and the improvements that could be gained by using VXD3.

7.1 VXD3, SLDs Vertex Detector Upgrade

In January 1996, SLD's pioneering 120 Mpixel vertex detector, VXD2, was replaced by VXD3, a 307Mpixel CCD vertex detector.

The construction of VXD3 on schedule involved a huge effort from both EEV and academia. 52 ladders were produced at EEV in an intense 14 week period, including the re-work of 10% of the ladders. The re-works were mainly due to charge traps that could not have been detected at EEV, as the devices needed to be cold (220K) and operating with small signals before their effect became apparent (Chapter 3). After testing at EEV and Brunel the ladders were sent to SLAC for further testing at the operating temperature. The ladders that passed were then sent to MIT for ladder survey measurements, then to Yale University for detector assembly, and once again back to MIT for detector survey. Then finally back to SLAC for final testing and installation.

During the 1996 SLD physics run the detector was commissioned. Apart from a few electronics problems VXD3 worked efficiently throughout the run. The only major problem was the efficiency loss in the inner barrel due to radiation damage

incured during the time undamped beam was passed through SLD. In the future this problem will be overcome by running the detector at a lower temperature, and no hostile beam will be allowed through SLD unless the solenoid is turned on.

Once the detector was aligned globally (Chapter 5) and internally [74], the tracking performance of the detector was very close to the design, with an impact parameter resolution given by:

$$\sigma_d^{r\phi} = 14 \oplus \frac{33}{p \sin^{\frac{3}{2}} \theta} \tag{7.1}$$

$$\sigma_d^{rz} = 26.5 \oplus \frac{33}{p \sin^{\frac{3}{2}} \theta} \tag{7.2}$$

The impact parameter resolution at low momentum was significantly improved, by comparison with VXD2, Figure 3.21. The improved vertex detector should improve the quality of the physics analyses at SLD, as many depend on some form of heavy quark tagging. The R_b group, using topological vertexing [93], have already carried out a preliminary analysis with the 1996 data [94] and show a marked improvement in the efficiency to tag b events. Figure 7.1 shows the efficiency versus purity plot for the hemisphere tag, compared with VXD2 and other experiments.

7.2 The Structure of $b\bar{b}g$ Events

The precise SLD tracking system (CDC and VXD2) has been used to tag $e^+e^- \rightarrow Z^0 \rightarrow b\bar{b}g$ events. Using a 2-D impact parameter tag the gluon jets were tagged on an event by event basis, with a high purity (91%) and an efficiency of 8.25%. The structure of $b\bar{b}g$ events has been studied in terms of the distributions of the scaled gluon energy (z), and the gluon polar angle with respect to the electron beam direction (θ_g). It was found that the $O(\alpha_s)$ and the $O(\alpha_s^2)$ QCD predictions describe the data well except in the region $0.2 < z < 0.4$, whereas the parton shower QCD prediction describes the data well across the full z range, suggesting that multiple orders of parton radiation are required for a good description of the data.

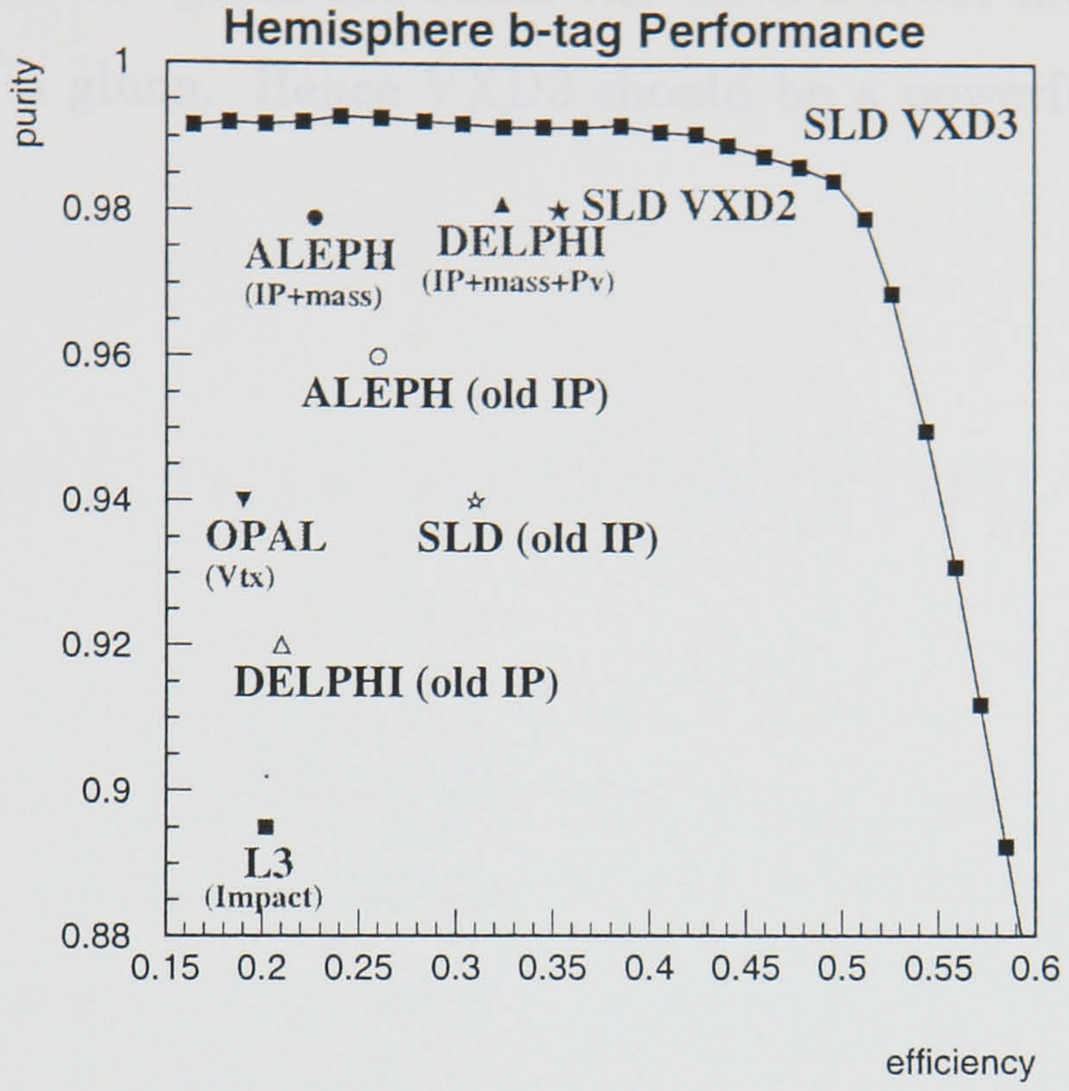

Figure 7.1: The efficiency vursus purity for tagging b events for VXD3 and various other detectors.

The scaled gluon energy distribution is sensitive to an anomalous chromomagnetic moment (κ). As the value of κ increases from 0 (the Standard Model value), the spectrum becomes harder i.e. more high energy gluons are emitted by the b or $\overline{b}$ quarks. A fit was performed to the scaled gluon energy distribution and a value of:

$$\kappa = -0.031^{+0.38}_{-0.39}(Stat.)^{+0.003}_{-0.004}(Syst.) \tag{7.3}$$

was obtained. This value is consistent with the Standard Model. A 95% confidence-level limit of:

$$-0.106 < \kappa < 0.044 \tag{7.4}$$

was set.

The new vertex detector should be very useful for this and similar analyses, (such as R_b, R_c, A_b etc.) because as we have seen the impact parameter resolution has been improved, especially for low momentum tracks. This is particularly important

for this analysis as tracks coming from the hadrons containing the primary b or $\overline{b}$ quark which emitted the gluon are softer i.e. have a lower momentum than those which do not emit a gluon. Hence VXD3 should be a powerful aid in tagging the gluon jets.

Appendix A

Abbreviations and Acronyms

A/D	Analogue to Digital Converter
CCD	Charge Coupled Device
CDC	Central Drift Chamber
CRID	Čerenkov Ring Imaging Detector
EDC	End Cap Drift Chamber
FET	Field Effect Transistor
Iϕ1,2,3	The Clock Voltage in the Image Section
LAC	Liquid Argon Calorimeter
LUM	Luminousity Monitor
MIT	Massachusetts Institute of Technology
MOS	Metal Oxide Semiconducter
Rϕ1,2	The Clock Voltage in The Readout Section
SLAC	The Stanford Linear Accelerator Center
SLC	The SLAC Linear Collider
SLD	The SLC Large Detector
EDC	End Cap Drift Chamber
VOD	Output Drain Voltage
VOG	Output Gate Voltage
VOS1,2,3,4	Output Voltage for each channel
VRD	Reset Drain Voltage
VSS	Substrate Voltage

WIC Warm Iron Calorimeter

VXD Vertex Detector

ϕR Reset Voltage

Appendix B

The Charge Coupled Device (CCD)

B.1 Introduction to the CCD

A Charge Coupled Device (CCD) is a semiconductor device consisting of a tightly packed array of Metal Oxide Semiconductor (MOS) structures, formed on a silicon substrate. The charge produced by the passage of minimum ionising particles is stored in these structures. By applying the correct bias voltages this charge can be moved from structure to structure and transferred to an output system which can be used to determine the amount of charge that was stored.

The first CCD was produced in 1970 [95]. This was a surface channel device, as the charge is stored at the silicon/silicon dioxide interface. Later a more sophisticated device known as the buried channel device was invented [96]. In this device the charge is stored $\sim 1\mu$m below the surface, in the bulk silicon, away from interface states that can trap the signal charge. The buried channel device is the type used in particle physics applications as they involve small signals, hence are very sensitive to charge traps. CCDs were first used in particle physics in the NA32 fixed target experiment [97].

This Appendix gives a brief description of the operation of a CCD. For a more detailed account see [98] and [99]. Reference [100] discusses the use of CCDs as vertex detectors in particle physics experiments.

B.2 Structure

The structure of a buried channel CCD, consists of a low-resistivity p^+ substrate onto which is grown an epitaxial layer of higher resistivity silicon with a thickness adequate to contain all the necessary structures and associated field penetration. Then a layer of n-type dopant is introduced by a shallow implant. The surface is then oxidised. There are in fact two oxide layers, the first is silicon dioxide the second is a layer of silicon nitride, which should cover any pin holes in the silicon dioxide. Then the surface is covered with a thin conducting layer of polysilicon. This conducting surface is called a gate. Figure B.1 shows the MOS structure used in buried channel CCDs.

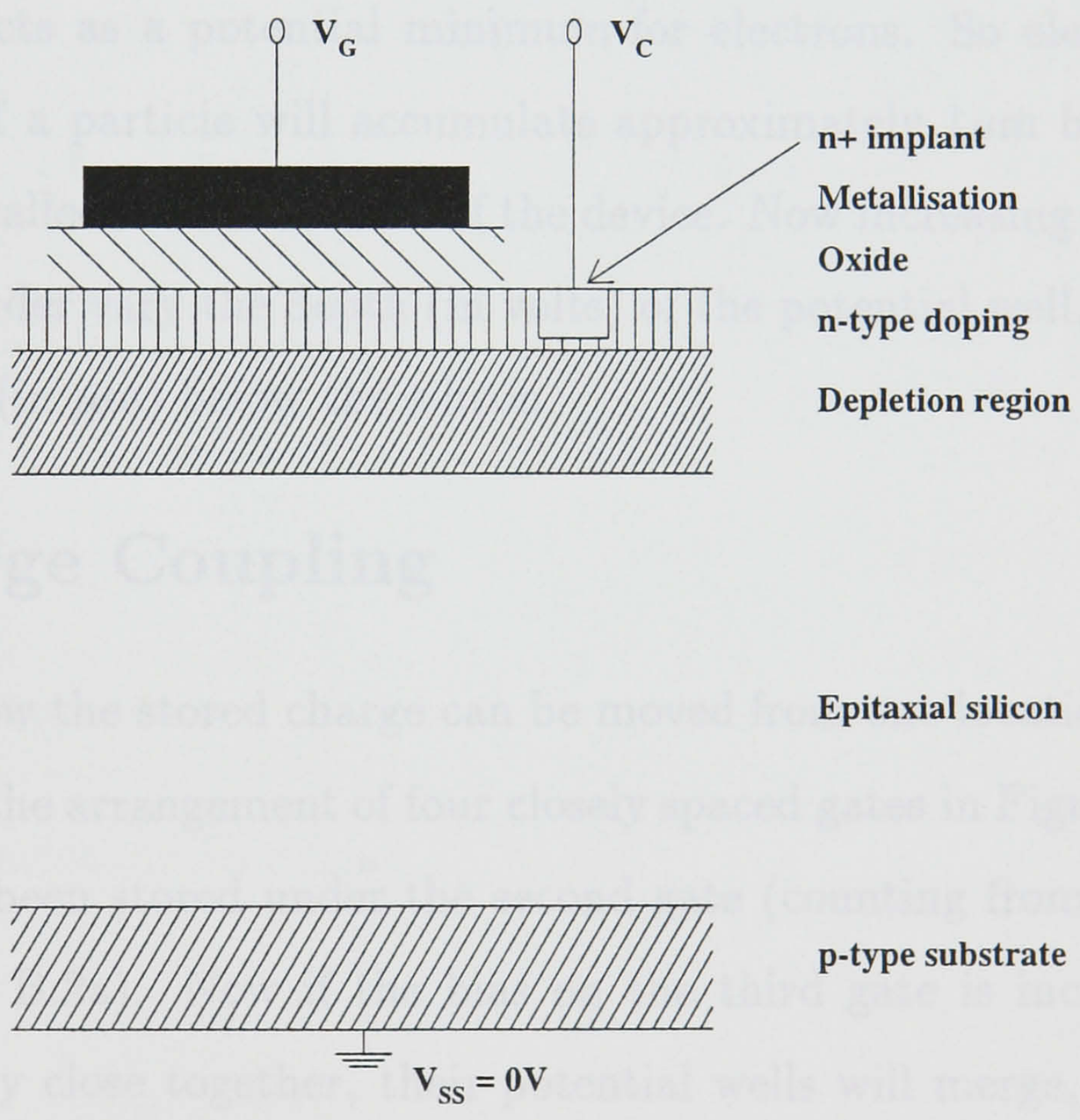

Figure B.1: The structure of a MOS device, used in CCDs.

Now consider what happens when biases are applied to the MOS structure. With the substrate (VSS) grounded, V_C is applied to the n-channel and V_G applied to the gate. Initally assume V_C=V_G. Even with V_C=0V, there will be a thin depletion layer around the interface between the p and n type silicon. By increasing V_C the

depletion region will increase as the junction becomes more strongly reverse biased. Now if V_C is increased from 0V while V_G is held at 0V, the large capacitance between the n-channel and the gate provides a further mechanism for depletion. The depletion around the pn junction proceeds as before, but the voltage across the oxide induces an increasing positive space-charge, starting at the silicon/oxide surface and grows into the n-channel. At a certain value of V_C, these two depletion regions meet, causing the phenomenom known as pinch-off. The corresponding value of V_C is called the pinch-off voltage, and when it is reached further increases of V_C have no influence on the potential under the gate. The depletion depth in the p-type material is only about 6μm. What is interesting is the potential distribution in the silicon. There is now a maximum in the electric potential just above the pn junction. This acts as a potential minimum for electrons. So electrons liberated by the passage of a particle will accumulate approximately 1μm below the silicon surface in the so called buried channel of the device. Now increasing the gate voltage V_G will to first order vary the depth (in volts) of the potential well, but will hardly change its depth (in μm) below the silicon.

B.3 Charge Coupling

To understand how the stored charge can be moved from one location to another in a CCD, consider the arrangement of four closely spaced gates in Figure B.2. Assume some charge has been stored under the second gate (counting from the left) which is biased (Figure B.2a). Now if the bias on the third gate is increased, and the two gates are very close together, their potential wells will merge, and the charge originally under the second gate, will now be shared between the wells under gates two and three (Figures B.2b and c). If the bias on gate two is reduced the well will begin to collapse and the charge in the well will be shifted into the third well (Figure B.2d). Finally all the charge originally stored under gate two, is now stored under gate three (Figure B.2e). Figure B.3 shows the clocking sequence.

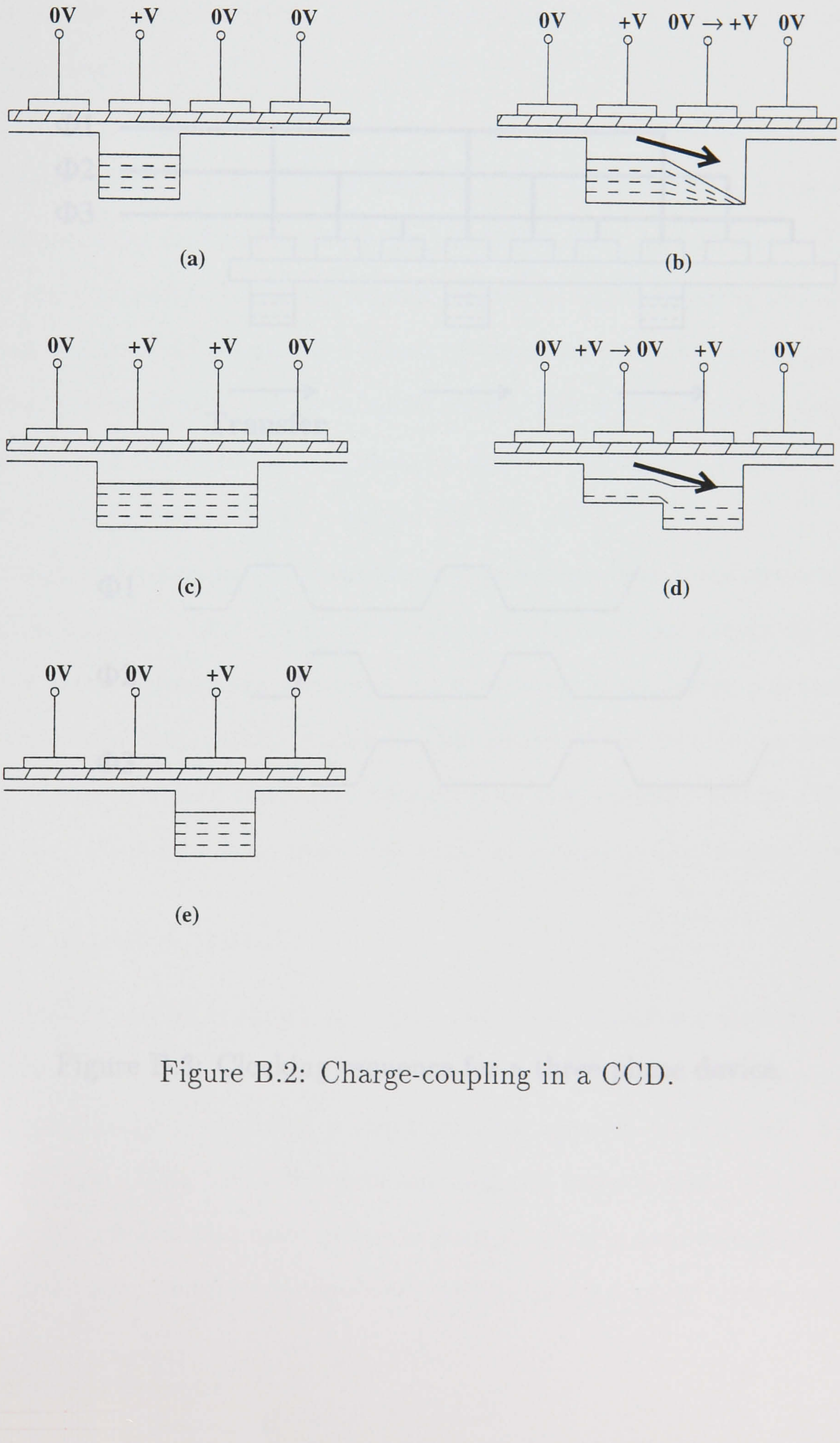

Figure B.2: Charge-coupling in a CCD.

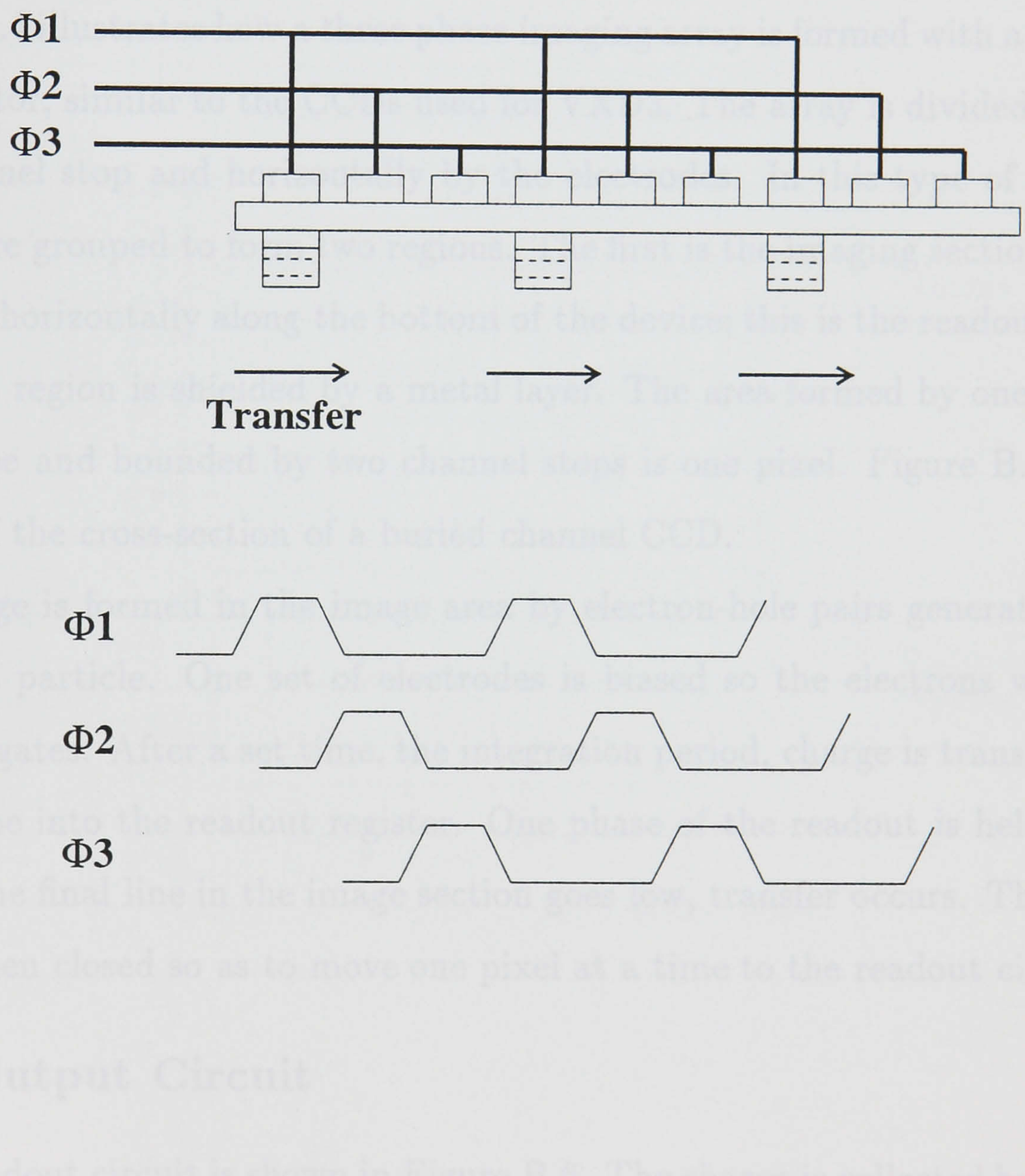

Figure B.3: Clocking sequence for a three phase device.

B.4 CCD array

So far only a linear (single line) CCD has been considered. If an array is to be formed a number of linear devices must be joined together. To prevent charge from flowing perpendicular to the direction of transfer a channel diffusion or implant "stop" is used. In this technique, a region of material of the same majority carrier type as the substrate, but with a higher doping concentration, is diffused or implanted on either side of the channel region. If the diffusion is abrupt there is a clear boundary for a channel region.

Figure B.4 illustrates how a three phase imaging array is formed with a two phase output resistor, similar to the CCDs used for VXD3. The array is divided vertically by the channel stop and horizontally by the electrodes. In this type of CCD, the electrodes are grouped to form two regions. The first is the imaging section, and the second runs horizontally along the bottom of the device; this is the readout register. The readout region is shielded by a metal layer. The area formed by one electrode of each phase and bounded by two channel stops is one pixel. Figure B.5 shows a schematic of the cross-section of a buried channel CCD.

The image is formed in the image area by electron-hole pairs generated by the passage of a particle. One set of electrodes is biased so the electrons will collect under these gates. After a set time, the integration period, charge is transferred one line at a time into the readout register. One phase of the readout is held high, so that when the final line in the image section goes low, transfer occurs. The readout register is then closed so as to move one pixel at a time to the readout circuitry.

B.4.1 Output Circuit

A typical readout circuit is shown in Figure B.6. The charge is collected by a reverse biased diode.

Before the charge is readout, a reset pulse is applied to the reset FET (Field effect transistor). This turns the gate on and the output node is charged to the VRD potential. When the reset pulse is turned off the node remains charged. If Rϕ2 then goes low, charge is transferred to the output node which will partially

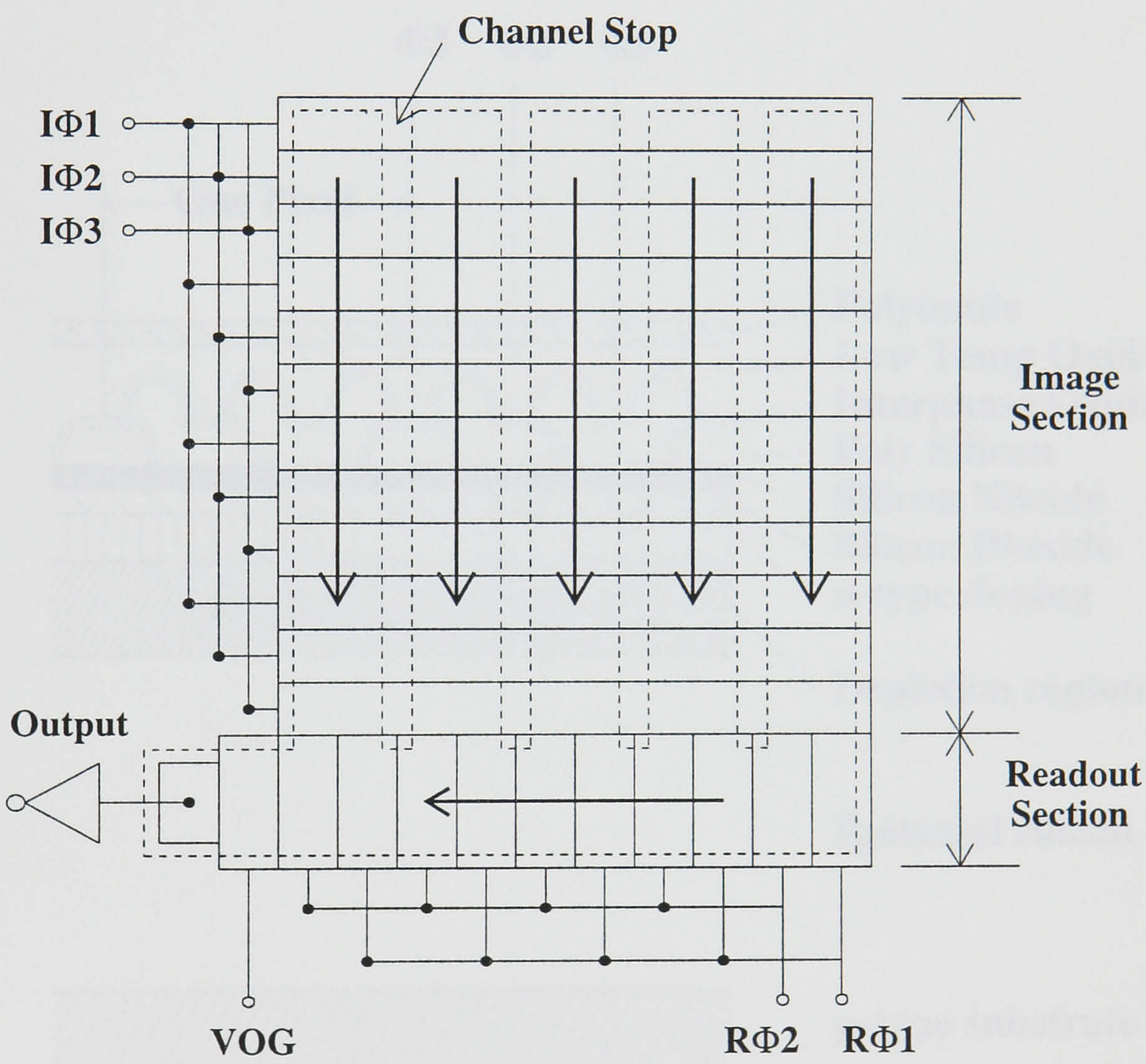

Figure B.4: Schematic of a CCD array.

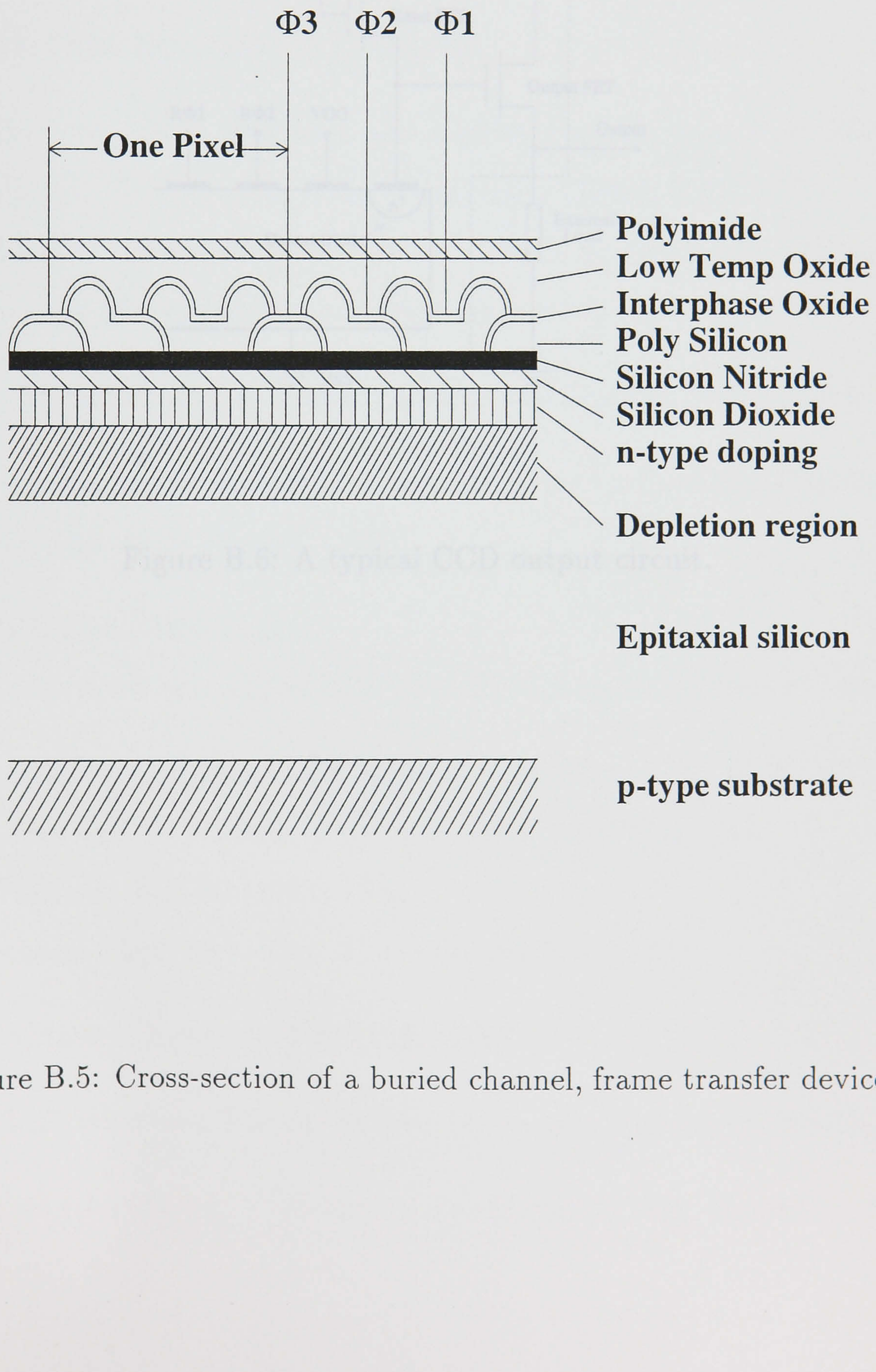

Figure B.5: Cross-section of a buried channel, frame transfer device.

discharge the capacitance causing the potential to drop. This change in potential is proportional to the charge tranferred from the CCD. The output FET provides a low impedence output at its source to drive off-chip circuitry.

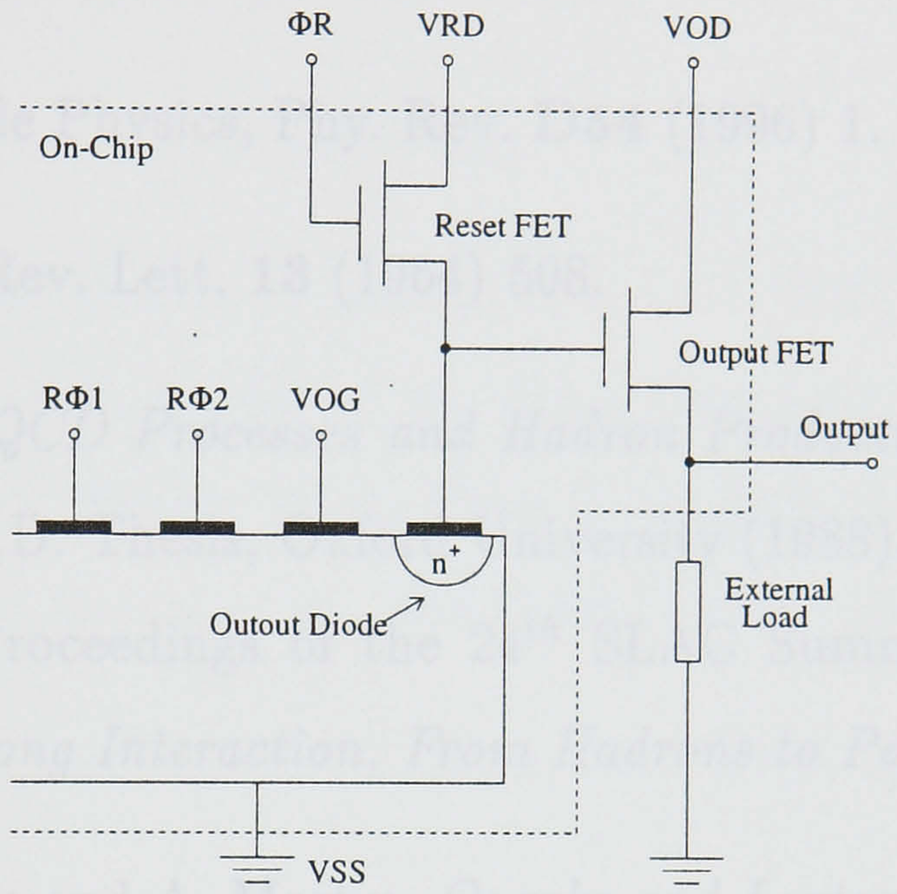

Figure B.6: A typical CCD output circuit.

Bibliography

[1] Review of Particle Physics, Phy. Rev. **D54** (1996) 1.

[2] P. Higgs, Phys. Rev. Lett. **13** (1964) 508.

[3] P. N. Burrows, *QCD Processes and Hadron Production in High Energy* e^+e^- *Annihilation*, Ph.D. Thesis, Oxford University (1988), RALT-071.
P.N. Burrows, Proceedings of the 24^{th} SLAC Summer Institute on Particle Physics, *The Strong Interaction, From Hadrons to Partons*, 1996.

[4] See e.g. F. Halzen and A. Martin, *Quarks and Leptons*, Wiley (1984).

[5] I.J.R. Aitchison and A.J. Hey *Gauge Theories in Particles Physics*, Second Edition, Institute of Physics, (1989).

[6] ALEPH Collab., Web page,
http://alephwww.cern.ch/ALEPHGENERAL/reports/figures/ew/xsec.gif

[7] H. Fritzsch, M. Gell-Mann, and H. Leutwyler, Phys. Lett. **47B** (1973) 365.
D. J. Gross and F. Wilczek, Phys. Rev. Lett. **30** (1973) 1343.
H. D. Politzer, *ibid.* **30** (1973) 1346.
S. Weinberg, Phys. Rev. Lett. **31** (1973) 494

[8] M. Gell-Mann, Phys. Rev. **125** (1962) 1067.

[9] See *eg* R.P. Feynman, Photon-Hadron Interaction, Benjamin, Reading (1972).

[10] See *eg.*, M. Gell-Mann, Y. Ne'eman, The Eightfold Way, Benjamin, New York (1972).

[11] Mark I Collab., G.Hanson *et. al.*, Phys. Rev. Lett. **35** (1975) 1609.

[12] J.D. Bjorken, S.J. Brodsky, Phys. Rev. **D1** (1970) 1416.

[13] TASSO Collab., M. Althoff *et. al.*, Z. Phys. **C22** (1984) 307.

[14] S. Brandt *et. al.*, Phys. Lett. **12** (1964) 57.
E. Farhi, Phys. Rev. Lett. **39** (1977) 1587.

[15] R. Marshall, Z. Phys. **C43** (1989) 595.

[16] TASSO Collab., R. Brandelik *et al.*, Phys. Lett. **86B** (1979) 243.
Mark J. Collab., D. P. Barber *et al.*, Phys. Rev. Lett. **43**, (1979) 830.
PLUTO Collab., C. Berger *et al.*, Phys. Lett. **86B** (1979) 418.
JADE Collab., W. Bertal *et al.*, *ibid.* **91B** (1980) 142.

[17] J. Ellis, M. K. Gaillard, and G. G. Ross, Nucl. Phys. **B111** (1976) 253; *erratum* **B130** (1977) 516.

[18] J. Ellis, I. Karliner, Nucl. Phys. **B148** (1979) 141.

[19] P. Hoyer, P. Osland, H.G. Sander, T.F. Walsh and P.M Zerwas, Nucl. Phys. **B161** (1979) 349.
E. Laermann, K.H. Streng and P.M.Zerwas, Z. Phys. **C3** (1980) 289; *erratum ibid* **C52** (1991) 352.

[20] SLD Collab., K. Abe *et. al.*, Phys. Rev. **D55** (1997) 2533.
OPAL Collab., G. Alexander *et. al.*, Z. Phys. **C52** (1991) 543. ALEPH Collab., R. Barate *et. al.*, CERN-PPE-96-186 (1996), Submitted to Phys. Rept.

[21] S.L. Wu, Phys. Rep. **107** (1984) 59.

[22] W.J. Marciano, Phys. Rev. **D12** (1975) 3861.
G.A. Leibbrandt, Rev. Mod. Phys. **47** (1975) 849

[23] G. Sterman, S. Weinberg, Phys. Rev. Lett. **39** (1977) 1436.

[24] G. Kramer, B. Lampe, DESY 86-119 (1986).

[25] G. Kramer, Theory of Jets in Electron Positron Annihilation, Springer Tracts of Modern Physics, Vol **102**, Springer (1984).

[26] T. Appelquist, H. Georgi, Phys. Rev. **D8** (1973) 4000.
A. Zee, Phys. Rev. **D8** (1973) 4038.

[27] SLD Collab., K. Abe *et al.*, Phys. Rev. **D51** (1995) 962.

[28] G. Altarelli, G. Pairsi, Nucl. Phys. **B126** (1977) 298.

[29] R.D. Field and R.D. Feynman, Nucl. Phys. **B136** (1978) 1.

[30] F.E. Paige and S.D. Protopopescu, in Physics of the Superconducting Supercollider-1986 (1987) 320.

[31] X. Artru and G. Mennessier, Nucl. Phys. **B70** (1974) 93.

[32] T. Sjöstrand, Comp. Phys. Commun. **82** (1994) 74.

[33] T. Sjöstrand, Comp. Phys. Commun. **43** (1987) 3.

[34] T. Sjöstrand, CERN-TH-7112/93 (1993).

[35] B. Foster, Electron-Positron Annihilation Physics, 1990.

[36] G. Marchesini and B.R. Webber, Nucl. Phys. **B310** (1988) 461. w

[37] G. Marchesini *et. al.*, Comp. Phys. Comm. **67** (1992) 465.

[38] S. Bethke *et. al.*, Nucl. Phys. **B370** (1992) 310.

[39] JADE Collaboration, W. Bartel *et. al.*, Z. Phys. **C33** (1986) 23.

[40] P.N. Burrows, Z. Phys. **C41** (1988) 375.

[41] OPAL collaboration, M.Z. Akrawy *et. al.* Z. Phys. **C47** (1990) 505.

[42] P.N. Burrows and H. Masuda, SLD Physics Note-36 (1996).

[43] C. Peterson *et. al.* Phys. Rev. **D27** (1983) 105.

[44] SLD Collaboration, K. Abe *et. al.*, Phys. Rev. **D53** (1996) 1023.

[45] R. Brun *et. al.*, CERN DD/EE/84-1 (1987).

[46] T. J. Pavel, *Measurement of Charged Spectra at the Z^0 with Čerenkov Ring Imaging*, Ph.D Thesis, SLAC(1997), SLAC-R-491.

[47] M. Briedenbach *et. al.*, **SLAC-PUB-6313**. Presented at the 2^{nd} International Workshop on Physics Experiments with Linear Colliders, Waikala, Hawai, April 1993.

[48] R. Koontz *et. al.*, **SLC-PUB-5890**. Presented at Linac '92 Conference, Ottawa, Canada, Aug. 1992.

[49] M.Woods, SLAC-PUB-6694. Polarization at SLC, Presented at the Eleventh International Symposium on High Energy Spin Physics, 1995.

[50] N. J. Allen, *A Measurement of the Tau Neutrino Helicity at SLD*, Ph.D. Thesis, Brunel University (1997).

[51] T. Maruyama *et. al.* Phys. Rev **B46** (1992) 4261.

[52] SLD Collab., K. Abe *et. al.*, "Measurement of A_b from the left-right forward-backward asymmetry of B quark production in Z^0 decays using a momentum weighted track charge technique.", Phys. Rev. Lett **74** (1995) 2890.
SLD Collab., K. Abe *et. al.*, "An improved measurement of the left-right Z^0 cross-section asymmetry.", Phys. Rev. Lett **78** (1997) 2075.
SLD Collab., K. Abe *et. al.*, "Direct measurement of leptonic coupling asymmetries with polarised Z^0s", Phys. Rev. Lett **79** (1997) 804.

[53] SLD Collab., SLD Design Report, SLAC-0273 (1984).

[54] C.J.S. Damerell *et. al.*, Nucl. Inst. Meth. **A288** (1990) 236.

[55] M.S. Robbins, *Radiation Damage Effects in Charged Coupled Devices*, Ph.D. Thesis, Brunel University (1992).

[56] S.C. Berridge *et. al.*, IEEE Trans. Nucl. Sci. **39**, 1242 (1992)

[57] M.D. Hildreth *et. al.*, IEEE Trans. Nucl. Sci. **42** (1994) 451.
M.D. Hildreth *et. al.*, Nucl. Inst. Meth **A367** (1995) 111.

[58] G. Knoll, *Radiation Detection and Measurement*, Second Edition, Wiley, Chichester, UK (1989).

[59] K. Abe *et. al.*, Nucl. Inst. Meth. **A343** (1994) 74.

[60] D. Axen *et. al.*, Nucl. Inst. Meth. **A328** (1993) 472.

[61] S. Gonzalez Martirena, *A calorimetric Measurement of the Strong Coupling Constant in Electron - Positron Annihilation at a Center-Of-Mass Energy of 91.6 GeV*, Ph.D. Thesis *SLAC-R-439*

[62] A.C.Benvenuti *et. al. Nucl. Inst. & Meth.* **A276** (1989) 94.

[63] D. Williams, *The Left-Right Forward-Backward Asymmetry for B Quarks at the SLD.*, Ph.D. Thesis, MIT (1994) SLAC-R-445.

[64] P. Billoir, Nucl. Instr. Meth. **225** (1984) 352.

[65] M.G. Strauss, *Performance of the SLD CCD pixel vertex detector and design of an upgrade*, Proceedings of 1994 ICHEP, Glasgow, 1179-1184.

[66] Su Dong, private communication (1997).

[67] EEV, *CCD32-60 Sensor design specification for SLAC*, DAS 532802 (1994).

[68] The CCDs were manufactured by the EEV Company, Chelmsford, Essex, United Kingdom.

[69] S.M. Sze, *Semiconductor Devices, Physics and Technology*, Wiley (1985).

[70] S.J. Hedges, *Production and Reliability Aspects of the CCD Mosaic for the SLD Vertex Detector*, Ph.D. Thesis, Brunel University (1991).

[71] CV-1142 adhesive produced by McGlen NuSil Corporation, Carpinteria, California, U.S.A.

[72] G.G. Harman, IEEE Trans. on parts, hybrids and packaging, Vol 13 (1977) 406.

[73] V.H. Winchell and H.M. Berg, IEEE Trans. Components and Hybrids, Manu. Tech., Vol 1 (1978) 211.

[74] VXD3 Group, K. Abe *et. al.*, To appear in *Nucl. Inst. & Meth.* (SLAC-PUB-7385, July 1997)

[75] Instrument grade hot isostatically pressed beryllium I-250 from Brush Wellman.

[76] P.J. Dervan and E. Etzion, SLD-Note 253 (1996).

[77] Capacitec Inc., Ayer, Massachusetts, USA. The 4100-S amplifier units and HPB-375 probes were used.

[78] C.J.S.Damerell et al, Proceedings of the 26th Int. Conf on High Energy Physics, Dallas, 1992 World Scientific, New York, (1992) Vol 2, 1862.

[79] F. James and M. Roos, Comp. Phys. Comm. **10** (1975) 343.

[80] TASSO Collab., R. Brandelik *et al.*, Phys. Lett. **97B** (1980) 453.
PLUTO Collab., C. Berger *et al.*, Phys. Lett. **97B** (1980) 459.
CELLO Collab., H. J. Behrend *et al.*, Phys. Lett. **110B** (1982) 329.

[81] L3 Collab., B. Adeve *et al.*, Phys. Lett. **B263** (1991) 551.
OPAL Collab., Z. Phys. **C52** (1991) 543.
DELPHI Collab., P. Abreu *et al.*, Phys. Lett. **B274** (1992) 498.
SLD Collab., K. Abe *et al.*, Phys. Rev. **D55**, (1997) 2533.

[82] OPAL Collab., G. Alexander *et al.*, Phys. Lett. **B388** (1996) 659.

[83] G. C. Ross, Electroweak Interactions and Unified Theories, Proc. XXXI Rencontre de Moriond, 16-23 March 1996, Les Arcs, Savoie, France, Editions Frontieres (1996), ed. J. Tran Thanh Van. p481.

[84] T. Rizzo, Phys. Rev. **D50** (1994) 4478.

[85] T. Rizzo, private communication (1996).

[86] J.M. Yamartino, *A Measurement of the e^+e^- Decay Width of the Z^0*, PhD Thesis, MIT, February 1994; SLAC-R-426, Chapter 4; J. M. Yamartino, *Hadronic Event Selection Using the LAC*, SLD Physics Note 14, 1993.

[87] H.A. Neal, *Measurements of the $\Gamma(Z^0 \to b\bar{b})/(Z^0 \to hadrons)$ using SLD*, Ph.D Thesis, SLAC(1995), SLAC-R-95-473.

[88] SLD Collaboration, K. Abe *et. al.*, Phys. Rev. **D53** (1996) 1023.

[89] K. Hayes, Proceedings of the Third Mark II Workshop on SLC Physics, SLAC-R-315, July 1987.

[90] Mark II Collaboration, R.G. Jacobsen *et. al.*, Phys. Rev. Lett. **67** (1991) 3347.

[91] V. Blobel, CERN 85-09, "Unfolding Methods in High Energy Physics Experiments," Proceeding of the CERN school of Computing (1984) 88.

[92] J. Coller *et. al.*, SLD Physics Note 57, May 1997.

[93] D.J. Jackson, Nucl. Inst. Meth. **A388** (1997) 247.

[94] SLD Collab., K.Abe *et. al.*, SLAC-PUB-7585, Submitted to the International Europhysics Conference on High Energy Physics (HEP97) EPS-118, 19-26 August 1997, Jerusalem, Israel.

[95] W.S. Boyle and G.E. Smith, Bell Syst. Tech. Journal, **49** (1970) 587.

[96] R.H. Walden *et. al.*, Bell Syst. Tech. Journal, **51** (1972) 1635.

[97] C.J.S. Damerell *et. al.*, SPIE, Vol. **591** Solid State Imagers and Their Applications (1985), 19.

[98] M.J. Howes and D.V. Morgan (ed), *Charge-Coupled Devices and Systems*, Wiley (1979).

[99] J.D.E. Beynon and D.R. Lamb, *Charge-Coupled Devices and their Applications*. McGraw-Hill (1982).

[100] C.J.S. Damerell, *Vertex Detectors: The State of the Art and Future Prospects*, RAL-P-95-008 (1995).